Ultrafast optically-induced magnetization and conductivity dynamics in the europium chalcogenides

M.C. Donker

Ultrafast optically-induced magnetization and conductivity dynamics in the europium chalcogenides

Michiel Christiaan Donker

Zernike Institute PhD thesis series 2014-12
ISSN: 1570-1530
ISBN (book): 978-90-367-7008-8
ISBN (electronic version): 978-90-367-7007-1

The work presented in this thesis was performed in the Optical Condensed Matter Physics research group of the Zernike Institute for Advanced Materials at the University of Groningen in the Netherlands.

Printed by: Ipskamp drukkers
Cover: Hans Sombekke

university of groningen

university of groningen

Ultrafast optically-induced magnetization and conductivity dynamics in the europium chalcogenides

Proefschrift

ter verkrijging van de graad van doctor aan de
Rijksuniversiteit Groningen
op gezag van de
rector magnificus prof. dr. E. Sterken
en volgens besluit van het College van Promoties.

De openbare verdediging zal plaatsvinden op

vrijdag 20 juni 2014 om 11:00 uur

door

Michiel Christiaan Donker

geboren op 24 september 1982
te Zwolle

Promotor
Prof. dr. ir. P.H.M. van Loosdrecht

Beoordelingscommissie
Prof. dr. R. Broer
Prof. dr. B. Koopmans
Prof. dr. L.H. Tjeng

Contents

Chapter 1

Introduction

The title of this thesis is “ultrafast optically-induced magnetization and conductivity dynamics in the europium chalcogenides”. From the title it is clear what kind of materials are studied in this thesis: the europium chalcogenides (EuO/EuS/EuSe/EuTe), which belong to a group of magnetic semiconducting materials. In this thesis we particularly focus on EuO/EuTe. It is also clear what physical observables we study: the conductivity and the magnetization versus time during or after an optical perturbation. What remains unclear is the most important thing: what kind of physics are we looking for? This is the first thing we will discuss in this Chapter. After having discussed the main physics, we turn to the materials and methods used in this work and end this introductory Chapter with a discussion of the scope of this thesis and giving an overall outline.

1.1 The Physics: the interaction of conduction electrons and localized magnetic moments

The interaction between conduction electrons and localized moments is a widely studied topic in condensed matter physics and is interesting both from a purely scientific as well as from a technological point of view. We will give some examples which will serve as an introduction to the topic, before specifying what we are exactly studying.

1.1.1 Magnetic impurities in metals: the RKKY interaction

The exchange interaction (J_{RKKY}) between itinerant electrons and magnetic impurities in metals has an oscillatory behavior as a function of the distance to the impurity, and can be both ferromagnetic and antiferromagnetic, see Fig 1.1 (left). This interaction is known as the RKKY interaction and can be seen as the Friedel oscillations of the spin density due to a delta function magnetic field $H=H_0\delta(r)$ [1].

The discovery of the Ruderman-Kittel-Kasuya-Yoshida (RKKY) interaction made scientist realize the possibility of coupling two ferromagnetic layers (with a non-magnetic spacer in between) antiferromagnetically, which in turn has been essential for the development of so-called spin valves devices [2,3]. In a spin valve device the conductivity is high when the metallic layers are antiferromagnetically aligned (B = 0 T, see Fig 1.1, middle), and low when the metallic layers are ferromagnetically aligned. Small external magnetic fields (B) may switch the alignment, making spin-valve devices excellent magnetic field sensors [1]. These spin valves, which are based on the Giant Magneto-Resistance (GMR) effect [1], were widely used as magnetic field sensor in for instance magnetic storage technology.

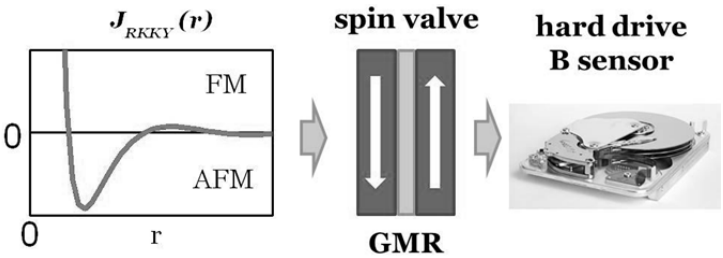

Figure 1.1 | Left) Strength of the RKKY exchange interaction constant, J_{RKKY}, in a metal versus distance to a magnetic impurity. Middle) Spin valve configuration. The magnetic layers are dark grey and the non-magnetic spacer is light grey. Arrows indicate the direction of the magnetization. Right) Hard drive. The magnetic field sensor in a hard-drive was based on the GMR effect.

The RKKY coupling can also lead to ferromagnetism in materials with a *lattice* of localized moments and itinerant electrons, as is the case in Gadolinium. Gadolinium is magnetic because of the localized *f* moments, and metallic due to the partial filled 5d/6s conducting band [4]. The nearest neighbor (nn) 4*f*-4*f* direct exchange interaction is small due to the localized nature of the *f* states and hence the small orbital overlap, and cannot account for the observed ferromagnetism in Gd. Instead, the ferromagnetic coupling between localized *f*-moments is mediated by the 5*d*/6*s* conduction electrons. This spin-polarized conduction electron mediated coupling between the localized moments is strong, leading to a magnetic ordering temperature of about 300 K for Gd metal.

The discussion of the RKKY interaction is based on perturbation theory in J/ε_F, in which J is the localized moment-itinerant electron exchange interaction and ε_F is the Fermi energy (defined as the energy difference between the highest and lowest occupied single-particle states, in a system of non-interacting fermions at absolute

zero temperature) [5]. The condition that J/ε_F is small (small exchange interaction, high free electron concentration) is satisfied in most (if not all) metals. However later on, when we discuss the magnetic properties of diluted ferromagnetic semiconductors, we are in a situation where ε_F is small and J/ε_F large due to the small conduction electron density. In this case one needs to consider a modified RKKY model.

1.1.2 Kondo and Heavy fermion systems

More exotic effects may occur at very low temperatures. In normal metals, the conductivity is expected to increase with decreasing temperature due to the increase of the scattering time. This is not always true for metals which are doped with magnetic impurities. At very low temperatures, a decrease of the conductivity can be observed in these materials, which is named the Kondo effect [5]. The decrease of the conductivity at low temperature is related to the increased scattering rate between the antiferromagnetically coupled conduction electron spin and the impurity spins. Interesting effects can also happen in materials with a magnetic *lattice*, instead of magnetic *impurities*. In certain rare-earth intermetallic compounds with a lattice of localized 4f/5f moments, it was found that the effective electron mass can be up to 1000 times larger than the free electron mass [5,6], which lead to the name 'heavy fermion compounds' for these systems. The phenomenon is explained in terms of an antiferromagnetic localized moment-itinerant electron interaction. In some systems with itinerant electrons and localized moments, like the Kondo systems, there exists a strong correlation between the transport and magnetic properties. In this case apart from determining the transport properties at low temperature, the localized moment-itinerant electron interaction also strongly affects the magnetic properties, leading for instance to the quenching of the impurity moment through the formation of a singlet state at low temperatures [1].

1.1.3 Double exchange and colossal magneto resistance

A strong correlation between the magnetic and transport properties was also found in the well-known Colossal Magneto-Resistance (CMR) manganites (like $La_{1-x}Ca_xMnO_3$) in which there is a magnetic lattice consisting of 3*d* Mn^{3+} and Mn^{4+} moments [7]. $LaMnO_3$ (x=0) is a Mott-Hubbard insulator and the exchange is antiferromagnetic because of superexchange interactions [5]. For hole-doped $La_{1-x}Ca_xMnO_3$ with *x*=0.3 the situation is quite different [8]. The net exchange is

ferromagnetic since there is, apart from antiferromagnetic super exchange, a ferromagnetic contribution coming from the double exchange mechanism. In the double exchange mechanism, we have to consider the intra-atomic Hund's rule exchange J_H between the *d* holes and localized 3*d* magnetic moments, see the left picture in Fig. 1.2. When the intra-atomic Hund's rule exchange is strong, the hole spin tends to be antiparallel to the localized electron spins which can lead to ferromagnetism. In order to understand this, we consider the hopping of a hole, with hopping matrix element *t*, from one site to a neighboring site. We can distinguish two cases: in the case that the localized moments of two nearest neighbors are parallel, the hole can delocalize and therefore minimize its kinetic energy. The situation is different when the moments of two nearest neighbors are antiparallel. In this case the hole will not delocalize since the energy loss ($\sim J_H$) will exceed the energy gain ($\sim t$) [5]. This explains the tendency for ferromagnetism in hole-doped $La_{0.7}Ca_{0.3}MnO_3$. It also explains that the material is a ferromagnetic metal below the Curie temperature (all spins aligned, hopping costs no energy), while it is a paramagnetic insulator above T_c (random spin orientation, hopping typically costs energy $\sim J_H$). In the case for $La_{0.7}Ca_{0.3}MnO_3$, the conductivity is predominantly dependent on the magnetization and much less on the temperature and applied magnetic field (other than that the magnetization *M* is temperature and magnetic field dependent *M*[*B*,*T*]) [8]. The magneto-resistance versus applied magnetic field near $T=T_c$ is shown in the right graph of Fig. 1.2, from which we can see the negative colossal magneto-resistance (CMR). The MR around T_c is large due to the fact that that the magnetic susceptibility is very high at T_c, which means that it is easy to align the spins after which the conduction electrons can delocalize [5,8].

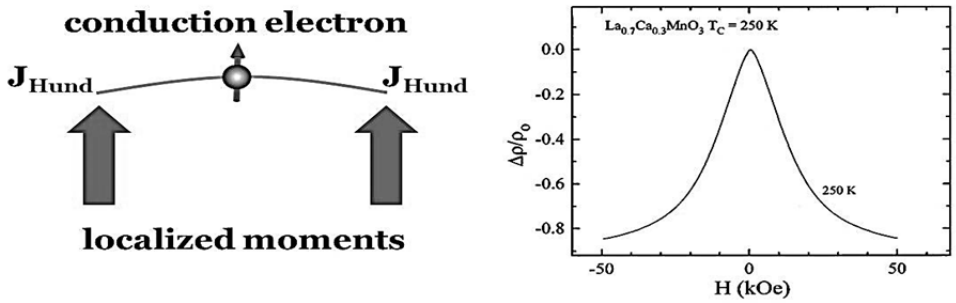

Figure 1.2 | Left) Hund's rule intra-atomic exchange interaction between localized moments and a conduction electron. Right) CMR in $La_{1-x}Ca_xMnO_3$ with x=0.3 at 250 K ($\approx T_c$) taken from [8], with permission. ρ_0= resistivity at H=0 Oe. $\Delta\rho$= resistivity at field *H* minus ρ_0.

1.1.4 Ferromagnetic semiconductors

Until now we mainly focused on the interaction between conduction electrons and localized moments in metallic systems. The focus of the present thesis is however on electronically gapped systems, *i.e.* magnetic semiconductors, where the conduction electron concentration is much lower. In this category of semiconducting magnetic materials we can distinguish two different types:

1) *Extrinsic magnetic semiconductors* in which the magnetism in an otherwise non-magnetic semiconductor is introduced by including magnetic dopants. Very well-known are the transition metal doped III/V and II-VI semiconductors. In Mn-doped GaAs for instance, the density of magnetic moments and the holes is varied by changing the Mn (acceptor) concentration [9]. The magnetic ion concentration is *diluted* and Mn-doped GaAs is therefore called a diluted magnetic semiconductor (DMS). The physics of DMS is interesting and intricate, for a review see [10]. In this review magnetic exchange mechanisms are discussed where localized Mn *d* magnetic moments interact either with itinerant *p*-holes (*p*-*d* Zener model) or with *d*-holes (double exchange). Here we use the term "double exchange" in the case that there is exchange due to (*d*) electron hopping between (*d*) magnetic ions with *different* valencies, as discussed before; see also Figure 1.3 (left). In this case the itinerant electron (e_g) and localized moments (t_{2g}) are in the same *d*-shell but in different sub bands [11].

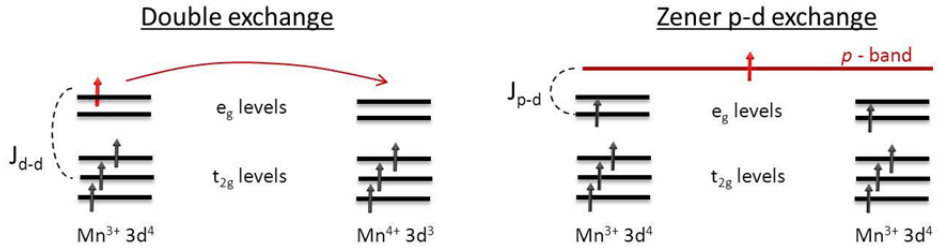

Figure 1.3 | Different exchange mechanisms active in diluted magnetic semiconductors. In the picture the black arrows represents localized electron spins whereas the red arrow are itinerant electron spins. Left) Double exchange mechanism where there is intra-atomic *d*-*d* exchange (Hund's) between the e_g electron the other Mn *d*-electron spins. Right) Zener *p*-*d* exchange where there is *p*-*d* exchange between Mn^{3+} *d*-electron spins and valence band *p*-holes.

The ferromagnetic exchange in the *p*-*d* Zener model is coming from the exchange interaction of itinerant electrons in the valence band (*p*) with

localized magnetic ions (*d*) which can have the *same* valence, see Figure 1.3 (right). In this case the itinerant electron (*p*) the localized moments (d) are in different bands [11]. Note that in the *p-d* Zener model the *p*-electrons are always mobile (band conduction) while in the double exchange model the *d*-holes have a high mobility only in the case of ferromagnetic alignment.

Apart from the hole mediated ferromagnetism, different contributions to the ferromagnetic exchange can come from mechanisms in which no mobile carriers are involved, including the occurrence of bound magnetic polarons, or exchange interactions coming from electrons which are bound by defects/vacancies/impurities [10]. The physics in these systems is still not understood in all its details but there is a consensus that the main characteristics for lightly doped DMS can be understood in terms of hole mediated ferromagnetism in the *p-d* Zener model [9,10]. In lightly doped DMS, due to the large separation between the transition metal ions, the transfer integral is small and the contribution from double exchange is minor.

2) *Intrinsic magnetic semiconductors.* In these semiconductors there is a magnetic lattice, and therefore they are also called concentrated magnetic semiconductors. Intrinsic magnetic semiconductors can be (anti) ferromagnetic even without the presence of itinerant holes/electrons, due to the high density of magnetic ions. The europium chalcogenides belong to this category of intrinsic magnetic semiconductors. The magnetic lattice in the europium chalcogenides is formed by Eu^{2+} 4*f* magnetic ions [12]. Due to the localized nature of 4*f* states, which form the upper valence band, the 4*f* holes are considered to have a negligible contribution to the conductivity. The valence band is separated by about 1.2 eV from the 5*d*/6*s* conduction band. Due to the high density of magnetic ions, there is a considerable superexchange interaction in the europium chalcogenides, see the next section for more details [12]. Apart from the next-nearest neighbor (oxygen mediated) exchange interaction, there is also a nearest neighbor (nn) exchange interaction. This nn exchange is the main reason of the ferromagnetism in EuO. We can understand this from a model which is *similar* (but quite different) to the *p-d* Zener model mentioned above. Here instead of Mn-*d* localized magnetic moments, we have to consider Eu-*f* localized magnetic moments and instead of itinerant *p*-holes, we have to consider itinerant Eu *d*-conduction electrons. There is one observation which makes clear why EuO is much different than Mn-doped GaAs: intrinsic EuO (non-doped) is also ferromagnetic at T=0 K (T_c= 69K) when

there are no *d* conduction electrons [12]. In order to understand this, one needs to consider virtual excitations from the 4*f* valence band to the 5*d* conduction band, and from the 5*d* conduction band back to the 4*f* conduction band. The ferromagnetic *d-f* exchange between the *f* localized moments and the 'virtual' itinerant *d* electrons, is at the origin of the ferromagnetism in intrinsic EuO.

1.1.5 Comparison of different well-known CMR materials: n-doped EuO and $La_{0.7}Ca_{0.3}MnO_3$

The situation in intrinsic ferromagnetic semiconductors becomes even more interesting when EuO is electron-doped. In this case, EuO exhibits the CMR effect as well as a metal insulator transition near or at the magnetic ordering temperature; these effects are not observed in intrinsic EuO [8,13]. The physics behind these interesting phenomena will be discussed later on. Right now we will only compare the situation in EuO with the situation in another well-studied and well-known CMR compound: $La_{0.7}Ca_{0.3}MnO_3$. Although there are large differences between the EuO and $La_{0.7}Ca_{0.3}MnO_3$, it is interesting to observe that in both cases the conductivity is depends exponentially on the magnetization, *i.e.* is proportional to $e^{a\,M_r}$, in which *a* is a constant and M_r is the reduced magnetization [8].

Let us compare the systems in order to see the main differences. As discussed before, non-doped (x=0) $La_{1-x}Ca_xMnO_3$ is a Mott-Hubbard insulator for *x*=0 and is antiferromagnetic due to superexchange interactions. There is an antiferromagnetic background and the ferromagnetic component is coming from the interaction of *d*-holes with *d* magnetic moments. This is the double exchange contribution. In $La_{1-x}Ca_xMnO_3$, the doped electrons end up in the same band (*d*) as where the magnetism is (*d* magnetic moments).

The situation in EuO is different. Non-doped EuO is a ferromagnetic semiconductor and is already ferromagnetic due to the interaction of the 'virtual' itinerant *d* conduction electrons with localized *f* magnetic moments (nearest neighbor) and due to *ferromagnetic* superexchange (next nearest neighbor). In this case there is a ferromagnetic background. Another ferromagnetic component can come from the interaction of 'real' *d* electrons, when present, with the lattice of localized *f* magnetic moments. In EuO, the doped electrons end up in a different band (*d*) than where the magnetism is (*f* magnetic moments) [13].

Compared to the CMR material $La_{1-x}Ca_xMnO_3$, EuO is a much less complicated system. There is no charge or orbital order, no Jahn-Teller effect, there are no large

temperature dependent changes in the (simple rocksalt) crystal structure, and there is a ferromagnetic background in the non-doped case. Also the fact that the itinerant carriers reside in a different band than the one from which the magnetism originates makes the situation in EuO less complicated. This means that EuO can be considered as a model CMR system where the interaction between (doped) electrons and a ferromagnetic lattice of localized moments can be studied. In this thesis the interaction of the 'real' conduction electrons and the localized *f* magnetic moments in EuO and EuTe is studied. Before going into more details, we will first discuss the physical properties of the europium chalcogenides.

1.2 The Material: europium chalcogenides, a class of intrinsic magnetic semiconductors

In this section we describe the physical properties of the europium chalcogenides. It is not our intention to give a complete review about these materials and we only focus on some of the properties which are relevant for this thesis. For some excellent reviews, we refer to the Ph.D. thesis of Steeneken [12] and to the review paper by Mauger and Godart [14].

1.2.1 Introduction

The europium chalcogenides are well-studied materials, which have attracted a lot of interest since the 1950's [14]. The main reason for the strong interest is that they belong to the rare group of intrinsic magnetic semiconducting materials. There are not so many intrinsic magnetic semiconducting materials; most magnetic materials are either metals or insulators. Apart from this, in intrinsic and *n*-doped europium chalcogenides, the materials are archetypical systems in which the interaction between conduction electrons and a lattice of localized moments can be studied. This interaction leads to a variety interesting phenomena like a metal insulator transition (MIT) and colossal magneto-resistance. Moreover the magnetic ordering temperature is strongly dependent on the free carrier concentration (T_c in doped EuO can be increased by 50 K with respect to intrinsic EuO [16]) and the conduction bottom in EuO is fully spin-polarized at low temperatures [12]. A lot of different theoretical models have been proposed to account for the increase in T_c and the presence of a MIT and CMR, see [12,14] and the next sections. However, partially due experimental uncertainties, the discussion is still ongoing.

The problem in the study of this material has always been the stoichiometry control and stoichiometry determination. Small changes (<1%) in the stoichiometry can lead to huge changes in the transport (presence of CMR and MIT) and the magnetic properties (T_c) [12]. Therefore a careful comparison with different theoretical models only makes sense when for a certain sample the exact stoichiometry, the transport properties (free carrier concentration, conductivity, magneto-resistance) and magnetic properties are known. A combination of these measurements on high quality films has been performed only recently, see for instance [13].

The improved preparation quality [15--17] and the development of novel and better experimental and theoretical methods has led to a re-gained interest in the europium chalcogenides and will help to give a more detailed picture of what is happening in these materials. The interest is also boosted by the spintronics field which is looking for magnetic semiconducting materials with a high degree of spin-polarization in the conduction band. The improved synthesis and the integration of EuO with silicon [18] make EuO a promising material for future applications. However for this to happen, the magnetic ordering temperature has preferably to be increased to room temperature values (or even more). In the next section we discuss the structural, electronic, magnetic and transport properties of the europium chalcogenides. The optical properties are discussed extensively in Chapter 2.

1.2.2 Structure

The europium monochalcogenides ($Eu^{2+}Ch^{2-}$) all have a simple rock salt structure; see the Fig 1.3 [14]. Eu^{2+} is octahedrally surrounded by O^{2-} ions. In the rock salt structure there are alternating [111] layers of europium ions and chalcogenides ions, see the right picture in Fig. 1.3. Each Eu^{2+}ion has 12 nearest neighbor Eu^{2+}ions, and 6 next nearest neighbor Eu^{2+}ions. The lattice constant is about 5.1 Å for EuO, and increases to 6.6 Å for EuTe which can be understood from the fact that the ion radius is larger for the heavier chalcogenide elements [12]. The lattice constant in EuO decreases from 5.144 Å at room temperature towards 5.127 Å at 10 K (-0.3%) [12]. Below the magnetic phase transition there is an additional lattice constant contraction due to magnetostriction of about -0.16% [19]. Based on this we can conclude that in EuO, there are no large structural changes at the phase transition and that the structural and magnetic degrees of freedom are weakly coupled only.

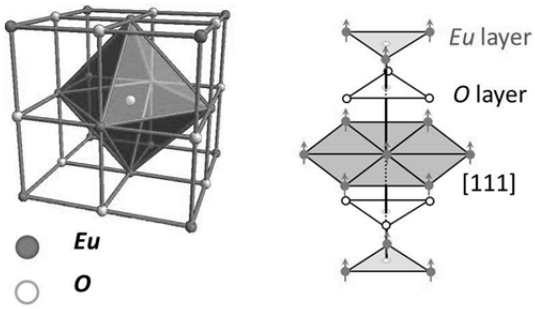

Figure 1.3 | Rock salt structure of EuO. Eu^{2+} is octahedrally surrounded by O^{2-}. In the europium monochalcogenides there are alternating [111] layers of europium ions and chalcogenides ions. In the right picture, the interlayer separation has been enhanced in order to make the picture more clear.

1.2.3 Electronic properties

In EuO, europium is divalent (Eu^{2+}). Europium can be both divalent and trivalent which leads to the fact that in air EuO can oxide further to unwanted Eu_2O_3 [12]. Eu^{2+} is a $4f^7$ ion which means that the 4*f* shell is half filled. According to Hund's rule, the ground state is ^8S (S=7/2, L=0). The next higher lying state with ^6S (S=5/2) is far away: 5.4 eV [12]. The energy cost of making a $4f^7+4f^7 \rightarrow 4f^6+4f^8$ transition, where one electron is transferred from one to another ion, is 11 eV [12]. Without the presence of these electronic correlations, EuO would have been a metal with a half filled *f* shell. Due to the large intra-atomic Coulomb and exchange interaction, EuO is a semiconductor with a 4*f* valence band, and a 5*d*/6*s* conduction band. The electronic energy gap is about 1.2 eV at 4.2K. Due to the fact that the 4*f* states are localized, and the overlap between different ions is small, the 4*f* valence band is rather narrow. The 5*d*/6*s* states are more extended resulting in a larger bandwidth for the conduction band. The oxygen 2*p* band lays several eV (≈3.7) below the 4*f* valence band. The 5*d*/6*s* band and 2*p* band are hybridized which means that the conduction band also has some oxygen 2*p* character. The oxygen character of the conduction band can be probed by oxygen K-edge (1*s* to 2*p*) X-ray absorption spectroscopy [12]. Apart from demonstrating the hybridization, these experiments have also shown that the conduction band minimum shows a red shift below T_c which is proportional to the magnetization. At 10K there is a -0.3 eV red shift relative to the value at 69 K.

Also photoemission spectroscopy can be done at the oxygen K-edge. By an Auger process, an oxygen 2p electron (which is the Auger electron) is ejected after which

its energy and spin can be analyzed. In this way the conduction band position and spin-polarization could be determined as was done in [12].The spin-polarization at 10 K is close to 100% (while it is 0% above T_c). The conduction band shift and spin-polarization can be understood in terms of the 4f-5d/6s exchange interaction. More details about the electronic properties will be given in Chapter 2 where we discuss the magneto-optical properties of EuO.

1.2.4 Magnetic properties of intrinsic EuO and EuTe

While EuO is ferromagnetic, EuTe (which has the same structure) is antiferromagnetic. This can be understood from the competition between different lattice constant dependent exchange mechanisms [12,14]. The most strong exchange interaction in EuO is the nearest neighbor (nn) exchange interaction between nearest neighbor Eu^{2+} ions. Central to this exchange mechanism is a virtual excitation from the localized 4*f* state to more extended 5*d*/6*s* states and back to the 4*f* state, see Fig 1.5 (left). This ferromagnetic nn 4*f*-5*d*-4*f* interaction is the origin of ferromagnetism in EuO. In the other europium chalcogenides (S/Se/Te), the nn 4*f*-5*d*-4*f* interaction is also ferromagnetic. However due to the larger lattice constant (+30%), the nn exchange in EuTe is substantially weaker than in EuO (by -92%). The nn 4*f*-4*f* direct exchange interaction is small due to the small 4*f*-4*f* transfer integral and the large intra-atomic Coulomb repulsion.

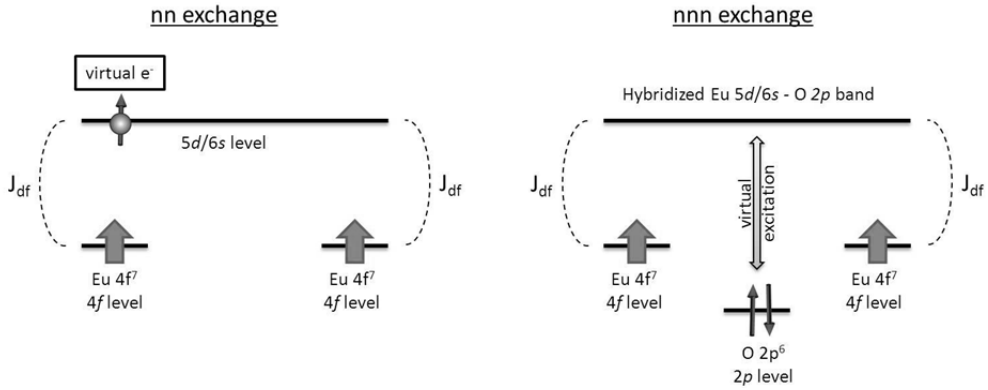

Figure 1.5 | Different exchange mechanisms: nn exhange (left) and nnn exchange (right).

Also Eu 4*f*-O 2*p*-Eu 4*f* superexchange could play a role in determining the magnetism in EuO, as it does in for instance the transition metal (TM) oxides. However, due to the localized nature of the 4*f* states and the large intra-atomic Coulomb repulsion, the Eu 4*f*-O 2*p*-Eu 4*f* Kramers-Anderson superexchange is very small (and antiferromagnetic in sign). This is in contrast to the situation in many of

the transition metal (TM) oxides, where the antiferromagnetic Kramers-Anderson TM *d*-O 2*p*-TM *d* superexchange is quite strong due to the better overlap between the oxygen and the TM orbitals. Other superexchange contributions in the europium chalcogenides come from mechanisms where there is a virtual excitation from the O-2*p* levels to the Eu 5*d*/6*d* conduction band, see Fig 1.5 (right) [12]. The effective exchange interaction in the Eu-chalcogenides is the sum of the different contributions discussed here. It is ferromagnetic in sign for EuO and EuS, and is antiferromagnetic in sign for EuSe and EuTe. The nnn superexchange is the reason for antiferromagnetism in EuTe [12].

1.2.5 Transport and magnetic properties of n-doped EuO: the experimental observations

Intrinsic EuO and EuTe are semiconductors with a 4*f* valence band and a 5*d*/6*s* conduction band. The resistivity in EuO is decreasing with increasing temperature and there is no appreciable change in the electrical resistivity at the magnetic ordering temperature (T_c). The situation changes when the material is *n*-doped. For *n*-doped EuO, a metal insulator transition at T_c and colossal magneto-resistance can be observed. EuO can be *n*-doped in different ways:

- By introducing oxygen vacancies: $Eu_{1+x}O$ with $x>0$ [12].
- By introducing other trivalent magnetic donors like Gd^{3+} in $Eu_{1-x}Gd_xO$. Gd^{3+} and Eu^{2+} are isoelectronic $4f^7$ and the gadolinium ions substitute the europium ions. Moreover, it has been shown that the exchange interaction between Gd^{3+} and Eu^{2+} is also ferromagnetic in EuO [20]. This makes Gd^{3+} ions ideal electron donors which do not disrupt the magnetic lattice too much.
- By photo-excitation (4*f* to 5*d*, valence band to conduction band). In this case also 4*f* holes are generated. This is what we will do throughout this thesis.

Here we focus on $Eu_{1-x}Gd_xO$ thin films since for this material systematic resistivity, magnetization, free carrier concentration and Gd-doping concentration measurements have been performed on high quality samples [13,16]. $Eu_{1+x}O$ with $x>0$ will be discussed in Chapter 6. The *T*-*x* phase diagram of Gd-doped EuO is shown in Fig. 1.6. The data in Fig. 1.6 have been taken from references [13] and [16]. We shall call a system with $\partial\rho(T)/\partial T<0$ a semiconductor and a system with $\partial\rho(T)/\partial T>0$ a metal. For x=0 and $T<T_c$, EuO is a ferromagnetic semiconductor,

while for $T>T_c$ the material is a paramagnetic semiconductor. The behavior for n-doped EuO ($Eu_{1-x}Gd_xO$) is quite different than for intrinsic EuO. In the x=0.25-19.5% range, $Eu_{1-x}Gd_xO$ is a ferromagnetic metal below T_c and a paramagnetic semiconductor above T_c, at least in the temperature range we show (in between 250-300K, the slope $\partial\rho(T)/\partial T$ is small but positive for all the doping concentrations x=0.25-19.5%). Interestingly, even for the lowest doping concentration (x=0.25%), $Eu_{1-x}Gd_xO$ already has a metallic conductivity with $\partial\rho(T)/\partial T>0$ for $T<T_c$. This in contrast with Mott-Hubbard CMR systems like $La_{1-x}Ca_xMnO_3$ which becomes metallic only at a much larger doping concentration, x=23%. The situation for $Eu_{1-x}Gd_xO$ with x=0.25% is consistent with the picture in which EuO is a non-degenerate semiconductor for $T>T_c$ and a degenerate semiconductor for $T<T_c$. The reason for this we will discuss later on.

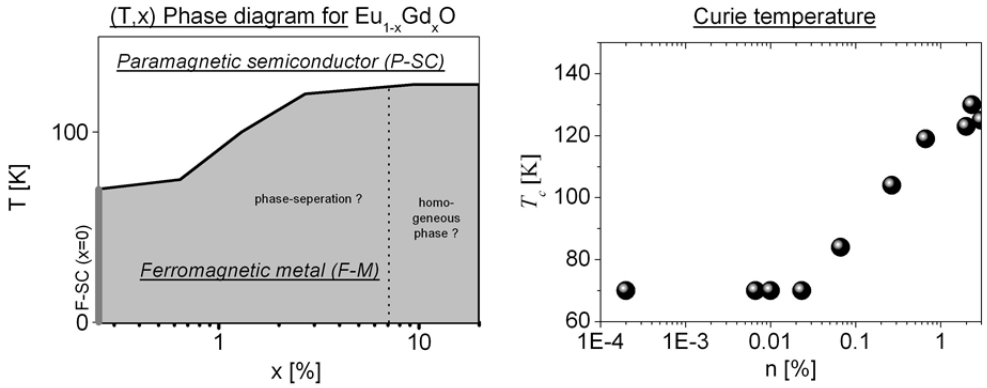

Figure 1.6 | Left) T-x phase diagram of $Eu_{1-x}Gd_xO$. Right) T_c versus carrier concentration n at 4.2K, which was determined from Hall measurements. The data in both figures has been taken from [13,16], with permission.

We can also see from Fig 1.6 that the magnetic ordering temperature is dependent on x. T_c increases from about 70 K for x=0% to about 125 K for x=2%. For higher doping concentrations, T_c saturates to about 125 K. The fact that in the x=0.25-19.5% range, ferromagnetism is always accompanied by metallicity suggests that *mobile* carriers are involved in the increase of T_c.

The dotted line in the phase-diagram represents the boundary between a possible phase separated ferromagnetic phase and a homogeneous ferromagnetic phase. Phase separation could occur due to the formation of ferromagnetic islands in a paramagnetic background due to magnetic polaron formation around a conduction electron or around the Gd^{3+} ion, as was suggested in [16]. It was suggested there that the magnetic polaron regions in EuO have a different and higher T_c than the

surrounding EuO (T_c=69K). At larger doping concentrations, the magnetic polaron islands overlap, resulting in a homogeneous phase with a T_c of about 120 K. When we assume that for the lowest doping concentration (x=0.25%) one is far below the percolation threshold, we can conclude that either these magnetic polarons are mobile (conductive) or that they do not exist. This is based on the fact that even for a low doping concentration of x=0.25% there is a MIT, while there is no MIT for intrinsic EuO (x=0%).

More about the system can be learned by looking at the measured (Hall effect) carrier concentration. It appears that not all Gd atoms donate one electron into the conduction band. Depending on the doping concentration, 0-35% of the Gd atoms donate one electron to the conduction band [13]. The origin of this is unknown but probably there are compensating acceptors like defects or impurities. T_c versus the conduction electron concentration n is shown in the right graph of Fig. 1.6. n has been determined in [13] at 4.2 K. Below n=0.023%, there is no *measurable* increase in T_c. Above n=0.023% T_c starts to increase and there is a strong correlation between the electron concentration and the increase in T_c. Based on this data it was suggested that mobile carriers are responsible for the increase in T_c for n>0.023% rather than *bound* magnetic polarons (bound to donor), as was implied in [16].

One last point we want to discuss is what the origin of the MIT is: a change in the mobility and/or a change in the carrier concentration. Unfortunately we could not find temperature dependent mobility and carrier concentration data in the literature for $Eu_{1-x}Gd_xO$, however this data is available for $Eu_{1+x}O$ (x>0). Depending on the sample and off-stoichiometry the MIT was either due to a change in the mobility (constant n) or due to a change in both of them [21,22]. Large MIT (several orders of magnitude change of conductivity) where shown to be mostly due to large changes in n; the origin of which we will discuss in the next section. The fact that also the mobility can change (increase) by one order of magnitude upon magnetic ordering indicates that we are in a situation where $J_{df} \geq t_d$, in which J_{df} is the intra-atomic *d-f* exchange constant and t_d is the *d* transfer integral. In this case the physics behind the change in *mobility* is similar to the double exchange physics in $La_{0.7}Ca_{0.3}MnO_3$ where the conduction electron can delocalize when the localized moments orders ferromagnetically.

1.2.6 Transport and magnetic properties of n-doped EuO: the model

Below we describe a simple qualitative picture which can account for the transport and magnetic behavior observed in *n*-doped EuO [13]. The increase of the Curie temperature in Gd-doped EuO has been attributed to an indirect exchange interaction (Zener *d-f* like) which is mediated via (mobile) 5d/6s conduction electrons. Upon ferromagnetic ordering, the majority and minority spin conduction band will split due to the intra-atomic *d-f* exchange interaction, see Fig 1.7. The majority-minority spin-splitting is 0.6 eV [12]. For simplicity, in this picture, the donor impurity level (dashed line) is not spin-split and is not temperature dependent. Above T_c the chemical potential is in between the conduction band bottom and the donor level, and the charge transport has an activated nature. In this case EuO is a non-degenerate semiconductor. Below T_c, due to the conduction band spin-splitting, the chemical potential is within the majority-spin band, but below the minority-spin band bottom, and EuO is a degenerate semiconductor. In the picture the onset of ferromagnetism and metallicity are correlated, as was experimentally observed for n>0.023% [13].

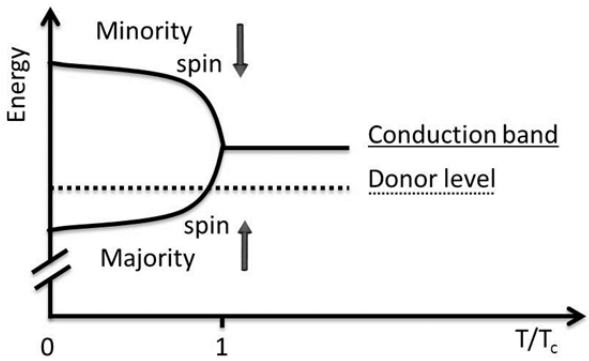

Figure 1.7 | Simple model for the MIT. For details, see text.

In the next section we discuss our experimental methods, after which it will become clearer what we are actually studying.

1.3 The Methods: laser-induced ultrafast magnetization and conductivity dynamics

Our main experimental tools that we used for the work described in this thesis are different variations of pump-probe spectroscopy. These spectroscopies were used to probe magnetization and conductivity dynamics after optical excitation, from

which one can learn more about the conduction electron-localized moment interaction in EuO and EuTe. First we will shortly describe pump-probe spectroscopy and carrier dynamics in semiconductors after which we briefly discuss magnetization dynamics and conductivity dynamics experiments.

1.3.1 Pump-probe spectroscopy

Throughout this thesis, we describe experiments in which EuO or EuTe are perturbed, and in which we follow the behavior of the system during or after the perturbation. The perturbation is a strong, short optical laser pulse with a central wavelength of 800 or 400 nm and pulse duration of about 100 fs. The optical excitation, which is represented by a hammer in Fig. 1.8, is also called the pump (pulse). After the optical excitation we probe the changes in the material using another time-delayed, short, weak, optical pulse. The pulse duration of this so-called probe pulse (represented by the magnifying glass in Fig. 1.8) was in the 0.1-50 ps range, depending on the experiment.

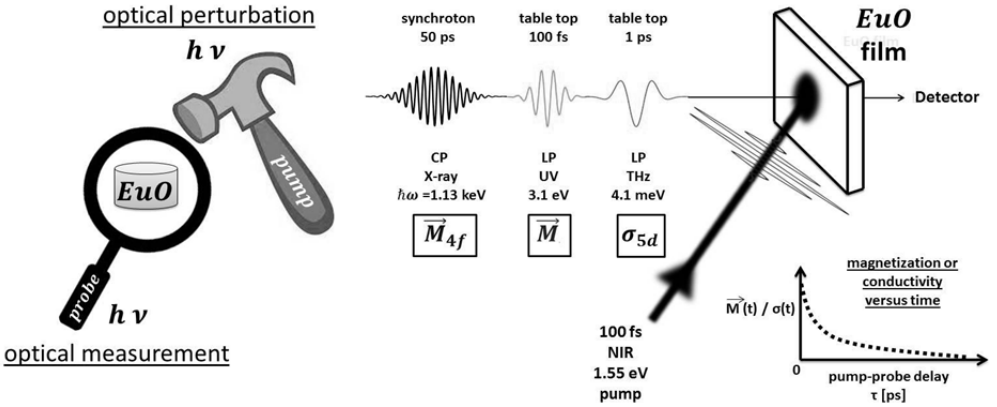

Figure 1.8 | Description of optical pump- optical probe experiments. Left) In a pump probe experiment the sample is excited by an optical pump (hammer) after which the sample is probed by an optical probe (magnifying glass) Right) Pump-probe experimental configuration. We used optical probes with different photon energies (X-ray/UV/THz region) and polarizations (CP=circularly polarized light, LP=linearly polarized light).

The magnetization or conductivity dynamics of the system can be measured by recording the polarization state or the intensity of the probe pulse for different pump-probe delays after optical perturbation, *i.e.* in a stroboscopic manner. The time-resolution in these experiments is limited by the cross-correlation between the pump and probe and was in our case between 0.1-50 ps, again depending on the exact type of experiment. Depending on what we exactly want to probe (magnetization, conductivity), the photon energy of the probe pulse pulse is either,

4.1 meV, 1.55 eV, 3.1 eV or 1.13 keV. The magnetization was probed using photon energies of 1.55 eV, 3.1 eV or 1.13 keV while the conductivity was probed using 4.1 meV pulse. The reason for this we discuss later on. The 4.1 meV, 1.55 eV and 3.1 eV pulses could be generated easily using table-top Ti:sapphire oscillators/amplified laser systems (output=1.55 eV, 100 fs) and non-linear optics. This does not hold for soft X-ray pulses (1.13 keV). These measurements where done in Berlin at a synchrotron facility (Helmholtz Zentrum) where circularly polarized soft X-ray pulses with a pulse duration of 50 ps could be generated. For details, see Chapter 4-6. For clarity, the pump-probe scheme is shown in the right picture of Fig. 1.8. First we excite the material using a pump pulse after which we observe the changes in the material properties by a time-delayed optical probe pulse. Typical carrier and lattice dynamics in semiconductors after a valence to conduction band optical excitation are discussed in the next subsections. From these subsections it will become clearer what the pump exactly does. First we shortly introduce the broad field of laser-induced magnetization dynamics.

1.3.2 Laser-induced magnetization dynamics: a broad field

In thesis we describe several laser-induced magnetization dynamics experiments with a temporal resolution which is better than 50 ps, in most cases around 200 fs. The field of *ultrafast* laser-induced magnetization dynamics started by experiments on the ferromagnetic transition metal Nickel in 1996, see Chapter 3 [23]. Since then the field grew rapidly, and there are many sub-fields and directions. In Fig. 1.9 we categorize the field by looking at different materials, magneto-optical probes, optical pumps and physics. Below we will shortly introduce the field and we will specify in what sub-category of the field we are working.

Materials: Laser-induced magnetization experiments has been performed on different materials with different conductivity (metals, half metals, semiconductors, insulators) and magnetic order (ferromagnetic, antiferromagnetic, ferromagnetic, non-magnetic) [24--27]. Apart from that, experiments have been done on weakly and strongly correlated materials, on transition metals and rare earth metals, and on systems with localized moments and/or itinerant electrons. Depending on the material and pump excitation, a wide range of phenomena can be observed which is much too diverse to discuss here in detail. For a review, see ref. [27]. In this thesis we mainly focus on ferromagnetic materials, which are briefly reviewed in Chapter 3. In our case we study a strongly correlated,

ferromagnetic (or antiferromagnetic) semiconductor with itinerant electrons and localized moments (see also Appendix A for a comparison with different materials). The magnetism comes from the rare earth metal ion Europium.

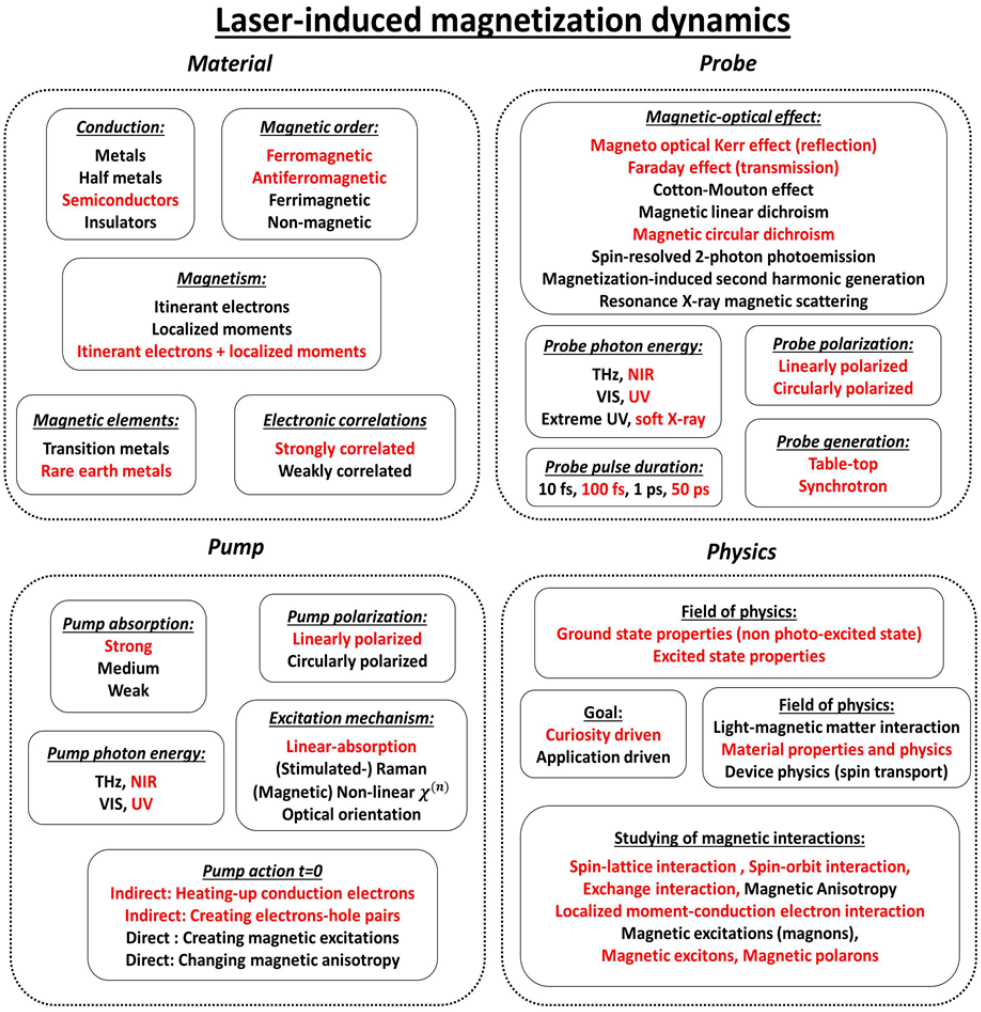

Figure 1.9 | Overview of the field of laser-induced magnetization dynamics, categorized according to materials, experimental approaches, and the physics addressed. The red text refers to aspects relevant to this thesis.

Probe: A wide variety of optical probes have been used in the literature to probe the changes in the magnetic behavior, each with their own characteristics, advantages, and disadvantages. The probes are generally based on different magneto-optical effects which include the Faraday effect, magnetic optical Kerr effect, magnetic circular dichroism and many others (see Fig. 1.9). Probe photon

energies ranging from the THz domain to soft X-ray frequencies, and pulse durations ranging from 10 fs-50 ps has been used in different experiments in the literature. Some experiments where performed using a table-top laser setup while others were done at a synchrotron or free electron laser facility. In our experiments we employed the magneto-optical Kerr effect, Faraday effect and magnetic circular dichroism and we used NIR, UV, and soft X-ray probes which could be both linearly or circularly polarized. These effects will be introduced in chapters 2-5. While most experiments where done with table-top systems, the experiments with the soft-X-ray probe where done at a synchrotron facility.

Pump: In laser-induced magnetization dynamics experiments a wide range of different optical perturbations have been used. Experiments have been performed on weakly or strongly absorbing materials, using pump photon energies in the THz, NIR, VIS or UV range, and using both linearly or circularly polarized pump pulses. EuO is a strongly absorbing material at the pump photon energies used in our work. We used both linearly polarized NIR and UV pump pulses.

Based on the different excitation mechanisms and excitation characteristics, the sample is excited in different ways. The pump action during pump-probe overlap at t = 0 s can be quite diverse. Some possibilities are listed in Fig. 1.9. We can differentiate between indirect and direct mechanisms. In direct mechanisms, magnetic excitations are generated directly (by for instance stimulated Raman scattering or by optical orientation), due to the light-matter interaction with the pump pulse [27]. In another direct mechanism, the light-matter interaction during pump overlap directly changes the magnetic anisotropy, which can affect the magnetization orientation [27]. In this thesis we will not focus on those direct excitation mechanisms. Instead, in our experiments the magnetization is affected in an indirect manner. By the pump pulse, hot conduction electrons are created at t = 0 s, which influences the magnetization via various relaxation pathways [24]. We will describe these pathways briefly later on in this Chapter, and more extensively in Chapters 3-5.

Another interesting categorization can be made by the physical mechanism of excitation. Some experiments are based on the (normal) linear absorption of the pump, while other rely on the stimulated-Raman excitation of spin excitations (mostly in transparent media) using very high pump fluences [27]. Also magnetic non-linear excitation mechanisms have been used to magnetically excite the

sample. In our experiments we rely on the linear absorption of the pump pulse and we will limit ourselves to the discussion of this particular case.

Physics: The last point we want to discuss is the physics that can be studied by laser-induced magnetization dynamics. After the optical perturbation, the magnetization will react by either changing its magnitude, or its direction. In the latter case the magnetization can precess around and effective magnetic field leading to an oscillatory probe response [27]. Throughout this thesis, we (mostly) observed changes in the magnitude of the magnetization vector, and we will limit us to this case.

Whereas some work in the literature focusses on the light-magnetic matter interaction during the presence of the pump pulse, other work focusses more on the materials' magnetic properties after photo-excitation. In this case the pump pulse is just a perturbation and one is not specifically interested in the light-matter interaction itself. In this thesis we will discuss experiments which are in the last category (magnetic material properties). One can also make a distinction between experiments in which the material is perturbed in order to learn something more about the ground state properties or to learn especially something about the excited state properties (like excitons for instance). In this thesis we describe experiments which belong to both of these categories.

Finally, we can also categorize the field according to what kinds of interactions are studied. From the time-dependent changes of the magnetization vector one can learn more about (for instance) the spin-lattice interaction, spin-orbit coupling, exchange interaction, but also about the interaction between itinerant electrons and localized moments, as we will see later [27].

1.3.3 Laser-induced carrier and lattice dynamics in semiconductors (GaAs): typical dynamics

Before discussing the expected dynamics (what can we expect?) in the Eu-chalcogenides, we first discuss the simpler situation of laser-induced carrier and lattice dynamics in semiconductors, focusing on the GaAs case. The relaxation dynamics after optical electron-hole excitation in GaAs is well-studied. The different relaxation processes and timescales are depicted in Fig. 1.9. Right after the optical excitation, there are non-thermalized electrons and holes [28,29]. The electron and holes lose their coherence by momentum scattering on a time scale well below 100 fs. By electron-electron scattering, the electrons thermalize after

which they obtain a Fermi distribution and one can define a new electronic temperature. This is happening at timescales of about 10-200 fs in GaAs, depending on the pump fluence. When the electron-hole scattering is not to strong, the situation is different. In this case the electrons and holes are not in thermal equilibrium and their distributions needs to be described by separate hole and electron quasi-Fermi (chemical potential) levels [30]. Only after electron-hole scattering, the distribution can be described by a single Fermi distribution.

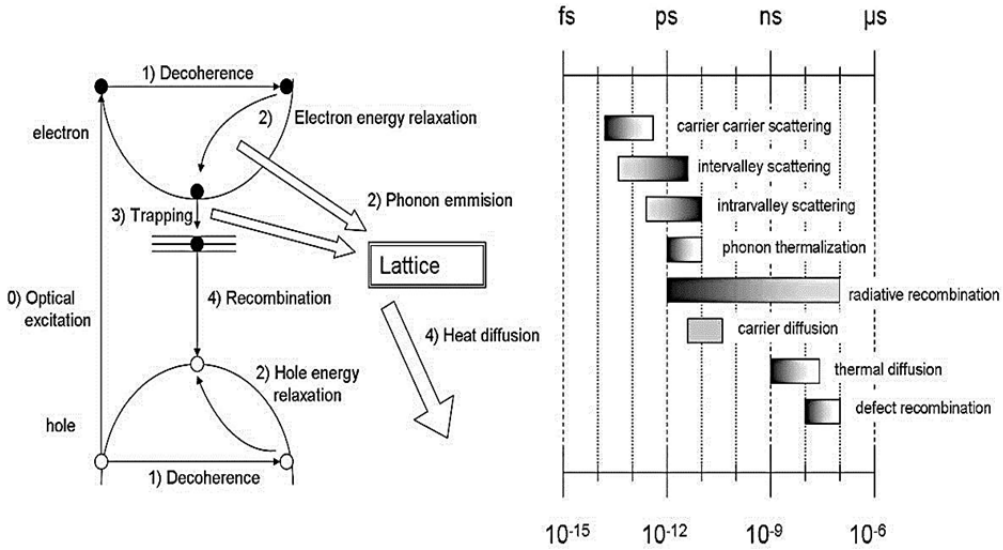

Figure 1.10 | Carrier dynamics in semiconductors: different relaxation processes (left) and timescales for GaAs (right) [28,29]. The gray scale in the right picture refers to the fluence. Black-white=high-low fluence. Pictures taken/adapted from [28,29].

The next step in the relaxation cascade is the energy relaxation of the thermalized electrons. The hot electrons can give energy to the lattice by emitting optical phonons (electron-phonon scattering) [29]. The higher the energy difference between the conduction electron and the conduction band minimum, the more phonons needs to be emitted before the electrons reach the bottom of the band. This is happening at the 0.2-10 ps timescale in GaAs, depending on the fluence [29]. By this process, the temperature of the electrons will drop while the lattice temperature will increase. The new increased lattice temperature can only be defined after phonon thermalization (by phonon-phonon scattering) which is happening at the 1-10 ps timescale. After the electron-phonon and phonon-phonon thermalization time, the electronic sub-system and the lattice sub-system have the same, elevated temperature and the material is in quasi-equilibrium [29].

Until now we discussed the situation where the valence band hole and conduction electron concentrations are constant (after excitation). Several processes can result in a drop of the hole and electron concentrations. One of them is trapping. Electrons and holes can be trapped which typically happens at the sub-picosecond or picosecond timescales in GaAs, depending on the fluence and on the trap nature and density [29]. On the picosecond time-scale, the charge carriers can also diffuse away from the photo-excited volume, again leading to a drop in the carrier concentration. Another process which can lead to a drop in the carrier concentration is radiative or non-radiative electron-hole recombination, which is typically much slower (sub-nanosecond or nanosecond timescale). While in radiative processes the energy is transferred to the photons, in non-radiative recombination energy is transferred to the lattice (phonon emission). Another important relaxation process on the nanosecond (or longer) timescale is thermal phonon diffusion. Only after thermal diffusion the system can relax back to the state in which it was before it was excited.

1.3.4 Laser-induced carrier and lattice dynamics in EuO: what can we expect?

Let us now return to EuO. In our experiments, the optical pump pulse excites electrons from the 4f valence band to the 5d conduction band. The subsequent relaxation process will affect the *magnetization* and *conductivity*, from which we can learn more about the conduction electron-localized moment interaction. In EuO the exact timescale of most of the described relaxation processes is unknown, but we can get a rough estimate based on what is known in other semiconductors. There are some important differences with semiconductors like GaAs which we can discuss already. In EuO we make a 4*f* to 5*d* excitation, which means that we create 4*f* holes and 5*d* conduction electrons. Since the 4*f* orbitals are very small and therefore the overlap between them is small as well, the 4*f* bandwidth is small. Now, for simplicity, we can assume that the 4*f* states do not form a band but are just atomic levels. In this case we cannot define a quasi-Fermi level or an electronic temperature for the holes. The situation in EuO is depicted in Fig. 1.11 and Fig 1.12.

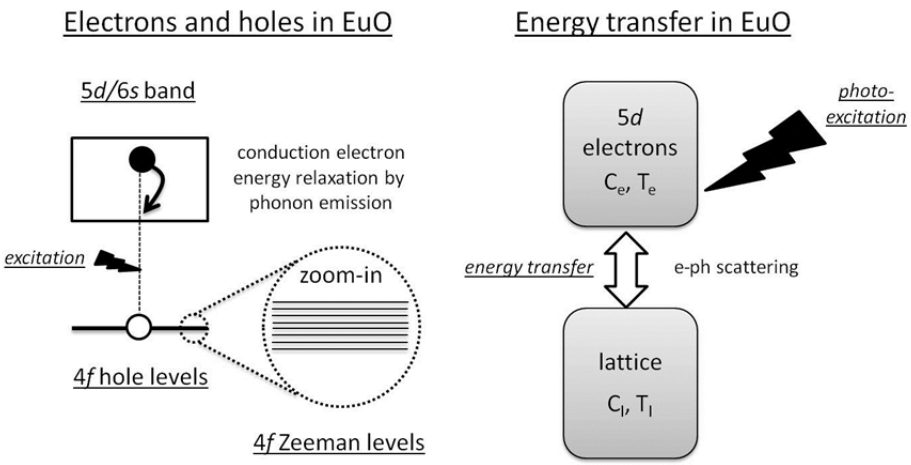

Figure 1.11 | Electron and hole dynamics in EuO (left) and energy transfer in EuO (right).

After the absorption of a 1.55 eV photon, the conduction electron relaxes to bottom of the conduction band by phonon emission, see Fig 1.11 (left). Since the bandgap is about 1.2 eV, 1.55-1.2=0.35 eV is transferred to the lattice [14]. Due to the narrow 4*f* bandwidth, the energy transfer to the lattice due to hole relaxation is minimal. This point becomes important if one wants to use the so-called two-temperature model (2TM) which is helpful for the analysis later on [24,28]. The 2TM is used in order to describe the energy transfer between two sub-systems: the electrons (e) and the lattice (l). Each sub-system has its own heat capacity (C_e and C_l) and temperature (T_e and T_l). The 2TM is widely used as a phenomenological approach to describe the laser-induced dynamics in metals after an optical excitation which heats up the electrons. In the 2TM the number of electrons is fixed, a condition which is satisfied in metals. Right after photo-excitation in EuO, and at time-scales where the conduction electron concentration is constant (see Fig 1.12 left), we can also define two sub-systems: the 5*d* conduction electron sub-system, and the lattice sub-system (see Fig. 1,11 right). The two systems are in contact via electron-phonon scattering. Due to the small electron concentration in semiconductors, the lattice heat capacity is much larger and we are in the regime that $C_l >> C_e$. The situation is summarized in Fig. 1.12, where the carrier concentration and lattice/electronic temperature versus pump probe delay is schematically shown.

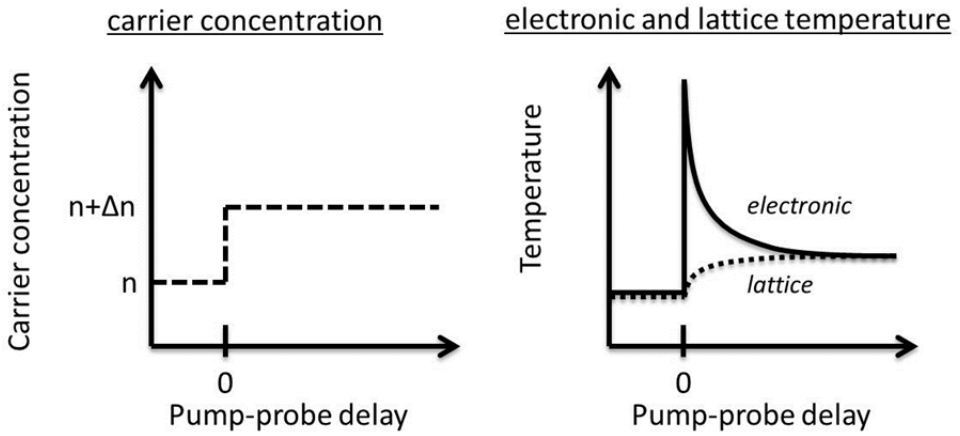

Figure 1.12 | Carrier concentration versus pump-probe delay (left) and electronic temperature and lattice temperature in the 2TM.

The situation becomes more complicated when the electron concentration is not constant due to different processes like trapping, diffusion, recombination or other possible competing relaxation phenomena like (magnetic) exciton or (magnetic) polaron formation.

Summarizing, in this section we learned that in a typical semiconductor after a few 100 fs there is a hot conduction electron gas, which equilibrates with the cold lattice at the picosecond time-scale. This is only the *starting point* in our experiments. What we are really interested in is how the magnetization changes due to the presence of photo-excited conduction electrons and to the elevated electron and lattice temperatures. This can provide valuable information about the coupling between localized moments and itinerant electrons, as we will see later on. In the next section we introduce the topic of magnetization dynamics in ferromagnets due to lased-induced hot free electrons.

1.3.5 Magnetization dynamics in ferromagnets due to lased-induced hot free electrons: the theoretical framework

Now we will now focus on experiments were the pump creates hot conduction electrons in a ferromagnet at t=0 s, and in which changes in the magnitude of the magnetization vector is probed for different pump-probe delays. As discussed above, the hot conduction electron gas will equilibrate with the cold lattice,

typically at the picosecond time-scale, see also Fig 1.13. The question now is what will happen to the magnetism (spins)?

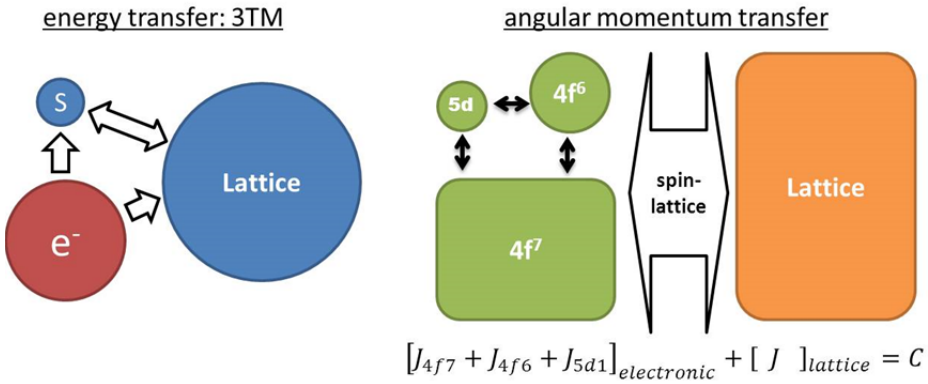

Figure 1.13 | Energy transfer (3TM) between 5*d* conduction electrons (e^-), 4*f* spins (S) and the lattice (left). The size of the diameter is a representation of the size of the heat capacity of the sub-system. Angular momentum transfer between different electronic-systems and the lattice (right). The total angular momentum is constant (*C*).

First we look to the problem from an energy transfer point of view (Fig. 1.13 left) in the simple case that the conduction electron concentration after photo-excitation is constant; this is a good starting point for the discussion. As we discussed before, in the 2TM there can be energy transfer between the hot electrons and the cold lattice. For more details on the 2TM, see Chapter 3. Assuming, for simplicity, that the electronic and lattice heat capacities are temperature independent (which is actually not the case), and noting that in semiconductors one generally has $C_L >> C_e$, the electron-phonon equilibration time τ_{eL} is proportional to C_e. For free electrons C_e is proportional to $n^{1/3}$ (free electron concentration) which means that $\tau_{EL} \sim n^{1/3}$. In the same limit, the lattice temperature increase after equilibration is inversely proportional to C_L.

Alternatively, there can also be energy transfer between the conduction electrons and the spins. The spins system is a third thermal bath (with its own heat capacity) and therefore the laser-induced demagnetization dynamics in metals is often described in terms of the so-called three temperature model (3TM): there are electrons, the lattice and the spins [31]. See for more information on the 3TM Chapter 3. In the fully ferromagnetically ordered state far below T_c, the magnetic heat capacity is small. In this limit and when the conduction concentration is not too small the following relation holds: $C_e >> C_S$. When we assume again for simplicity that C_e and C_S are temperature independent, the electron-spin equilibration time

τ_{eS} (within the 2TM) is proportional to C_S while the spin temperature increase after equilibration is inversely proportional to C_e. The different cases are summarized in Table 1.1, in which g is the coupling constant between the subsystems with g_{eL} and g_{eS} the electron-lattice and electron-spin coupling constants, respectively.

Table 1.1 | 2TM model, $C_{e,S,L}$ are taken as temperature independent.

Energy transfer in 2TM	Conditions	Equilibration time	Temperature increase
$e^- \rightarrow$ Lattice	$C_L >> C_e$ $\tau_{eL} << \tau_{eS}$	$\tau_{eL} = C_e/g_{eL}$	$\Delta T_L \sim 1/C_L$ 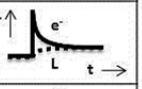
$e^- \rightarrow$ Spins	$C_e >> C_S$ $\tau_{eS} << \tau_{eL}$	$\tau_{eS} = C_S/g_{eS}$	$\Delta T_S \sim 1/C_e$ 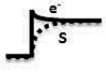
Lattice $\rightarrow$ Spins	$C_L >> C_S$	$\tau_{LS} = C_S/g_{LS}$	$\Delta T_S \sim 1/C_L$ 
$e^- \rightarrow$ Lattice $\rightarrow$ Spins	$C_L >> C_{S,e}$ $\tau_{eL} << \tau_{LS} << \tau_{eS}$	$\tau_{eLS} = C_S/g_{LS}$	$\Delta T_S \sim 1/C_L$ 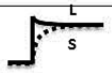

Depending on the magnitude of (C_e,g_{eL}) and (C_S, g_{eS}) the equilibration between the electrons and the lattice/spins can be faster or slower. The interesting physics is hidden in the coupling constant g, as is discussed in Chapters 3-5. In the case that τ_{eS} <<τ_{eL}, the spin system obtains an elevated temperature after electron-spin equilibration: the temperature increase is inversely proportional to the spin specific heat, $\Delta T_S \sim 1/C_e$. Subsequently, the electrons and spins can cool down by energy transfer to the lattice.

In the case that τ_{eL} <<τ_{eS}, the energy of the hot electrons is first transferred to the lattice. In this case the spin system can obtain an elevated temperature after spin-lattice equilibration. In this case the temperature increase is inversely proportional to the spin specific heat, $\Delta T_S \sim 1/C_L$. Due to the fact that one generally has $C_L >> C_e$ in semiconductors, ΔT_S is smaller in the electron→lattice→spins pathway than in the direct electrons→spins pathway.

As mentioned, the situation becomes more complicated when the electron concentration is not constant due to trapping, diffusion, recombination or due to processes that we want to study like (magnetic) exciton/polaron formation. In a magnetic polaron there is an increased exchange interaction between localized moments due to the intra-atomic exchange interaction between the localized moments and the conduction electron. The conduction electron can be free (free magnetic polaron), or bound by a vacancy, defect, impurity or valence band hole

(magnetic exciton) [12,14,32,33]. Around the conduction electron, the ferromagnetic order can be enhanced. We will discuss the existence of magnetic polarons and excitons extensively throughout this thesis. A deviation from the "simple" behavior which can be expected from the 3TM can give information about the formation of magnetic excitons/magnetic polarons.

Until now we discussed the problem from an energy transfer point of view (Fig. 1.13 left). Since we measure the magnetization dynamics, we also have to look at the problem from an angular momentum transfer point of view. In EuO, there are different angular momentum reservoirs. We can distinguish electronic angular momentum and the angular momentum of the lattice. Since the total angular momentum is a conserved quantity, a change of the magnitude of the magnetization vector can only occur when there is angular momentum transfer between the electrons and the lattice, see Fig. 1.13 right (white arrow). Within the electronic angular momentum reservoir, we can distinguish different sub-systems: 1) the unexcited Eu 4f moments, Eu^{2+} $4f^7$ S=7/2, L=0, 2) the photo-excited 4*f* moments, Eu^{3+} $4f^6$ S=3, L=3 [12], and 3) the conduction electrons $5d^1$, S=1/2. There are exchange interactions between the different sub-systems (black arrows in Fig. 1.13) which can lead to ferromagnetic order, or to the (possible) formation of magnetic excitons or polarons. For the magnitude of the electronic angular momentum sub-systems (represented by the size of the boxes in Fig. 1.13) one has: 1>>2>>3 in the low fluence pump regime, and 1>2>>3 in the high pump fluence regime. Since the total magnetic moment of system 3 (5*d* electrons) is small compared to system 1 and 2, the total magnetization of the sample is mainly sensitive to changes in the 4*f* magnetism. Although the magnitude of the angular momentum of system 3 is much smaller than that of system 1 and 2, we will see that the conduction electrons play a very important role in the magnetization dynamics and cannot be neglected. This will become clearer by considering angular momentum transfer between the lattice and itinerant electrons/localized magnetic moments.

From literature it is known that there are different mechanisms and timescales for angular momentum transfer between localized magnetic moments and the lattice and itinerant electrons and the lattice, see Fig 1.14 [25]. The mechanisms will be discussed in Chapter 3.

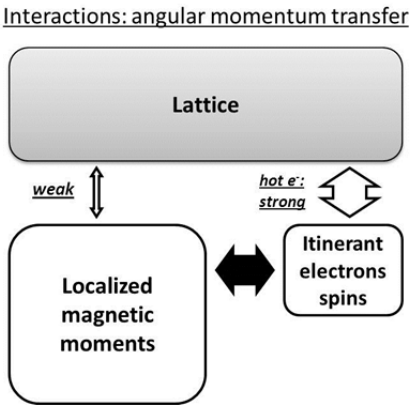

Figure 1.14 | Angular momentum transfer between the lattice and localized moments/ itinerant electron (open double arrows). There can be also angular momentum transfer between the localized moments and itinerant electrons (filled double arrow).

Whereas the localized moment ⇔ lattice angular momentum transfer is typically slow (ns, sub-ns), the (hot) itinerant electron ⇔ lattice angular momentum transfer can be fast (sub-ps) [25]. This opens the question in EuO what will be the fastest pathway: A) the direct pathway, localized moment→lattice. B) the indirect pathway, localized moment→itinerant electrons→lattice. In the latter case the localized moment-itinerant electron interaction is crucial. Only when there is an efficient angular momentum transfer between the electrons and the lattice, there can be ultrafast changes in the size of the magnetization vector. The details of this processes is the topic that we want to study in this thesis, see for more details the motivation and scope section. More can be learned by also looking to the conductivity dynamics.

1.3.6 Conductivity dynamics: the role of the conduction electrons

In Chapter 6 we describe the change in the conductivity, which is probed using THz pulses, after an optical excitation (valence to conduction band, see the previous section). Using THz spectroscopy, in our case, we are sensitive to *free* electrons. This is important since in the 3TM, one assumes that the *free* electron concentration is constant. By probing the conductivity with picosecond temporal resolution, we can check the assumptions in the 3TM that: i) there are (optically generated) free electrons and ii) the conduction electron concentration is constant on the time-scales we are looking. As mentioned, the conduction electron concentration after photo-excitation can drop due to trapping, diffusion,

recombination or also due to processes we are especially interested in: (magnetic) exciton/polaron formation, see Fig. 1.15.

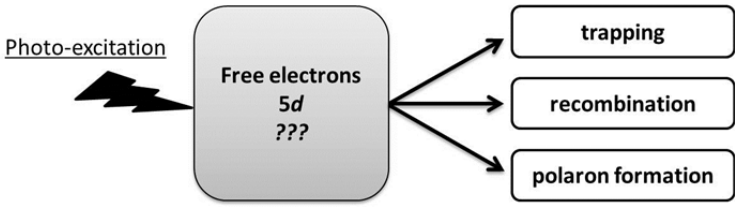

Figure 1.15 | Free electrons generation and different possible relaxation processes.

The combination of magnetization and conductivity dynamics provides a detailed insight into what is happening in EuO after photo-excitation. Whereas in the magnetization dynamics experiments we are sensitive the localized moment 4*f* magnetism and the angular momentum transfer, in the conductivity dynamics experiments we are sensitive to 5*d*/6*s* conduction electrons from which we can also learn more about magnetic exciton/polaron formation.

1.4 Scope

In the previous sections we gave an introduction on the physics we want to study, and on the materials and methods we used. In this section we focus on the scope of this Thesis, which is centered around two quite specific questions.

What is rate of demagnetization due to lased-induced hot free electrons in an intrinsic ferromagnetic semiconductor?

Demagnetization dynamics due to lased-induced hot free electrons has been studied in a wide range of ferromagnetic systems: ferromagnetic metals (transition/rare earth/alloys), half-metals and diluted ferromagnetic semiconductors [24--27]. At the start of my PhD, no ultrafast demagnetization experiments on intrinsic concentrated ferromagnetic semiconductors (like EuO) has been reported in the literature. The study of magnetization dynamics in EuO can give information on the magnetic interactions in EuO. At the same time it also can provide insight into demagnetization mechanisms in solids in general. Although there is a great diversity in the behavior and time-scales in different materials, most of the observed dynamics can satisfactorily be described within the phenomenological framework of the so-called microscopic 3TM (M3TM, see for

details Chapter 3). The M3TM is a microscopic version of the 3TM that was mentioned described before, and only considers the spin-lattice interaction (angular momentum transfer, see Fig. 1.14) between conduction electrons and the lattice. The M3TM can however not be applied:

i. When there is strong interaction between localized moments and the lattice, as was suggested for the ferromagnetic rare-earth metal terbium [26]. Due to the large orbital momentum of Tb (L=3) the interaction between localized moments and the lattice can be stronger than in transition metals where the orbital moment is usually quenched.
ii. When the conduction electron concentration is not constant due to trapping, diffusion, recombination or due processes that we want to study like (magnetic) exciton/polaron formation.
iii. When there is more than one (magnetic) sub-system and when these sub-systems are weakly coupled. In this case a for instance a M4TM needs to be used.

What can we expect for EuO? Unexcited Eu has a L=0 configuration (Eu^{2+}) and therefore point i) does not apply to unexcited EuO. This does not hold for excited Eu which has a L_{4f}=3 configuration (Eu^{3+}). In the high fluence regime and in the case that the Eu^{3+} and Eu^{2+} magnetic moments are weakly coupled, point i) and iii) may apply to EuO. The same holds for point ii); the free conduction electron concentration versus time is measured in Chapter 6 using THz spectroscopy. This means that deviation from the behavior which can be expected from the M3TM can give information about a possible special role of the Eu^{3+} moments (see i) and iii), strong spin-lattice interaction, second magnetic sub-system) or to magnetic exciton or polaron formation (see point ii)).
The interaction between localized moments and conduction electrons which may lead to magnetic exciton and magnetic polaron formation is discussed in Chapters 4, 5, and 7 (magnetization dynamics) as well as in Chapter 6 (conductivity dynamics).

Is the main peak in the absorption spectrum in the NIR/VIS range of EuO of magnetic-excitonic origin?

In the absorption spectrum of EuO there is a large peak around 1.6 eV (main peak, see Chapter 2). Upon ferromagnetic ordering there is a large red shift of this peak and the optical absorption edge which is related to the interaction between the

conduction electrons and the localized magnetic moments. The large peak around 1.6 eV has been interpreted in different ways. It was either attributed to a transition from the valence band to the narrow conduction band (valence-conduction band transition, VCBT), or due to magnetic excitons [12,32,34,35]. In a magnetic exciton the conduction electron is bound by the 4*f* hole, but also by the *d-f* exchange interaction with the nearest neighbors of the hole. In the magnetic-exciton model the bandwidth of the conduction band (several eV) is much broader than in the VCBT model (several hundreds of meV) [32,34,35]. A better understanding of the origin of this peak is important in order to understand the temperature and magnetization dependent band structure of EuO and the large magneto-optical effects in this range. Since in Chapter 5 and 7 we employ these magneto-optical effects to probe the magnetization in EuO and EuTe, this is essential for us. Whereas in Chapter 2, the optical and magneto-optical spectra in the NIR/VIS range are calculated within the VCBT framework, in Chapter 6 we look for magnetic excitons by measuring the conductivity right after photo-excitation with a sub-picosecond resolution.

1.5 Outline

The thesis is organized as followings:

Chapter 2 Magneto-optical properties of EuO: *In this Chapter we discuss the electronic and optical properties of EuO. Using an atomistic model, the (magneto) optical spectra in the near-infrared/visible range for different temperatures and magnetic fields are calculated. By considering the interaction between localized 4f moments and 5d conduction electrons, the optical polarization dependent red-shift of the optical absorption edge is modeled, from which we obtain estimates for the 4f spin-orbit coupling strength and for the 5d conduction band-width in EuO. Also the linearity between the magneto-optical signals and the magnetization is addressed.*

Chapter 3 Laser-induced demagnetization dynamics due to hot conduction electrons in ferromagnets, an introduction: *This Chapter gives an extensive introduction to the field of laser-induced demagnetization dynamics which is based on the present literature. It discusses the dynamics in itinerant ferromagnets (Ni, Fe, Co) and half metals (CrO_2), but also in systems with both localized magnetic moments and itinerant electrons like diluted magnetic semiconductors (Ga/Mn As) and rare-earth metals (Gd, Tb). We discuss different demagnetization mechanisms which involve either localized spin-phonon interactions or itinerant electron (spin)-phonon interactions.*

Chapter 4 Laser-induced demagnetization dynamics in EuO probed by XMCD: *Using time-resolved XMCD spectroscopy, the laser-induced magnetization dynamics is probed with a*

temporal resolution of 50 ps. XMCD spectroscopy is known to be a clean optical probe for the magnetization. In this way, we can circumvent the usual discussion in interpreting magneto-optical data in the NIR/VIS/UV range which may suffer from non-magnetic components. We observe a slow nanosecond demagnetization, which we relate to the weak localized 4f spin-lattice interaction.

Chapter 5 Laser-induced (de/re)-magnetization dynamics in EuO probed by magneto-optics with 100 fs resolution: *Using time-resolved magneto-optical spectroscopy (Faraday/Kerr, λ=800/400 nm), the laser-induced magnetization dynamics in EuO is probed with a temporal resolution of about 150 fs. We observe a sub-picosecond demagnetization, followed by a 15 ps re-magnetization which in turn is followed by a slow demagnetization (nanosecond). The ultrafast demagnetization (<1 ps) we relate to spin-flip electron-phonon scattering of 5d conduction electrons, which are strongly coupled to the localized 4f moments. The re-magnetization (15 ps), we relate to the formation of magnetic excitons. This re-magnetization is quite unique in the* that the vast majority of observations concerns laser-induced demagnetization.

Chapter 6 Ultrafast conductivity dynamics in EuO: signatures of magnetic excitons and magnetic polarons: *In this Chapter we study the ultrafast conductivity dynamics in EuO after an optical excitation (4f to 5d), using short, optically generated, THz electric field (probe) pulses. The different components in the conductivity dynamics are related to the presence of magnetic excitons (right after photo-excitation) and magnetic polarons (after 20 ps).*

Chapter 7 Laser-induced magnetization dynamics in EuTe and other multi-sublattice systems: theory and experiments: *In this Chapter we focus on the magnetization dynamics in multi-sublattice systems, like the simple antiferromagnet EuTe, with a focus on inter-sublattice angular momentum transfer. In a qualitative way, we develop a framework in which the laser-induced dynamics in antiferromagnets can be understood. Also some experimental results on EuTe will be presented. Using time-resolved magneto-optical spectroscopy (Faraday, $\lambda_{pump}=\lambda_{probe}=400$ nm), the laser-induced magnetization dynamics in EuTe is probed with a temporal resolution of about 150.*

Appendix: positioning of EuO in the field of laser-induced demagnetization dynamics in ferromagnetic materials

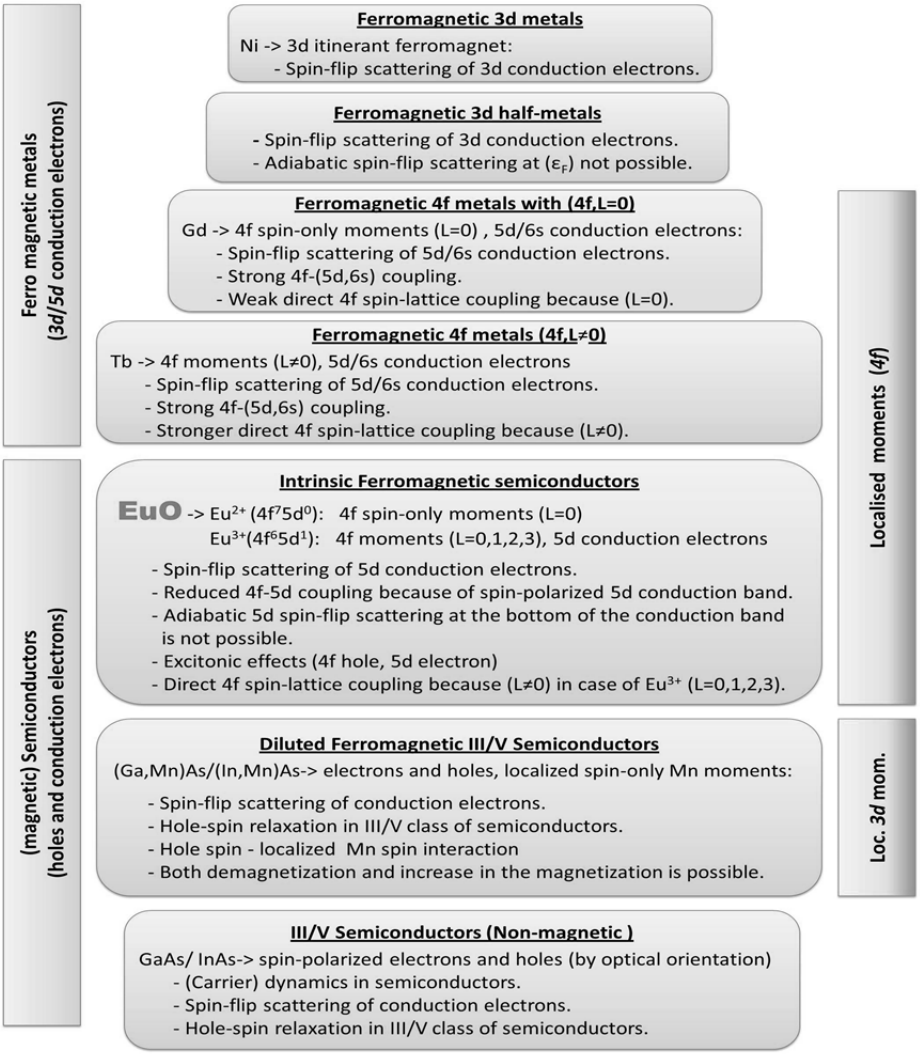

References

[1] S. J. Blundell, *Magnetism in Condensed Matter* (oxford university press, 2011).

[2] B. Dieny, V. Speriosu, S. Metin, S. Parkin, B. Gurney, P. Baumgart, and D. Wilhoit, J. Appl. Phys. **69**, 4774 (1991).

[3] S. A. Wolf, D. D. Awschalom, R. A. Buhrman, J. M. Daughton, S. von Molnar, M. L. Roukes, A. Y. Chtchelkanova, and D. M. Treger, Science **294**, 1488 (2001).

[4] C. Santos, W. Nolting, and V. Eyert, Physical Review B **69**, 214412 (2004).

[5] D. I. Khomskii, *Basic Aspects of the Quantum Theory of Solids: Order and Elementary Excitations* (cambridge university press, 2010).
[6] C. Kittel, *Introduction to Solid State Physics* (Wiley, 1996).
[7] M. B. Salamon and M. Jaime, Reviews of Modern Physics **73**, 583 (2001).
[8] M. F. Hundley, M. Hawley, R. H. Heffner, Q. X. Jia, J. J. Neumeier, J. Tesmer, J. D. Thompson, and X. D. Wu, Appl. Phys. Lett. **67**, 860 (1995).
[9] A. H. Macdonald, P. Schiffer, and N. Samarth, Nature Materials **4**, 195 (2005).
[10] T. Dietl, Nature Materials **9**, 965 (2010).
[11] R. Knut, *New Materials for Spintronics: Electronic structure and magnetism* (Acta Universitatis Upsaliensis, 2012).
[12] P. Steeneken, *PhD thesis: New light on EuO thin films* (Rijksuniversiteit Groningen, 2002).
[13] T. Mairoser, A. Schmehl, A. Melville*, et al*, Phys. Rev. Lett. **105**, 257206 (2010).
[14] A. Mauger and C. Godart, Physics Reports-Review Section of Physics Letters **141**, 51 (1986).
[15] R. Sutarto, S. G. Altendorf, B. Coloru*, et al*, Physical Review B **79**, 205318 (2009).
[16] R. Sutarto, S. G. Altendorf, B. Coloru*, et al*, Physical Review B **80**, 085308 (2009).
[17] S. G. Altendorf, A. Efimenko, V. Oliana, H. Kierspel, A. D. Rata, and L. H. Tjeng, Physical Review B **84**, 155442 (2011).
[18] A. Schmehl, V. Vaithyanathan, A. Herrnberger*, et al*, Nature Materials **6**, 882 (2007).
[19] G. Busch and F. Levy, Physics Letters a **A 27**, 37 (1968).
[20] H. Ott, S. Heise, R. Sutarto, Z. Hu, C. Chang, H. Hsieh, H. Lin, C. Chen, and L. Tjeng, Physical Review B **73**, 094407 (2006).
[21] Y. Shapira, S. Foner, and T. B. Reed, Physical Review B **8**, 2299 (1973).
[22] T. Yamasaki, K. Ueno, A. Tsukazaki, T. Fukumura, and M. Kawasaki, Appl. Phys. Lett. **98**, 082116 (2011).
[23] E. Beaurepaire, J. Merle, A. Daunois, and J. Bigot, Phys. Rev. Lett. **76**, 4250 (1996).
[24] B. Koopmans, G. Malinowski, F. Dalla Longa, D. Steiauf, M. Faehnle, T. Roth, M. Cinchetti, and M. Aeschlimann, Nature Materials **9**, 259 (2010).
[25] G. M. Mueller, J. Walowski, M. Djordjevic*, et al*, Nature Materials **8**, 56 (2009).
[26] M. Wietstruk, A. Melnikov, C. Stamm, T. Kachel, N. Pontius, M. Sultan, C. Gahl, M. Weinelt, H. A. Duerr, and U. Bovensiepen, Phys. Rev. Lett. **106**, 127401 (2011).
[27] A. Kirilyuk, A. V. Kimel, and T. Rasing, Reviews of Modern Physics **82**, 2731 (2010).
[28] D. A. Mazurenko, *Ultrafast optical swiching in three-dimensional photonic crystals* (University of Utrecht, 2004).
[29] J. P. Callen, *Ultrafast Dynamics and Phase Changes in Solids Excited by Femtosecond Laser Pulses* (Harvard University, 2000).
[30] M. Breusing, C. Ropers, and T. Elsaesser, Phys. Rev. Lett. **102**, 086809 (2009).
[31] E. Beaurepaire, J. C. Merle, A. Daunois, and J. Y. Bigot, Phys. Rev. Lett. **76** (1996).

[32] T. Kasuya, J Magn Magn Mater **195**, 141 (1999).
[33] M. Umehara, Physical Review B **65**, 205208 (2002).
[34] Guntherodt.G, P. Wachter, and D. M. Imboden, Physik Der Kondensiterten Materie **12**, 292 (1971).
[35] A. B. Henriques, M. A. Manfrini, P. H. O. Rappl, and E. Abramof, Physical Review B **77**, 035204 (2008).

Chapter 2

The Magneto-Optical properties of EuO

The europium chalcogenides are well known for their large magneto-optical effects. In the next chapters, these magneto-optical effects are employed in order to probe the samples' magnetization. This chapter is aiming to describe the origin of the large magneto-optical effects. Magneto-optical spectra are calculated as function of internal magnetic field and temperature. A good understanding of the magnetic field and temperature dependence not only allows us to interpret the optical pump–magneto optical probe measurements but also provides valuable information on the 4f-5d exchange interaction, short- and long-range magnetic order, and the spin-orbit coupling.

2.1 Introduction

The optical properties of the europium chalcogenides have been studied extensively in the sixties and seventies, see for instance references [1--3] (and references in there). Scientists were especially puzzled by the large red-shift of the absorption edge in ferromagnetic EuO and EuS, when the sample is cooled down below the magnetic ordering temperature, and by the large magneto-optical effects observed in these materials. To understand the origin of these phenomena, it is instructive to first consider the absorption spectrum, which shows two strong absorption peaks around 2 eV and 5 eV, respectively (see later on, Fig.2.4). One group of scientists assigned the first peak in the absorption spectrum to a transition from the 4*f* valence states towards a relatively narrow (bandwidth W=1.1 eV) 5*d* conduction band, see for instance [1,2,4,5]. The 4*f* states were considered to be atomic like, not showing much dispersion, while the 5*d* states are considered delocalized to form a band. The red shift in the absorption edge shift was then explained in terms of the exchange interaction of the delocalized 5*d* electrons with the localized 4*f* magnetic moments: as an approximation, the 4*f*-5*d* exchange (spin) splitting of the conduction band can be considered to be proportional to the macroscopic magnetization [3,6]. In this way, the absorption edge shift is a result of a conduction band shift and can be used as an estimate for 4*f*-5*d* exchange interaction. The fact that there is a strong polarization dependence of the

absorption edge shows that this interpretation cannot be fully correct [6]. Also the fact that the red shift already starts to appear above T_c, and is also observed in samples without macroscopic magnetization cannot be explained by this simple model. These latter observations suggest that the 5*d* electron is (partially) localized and sensitive to the short range order.

Other scientists came up with a different idea. They considered the 5*d* conduction band to be broad (consistent with band-structure calculations) and they assigned the first peak in the absorption spectrum to the presence of a magnetic exciton, see for instance [7,8] in references in there. In a magnetic exciton, the 5*d* conduction electron is bound by both the charge of the central Eu atom (hole) and by the 4*f*-5*d* exchange interaction with the spin density on neighboring Eu atoms. In this model the absorption edge shift naturally depends on short-range magnetic order which starts to develop already above T_c, and may be present in samples without a macroscopic magnetization. One of the arguments against this model is that the first absorption peak should be sensitive to the conduction electron concentration (in *n*-doped EuO samples) because of the screening of the charge of the hole [1]. Since no effect on the conduction electron concentration was observed, one can question whether the 5*d* conduction electron is really bound by the 4*f* hole. Currently, the general consensus is more towards the first picture (narrow, crystal field split, 5*d* bands) [4,5,9]. However, the conduction electrons do show some degree of localization and the conductivity is sensitive to short-range magnetic order. For more information on this topic we refer to the good reviews which have been written about this subject [1,3,6], or see for more recent developments [4,5,9]. Also in Chapter 6, we will continue this discussion.

In this chapter the (magneto) optical spectra are discussed in the framework of the first model (described above). In literature, already results have been presented where the absorption spectrum was calculated in the fully ferromagnetically ordered state at T=0K [2,4,6], the antiferromagnetically ordered phase in EuTe at T=0K [5] and recently also the also the EuTe spectra were modeled at intermediate fields at T=0 K [9]. This requires the use of Wigner rotation matrixes which transform the reference frame (the quantization axis) of a certain spin in the magnetic unit cell to the reference frame of the light propagation (the wavevector of the light) [5]. By averaging over different spins in the unit cell, the optical spectrum can be calculated, when the orientation of the spins for different applied magnetic fields is known (at T=0 K) [5].

The situation becomes more complicated at higher temperatures (T> 0K) since the system is than (partially) disordered and one need to average over a huge amount of different spin orientations. In this case in a paramagnet where all the spin quantization axis are parallel to the applied magnetic field direction and propagation direction of the light, a different and more simple method can be developed, which we will do in this chapter. In this method, the spins can be all the different (initial state) Zeeman levels (M_J=-7/2...+7/2, according to Boltzmann distribution). This is different than in the previously described methods where the spins are always in the lowest Zeeman state (M_J=-7/2, T=0K) and where the quantization axis (and spin orientation) was adjusted by the Wigner rotation matrix [5]. Without the use of the Wigner rotation matrixes in our method, it becomes more clear where the large magneto-optical effects originate from. As far as we know, the inclusion of the initial state Zeeman level population effects in the model is new and allows us to calculate the absorption edge as function of temperature (and applied magnetic field).

As we will see later, the absorption edge is shifting due to two different reasons. One of them is the aforementioned 4*f*-5*d* exchange spin splitting. However, also a shift in the absorption edge was observed when the 4*f*-5*d* exchange interaction was taken to be zero in our model. This effect was named a “dichroic effect” before in literature [6]. As far as we know, for the first time both effects could be separated. This result is important if one wants to determine the size of the exchange splitting from the optical absorption edge shift measurements, as was done may times in the literature. After the absorption coefficient has been calculated, the refractive index was determined by a Kramers-Kronig transformation, and the magneto-optical Kerr spectrum was simulated. By comparing the (magneto-) optical spectrum with the experimental results, an estimate was made for the conduction band bandwidth and the 4*f* spin-orbit coupling constant.

The results presented in this chapter are also insightful for the next chapters: by assigning the different peaks/bands in the (magneto) optical spectrum, we can understand what is exactly excited by the pump-pulse, and what is exactly probed by the probe pulse in the pump-probe measurements discussed in Chapters 3-5. However, this chapter also serves as an introduction into the electronic properties of EuO. The following section focuses on the electronic configuration of Eu^{2+} in the presence of a crystal field, spin-orbit coupling and exchange interactions. The next section focuses on the atomistic model which has been used to model the

(magneto) optical spectra of EuO. In the results section, (magneto-optical) spectra for different temperatures and applied magnetic fields are shown and discussed. Important for the next chapters, also non-linear magneto-optic phenomena are discussed. The last section of this chapter focuses on how the magneto-optical effects can be measured experimentally.

2.2 Eu^{2+} ions in an octahedral crystal field

2.2.1 $4f^7$ electronic configuration

The magneto-optical properties in the NIR/visible region of Eu^{2+} ions are determined by optically allowed transitions from the $4f^7$ initial state towards a $4f^6 5d^1$ final state configuration. The ground state of the $4f^7$ configuration is $^8S_{7/2}$ (J=S=7/2, L=0). Since it cost 5.4 eV to flip one 4f spin in the ground state in EuO, higher lying states with different J, L, S do not have to be considered [6]. The Hamiltonian of the ground state can be written as:

$$H_{4f^7} = H_{0,4f^7} + H_{z,4f^7} + H_{cf,4f^7} + H_{so,4f^7} + H_{ex,4f}, \quad (2.1)$$

in which $H_{0,4f^7}$ is the Hamiltonian of a free Eu^{2+} ion without spin-orbit coupling. The perturbations $H_{z,4f^7}$, $H_{cf,4f^7}$ and $H_{so,4f^7}$ are the Zeeman, crystal field and spin-orbit terms, and $H_{ex,4f}$ is the interatomic 4f-4f exchange interaction in EuO. Let us first focus on the interaction of Eu^{2+} with the crystal field. The crystal field can be written as a multipole expansion over reduced spherical harmonics. In an octahedral crystal field, the only non-vanishing terms are V_0^4 (and V_0^6) [10]. From anisotropic X-ray magnetic linear dichroism experiments, the V_0^4 parameter was determined to be 175 meV [10]. The resulting energy splitting due to V_0^4 is shown in Fig 2.1.

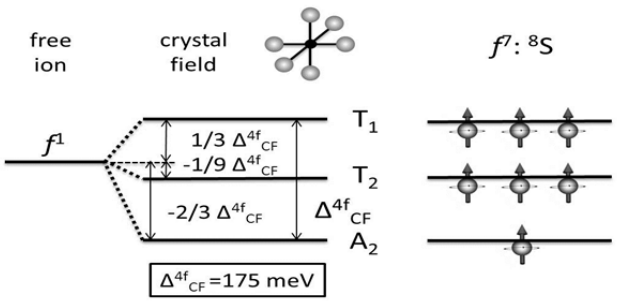

Figure 2.1 | Splitting of f-levels due to an octahedral crystal field. The total splitting is defined as $\Delta_{CF}^{4f} \equiv V_0^4 = 175$ meV.

Due to the large *U* (electron-electron repulsion) and the small crystal field spitting, the ground state of Eu^{2+} ions in EuO has a maximum spin configuration, ^8S. As we can see from Fig. 2.1, the energy of the ^8S term itself is not affected by the crystal field because the 4*f* shell is half-filled.

By Hund's rules, the orbital angular momentum is exactly zero (*L*=0). However there is a small orbital angular momentum component due the mixing and hybridization of the 4*f* sates with other states (higher lying/or oxygen states) [6,11]. The hybridization with oxygen orbitals could be understood in the framework of the ligand-field theory. In this theory, the atomic orbitals and the symmetry of the orbitals are taken into account whereas in the crystal field theory the ligands are considered as point charges. The Eu4*f* irreducible representations in the octahedral point group are (T_{1g}, T_{2g}, A_{2g}) [10]. O2*p* symmetry adapted linear combinations of molecular orbitals have the following irreducible representations: (T_{1u}, T_{2u}, T_{1g}, T_{2g}) [12]. The Eu4*f*-O2*p* interaction is depicted in Fig. 2.2: there is only interaction between states with the same symmetry.

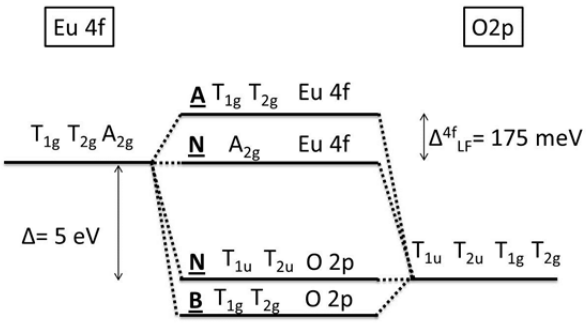

Figure 2.2 | *f*-level splitting due to the interaction with O2p states. Anti-bonding (A), bonding (B) and nonbonding (N) orbitals are depicted.

The interaction between the 4*f* sates and the O2*s* (σ-orbitals) is not included in the picture because this only leads to non-bonding orbitals. The Eu4*f* ligand-field splitting, due to the interaction with the O2*p* states, was taken from the AXMLD measurements (175 meV) [10]. ARPES measurements on EuO, however, reveal levels which were interpreted as anti-bonding and nonbonding with 4*f* character, separated by 0.8 eV [13]. This gap is much larger than the one estimated from AXMLD measurements, indicating that this gap is not only due the Eu4f-O2p interaction. Band structure calculations tell us that there is a sizeable Eu4*f*-Eu5*d* hybridization which might be the origin of the large gap between the non-bonding and bonding orbitals [6,11].

The main message from this section is that it is not sufficient to consider the Eu 4*f* valence band just as localized 4*f* states with no dispersion which are not affected by the ligands. There is a considerable interaction with the O2*p* orbitals as well as hybridization with the Eu5*d* sates. This means that the valence band states with 4*f* character do see the ligand/crystal field. This has important consequences for the magnetic anisotropy and spin-lattice relaxation times as we will see in the next chapter. The energy scales of the different perturbations in EuO are summarized in the first column of Table 2.1.

Table 2.1 | Energy scales of different perturbations in meV. In brackets the corresponding time scales (τ) are shown (τ=h/E). We consider 4*f* ground state configurations. $4f^7$: J=S=7/2, L=0.

	$4f^7$	$4f^6$	$5d^1$
spin-orbit constant λ	Taken 0	31 (133 fs) [6]	15 (67 fs) [6]
spin-orbit splitting	Taken 0	E(J=6)-E(J=0)= 650 (6 fs)	E(3/2)-E(1/2)= 45 (92 fs)
crystal field splitting	$4f^1$: 175 (24 fs) [10] $4f^7$ (^8S) : 0	$4f^1$: 175 (24 fs) [10]	3100 (1 fs) [6]
Zeeman splitting (2 μ_B B), B=1.0 T	0.12 (3.4 x 10^4 fs)	J=6: 0.09 J=0: 0	0.12 (3.4 x 10^4 fs)
4f-4f exchange splitting (2 μ_B B_{eff}), B_{eff}= 34 T	4.0 (1.0 x 10^3 fs)	J=6: 3.0 J=0: 0	4.0 (1.0 x 10^3 fs)
4f-5d exchange splitting (2 μ_B B_{eff}), B_{eff} = 5.2x 10^3 T	-	-	600 (at 20 K) [6] (7 fs)

Herein the spin-orbit splitting in the ground state was taken to be zero. The Zeeman splitting was calculated for a typical applied magnetic field of 1 Tesla. In EuO, within the mean field approximation, an effective magnetic field of 34 T is acting on the 4*f* ions. The resulting Zeeman splinting is shown in Table 2.1. We can conclude that for the $4f^7$ ground state splitting of Eu^{2+} in EuO [6]:

(2.2) $E_{4f\text{-}4f\ exchange} > E_{Zeeman} > E_{spin\text{-}orbit}, E_{crystal\ field}$.

2.2.2 $4f^6$ electronic configuration

Now the same analysis will be made for the $4f^6 5d^1$ final state. This state can be considered as one electron in a 5*d* shell and one hole in a half filled 4*f* shell. The Hamiltonian can be separated in a $4f^6$ and $5d^1$ part and an interaction part:

(2.3) $$H_{4f^6 5d^1} = H_{4f^6} + H_{5d^1} + H_{4f-5d}.$$

The $4f^6$ Hamiltonian we can be written as:

(2.4) $$H_{4f^6} = H_{0,4f^6} + H_{z,4f^6} + H_{cr,4f^6} + H_{so,4f^6},$$

in which $H_{z,4f^6}$, $H_{cr,4f^6}$ and $H_{so,4f^6}$ are perturbations analogous to Hamiltonian Eq. (2.1). We consider only low lying (spin-orbit split) $4f^6$ final states which have a (*L*=3, *S*=3) configuration with total angular momentum of *J*=0,1,2,3,4,5,6, see Fig 2.3 [1,2,6].

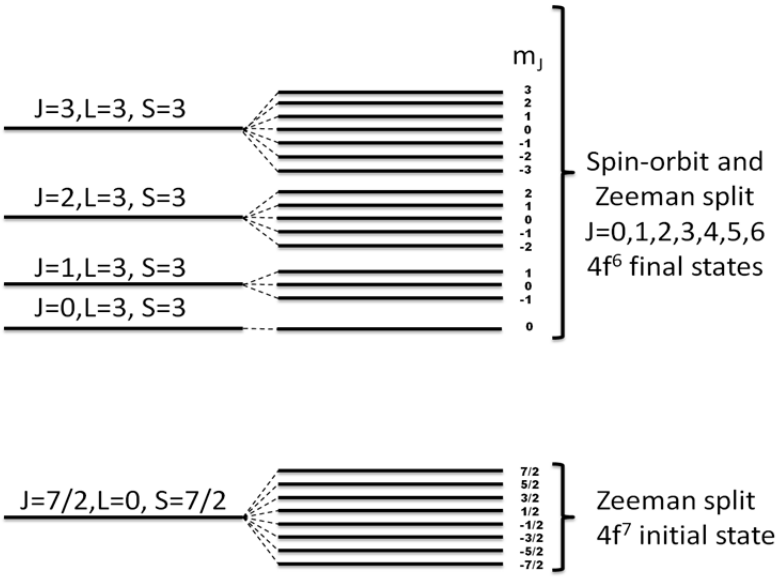

Figure 2.3 | Spin-orbit and Zeeman splitting in the initial $4f^7$ and final $4f^6$ states. The crystal and ligand field splittings are not depicted.

The energy scales of the different perturbations are shown in the second column of Table 2.1. The spin-orbit coupling is the most important perturbation:

(2.5) $$E_{spin\text{-}orbit} > E_{crystal\ field}, E_{4f\text{-}4f\ exchange}, E_{Zeeman}.$$

The $4f^7$ initial state and $4f^6$ final state energy level diagram is shown in Figure 2.3. The crystal field splittings are not depicted.

2.2.3 $5d^1$ electronic configuration

Now we focus on the $5d^1$ electronic configuration. For the (perturbation) Hamiltonian of the $5d^1$ electron we can write:

(2.6) $$H_{5d^1} = H_{z,5d^1} + H_{cr,5d^1} + H_{so,5d^1} + H_{ex,4f-5d},$$

where $H_{ex,4f-5d}$ is the 4f-5d exchange interaction. The effect of the octahedral crystal field on the 5*d* sates is much larger than on the 4f states. The crystal field splitting is 3.1 eV in EuO while the spin-orbit coupling strength is ~15 meV [6]. Therefore for the 5*d* electrons one has:

(2.7) $$E_{crystal\ field} > E_{spin\text{-}orbit} > E_{Zeeman}.$$

The energy level diagram for a *d*-electron in an octahedral crystal field is shown in Fig. 2.4. The crystal field splits the free-ion 5-fold degenerate levels in T_{2g} and E_g levels. The three T_{2g} levels can be considered as pseudo *p*-orbitals (denoted by a prime) with L'=1 and S=1/2. The orbital angular momentum of the E_g orbitals is quenched by the crystal field [14].

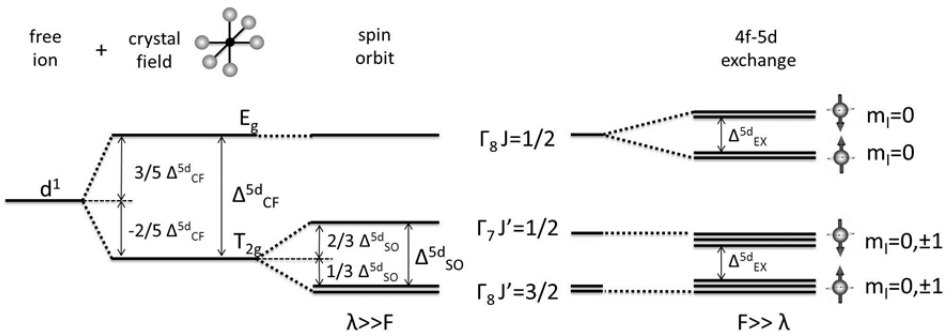

Figure 2.4 | Splitting of d-levels due to an octahedral crystal field, spin-orbit coupling and 4f-5d exchange interaction.

In the next step, a second (smaller) perturbation is considered, the spin-orbit coupling, see also Fig. 2.4. Spin-orbit coupling splits states with non-zero orbital angular momentum. This means that the T_{2g} states are split into one singlet and one doublet while the E_g states are unaffected [14]. The doublet has total angular momentum J'=3/2 while the upper state has J'=1/2. Now we will see what happens

when the 4*f*-5*d* exchange interaction is switched on. We consider the following limit: 4*f*-5*d* exchange >> spin-orbit. The 4*f*-5*d* exchange Hamiltonian can be written as [2]:

(2.8) $H_{ex,4f-5d} = -F\, S_z^{5d}$.

The 4*f*-5*d* exchange interaction in EuO at low temperature (20 K) can be considered as an effective magnetic field of 5.2 x 10^3T which only acts on the spin of the 5d electron. The effective magnetic field is recalculated from the 0.6 eV spin-splitting ($\Delta_{EX}^{5d} = 2F$) in EuO at 20K. As an approximation, *F* can be considered to be proportional to the magnetization in europium oxide. However a better result is obtained when *F* is assumed to be proportional the nearest neighbor spin-spin correlation function (short range order) [15]. The exchange-splitting is reduced when the temperature is increased because *F* is proportional to the short range order. However, an additional de-(spin)polarization can take place due to the 5*d* spin-orbit coupling. As we will see later, the large exchange-spitting of 0.6 eV [6] can have importance consequences for the demagnetization rate of the 5*d* electrons.

2.3 Modeling the optical absorption spectrum of EuO

In this section, the optical absorption spectra are calculated as function of temperature and magnetic field. First a microscopic model is presented from which the absorption spectrum is calculated. Using only two fitting parameters, the width of the first absorption peak can be fitted. By doing a Kramers-Kronig transform, the refractive index can be obtained after which the diagonal and off-diagonal parts of the dielectric function can be calculated. Using a boundary matrix method, the reflection, transmission, (Faraday or Kerr) rotation and ellipticity are calculated and compared to the experimental data.

As mentioned, the focus is on the 4*f*-5*d* transitions since these transitions are held responsible for the large magneto optical effects in EuO. The room temperature absorption spectrum of EuO is shown in Figure 2.5.

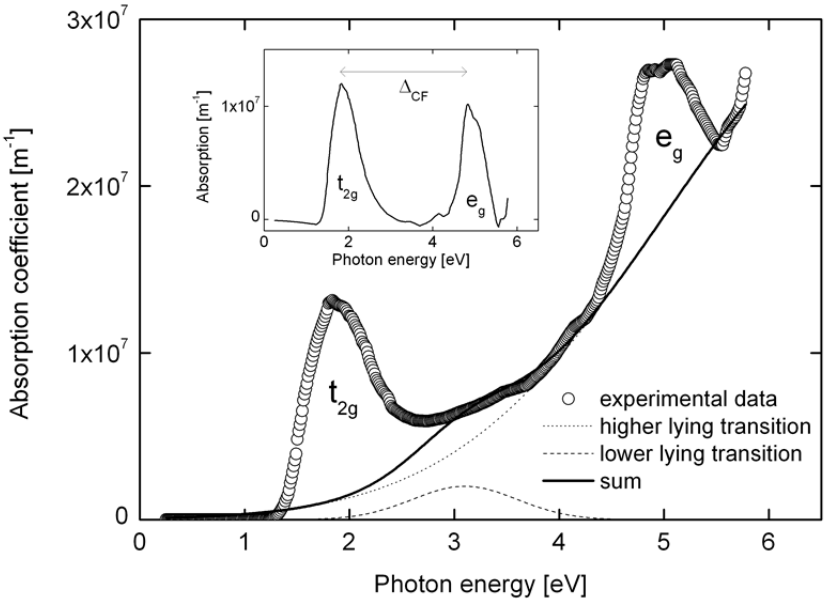

Figure 2.5 |Absorption coefficient of EuO at room temperature. The inset shows the spectrum after the subtraction of two Gaussians. The (digitized) experimental data has been taken from [2], with permission.

In order to make the 4*f*-5*d* transitions more visible, two Gaussians, which are representing other transitions (O2*p*->Eu5*d*, Eu4*f*->Eu6*s*), are subtracted from the experimental data. The result is shown in the inset. The peak at lower photon energies represents the 4*f*-(5*d*,t_{2g}) transition whereas the peak at higher photon energies is the 4*f*-(5*d*,e_g) transition. The difference in energy between the maxima is the crystal field splitting, Δ_{CF}= 3.1 eV.

2.3.1 The assumptions

In order to see where the large magneto-optical results originate from, we consider the following simplified picture:

1) We consider electric dipole allowed transitions from the $4f^7 5d^0$ initial state to the $4f^6 5d^1$ final state [2,5,6].

2) The initial state of the Eu^{2+} ion is $4f^7 5d^0$, which means that according to Hund's rules, S=7/2 and L=0. Though maybe not exactly zero, the orbital moment is expected to be small and will be taken as exactly zero [11].
3) We consider only transitions from the Hund's rule ground state since higher lying states are far away [6].
4) The octahedral crystal field splitting of the localized 4*f* sates is very small and will be taken as zero.
5) No Eu4f-O2p, Eu4*f*-Eu5*d*, Eu5*d*-O2*p* hybridization effects are included. The inclusion of hybridization complicates the calculations, and we will show that it is not really necessary to include these effects in order to understand where the magneto-optical effects are coming from.
6) For simplicity, the 4*f* orbitals are localized and there is no dispersion. We can do this since the measured dispersion of the 4*f* orbitals is small [13]. The width of the 4*f* band is therefore assumed to be a delta function.
7) The $4f^6$ final state has L=3, S=3 which means that J=0,1,2,3,4,5,6. The splitting of different J-levels can be calculated by the Landé interval rule: $E(J, \lambda_{4f})=1/2\lambda_{4f}\ J[J+1]$. The spin-orbit splitting constant λ_{4f} is a parameter which has to be determined [5].
8) The 5*d* levels are split by an octahedral crystal field, Δ_{CF}= 3.1 eV [6]. Δ_{CF}= 3.1 eV is assumed to be magnetic field and temperature independent in the 0-120 K range.
9) The spin-orbit coupling in both the 5*d* T_{2g} and E_g levels is small (see table 2.1) and assumed to be zero.
10) The 4*f*-5*d* exchange interaction leads to a spin-splitting of the 5*d* conduction band. The spin-down *5d* band decreases in energy by 0.3 eV·M_r, whereas the spin-up band increases in energy by 0.3eV·M_r [6]. M_r is the reduced magnetization of the sample or the reduced nearest neighbor spin correlation function.
11) The 4*f*-5*d* band gap is assumed to be 1.39 eV.
12) Since the 4*f* band is considered to be dispersion less, the width of individual J lines is proportional to the 5*d* DOS. The T_{2g} and E_g bands are approximated as Gaussians with a width of σ_{t2g} and σ_{eg} respectively. These widths are parameters which have to be determined but are assumed to be magnetization and temperature independent in the T=0-120 K range.

13) The initial state M_J occupation (J=3.5, M_J=-3.5, -2.5, -1.5, -0.5, +0.5, +1.2, +2.5, +3.5) is calculated using Boltzmann statistics. The effective (exchange) magnetic field at 0 K is taken to be 34 T .
14) The Zeeman splitting and exchange 4*f*-4*f* splitting in the spectrum are small and are taken to be zero. See Table 2.1. The fact that the Zeeman and exchange 4*f*-4*f* splitting is not important in determining the energies of the different transitions does not mean that they are not important. The Zeeman splitting in the initial $4f^7$ state determines the occupation of the different M_J levels, which in turn is crucial for the understanding of the large magneto-optical effects.
15) We write transitions between many electron wave functions in terms of single electron matrix elements. For the single electron wave functions we use hydrogen wave functions. We assume that the hydrogen wave functions are not affected by spin-orbit coupling, exchange interactions, the crystal field or an applied magnetic field.

To summarize, the only perturbations to a free Eu^{2+} atom without spin-orbit orbit are:

- The Zeeman splitting in the initial $4f^7$ state (determines the M_J occupation). The Zeeman energy can be calculated and is not a fitting parameter.
- The crystal field effect on the 5*d* orbitals (determines the T_{2g} and E_g splitting). The crystal field is taken from literature (3.1 eV) [6].
- The spin-orbit coupling in the $4f^6$ final state. The spin-orbit coupling constant is a fitting parameter.
- The 4*f*-5*d* exchange splitting. The spin-splitting at 20K is taken from literature (0.6 eV).
- The 5*d* band formation. The width of the T_{2g} and E_g bands are fitting parameters.

2.3.2 Calculation of the optical absorption spectrum

Optical transitions can be calculated using Fermi's golden rule:

$$W_{i\to f} = \frac{2\pi}{\hbar}\left|H_{fi}\right|^2 \delta(\omega - \omega_{fi}), \quad (2.9)$$

in which W is the transition rate and H_{if} in the dipole approximation is [16]:

$$H_{fi} = -\frac{e\,A_0}{m} p_{fi} \quad (2.10)$$ - perturbation Hamiltonian

(2.11) $p_{fi} = i\omega_{fi}\frac{m}{e}M_{fi}$

(2.12) $M_{fi} = e\langle\psi_f|x \pm iy|\psi_i\rangle$ - electric dipole matrix element

By using $I(\omega) = nA_0^2\varepsilon_0 c\omega^2$, we can write for $|H_{fi}|^2$ [16]:

(2.13) $|H_{fi}|^2 = \frac{I(\omega)\,|M_{fi}|^2}{\varepsilon_0 c\, n}$,

leading to the absorption coefficient :

(2.14) $\alpha_{fi}(\omega) = \frac{\hbar\omega\, N\, W_{i\to f}}{I(\omega)4} = \frac{\pi N}{2\varepsilon_0 c}\ \frac{\omega}{n(\omega)}\ |M_{fi}|^2\ \delta(\hbar\omega - \hbar\omega_{fi})$,

in which already has been taken into account that the density of europium atoms (*N*) is 4/*V* where *V* is the unit cell volume. For EuO, we need to replace the delta function by the 4*f*-5*d* joint density of states, G_{5d} (In our model we assume that the 4*f* initial state is dispersion less). For simplicity we assume the density of states to be Gaussian.

(2.15) $\alpha_{fi}(\omega) = \frac{\pi N}{2\varepsilon_0 c}\ \frac{\omega}{n(\omega)}\ |M_{fi}|^2\ G_{5d}(\hbar\omega - \hbar\omega_{fi})$.

At the end we need to sum over all the possible initial and (J_{4f}) final states:

(2.16) $\alpha(\omega) = \frac{\pi N}{2\varepsilon_0 c}\ \frac{\omega}{n(\omega)}\ \Sigma\,|M_{fi}|^2\ G_{5d}(\hbar\omega - \hbar\omega_{fi})$.

2.3.3 Calculation of the transition dipole matrix elements

First, we will determine the electric dipole matrix elements M_{fi}. In this (technical) section is explained how to do this. In order to determine M_{fi} , we need to consider the initial and final states and the electric dipole operator. As we have discussed before, the initial state (*i*) is characterized by a certain J_i (L_i ,S_i) and M_{J_i} of the seven 4*f* electrons. In our notation, we write for the initial state many electron wave function:

(2.17) $\left[4f^7\left({}^8S_{3.5}, J = 3.5, M_{J_i}\right) > \right.$,

where (${}^8S_{3.5}$) is the term symbol ${}^{2S_i+1}L_{J_i}$ of the ground state. Since *L=0*, and therefore *J=S*, the initial state (*i*) is fully characterized by the spin of the seven 4*f* electrons (S_i=3.5, $M_{i,S}$). For reasons which will become clear later on, it is useful to decompose the ($S_{i,7}$=3.5, M_{i,S_7}) state in terms of six electrons with parallel spin ($S_{i,6}$=3), and a single electron ($S_{i,1}$=1/2). The subscript (7,6,1) refers to the amount

of electrons contributing to the total spin angular momentum *S*. When we are going from a $(S_{i,7}, M_{i,S_7}, S_{i,6}, S_{i,1})$ basis to a $(S_{i,6}, M_{i,S_6}, S_{i,1}, M_{i,S_1})$ basis, we can write:

(2.18) $$[S_{i,7}, M_{i,S_7}, S_{i,6}, S_{i,1} >= a[S_{i,6}, M_{i,S_6}, S_{i,1}, M_{i,S_1} > + b[S_{i,6}, M_{i,S_6}, S_{i,1}, -M_{i,S_1} > .$$

Coefficients *a* and *b* are the well-known Clebsch-Gordon coefficients which can be written in the usual notation as:

(2.19) $$\alpha \equiv (S_{i,6}, M_{i,S_6}, S_{i,1}, M_{i,S_1} \mid S_{i,7}, M_{i,S_7}, S_{i,6}, S_{i,1}) = (3, M_{i,S_6}, 0.5, M_{i,S_1} \mid 3.5, M_{i,S_7}, 3, 0.5)$$

Now we can write for the $[3.5,2.5,3,0.5 >$ state for example:

(2.20) $$[3.5,2.5,3,0.5 >= 0.93[3,2,0.5,\uparrow > + 0.38[3,3,0.5,\downarrow > .$$

The other Clebsch-Gordon coefficients can be found in Table 2.2. Let us now focus on the final state. The final (*f*) state is characterized by a certain J_f (L_f, S_f) and M_{J_f} of the 4f^6 electrons, and by the spin of the 5*d* electron m_{s_D}. We know that all the spins are aligned in the 4f^7 initial state, S_7=3.5. Therefore the total spin angular momentum of the 4f^6 system in the final state is S_6=S_7 - S_1=3.5-0.5=3. According to Hund's second rule, low lying 4f^6 states have maximum orbital angular momentum, L_6=3. As a result, the 4f^6 term symbol is ^{7}F. We are considering only low lying final states with S_6=L_6=3. For these final states, the total angular momentum J_6 can range from 0 (L_6-S_6) to 6 (L_6+S_6). The Landé interval spitting of the J_6 final states gives rise to an effective broadening of the T_{2g} and E_g absorption peaks.

Table 2.2 | Clebsch-Gordon coefficients *α* of the initial state

$\|S_7, Ms_7>$	=	a	$\|S_6, Ms_6; S_1, Ms_1>$	+	b	$\|S_6, Ms_6; S_1, Ms_1>$
|3.5, 3.5>	=	1.0	|3,3; 0.5,0.5>	+	-	-
|3.5, 2.5>	=	0.93	|3,2; 0.5,0.5>	+	0.38	|3,3; 0.5,-0.5>
|3.5, 1.5>	=	0.85	|3,1; 0.5,0.5>	+	0.53	|3,2; 0.5,-0.5>
|3.5, 0.5>	=	0.76	|3,0; 0.5,0.5>	+	0.65	|3,1; 0.5,-0.5>
|3.5, -0.5>	=	0.65	|3,-1; 0.5,0.5>	+	0.76	|3,0; 0.5,-0.5>
|3.5, -1.5>	=	0.53	|3,-2; 0.5,0.5>	+	0.85	|3,-1; 0.5,-0.5>
|3.5, -2.5>	=	0.38	|3,-3; 0.5,0.5>	+	0.93	|3,-2; 0.5,-0.5>
|3.5, -3.5>	=	-	-	+	1.0	|3,-3; 0.5,-0.5>

Next, we decompose the 4f^6 final state $|J_f, , M_{J_f}, S_f, L_f>$ in terms of $|S_f, M_{S_f}, L_f, M_{L_f}>$. We do all these tedious decompositions in order to be able to write the 4*f* to 5*d* transition matrix elements in terms of $m_{l_i}, M_{J_i}, m_{s_D}, J_f$ and *D*:

m_{l_i}	Initial state $4f^7$ orbital angular momentum quantum number (*z*). This determines which 4*f* hydrogen wave function we have to use.
M_{J_i}	Initial state total angular momentum quantum number (*z*). This is important when the initial state is Zeeman split and is important in determining the size of the magneto-optical effects.
m_{s_D}	Final state 5*d* orbital angular momentum quantum number (*z*). Since the 5*d* band is spin split, the final state energy is dependent on m_{s_D}.
J_f	Final state $4f^6$ orbital angular momentum quantum number (*z*). Because of the Landé interval splitting, the final state energy is dependent on J_f.
D	*d* orbital label: T_{2g} or E_g. Since the d orbital are split by the crystal field, the final state energy is dependent on D.

The *f* in the symbols refers to the final state (*f*). Now we decompose $|J_f, , M_{J_f}, 3, 3>$ in terms of $|3, M_{S_f}, 3, M_{S_f}>$. The Clebsch-Gordon coefficients, which are connecting the two bases, are only non-zero when $M_{J_f} = M_{S_f} + M_{L_f}$. We make the following decomposition:

(2.21) $|J_f, M_{J_f}, 3, 3> = \sum \beta \, |3, M_{J_f} - M_{L_f}, 3, M_{L_f}>$

Where β is a Clebsch-Gordon coefficient. The Clebsch-Gordon coefficients in Eq. (2.21) are defined as:

(2.22) $\beta \equiv (S_f, M_{S_f}, L_f, M_{L_f} \mid J_f, M_{J_f}, S_f, L_f) = (3, M_{J_f} - M_{L_f}, 3, M_{L_f} \mid J_f, M_{J_f}, 3, 3)$,

where we use the relation: $M_{S_f} = M_{J_f} - M_{L_f}$; β is zero unless $M_{J_f} = M_{L_f} + M_{S_f}$. The total orbital angular momentum of the $4f^6$ final state (M_{L_f}) can also be written in terms of the single 4*f* electron initial state orbital angular momentum quantum number m_{l_i}. This can be seen from the following. When a single electron with orbital angular momentum m_{l_i} makes transition to a 5d state, then the remaining six 4*f* electrons will have a total orbital angular momentum of $M_{L_f} = -m_{l_i}$. Therefore we can write (2.21) as:

(2.23) $|J_f, M_{J_f}, 3, 3> = \sum \beta \; |3, M_{J_f} + m_{l_i}, 3, -m_{l_i}>$.

Since there are five possible crystal field split 5d states, the final state is also labeled by the *d* orbital (D). The radial part (r_d) for all the 5*d*-orbitals is the same. The angular parts of the T_{2g} and E_g states can be written in terms of the spherical harmonics $Y_{l,ml}$ [6]:

(2.24) $t_{2g}(D_{T1}) = \frac{-iY_{2,2}+iY_{2,-2}}{\sqrt{2}}$ $t_{2g}(D_{T2}) = \frac{-Y_{2,1}+Y_{2,-1}}{\sqrt{2}}$ $t_{2g}(D_{T3}) = \frac{iY_{2,1}+iY_{2,-1}}{\sqrt{2}}$,

(2.25) $e_g(D_{E1}) = \frac{Y_{2,2}+Y_{2,-2}}{\sqrt{2}}$ $\qquad e_g(D_{E2}) = Y_{2,0}$.

We can write for the final state:

(2.26) $|f> = \left[4f^6 \left({}^7F_{J_f}, J_f, M_{J_f} \right);\ 5d^1 \left(D, m_{s_D} \right) > = \right.$

$$\sum_{m_{l_i}=-3}^{3} \beta \left[\ 3, M_{J_f} + m_{l_i}, 3, -m_{l_i} \ ;\ 5d^1 \left(D, m_{s_D} \right) > . \right.$$

Let us now also find an expression for the initial state in terms of 4*f*^{6} final state quantum numbers (m_{s_D}, J_f, M_{J_f}). In the 4*f*-5*d* transition, the 4*f* electron which makes the transition is characterized by $S_{i,1}$ and M_{i,S_1}. Since the spin is conserved in electric dipole transitions, the spin of the 5*d* electron is equal to the one of the 4f electron: $m_{s_D} = M_{i,S_1} = \pm\frac{1}{2}$. Also we can write $M_{S_f} = M_{i,S_6} = M_{J_f} + m_{l_i}$. Therefore we write for the initial state (see Eq. 2.17):

(2.27) $|i> = \left[4f^7 \left({}^8S_{3.5}, J_i = 3.5, M_{J_i} \right) > = \right.$

$$\sum_{M_{J_f}+m_{l_i}=-3}^{3} \ \sum_{m_{s_D}=-\frac{1}{2}}^{\frac{1}{2}} \alpha \left[3, M_{J_f} + m_{l_i}, 0.5, m_{s_D} > . \right.$$

Now we are interested in the following electric dipole matrix element, which connects the initial and final state [5]:

(2.28) $M(M_{J_i}\ ;\ J_f, M_{J_f},\ D_k,\ m_{s_D}) = \sum_{n=1}^{7} \langle f | \boldsymbol{r_n} | i \rangle$,

which is characterized by the initial state quantum number M_{i,S_7}($J_i = 3.5$ for all the transitions), by the final state quantum numbers J_f, M_{J_f}, m_{s_D}, and by the final state 5*d* orbital label D_k. r_n represent the coordinates of the nth electron [5]. Eq. (2.28) is a multi-electron matrix element. However as can be seen from (2.24) and (2.25), it is possible to write the initial and final states in terms of the single electron initial 4*f* state quantum number m_{l_i}. As was also recognized for instance by [5,6], in this specific case, *M* can be written in single electron matrix element connecting a (single electron) 4*f* state with a (single electron) 5*d* state:

(2.29) $M(M_{J_i}\ ;\ J_f, M_{J_f},\ D_k,\ m_{s_D}) = \ \alpha\ \beta\ \left\langle 5d: D_k \middle| \boldsymbol{r} \middle| 4f:\ m_{l_i} = M_{S_f} - M_{J_f} \right\rangle$,

in which for m_{l_i} holds:

(2.30) $m_{l_i} = -M_{L_f} = M_{S_f} - M_{J_f}$.

Now by using that fact that α is zero unless:

(2.31) $M_{i,S_7} = M_{i,S_6} + M_{i,S_1} = M_{i,S_6} + m_{s_D}$,

we rewrite Eq. (2.30):

(2.32) $M_{S_f} = M_{i,S_6} = M_{i,S_7} - M_{i,S_1} = M_{i,S_7} - m_{s_D} = M_{J_i} - m_{s_D}$,

(2.33) $m_{l_i} = M_{S_f} - M_{J_f} = M_{J_i} - m_{s_D} - M_{J_f}$.

Finally we get:

(2.34) $M(M_{J_i}\,;\, J_f, M_{J_f}, D_k, m_{s_D}) = \alpha\,\beta\,\Theta$,

(2.35) $\Theta\left(D_k,\, M_{J_i},\, m_{s_D}, M_{J_f}\right) \equiv \left\langle 5d\colon D_k \middle| \boldsymbol{r} \middle| 4f\colon\, m_{l_i} = M_{J_i} - m_{s_D} - M_{J_f} \right\rangle$,

$\alpha = \left(S_{i,6}, M_{i,S_6}, S_{i,1},\, M_{i,S_1} \middle| S_{i,7}, M_{i,S_7}, S_{i,6}, S_{i,1}\right) = \left(3,\, M_{J_i} - m_{s_D}, 0.5,\, m_{s_D} \middle| 3.5,\, M_{J_i}, 3, 0.5\right)$,

$\beta = (S_f, M_{S_f}, L_f, M_{L_f} | J_f, M_{J_f}, S_f, L_f) = \left(3,\, M_{J_i} - m_{s_D}, 3, -\left\{ M_{J_i} - m_{s_D} - M_{J_f} \right\} \middle|\, J_f,\, M_{J_i}, 3, 3\right).$

With this equation we can determine matrix elements from the M_{J_i} initial state ($J_i = 3.5$) to a $(J_f, M_{J_f}, D_k, m_{s_D})$ final state by calculating the one-electron matrix element, connecting the 4*f* orbital with $m_{l_i} = M_{J_i} - m_{s_D} - M_{J_f}$ and the D_k-th 5*d*-orbital. This is the final expression we will use. *M* is only non-zero when the Clebsch-Gordon coefficients α,β are non-zero and the matrix element Θ is non-zero. The square of the absolute value of the matrix elements of the T_{2g} (T) and E_g (E) transitions are defined as:

(2.36) $\left|\Theta_T(D_T,\, M_{J_i},\, m_{s_D}, M_{J_f})\right|^2 = \sum_k \left|\Theta(D_{T,k}\,,\, M_{J_i},\, m_{s_D}, M_{J_f})\right|^2$,

(2.37) $\left|\Theta_E(D_E,\, M_{J_i},\, m_{s_D}, M_{J_f})\right|^2 = \sum_k \left|\Theta(D_{E,k}\,,\, M_{J_i},\, m_{s_D}, M_{J_f})\right|^2$,

where we sum over the different $D_{T/E,k}$ orbitals, which have the same energy. Now we can write for *M*:

(2.38) $\left|M_{DT}(M_{J_i}\,;\, J_f, M_{J_f},\, m_{s_D})\right|^2 = \alpha^2\,\beta^2\,|\Theta_T|^2$,

(2.39) $\left|M_{DE}(M_{J_i}\,;\, J_f, M_{J_f},\, m_{s_D})\right|^2 = \alpha^2\,\beta^2\,|\Theta_T|^2$.

The transition dipole matrix elements Θ for different polarizations are shown in Table 2.3, see also [6]. We will define the polarization later on, see starting from Eq. 2.48. While α was already tabulated (Table 2.3), due to the large amount of non-zero coefficients, β will not be shown over here.

Table 2.3 | Angular part of the transition dipole matrix elements Θ. RCP=right circularly polarized (parallel to B), LCP=left circularly polarized (parallel to B), //=polarization parallel to B, ⊥= polarization perpendicular to B.

$m_{l,i}$	$\varepsilon_{\perp}$	$\varepsilon_{//}$	ε_{RCP}	ε_{LCP}	ε_{avg}	$\varepsilon_{\perp}$	$\varepsilon_{//}$	ε_{RCP}	ε_{LCP}	ε_{avg}
3	45	0	0	90	30	45	0	0	90	30
2	60	30	0	120	50	0	30	0	0	10
1	3	96	6	0	34	39	0	6	72	26
0	36	0	36	36	24	0	108	0	0	36
-1	3	96	0	6	34	39	0	75	6	26
-2	60	30	120	0	50	0	30	0	0	10
-3	45	0	90	0	30	45	0	90	0	30
	$\lvert\Theta_T\rvert^2$ (x 420)					$\lvert\Theta_E\rvert^2$ (x 420)				

Now we can sum different transitions with the same frequency. As we will see later, the energies are determined by J_f and m_{s_D}, and we can sum different M_{J_f} states with the same J_f and m_{s_D}. Since we are not considering Zeeman splittings in the final state, we can define for the T_{2g} levels (denoted by subscript T) for instance:

$$(2.40)\quad \left|M_{DTZ}(M_{J_i}\,;\,J_f, m_{s_D})\right|^2 = \sum_{M_{J_f}} \left|M_{DT}(M_{J_i}\,;\,J_f, M_{J_f}, m_{s_D})\right|^2.$$

In order to calculate the magnetic field and temperature dependence, we need to calculate the population of the initial M_{J_i} states. The inclusion of the initial state population effects allows us to model the temperature and magnetic field dependent absorption spectrum and magneto-optical spectrum. The population (*p*) of a particular M_{J_i}state can be calculated according:

$$(2.41)\quad p_{M_{J_i}} = \frac{\exp(-\frac{M_{J_i} g\,\mu_B\, B}{k_B\, T})}{Z},$$

in which *Z* is the partition function:

$$(2.42)\quad Z = \sum_{M_{J_i}=-3.5}^{3.5} \exp(-\frac{M_{J_i} g\,\mu_B\, B}{k_B\, T}).$$

In order to account for initial state population effects, we multiply the square of the absolute value of Eq. (2.40) by the population factor:

$$(2.43)\quad \left|M_{DTZP}(M_{J_i}\,;\,J_f, m_{s_D})\right|^2 = p_{M_{J_i}} \left|M_{DTZ}(M_{J_i}\,;\,J_f, m_{s_D})\right|^2,$$

and we can sum over the different initial states M_{J_i} (same J_f and m_{s_D}):

(2.44) $\left|M_{DTZPM}(J_f, m_{s_D})\right|^2 = \sum_{M_{J_i}} \left|M_{DTZP}(M_{J_i}\,; J_f, m_{s_D})\right|^2$.

In the final expression, the element M_{DTZPM} is only a function of the final state quantum numbers (J_f, m_{s_D}); these quantum numbers determine the transition frequencies and these splittings are much larger than the Zeeman splittings that we neglected.

2.3.4 Transition energies

The transition energies can be written as:

(2.45) $\hbar\omega_{fi}(D_{T1}, D_{T2}, D_{T3}) = E_g + \frac{1}{2}\lambda_{4f} J_f\left(J_f + 1\right) + \frac{1}{2}\frac{M}{M_s} m_{s_D} \Delta_{EX}^{5d}$,

(2.46) $\hbar\omega_{fi}(D_{E1}, D_{E2}) = E_g + \frac{1}{2}\lambda_{4f} J_f\left(J_f + 1\right) + \Delta_{CF} + \frac{1}{2}\frac{M}{M_s} m_{s_D} \Delta_{EX}^{5d}$,

in which M_s is the saturation magnetization in μ_B per atom (7 μ_B). The magnetization is calculated according to:

(2.47) $M = \sum_{M_{J_i}=-3.5}^{M_{J_i}=+3.5} p_{M_{J_i}} M_{J_i}\ \mu_B$.

The equations for the energy (2.45) and (2.46), together with the equation for the matrix elements (2.44) are used in order to calculate the absorption coefficient using Eq. (2.16).

2.3.5 The dipole operator

$\boldsymbol{r}$ in Eq. (2.28) represents the coordinate of the electron which makes the transition. If ε is the polarization vector of the light ($\varepsilon \cdot \varepsilon = 1, \varepsilon \cdot k = 0$), then and according to [6], we can write $\varepsilon \cdot \hat{\boldsymbol{r}}$ in terms of spherical harmonics:

(2.48) $\varepsilon \cdot \hat{\boldsymbol{r}} = \sqrt{\frac{4\pi}{3}}\left(\varepsilon_z Y_{1,0} + \frac{-\varepsilon_x + i\varepsilon_y}{\sqrt{2}} Y_{1,1} + \frac{\varepsilon_x + i\varepsilon_y}{\sqrt{2}} Y_{1,-1}\right)$.

Therefore the different light polarizations can be written in terms of spherical harmonics:

(2.49) $\mathrm{RCP}, \vec{k}$ parallel with quantization axis(z): $\sim\ Y_{1,1}$

(2.50) $\mathrm{LCP}, \vec{k}$ parallel with quantization axis(z): $\sim\ Y_{1,-1}$

(2.51) $\mathrm{x-polarized}$: $\sim\ \frac{Y_{1,-1} - Y_{1,1}}{\sqrt{2}}$

(2.52) $\mathrm{y-polarized:} \sim i\ \frac{Y_{1,-1}+Y_{1,1}}{\sqrt{2}}$

(2.53) $\mathrm{z-polarized:} \sim Y_{1,0}$

Eq. (2.49)-(2.53) are used to calculate the absorption spectra for different polarizations.

2.3.6 The absorption spectrum and the refractive index

In this section we will describe how we will exactly determine the absorption coefficient. When Eq. (2.44) and (2.16) are combined, we get for the absorption coefficient:

(2.54) $\alpha(\omega) = \frac{\pi N}{2\varepsilon_0 c}\ \frac{\omega}{n(\omega)} \sum\left|M_{DkZPM}(J_f, m_{s_D})\right|^2\ G_{5d}(\hbar\omega - \hbar\omega_{fi})$,

in which *k* in between the vertical bars can be either T_{2g} (T) or E_g (E) and the summation is over the (J_f, m_{s_D}) final state quantum numbers. As one can see, the expression for the absorption coefficient is dependent on the frequency dependent refractive index. Since the refractive index is unknown, we will calculate the imaginary part of the dielectric function, which is not dependent on $n(\omega)$:

(2.55) $\mathcal{E}_2(\omega) = \frac{\pi N}{2\varepsilon_0}\ \sum\left|M_{DiZPM}(J_f, m_{s_D})\right|^2\ G_{5d}(\hbar\omega - \hbar\omega_{fi})$.

The matrix element $M_{DiZPM}(J_f, m_{s_D})$ in Eq. (2.55) can be separated in a radial part and a spherical part:

(2.56) $\left|M_{DiZPM}(J_f, m_{s_D})\right|^2 = R_{MDiZPM}\ S_{MDiZPM}(J_f, m_{s_D})$.

Since the radial part is the same for all the (J_f, D_i, m_{s_D}) transitions and is not responsible for (magnetic) dichroic effects, it is incorporated in a pre-factor *A*, which will be a fitting parameter:

(2.57) $\mathcal{E}_2(\omega) = A\ \ \sum S_{MDiZPM}(J_f, m_{s_D})\ \ G_{5d}(\hbar\omega - \hbar\omega_{fi})$.

Note that Eq. (2.57) does not contain the refractive index and we can calculate is easily. This does not hold for the absorption coefficient, Eq. (2.54). The expression for the absorption coefficient does contain the refractive index, which is a quantity we do not know yet but which can be obtained after a Kramers-Kronig transformation of $\kappa(\omega)$, which is the extinction coefficient ($\kappa(\omega) = c\alpha/2\omega$). The difficulty in this transformation is that for this one needs to know the spectrum

with frequencies ranging from zero to infinity while we only model the spectrum in the NIR/VIS range. Therefore we first assume that there is no dispersion ($n(\omega)$=constant); in this case both $\alpha(\omega)$ and $\kappa(\omega)$ are proportional $\mathcal{E}_2(\omega)$. The absorption edge shift will be studied in this approximation, since in this case no Kramers-Kronig transformation needs to be performed.

Now we will describe how we will calculate we calculate $n(\omega)$ and later $\alpha(\omega)$in a more correct way. First we determine $\kappa(\omega)$ by assuming that $\kappa(\omega) = \mathcal{E}_2(\omega)$. Then we compare the calculated $\kappa(\omega)$ with the experimental $\kappa_{exp}(\omega)$ at room temperature. The average of the calculated spectra for RCP and LCP, $(\kappa_+(\omega) + \kappa_-(\omega))/2$, is scaled to the experimental spectrum $\kappa_{exp}(\omega) - \kappa_{B.G.}(\omega)$, in which the background (B.G.) represents other transitions (4*f* to 6*s* for instance). After that the calculated $\kappa(\omega)$ is summed with $\kappa_{B.G.}(\omega)$. In order to obtain the refractive index $n(\omega)$, one needs to perform a Kramers-Kronig transformation. Before we discuss the Kramers-Kronig transformation, it is useful to consider a Hilbert transform:

(2.58) $g(y) = \mathcal{H}[f(x)] = \frac{1}{\pi} PV \int_{-\infty}^{\infty} \frac{f(x)dx}{x-y}$,

in which *PV* is the Cauchy principal value. The integral in Eq. (2.58) runs from $-\infty$ to $+\infty$. $\kappa(\omega)$ at negative frequencies can be calculated by using the fact that $\kappa(\omega)$ is an odd function:

(2.59) $\kappa(\omega) = -\kappa(-\omega)$.

Now in an insulating magnetic material, where the normal modes are $\tilde{n}_{\pm}(\omega)$, the refractive index can be calculated according [17,18]:

(2.60) $n_+(\omega) + n_-(\omega) = 2\left[1 + \mathcal{H}\left[\frac{\kappa_+(\omega\prime)+\kappa_-(\omega\prime)}{2}\right]\right]$,

(2.61) $n_+(\omega) - n_-(\omega) = 2\left[\mathcal{H}[\kappa_+(\omega') - \kappa_-(\omega')]\right]$.

Since not all transitions from $-\infty$ to $+\infty$ are taken into account in $\kappa(\omega)$, the calculated $n_{\pm}(\omega)$ curve is down-shifted with respect to the experimental value for the refractive index. Therefore, $n_+(\omega)$ and $n_-(\omega)$ needs to be shifted (by the same constant (n_0)) to match the experimental value for $n(\omega)$. Using the calculated refractive index (n^{old}), $\kappa(\omega)$ is re-calculated by using:

(2.62) $\kappa^{new} = \frac{\kappa^{old}}{2n^{old}}$,

in which $\kappa^{old}(\omega)$ is the refractive index by assuming $\kappa(\omega) = \mathfrak{E}_2(\omega)$ and $n^{old}(\omega)$ is the refractive index obtained from Eq. (2.60) and (2.61). Now, the whole procedure is repeated to obtain a better value for $n(\omega)$ and $\kappa(\omega)$. The calculation method is summarized in Fig. 2.6:

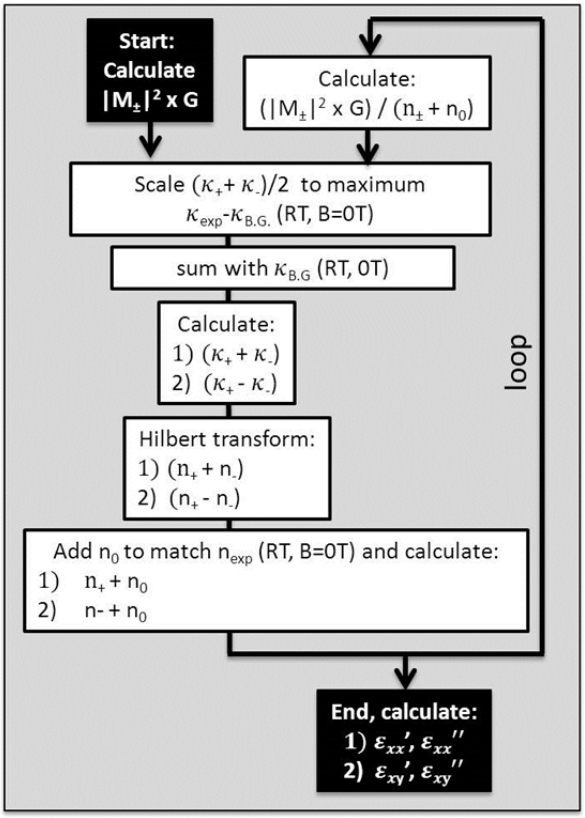

Figure 2.6 |Scheme of calculation of $n_{\pm}(\omega)$.

After we know $n_{\pm}(\omega)$ and $\kappa_{\pm}(\omega)$, we can calculate the magneto-optical effects which are linear in the magnetization. In literature, magneto-optical spectra are usually taken in the so-called polar geometry: the angle of incidence is 0° and the applied magnetic field is parallel to the wavevector of light beam. In this case, simple analytical expressions for the Kerr rotation and ellipticity are available. First we have to calculate the reflection coefficient for RCP and LCP ($\tilde{n} = n + i\kappa$) [19]:

$$(2.63)\quad r_{\pm}(\omega) = \frac{\tilde{n}_{\pm}(\omega)-1}{\tilde{n}_{\pm}(\omega)+1} = \frac{{n_{\pm}}^2(\omega)-1+{\kappa_{\pm}}^2(\omega)}{{n_{\pm}}^2(\omega)+2n_{\pm}(\omega)+1+{\kappa_{\pm}}^2(\omega)} + i\,\frac{2\kappa_{\pm}(\omega)}{{n_{\pm}}^2(\omega)+2n_{\pm}(\omega)+1+{\kappa_{\pm}}^2(\omega)}.$$

Now if we define:

(2.64) $r_{\pm}(\omega) = \rho_{\pm}(\omega)\, e^{i\Theta_{\pm}(\omega)}$.

We can write for the Kerr rotation (θ_{Kerr}) and ellipticity (ε_{Kerr}), respectively:

(2.65) $\theta_{Kerr}(\omega) = -\frac{1}{2}(\Theta_{+}(\omega) - \Theta_{-}(\omega))$,

(2.66) $\varepsilon_{Kerr}(\omega) = \frac{\rho_{+}(\omega)-\rho_{-}(\omega)}{\rho_{+}(\omega)+\rho_{-}(\omega)}$.

The magneto-optical effects for an arbitrary direction of the magnetization and angle of incidence are more complicated. In the following section a method will be presented which allows us to do this. First the properties of the dielectric tensor of EuO will be discussed.

2.3.7 Dielectric tensor of EuO

In order to calculate the magneto-optical effects for arbitrary configuration, it is useful to consider the dielectric function of EuO. The dielectric tensor of a cubic material, without a macroscopic magnetization, contains only diagonal tensor elements [19]:

(2.67) $\epsilon = \begin{pmatrix} \epsilon_{xx} & 0 & 0 \\ 0 & \epsilon_{xx} & 0 \\ 0 & 0 & \epsilon_{xx} \end{pmatrix}$.

However, when there is a macroscopic magnetization in the *z*-direction, the dielectric tensor also contains off-diagonal elements:

(2.68) $\epsilon = \begin{pmatrix} \epsilon_{xx} & \epsilon_{xy} & 0 \\ -\epsilon_{xy} & \epsilon_{xx} & 0 \\ 0 & 0 & \epsilon_{xx} \end{pmatrix}$.

Now, consider a light wave which is propagating along the magnetization direction (*z*-direction):

(2.69) $E = E_0 e^{-i\omega\left(t-\frac{\tilde{n}z}{c}\right)}$.

In which $\tilde{n}$ is the complex refractive index ($\tilde{n} = n + i\kappa$). Now, from the wave equation, it follows that the eigenmodes of propagation in the z-direction are [19,20]:

(2.70) $\tilde{n}_{\pm}^2 = \epsilon_{xx} \pm i\epsilon_{xy}$.

This means that there are two modes, with right and left circular polarization. Now we can write ϵ_{xx} and ϵ_{xy} in terms of $\tilde{n}_{\pm}$:

(2.71) $\epsilon'_{xx} = \frac{1}{2}([n_+^2 + n_-^2] - [\kappa_+^2 + \kappa_-^2])$,

(2.72) $\epsilon''_{xx} = n_+\kappa_+ + n_-\kappa_-$,

(2.73) $\epsilon'_{xy} = n_+\kappa_+ - n_-\kappa_-$,

(2.74) $\epsilon''_{xy} = -\frac{1}{2}([n_+^2 - n_-^2] - [\kappa_+^2 - \kappa_-^2])$.

Note that the *imaginary* part of ϵ_{xx} and the *real* part of ϵ_{xy} are zero in a non-absorbing medium. When ϵ_{xx} and ϵ_{xy} are known for the material, the magneto-optical Kerr effect and Faraday effect can be calculated for an arbitrary direction of the magnetization and angle of incidence using the boundary matrix method which is discussed in the next section. For later, it will be useful to define the following quantities:

(2.75) $Q = -i\,\frac{\epsilon_{xy}}{\epsilon_{xx}}$,

(2.76) $\tilde{n}^2 = \epsilon_{xx}$.

Q is called the magneto-optical parameter. In the next section we will work in the approximation that $Q \ll 1$. The refractive index $\tilde{n}$ will appear in Snell's law ($\tilde{n}_1 \sin(\theta_1) = \tilde{n}_2\, sin(\theta_2)$). For arbitrary direction of the magnetization, we can write for the dielectric tensor [21]:

(2.77) $$\epsilon = \tilde{n}^2 \begin{pmatrix} 1 & \mathrm{i}\cos(\varphi)\,Q & -i\ \sin(\varphi)\ \sin(\varphi)\,Q \\ -i\ \cos(\varphi)\,Q & 1 & \mathrm{i}\cos(\varphi)\ \sin(\varphi)\,\mathrm{Q} \\ \mathrm{i}\sin(\varphi)\ \sin(\varphi)\,Q & \mathrm{i}\cos(\varphi)\sin(\varphi)\,Q & 1 \end{pmatrix},$$

in which the angle (φ, γ) are the angles of the magnetization *M* relative to the boundary plane(*x*,*y*) and the plane of incidence (*y*,*z*), see also Fig. 2.7 [21].

(2.78) $m_x = \frac{M_x}{|M|} = \sin(\varphi)\ \cos(\gamma)$,

(2.79) $m_y = \frac{M_y}{|M|} = \sin(\varphi)\sin(\gamma)$,

(2.80) $m_z = \frac{M_z}{|M|} = \cos(\varphi)$.

2.3.8 Magneto-optics from thin solid films

In the next steps is shown how the reflection and transmission coefficients can be calculated in a magnetic medium with a dielectric tensor as is given by Eq. (2.76).

We follow method as is described in [22--24]. We consider a boundary between two media where we define the xy-plane as the boundary plane. Now the following vectors are defined:

(2.81) $F = \begin{pmatrix} E_x \\ E_y \\ H_x \\ H_y \end{pmatrix}$, $P = \begin{pmatrix} E_s^i \\ E_p^i \\ E_s^r \\ E_s^r \end{pmatrix}$.

F is built from the *x* and *y* components (subscripts) of the electric and the magnetic field at the boundary. *P* is built from the *s* and *p* components (subscripts) relative to the plane of incidence. The superscript indicates the direction of propagation which can be either parallel to the z-component of the wavevector of the incoming beam (superscript *i*) or parallel to the z-component of the wavevector of the reflected beam (superscript *r*). For instance, E_s^i is the electric field amplitude of the incident electric field perpendicular to the plane of incidence. Now a boundary matrix (*A*) can be defined which connects the vectors [22--24]:

(2.82) $F = AP$.

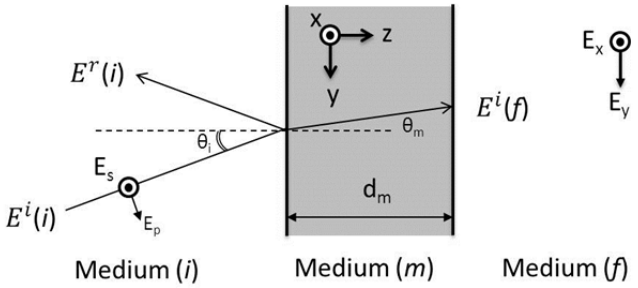

Figure 2.7 | Definition of the boundary plane and the plane of incidence.

Like in the derivation of the Fresnel equations, *F* is conserved on both sides of the boundary in medium (1) and medium (2):

(2.83) $F(1) = A(1)P(1) = A(2)P(2) = F(2)$,

in which the number in the braces refer to the medium in which we evaluate *F*. The propagation in medium 2 as function of the distance *z* can be described by a propagation matrix *D* [22--24]:

(2.84) $P_{z=0}(2) = D(2)P_z(2)$.

Now one can relate the P-vector in medium *i* to the P-vector in medium *f*. For a multilayer systems we can write [22--24]:

(2.85) $P(i) = A(i)^{-1}\,(\prod_m A(m)D(m)A(m)^{-1})\;A(f)P(f) \equiv Q\,P(f).$

We can write the 4x4 matrix *Q* in terms of 2x2 matrixes *G,H,I,J*:

(2.86) $Q \equiv \begin{bmatrix} G & H \\ I & J \end{bmatrix}.$

After that one can write for the total transmission and reflection coefficients (electric field) [22--24]:

(2.87) $t^i(f) = \begin{bmatrix} t_{ss} & t_{sp} \\ t_{ps} & t_{pp} \end{bmatrix} = G^{-1}\,,$

(2.88) $r^r(i) = \begin{bmatrix} r_{ss} & r_{sp} \\ r_{ps} & r_{pp} \end{bmatrix} = IG^{-1}.$

This means that the reflection and transmission can be calculated when the *A* and *D* matrixes in the different media are known. Expressions for the A and D matrixes for magnetic materials with a dielectric tensor as is described by Eq. (2.77) can be found in literature [22--24]. The A and D matrixes are a function of the following quantities:

- Dielectric function ($\tilde{n}$,*Q)*
- Direction of the magnetization (φ, γ)
- Thickness of the layer (*d)*
- Angle of incidence (θ_i)

In order to calculate the Magneto-optical effects, we need to define the rotation and the ellipticity [20]:

(2.89) $tan2\theta = \frac{2\,Re\chi}{1-|\chi|^2}\,,$

(2.90) $sin2\varepsilon = \frac{2\,Im\chi}{1+|\chi|^2}\,,$

(2.91) $\chi = E_p/E_s\,,$

in which E_p and E_s are the electric field components parallel (p) or perpendicular (s) to the plane of incidence. Now, we define the Faraday rotation and ellipticity angles as :

(2.92) $\theta_F(\vec{M}) = \frac{1}{2}\left[tan^{-1}\left(\frac{2Re\left(\chi_F(\vec{M})\right)}{1-\left|\chi_F(\vec{M})\right|^2}\right) - tan^{-1}\left(\frac{2Re\left(\chi_F(-\vec{M})\right)}{1-\left|\chi_F(-\vec{M})\right|^2}\right)\right],$

(2.93) $\varepsilon_F(\vec{M}) = \frac{1}{2}\left[sin^{-1}\left(\frac{2Im\left(\chi_F(\vec{M})\right)}{1+\left|\chi_F(\vec{M})\right|^2}\right) - sin^{-1}\left(\frac{2Im\left(\chi_F(-\vec{M})\right)}{1+\left|\chi_F(-\vec{M})\right|^2}\right)\right]$,

(2.94) $\chi_F(\vec{M}) = \left[E_p^i(f)\right]/\left[E_s^i(f)\right]$.

Finally, the Kerr rotation and ellipticity angles we define as :

(2.95) $\theta_K(\vec{M}) = \frac{1}{2}\left[tan^{-1}\left(\frac{2Re\left(\chi_K(\vec{M})\right)}{1-\left|\chi_K(\vec{M})\right|^2}\right) - tan^{-1}\left(\frac{2Re\left(\chi_K(-\vec{M})\right)}{1-\left|\chi_K(-\vec{M})\right|^2}\right)\right]$,

(2.96) $\varepsilon_K(\vec{M}) = \frac{1}{2}\left[sin^{-1}\left(\frac{2Im\left(\chi_K(\vec{M})\right)}{1+\left|\chi_K(\vec{M})\right|^2}\right) - sin^{-1}\left(\frac{2Im\left(\chi_K(-\vec{M})\right)}{1+\left|\chi_K(-\vec{M})\right|^2}\right)\right]$.

(2.97) $\chi_K(\vec{M}) = \left[E_p^r(i)\right]/[E_s^r(i)]$

The next section focusses on the results of the simulations.

2.4 Calculated magnetic field and temperature dependent magneto-optical properties in EuO

2.4.1 The origin of the large magneto-optical Kerr and Faraday effects

In order to see where the magneto-optical effects originate from, we are considering transitions to final states with $J_f = 6, M_{J_f} = \pm 6$. With the help of Eq. (2.34) and (2.35), transitions with non-zero matrix elements are shown in Fig 2.8.

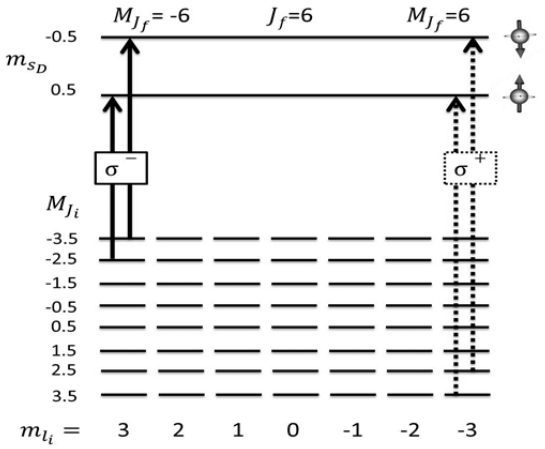

Figure 2.8 |Energy level diagram for the 4*f* to 5*d* transitions. Arrows represents non-zero matrix elements for transitions from the M_{J_i}initials state towards the $J_f = 6, M_{J_f} = \pm 6$ final state with $m_{S_D} = \pm 0.5$. Dotted arrows represent RCP transition while solid lines represent LCP transitions.

For RCP-light, there are only transitions from the initial state with $M_{J_i} = 3.5, 2.5$ while for LCP-light the only possible transitions are from initial states with $M_{J_i} = -3.5, -2.5$. In zero magnetic field, all the initial states are equally occupied and there will be no difference in the absorption for RCP and LCP (no magneto-optical effects). However at low temperature in the ferromagnetic phase, only the initial state with $M_{J_i} = 3.5$ is occupied. This means that only RCP transitions are allowed. We can also see that at low temperature, there are only transitions to the spin-up 5*d* band. We can understand this from the fact that at low temperature in a magnetic field, there are only spin-up 4*f* electrons and that spin flips are not allowed in electric-dipole transitions. The 4*f*-5*d* exchange interaction affects the transition frequency, while it is *not* responsible for the large magneto-optical effects in EuO. At higher temperatures, when the $M_{J_i} = 2.5$ state is occupied, also transitions to the spin-down state are possible for RCP. The spin-splitting, also in this case, only affects the transition frequencies.

2.4.2 The magnetic field dependent absorption spectrum

The simulated T_{2g} absorption spectra (or more accurately the ε_2 spectra, $\alpha \sim \varepsilon_2$ when there is no dispersion), as function of applied magnetic field for RCP and LCP light are shown in Fig. 2.9. The applied field is parallel to the wavevector of the light. In this graph we neglect the other (mostly higher lying) transitions (to 6s band, e_g band etc.) The exchange splitting that we use in Fig 2.9 is 2x0.3eV=0.6eV and the 4*f*-spin-orbit coupling constant is 30.5 meV, see Table 2.1.

The FWHM of the 5*d* density of states (Gaussian) was taken to be 158 meV. The maximum field was taken to be 34T (which is the effective mean field in EuO), which is the effective magnetic field in the mean-field approach in EuO at 0K. The spectrum in zero field is symmetrical for both RCP and LCP light because of the fact that all the initial state M_J levels are equally occupied. When a magnetic field is applied, the absorption maximum for RCP light shifts towards lower energies. For LCP light, the maximum first shifts to higher energies while for even higher fields, the maximum is red-shifted. The origin of this shifts is discussed in the next section. Apart from a shift also the FWHM of the absorption peak is decreased, and the maximum is increased. The narrowing can be explained by the fact that at the initial states M_{J_i} occupancies are changing when an magnetic field is applied. In high fields and low temperature, mainly the $M_{J_i} = 3.5$ levels are occupied. In this

case for RCP light there are mainly transitions to states with low J_f while for LCP light, there are mainly transitions to states with high J_f. The integrated absorption is constant which we expect from sum rules.

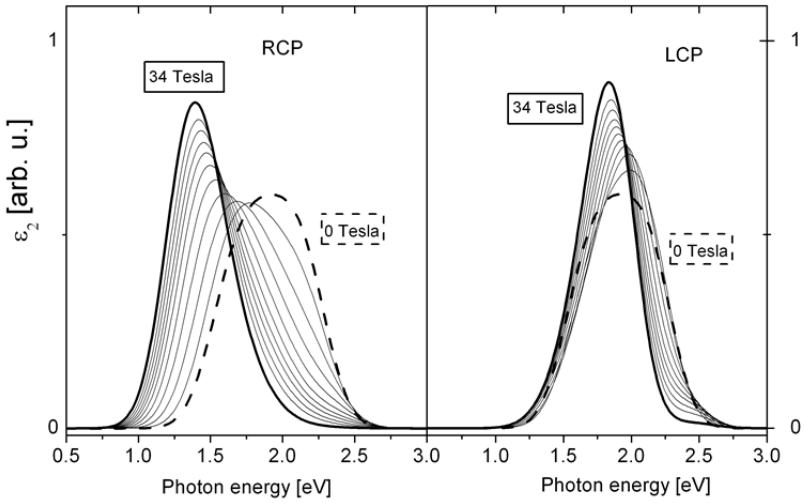

Figure 2.9 | ε_2 spectra in arbitrary units for RCP and LCP for different applied magnetic fields for T=20K. In the case that there is no dispersion, the absorption coefficient is proportional al to ε_2. In here we only consider transition from the 4*f* valence band to the 5*d* t_{2g} conduction band. The spin splitting is taken to be ±0.3 eV (literature value [6]). The 4*f* spin-orbit coupling constant is 30.5 meV (literature value [6]).

In Figure 2.10, the absorption ($\alpha \sim \varepsilon_2$ when there is no dispersion) to the 5d spin-up and spin-down bands is shown in the case of zero exchange-splitting at *T*=20 K in applied magnetic field of 10T. At these experimental conditions, the transition probability towards the 5*d* spin-up band is much higher than the transition probability towards the 5*d* spin-down band, due to the fact that the occupation of initial state spin-up levels is much higher than the occupation of initial state spin-down levels (and spin-flip transitions are not allowed).

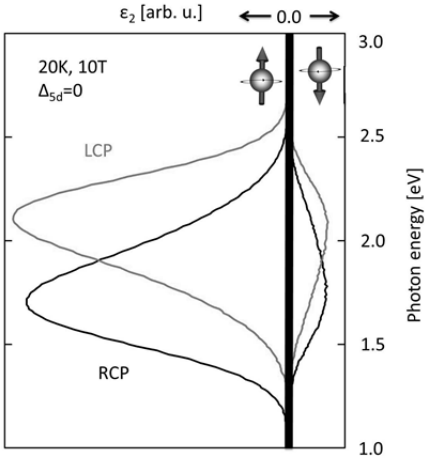

Figure 2.10 | ε_2 spectra for RCP (black) and LCP (red) for transition towards spin-up (left) and spin-down (right) 5d final states at T= 20K, B= 10T. In here we only consider transition from the 4*f* valence band to the 5*d* t_{2g} conduction band. The spin-splitting is taken to be 0. In the case that there is no dispersion, the absorption coefficient is proportional al to ε_2.

Another observation is that the absorption maxima for RCP and LCP are shifted with respect to each other (as we saw before in Fig 2.9) even when the spin-splitting in the conduction band is zero. As was already noticed in literature [4,5], this shift is related to the difference in magnitude of the matrix elements for different J_f final sates. As mentioned, for RCP light, the maximum is towards final states with small J_f while for LCP light, the maximum is towards final states with large J_f. The Landé splitting between the J_f=0 and J_f=6 state is 0.65 eV.

2.4.3 The absorption edge shift

Now we present the results on the absorption edge shift based on the spectra presented in Fig. 2.9. The absorption edge shift can provide valuable information about the 4*f*-5*d* exchange coupling, and about the 4*f* spin-orbit coupling strength. The absorption edge was defined as the photon energy at 25% of the normalized maximum of the absorption peak. The shift is calculated for different polarizations (RCP, LCP, LP) and the exchange splitting was taken to be 0.0 or 0.6 eV. Results were presented for positive and negative applied magnetic field and magnetization. The calculations hold for paramagnetic 'EuO' where the (effective) magnetic field at zero applied fields is zero. Only by applying a magnetic field, a magnetization (or short-range order) is created. The magnetization was calculated by Eq. (2.47). Due to the nonlinearity of the magnetization with respect to the applied magnetic field,

the behavior of the absorption edge shift is much more linear (in a larger range) in the magnetization (right figure) than it is in the applied magnetic field (left figure).

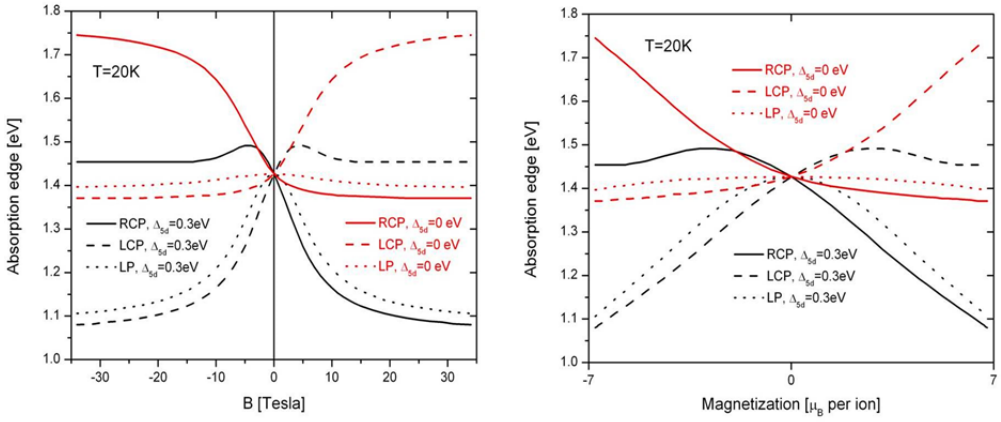

Figure 2.11 |Absorption edge shift for different polarization as function of the applied magnetic fields (left) and the magnetization (right) at T=20K. The spin splitting is taken to be 0 (red line) or ±0.3 eV (black lines). The 4f spin-orbit coupling constant is 30.5 meV.

In order to separate the shift due to the exchange splitting and the "dichroic shift", the absorption shift for zero exchange-splitting was calculated (red lines). One can see that the dichroic shifts for RCP and LCP light are large while it is small for LP light. Another thing that one can notice is the fact that the shift is even in the magnetic field for LP while it is odd for RCP and LCP. For CP light the shift is only dependent on the relative direction of the 'spin' of the photon and the applied magnetic field. Therefore the shift for RCP light at positive applied magnetic fields coincides with the shift for LCP at negative applied magnetic fields. The shift with respect to zero applied field is small and positive (red shift) for a parallel configuring (RCP, +B or LCP, -B), whereas it is large and negative (blue shifted) for an anti-parallel configuration.

For LCP light and an exchange splitting of 2x0.3eV= 0.6eV, two effects are competing at positive applied magnetic field: the red shift of conduction band due to the 4f-4d exchange interaction and the blue shift due to the dichroic effects. The dichroic effects occur only when not all the M_{J_i} initial states are equally occupied (which occurs in an magnetic field), and when the final state 4*f* spin-orbit coupling is nonzero. The result is that, at low applied magnetic fields, the absorption edge is blue shifted while at higher magnetic fields, the edge is red shifted. This behavior is

unique for the CP polarization and is also observed experimentally in the paramagnetic phase in EuO [6].

Experimental results for the magnetic field dependent, polarization dependent absorption edge shift at 77K in EuO are presented in Figure 2.12 . Qualitatively the results are the same. The red shift is larger for RCP than for LP and LCP shows a more complicated behavior. At low fields, there is a blue shift and a larger fields there is a red shift.

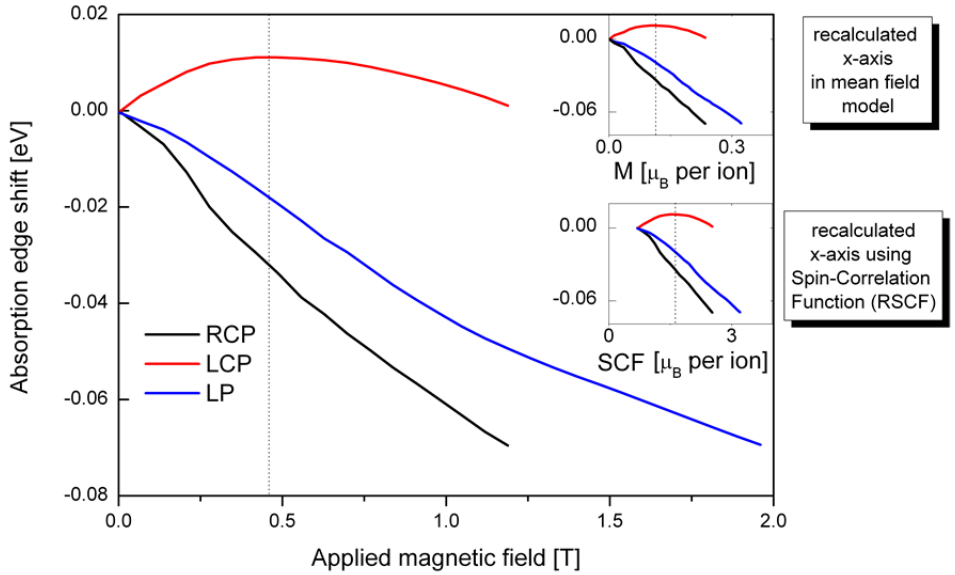

Figure 2.12 | Experimental absorption edge shift for different polarization as function of the applied magnetic fields at T=77K. The data has been (digitized and) taken from [6]. The insets shows the same data but with a recalculated x-axis. In the upper inset, this is done by considering EuO at 77K in the mean field model. In the lower inset this is done by considering the applied magnetic field dependence of the reduced nearest neighbor spin correlation function (RSCF) at $1.1xT_c$=77K for S=1.5. RSCFx7μ_B is used as x-axis. The RSCF has been taken from [25].

In order to compare the balance between dichroic an exchange splitting effects, we will compare the experimental data for LCP with our calculations. In the experimental data, the shift is plotted versus applied magnetic field, Fig 2.12. When we know the applied magnetic field dependence of the magnetization and spin-correlation function, we can plot the shift versus the magnetization or reduced spin-correlation function (RSCF), see the insets in Fig 2.12. In the upper inset, the magnetization is calculated from the mean field model by considering EuO at 77K.

In the lower inset, an estimate for the reduced spin-correlation function ($RSCF = \langle \overrightarrow{S_1} \cdot \overrightarrow{S_2} \rangle / S^2$) was made based on [25]. In this reference, the applied magnetic field dependence at 1.1xT_c=77K for S=1.5 and six nearest neighbors (z=6) was calculated. RSCFx7μ_B versus the absorption edge shift is plotted in the lower inset. The maxima of the absorption edge shift for LCP is shown in Table 2.4. As one can see, the agreement with the recalculated magnetization using the RSCF is reasonably good, taken into account that that we use a RSCF for S=1.5 and that there are many assumptions in our model. The recalculated (macroscopic) magnetization in the mean-field model is much lower than the value from our model. This results point out once more that the absorption shift is related to short-range magnetic order rather than to a macroscopic magnetization. The fact that the agreement is so good tells us that the minimum ingredients necessary to explain the observed experimental behavior are present in our model.

Table 2.4| Experimental and calculated LCP absorption shift maxima

Absorption shift maximum LCP	**Magnetization [μ_B]**
Calculated	2.8
Experiment (-> magnetization from mean field)	0.1
Experiment (-> magnetization in single domain from spin correlation function at=77K for S=1.5)	1.6

Now we turn into the discussion of the temperature dependent shift in the ferromagnetic phase, which provides information about the 4*f*-5*d* exchange coupling. We determine the temperature dependent shift, using the experimental temperature dependence of the spin correlation function at zero field for EuO. The results are shown in Fig. 2.13. The red line corresponds to the RSCF as was determined in [26,27] from the magnetic energy, assuming that the magnetic energy is proportional to the RSCF. The black line is the calculated shift, assuming that *F* in Eq. (2.8) is proportional to the RSCF. The data has been shifted vertically and normalized to reach agreement for T= 10K and *T*= 100K. There is a reasonable agreement with the between the calculated curve and the experimental absorption edge shift. One can also see that the calculated shift behaves different than the RSCF which we ascribe to dichroic effects. The inclusion of the dichroic effect gives a better correspondence between the calculated and experimental results. However it is not a bad assumption to consider the absorption edge shift for LP light to be proportional to the RSCF. These present results show that optically

induced changes in the short-range order in EuO can be measured by probing the absorption edge shift using a continuum probe pulse (in a pump-probe experiment).

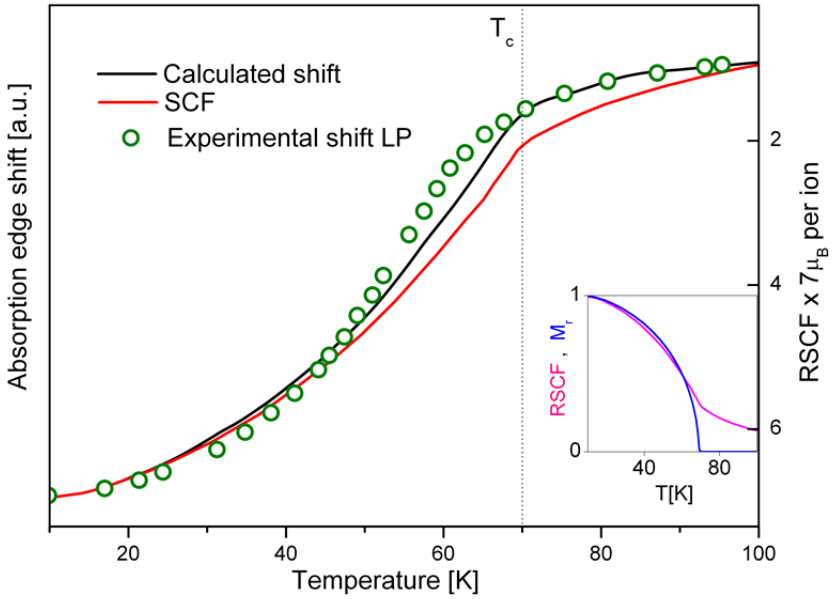

Figure 2.13 |Temperature dependence of the absorption edge shift (on a linear scale). The black line corresponds to the calculated shift using the RSCF from [15,26,27]. The red line represents the RSCFx7μ_B (right scale). The green circles, represent the experimental absorption edge shift for LP. The inset shows the RSCF and the reduced magnetic (M_r) versus temperature at zero applied magnetic field.

Qualitatively, there are differences between the experimental absorption edge shift and the calculated one. For the calculations, we used the (temperature dependent) RSCF at B=0T. Experimental and calculated values of the magnitude of the absorption edge shift are tabulated below (Table 2.5). For LP, where dichroic effects are almost absent, the calculated temperature dependent shift is a smaller than the experimental (Exp.) values Exp. 2 and Exp. 3 in Table 2.5. One of the reasons for this might be the presence of free carriers in these samples; it is known that the absorption edge shift decreases upon increasing carrier concentration. This decrease can be explained in terms of a conduction band electron state-filling effect, the Moss-Burstein effect [28,29]. When the bottom of the conduction band is occupied, the absorption edge appears at higher energies. This effect is larger at low temperatures because of the spin-splitting since at low temperature the conduction electrons fill-up only the spin-up band while at higher temperature they

occupy both the spin-up and spin-down bands. The Moss-Burstein shift could be as large as 80 meV and could be used as an optical probe for the amount of free carriers.

The dichroic effect (absorption edge RCP- absorption edge LCP) at 30 K and at 90K are also depicted in Table 2.4. The calculated values using a 4*f* spin-orbit coupling strength of 30.5 meV and a FWHM of 158 meV are higher than the experimental ones. Taking into account that the maximum of the LCP absorption occurs at higher energies than for RCP, we expect the Moss-Burstein effect to be much larger for RCP than for LCP and this can be one of the reasons of the observed difference in the experiential dichroic shift and the calculated one. However since the maximum observed Moss-Burstein shift is 80 meV, other factors also need to be considered. The actual 4f spin-orbit coupling strength might be reduced significantly compared to the value of 30.5 meV. This value is taken form EuF_2, where seven lines (J=0,1,2,3,4,5,6) can be distinguished in the absorption spectrum [6,30]. It is unclear where this reduction in the spin-orbit coupling strength of the localized 4f state is coming from, but it might involve hybridization effects (Eu 4*f*/O2p). We will continue this discussion in the next section where we discuss the magneto-optical (Kerr/Faraday) spectra.

Table 2.5| Experimental and calculated absorption edge shifts in [meV]. For the calculations, we used the (temperature dependent) RSCF at B=0T. In the first two columns (RCP/LCP) and the last column (LP), the absorption edge at high temperature is compared to the absorption edge at low temperatures. In the middle columns (named T[K]) the absorption edge of RCP light (at a fixed temperature) is compared with the absorption edge of LCP light.

	RCP	**LCP**	**T [K]**	**T [K]**	**LP**
Calculated	90K-6K ***289***	90K-6K ***13***	RCP-LCP ***373*** [at 6K]	RCP-LCP ***97*** [at 90K]	90K-6K ***297***
Exp. 1 [31]	90K-30K ***282***	90K-30K ***197***	RCP-LCP ***129*** [at 30K]	(RCP-LCP) ***44*** [at 90K]	-
Exp. 2 [15]	-	-	-	-	90K-6K ***260***
Exp. 3 [6]	-	-	-	-	90K-6K ***220***

Concluding: we observed that the absorption edge shift for LP light is a good probe for the 4*f*-5*d* exchange splitting while for RCP and LCP light strong so-called dichroic

effects were present. The magnitude of these dichroic effects is a good measure for the 4*f* spin-orbit coupling strength. Based on this we suggest that the 4*f* spin-orbit coupling strength is smaller than the 31 meV (EuF_2).

2.4.4 Magneto-optical Kerr, Faraday and MCD spectra

More information about the conduction bandwidth and 4*f* spin-orbit coupling strength can be obtained from the magneto-optical spectra. Based on the previously described method, we may calculate the refractive index for RCP and LCP from which we can determine the polar Kerr spectrum. In order to try to get a satisfactory agreement with the experimental results at low temperature (<20K) in an applied magnetic field which is large enough to align the ferromagnetic domains, we varied both the 4*f* spin-orbit coupling strength and the width of Gaussian 5*d* density of states, see Fig. 2.14 and 2.15.

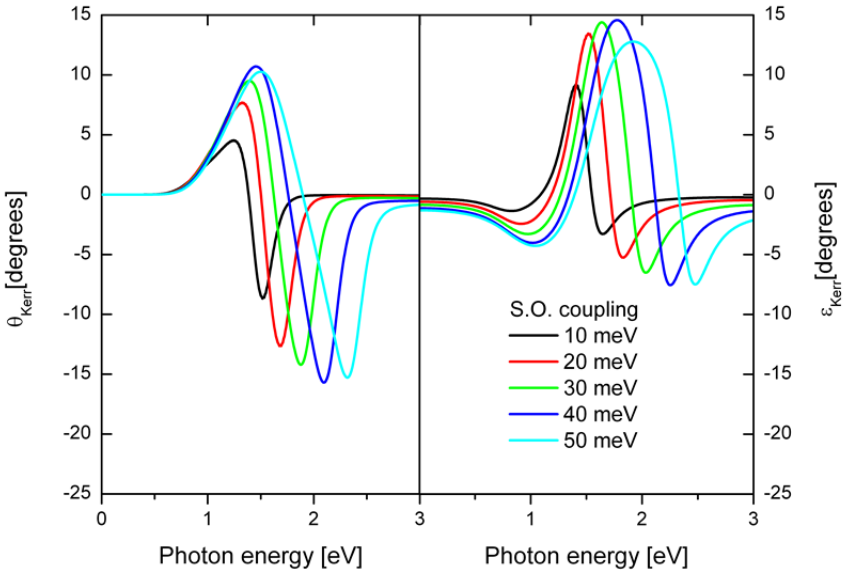

Figure 2.14 |Calculated magneto-optical spectra. σ of the conduction band is 183 meV. B=34T, T=10K.

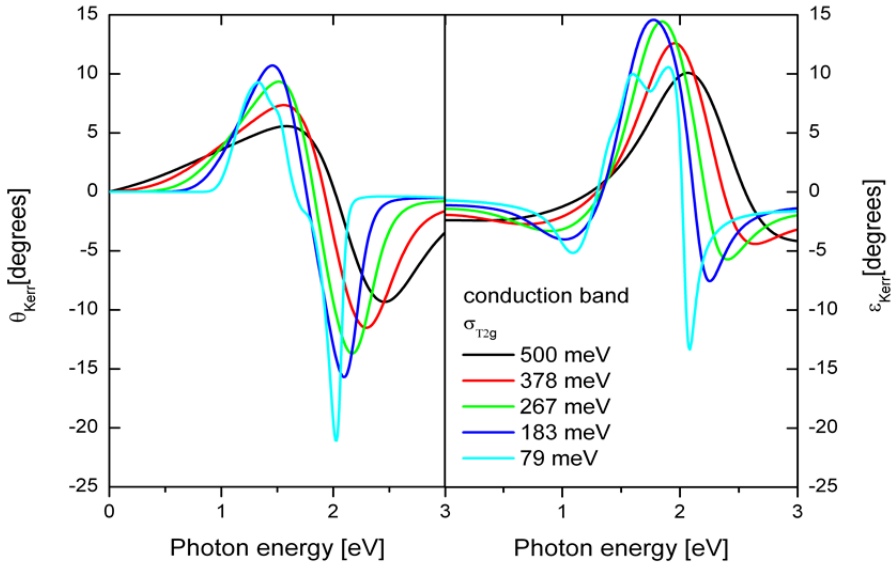

Figure 2.15 |Calculated magneto-optical spectra. The spin-orbit coupling strength is 40 meV. B=34T, T=10K.

An increase of the spin-orbit coupling leads to both an increase of the extreme values (maxima/minima) of the Kerr rotation and ellipticity spectra as well as to a shift of the energies at which these extremes occur. The increase of the maxima can be explained by the fact that in our model: when the spin-orbit coupling strength is zero, the J_f final-states do not split and the transition frequencies and intensities are the same for RCP and LCP, resulting in a zero Kerr effect. The shift can be explained by considering the Landé interval spitting $E = \frac{1}{2}\lambda_{4f} J_f (J_f + 1)$ which is depends on the spin-orbit coupling strength. When λ_{4f} increases, the states with J≠0 appear at higher energies.

The influence on the 5*d* conduction bandwidth is shown in Fig 2.15. An increase of the width leads to a decrease of the magnitude of the Kerr rotation and ellipticity. For the a more smaller conduction band width, more structure appears in the spectra due to the fact that the different J_f final states peaks are not overlapping anymore.

The results were compared with different experimental spectra from literature: MCD spectra($MCD \propto [\kappa_+ - \kappa_-]$), Faraday rotation spectra ($\theta_F \propto [n_+ - n_-]$) and Kerr spectra ($\theta_K = f(n_+, n_-, \kappa_+, \kappa_-), \epsilon_K = g(n_+, n_-, \kappa_+, \kappa_-)$) were available. One should note that when ($\kappa_+ = \kappa_- = 0$), the Kerr rotation and Faraday ellipticity and

MCD are zero. Therefore we call the Kerr rotation, Faraday ellipticity and MCD absorptive effects while the Kerr ellipticity and Faraday rotation are refractive effects. The normalized experimental magneto-optical spectra are shown in Figure 2.16 (data taken from [32--35]). Unlike the transmission experiments (MCD/Faraday), the reflection experiments (Kerr) at the T_{2g} transition frequency show some structure. Since both the Kerr/Faraday and MCD effect are a function of (the same) $n_+/n_-/\kappa_+/\kappa_-$, this hints to sample quality issues. From Fig. 2.16 it is also clear that there are also inconstancies within the transmission measurements; the Faraday rotation determined by two different groups shows quite some differences. Therefore we choose not to make a very detailed discussion about the differences between the calculated data and the experimental data because of the inconsistencies in the experimental data. However we can say that in the used parameter space (σ_{t2g}=79-500 meV, λ_{4f}=10-50meV), the calculated size of the Kerr rotation and ellipticity are in the same order of magnitude as the experimentally observed one.

Since we are still interested in the magnetic field and temperature dependence of the magneto-optical effects, we chose to optimize the values for σ_{t2g} and λ_{4f} by comparing the calculated reflectivity spectrum with the experimental low temperate (T=2K) spectrum, see Fig 2.17. The experimental data has been taken from [36]. A reasonable agreement with the experimental reflectivity is obtained when we use σ_{t2g}=287 meV and λ_{4f}=30meV, see Figure 2.17. The difference between the calculated and measured spectra is the largest at higher photon energies (2.5-3 eV). In order to get a better correspondence, we have to more carefully model the higher lying transition (Eu4*f* to Eu5*d* e_g, hybridized Eu4*f*/Eu5*d* to Eu6*s*).

Concluding, the 4*f* spin-orbit coupling strength is in the order of tens of meV while the 5*d* t*2g* conduction band width is several hundreds of meV. In chapter 6 we will come back on this, when we discuss the possibility that the peak largest peak in the absorption spectrum (NIR-IV range) is due to a magnetic excitonic transition.

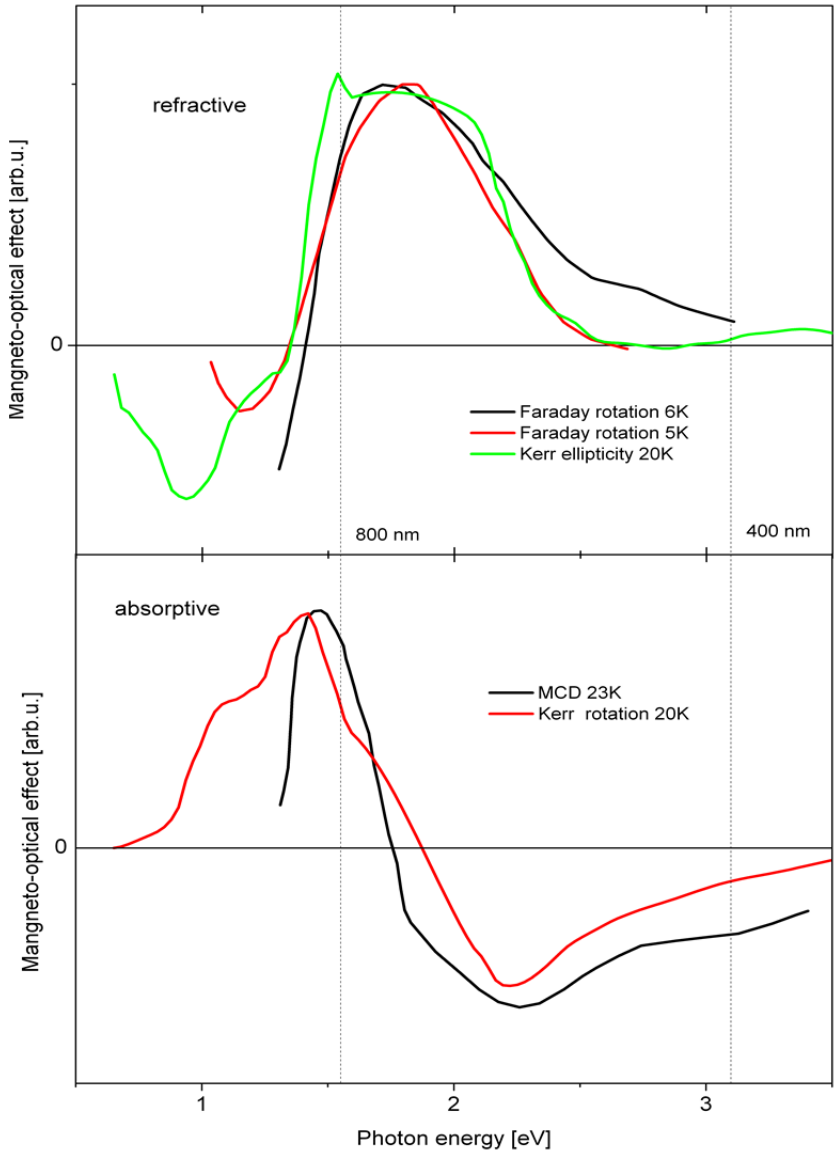

Figure 2.16 |Different (normalized) magneto-optical spectra from literature. In the upper panel the Faraday rotation (6K at 2T, 5K at 2.1T) and Kerr ellipticity (4T) are shown whereas in the lower panel the MCD (0.14T) and Kerr rotation (4T) spectra are shown. The upper panel is therefore more related to refractive effects while the lower panel is related more to absorptive effects. Kerr data taken from [34]. MCD data taken from [33]. Faraday 6K data taken from [35]. Faraday 5K data taken from [32].

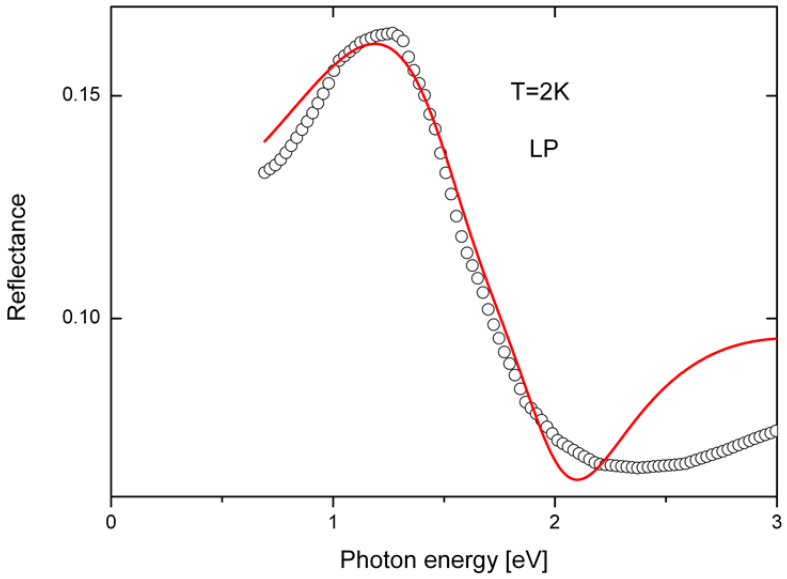

Figure 2.17 |Calculated (red line) and experimental magneto-optical spectra at 2K. The spin-orbit coupling strength is 30 meV and B=34T (which is the mean field in EuO) for the calculated spectrum. The experimental spectrum is taken with at 2K with LP light with B=0T. Although the experiential spectrum is taken at 0 T, the internal mean magnetic field within a small magnetic domain is about 34T. The experimental data has been taken from [36].

2.4.5 Magnetization dependence of the dielectric function

Since later on we probe the magnetization using a photon energy of 1.55 eV, it is important to know how the dielectric function around 1.55 eV is dependent on the magnetization. Using a conduction band width of σ_{t2g}=287meV and a spin-orbit coupling strength of λ_{4f}=30meV, dielectric function spectra are calculated for different values of the magnetization. The results are shown in Fig. 2.18. The magnetization dependent shift of ε_{xx}'' has been discussed before. However we can see from Fig. 2.18 that the real part of the diagonal part of the dielectric function ε_{xx}' is also shifting. This is not surprising since they are Kramers-Kronig transform related.

Let us now focus on off-diagonal part of the dielectric function. We can see that ε_{xy} is large (up to about 50% of ε_{xx} for large magnetization at particular frequencies) and has a so-called diamagnetic line shape. Spin and electric-dipole transitions, like the case of EuO, are known to have a so-called diamagnetic line shape. We can explain this line shape by the fact that ε_{xy}' is proportional to the difference in the

absorption for RCP and LCP light while ε_{xy}'' is the difference between the refractive index for RCP and LCP light. Like for the diagonal part, the peaks in the off-diagonal part are also red shifted because of conduction band shift and dichroic effects.

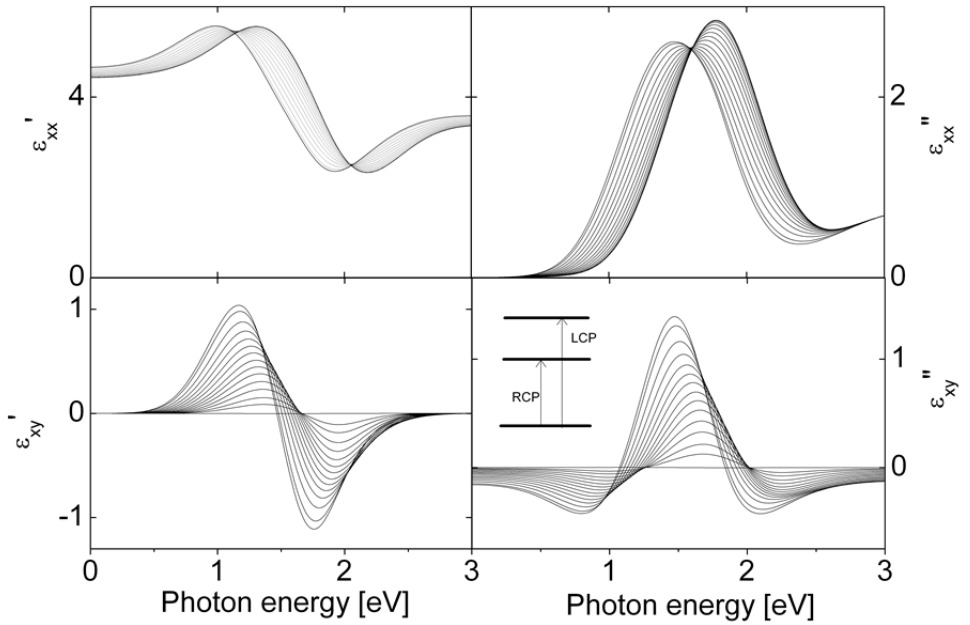

Figure 2.18 |Calculated dielectric function spectra for different magnetizations: 0.00, 0.55, 0.96, 1.49, 1.99, 2.52, 3.01, 3.49, 4.03, 4.51, 5.01, 5.50, 6.01, 6.51, 6.77 μ_B per ion. σ_{t2g}=287meV and λ_{4f}=30meV.

2.4.6 Magnetization dependence of the reflectance, tranmittance and absorbance

The reflectance (vacuum/EuO interface), transmittance (vacuum/EuO interface), absorbance (25 nm film) and absorption coefficient spectra for LP at normal incidence at the polar geometry for different magnetization are shown in Fig 2.19.

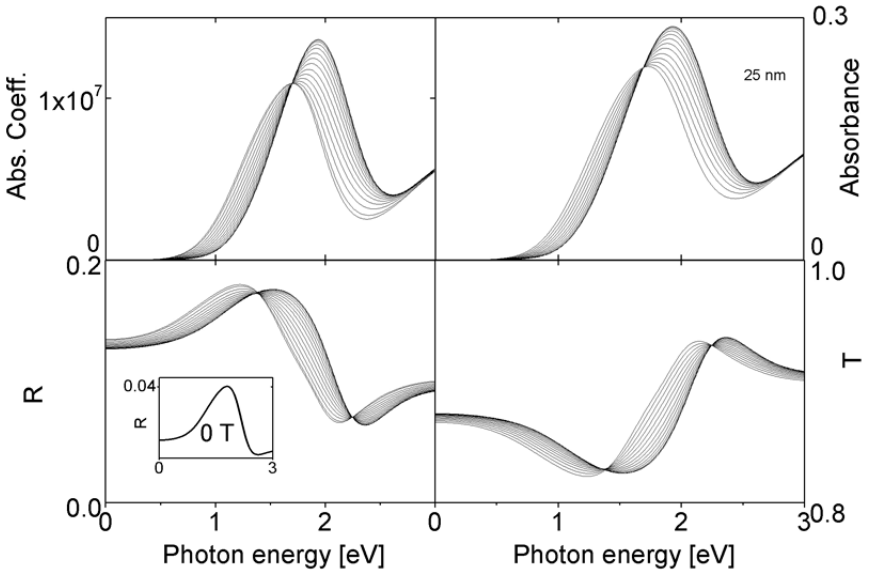

Figure 2.19 | Calculated absorption coefficient, absorbance (25nm thick film), reflectance (vacuum/EuO) and transmittance (vacuum/EuO) spectra for different magnetizations: 0.00, 0.55, 0.96, 1.49, 1.99, 2.52, 3.01, 3.49, 4.03, 4.51, 5.01, 5.50, 6.01, 6.51, 6.77 μ_B per ion. σ_{t2g}=287meV and λ_{4f}=30meV. The inset shows the reflectivity spectrum for a MgO/EuO interface.

In the upper left panel, we can see that the maximum in the absorption coefficient is shifting towards lower energy and that the maximum is decreasing with increasing magnetization. This can be understood from the fact the absorption coefficient is proportional to $\varepsilon_{xx}"/n$ (we discussed the magnetization dependence of $\varepsilon"$ and n before). At 800 nm, which will be the pump and probe frequency in the next chapters, the absorption is increasing with increasing magnetization. The absorbed energy in a 25 nm film (typical film thickness which has been used) is shown in the upper right panel of Fig 2.19. The absorbance (*A*) for a 25 nm film with a magnetization of 0 and 6.8 μ_B per ion is ~18% and ~ 22% respectively. In the lower panels, the reflectance (*R*) and transmittance (*T*) is shown for a vacuum/EuO interface. R at 800 nm for a vacuum/EuO interface for a magnetization of 0 μ_B per ion is about 18%. 800 nm is the probe wavelength that we used in most of the cases, see chapter 5. The same but than for a MgO/EuO interface (most of our samples are grown on a MgO substrate with a MgO capping layer) is shown in the inset. Due to the fact that the reflective index of MgO is more comparable to the refractive index of EuO, the reflection coefficient is much smaller, 3.6% at 800 nm.

The magnetization dependence of *R* and *A* at 800 nm is shown in the right panel of Fig 2.20. Whereas *R* is decreasing with increasing magnetization (or decreasing temperature), *A* is decreasing which can be understood for magnetization dependent shift of the optical absorption edge.

2.4.7 Magnetization dependence of the MO-Kerr effect: a linearity check

Also the magnetization dependence of the Kerr ellipticity and rotation are shown in Fig. 2.20. This dependence is important since later on we want to use the Kerr effect as a linear probe for the magnetization.

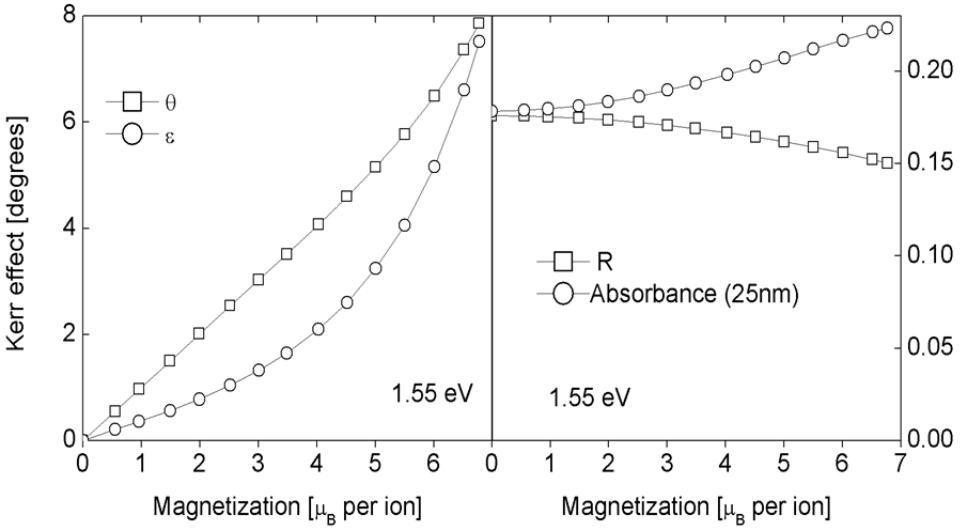

Figure 2.20 | Calculated Kerr rotation and ellipticity (left panel) and reflectance (R) and absorbance (right panel) versus the magnetization for a vacuum/EuO interface or a 25 nm film at 800 nm. σ_{t2g}=287meV and λ_{4f}=30meV.

We can see the dependence is nonlinear, especially for the Kerr ellipticity. The non-linearity of the Kerr ellipticity with the magnetization is due to the absorption edge shift, as can be seen from the magnetization dependence of the calculated polar Kerr spectra, Fig 2.21. In here we can observe a frequency shift of the maxima/minima and amplitude increase, with increasing magnetization. The origin of the shift was discussed before. The non-linearity due the absorption edge shift makes it difficult to use the Kerr effect as a simple (linear) probe for the magnetization. For this reason, the magnetization was also probed using X-ray Magnetic Circular Dichroism techniques. See Chapter 4 for more details.

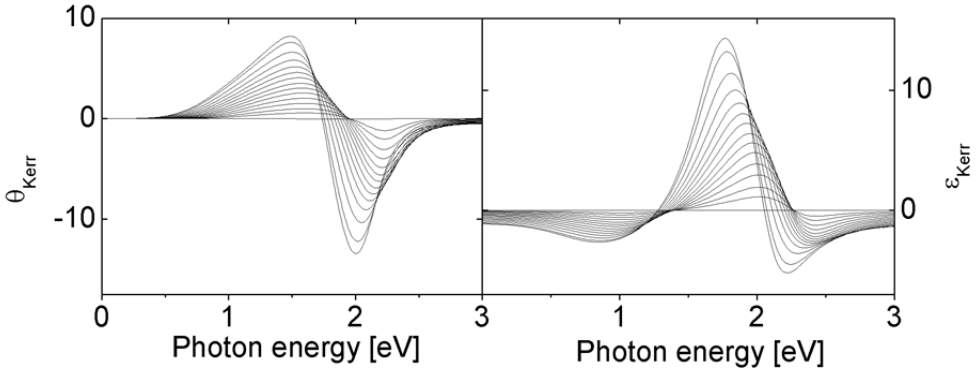

Figure 2.21 | Calculated Kerr rotation spectrum (left panel) and ellipticity spectrum (right panel) for a vacuum/EuO interface for different magnetizations: 0.00, 0.55, 0.96, 1.49, 1.99, 2.52, 3.01, 3.49, 4.03, 4.51, 5.01, 5.50, 6.01, 6.51, 6.77 μ_B per ion. σ_{t2g}=287meV and λ_{4f}=30meV. The Kerr effect is increasing with increasing magnetization.

2.4.8 Non-linear magneto-optics

Also for the pump-probe experiments, it is important to discuss the linearity issues between the MO-effect magnitude and the magnetization. When the changes in the rotation ($\Delta\theta$) and ellipticity ($\Delta\varepsilon$) are proportional to the changes in the magnetization (ΔM), the following relation should hold [41,42]:

(2.98) $\Delta\theta/\theta = \Delta\varepsilon/\varepsilon = \Delta M/M$.

The inequality of $\Delta\theta/\theta$ with respect to $\Delta\varepsilon/\varepsilon$ hints to the presence of optical effects in the magneto-optical signal. In Nickel, state filling effects are held responsible for the difference in of $\Delta\theta/\theta$and $\Delta\varepsilon/\varepsilon$ on sub-ps timescale [41]. However even when $\Delta\theta/\theta = \Delta\varepsilon/\varepsilon$, one should be careful for optical artifacts and a straightforward interpretation of magneto-optical data is in general problematic. Especially when a transfer between the orbital and spin angular momentum within a magnetic-ion is anticipated, large changes in the magneto-optical proportionality constant for the rotation and ellipticity can be expected and the proportionality is lost [42]. Therefore before we analyzing the magneto-optical transients (in chapter 5) as if they were true magnetization transients, we perform the followings steps and checks:

1) Measure apart from $\Delta\theta/\theta$, $\Delta\varepsilon/\varepsilon$ also $\Delta R/R$ or $\Delta T/T$ at the same wavelength. R and T are the reflectance and transmittance respectively. We consider the simplified case where we assume that $\Delta R/R$ and $\Delta T/T$ are sensitive to the

carrier dynamics while $\Delta\theta/\theta$ and $\Delta\varepsilon/\varepsilon$ are mostly sensitive to magnetization dynamics.

2) Check whether $\Delta\theta/\theta$ equals $\Delta\varepsilon/\varepsilon$. If not, there is no linear relationship between the magnetization and $\Delta\theta/\theta$, and the interpretation of the data is problematic.
3) Check whether the $\Delta\theta/\theta$ *or* $\Delta\varepsilon/\varepsilon$ dynamics are the similar to the $\Delta R/R$ or $\Delta T/T$ dynamics, and check whether the changes in *R* and *T* are in the same order of magnitude as the changes in θ and ε. When this is the case, this is another indication that one probably probes *optical* effects in the $\Delta\theta/\theta$ and $\Delta\varepsilon/\varepsilon$ signals (and not the magnetization).

2.4.9 Conclusion

In this Chapter we calculated the absorption spectra for different values of the magnetization and the temperature, as well as for different polarizations. We made several interesting observations:

- We observed that the absorption edge shift for LP light is a good probe for the 4*f*-5*d* exchange splitting while for RCP and LCP light strong so-called dichroic effects were present.
- The magnitude of these dichroic effects is a good measure for the 4*f* spin-orbit coupling strength. Based on this we suggest that the 4*f* spin-orbit coupling strength is smaller than the 31 meV; this value is taken from EuF_2, where seven lines (J=0,1,2,3,4,5,6) could be distinguished in the absorption spectrum. The origin might lie in the hybridization effects (Eu 4*f*/O2*p*).
- Within the model discussed in this Chapter model, the 5*d*-T_{2g} conduction band width (which was assumed to be Gaussian) is quite narrow: about σ_{5d}=290meV.
- We saw that the spin-splitting of the conduction band is *not* important in determining the size of the magneto-optical effects in the fully magnetized state. However the shift is important for the frequency at which maxima in the magneto-optical spectra occur.
- The (for the magneto-optical effects) required spin-orbit coupling is not present in the initial state (L=0 in our model) but is large in the final state of the 4*f* system and is responsible for the large magneto-optical effects in EuO. The size of the final state 4*f* spin-orbit coupling strength is also

important in determining the frequency at which maxima in the magneto-optical spectra occur.

- We saw that the spin-splitting of the conduction band can result in a nonlinear behavior of the magneto-optical Kerr ellipticity as function of the magnetization at particular frequencies.

Based on our results we suggest (in a later work) to perform optical pump-continuum probe experiments in which the absorption edge shift could be probed for varying pump-probe delay. Since the absorption edge shift is sensitive to short range order, the experiments can be done in zero applied magnetic field. Our model for the optical absorption provide a framework in which these results can be understood. The short range order dynamics can show in principle completely different demagnetization dynamics that the macroscopic magnetization (which can be probed by the Faraday/Kerr effect or XMCD spectroscopy) since it does not have to involve exchange of angular momentum between the lattice and the spin. An exchange of momentum between neighboring localized magnetic moments can already result in a change of the short range order, see for details Chapter 7. In this way the intrinsic dynamics of the spin system can be probed, which cannot easily be accessed by other experimental techniques.
In the next chapter we give an introduction to the field of laser-induced demagnetization dynamics due to the excitation of hot conduction electrons in ferromagnets.

References

[1] G. Guntherodt, Physics of Condensed Matter **18**, 37 (1974).
[2] G. Guntherodt, P. Wachter, and D. M. Imboden, Physik Der Kondensiterten Materie **12**, 292 (1971).
[3] A. Mauger and C. Godart, Physics Reports-Review Section of Physics Letters **141**, 51 (1986).
[4] A. B. Henriques, A. Wierts, M. A. Manfrini, G. Springholz, P. H. O. Rappl, E. Abramof, and A. Y. Ueta, Physical Review B **72**, 155337 (2005).
[5] A. B. Henriques, M. A. Manfrini, P. H. O. Rappl, and E. Abramof, Physical Review B **77**, 035204 (2008).
[6] P. Steeneken, *PhD thesis: New light on EuO thin films* (Rijksuniversiteit Groningen, 2002).
[7] O. Sakai, A. Yanase, and T. Kasuya, Journal of the Physical Society of Japan **42**, 596 (1977).
[8] T. Kasuya, J Magn Magn Mater **195**, 141 (1999).

[9] A. B. Henriques, G. D. Galgano, B. L. Diaz, P. H. O. Rappl, and E. Abramof, Journal of Physics-Condensed Matter **19**, 406234 (2007).
[10] G. van der Laan, E. Arenholz, A. Schmehl, and D. G. Schlom, Phys. Rev. Lett. **100**, 067403 (2008).
[11] D. B. Ghosh, M. De, and S. K. De, Physical Review B **70**, 115211 (2004).
[12] G. H. Hayes, *Handout #8 (Ligand field theory) of Chemistry course 3820:Transition Metal Chemistry (Fall 2006)* (University of Lethbridge, 2013.
[13] H. Miyazaki, T. Ito, H. J. Im, S. Yagi, M. Kato, K. Soda, and S. Kimura, Phys. Rev. Lett. **102**, 227203 (2009).
[14] C. J. Ballhausen, *Introduction to ligand field theory* (McGraw Hill, 1962).
[15] J. Schoenes and P. Wachter, Physical Review B **9**, 3097 (1974).
[16] H. Kuzmany, *Solid-State Spectroscopy* (Springer, 1998).
[17] J. F. Peters, *Resonant soft x-ray scattering studies of the magnetic nanostructure of stripe domains* (Universiteit van Amsterdam, 2003).
[18] D. Y. Smith, Physical Review B **13**, 5303 (1976).
[19] W. F. J. Fontijn, *Magneto-Optical Spectroscopy of Spinel Type Ferrites in Bulk Materials and Layered Structures* (Technische universiteit Eindhoven, 1998).
[20] A. K. Zvezdin and V. A. Kotov, *Modern Magnetooptics and Magnetooptical Materials* (Taylor & Francis, 2010).
[21] Z. J. Yang and M. R. Scheinfein, J. Appl. Phys. **74**, 6810 (1993).
[22] J. Zak, E. R. Moog, C. Liu, and S. D. Bader, Physical Review B **43**, 6423 (1991).
[23] J. Zak, E. R. Moog, C. Liu, and S. D. Bader, J. Appl. Phys. **68**, 4203 (1990).
[24] J. Zak, E. R. Moog, C. Liu, and S. D. Bader, J Magn Magn Mater **89**, 107 (1990).
[25] E. Callen, Phys. Rev. Lett. **20**, 1045 (1968).
[26] E. Callen and H. B. Callen, Physical Review **139**, A455 (1965).
[27] H. B. Callen and E. Callen, Physical Review A-General Physics **136**, 1675 (1964).
[28] T. S. Moss, *Optical properties in semiconductors* (Butterworths Scientific Publications, 1959).
[29] E. Burstein, Physical Review **93**, 632 (1954).
[30] M. Freiser, S. Methfess, and F. Holtzber, J. Appl. Phys. **39**, 900 (1968).
[31] C. Llinares, E. Monteil, G. Bordure, and Paparodi.C, Solid State Commun. **13**, 205 (1973).
[32] K. Y. Ahn and J. C. Suits, IEEE Trans. Magn. **MAG3**, 453 (1967).
[33] J. Ferre, J. P. Badoz, Paparodi.C, and Suryanar.R, IEEE Trans. Magn. **MAG7**, 388 (1971).
[34] H. Y. Wang, J. Schoenes, and E. Kaldis, Helvetica Physica Acta **59**, 102 (1986).
[35] T. R. Mcguire, G. F. Petrich, B. L. Olson, V. L. Moruzzi, and K. Y. Ahn, J. Appl. Phys. **42**, 1775 (1971).
[36] J. Feinleib, W. J. Scouler, J. O. Dimmock, J. Hanus, T. B. Reed, and C. R. Pidgeon, Phys. Rev. Lett. **22**, 1385 (1969).

[37] B. Kaminski, M. Lafrentz, R. V. Pisarev, *et al*, Phys. Rev. Lett. **103**, 057203 (2009).
[38] M. Matsubara, A. Schmehl, J. Mannhart, D. G. Schlom, and M. Fiebig, Physical Review B **81**, 214447 (2010).
[39] M. Matsubara, C. Becher, A. Schmehl, J. Mannhart, D. G. Schlom, and M. Fiebig, J. Appl. Phys. **109**, 07C309 (2011).
[40] M. Matsubara, A. Schmehl, J. Mannhart, D. G. Schlom, and M. Fiebig, Physical Review B **86**, 195127 (2012).
[41] B. Koopmans, M. van Kampen, J. Kohlhepp, and W. de Jonge, Phys. Rev. Lett. **85**, 844 (2000).
[42] B. Koopmans, M. van Kampen, and W. J. M. de Jonge, Journal of Physics-Condensed Matter **15**, S723 (2003).

Chapter 3

Laser-induced Demagnetization Dynamics due to hot Conduction Electrons in Ferromagnets: an Introduction

3.1 Introduction

In this chapter we will give an introduction to the field of laser-induced demagnetization dynamics arising from hot conduction electrons in ferromagnets. We start with ferromagnetic metals, while later on we will discuss ferromagnetic semiconductors.

3.2 Demagnetization dynamics in Ferromagnetic Metals

If one would have asked a condensed matter physicist in the beginning of the nineties what would happen to the magnetization of a ferromagnetic metal after it has been excited with a 100 fs optical laser pulse, the physicist probably would have answered that it will decrease with a characteristic time which corresponds to the electronic spin-lattice relaxation time. Depending on the temperature and the strength of the spin-orbit coupling in the metal, this can range typically from tens of picoseconds to hundreds of nanoseconds. The picture that one did have in mind was the following [1]. The laser pulse does not directly excite the spin system; instead, the laser excites the electrons into a highly non-equilibrium state. Electron-electron scattering leads to electronic thermalization at the 50-100 fs timescale. Energy transfer between the hot electrons and the cold lattice takes place at the picosecond time scale. Subsequent energy and angular momentum transfer

between the hot lattice and the spins leads to a demagnetization at the spin-lattice relaxation timescale.

Pioneering experiments by Beaurepaire *et al*. in 1996 showed that this picture does not hold, at least not for Nickel [2]. Using the magneto-optical Kerr effect (MOKE) as a probe for the magnetization, they argued that the magnetization decay takes place with a time constant in the sub-picosecond range, much faster than expected. After these experiments an intense discussion ensued whether the MOKE was a good probe for fast magnetization dynamics [3], see also Chapter 2. It was found that time-resolved rotation measurements often differ qualitatively from ellipticity measurements, showing that that the magneto-optical signal may also contain non-magnetic contributions. No solid agreement on the demagnetization time was made until 2007, when it became possible to probe the ultrafast magnetization dynamics in Nickel by time-resolved X-ray Magnetic Circular Dichroism (XMCD) using short circularly polarized soft-X-ray pulses [4]. It was found that demagnetization occurs with a time constant of 120 ± 70 fs.

For Nickel, several microscopic mechanisms were proposed to explain the unexpectedly fast demagnetization. They can be mainly distinguished in two categories. In the first category one explicitly considers the light-matter interaction [5]. It was argued that the optical excitation together with spin-orbit coupling could account for the observed demagnetization. Since the model does not consider the lattice and therefore also not spin-lattice relaxation, demagnetization can only occur because of an exchange of angular momentum between the photons and the spins. This is depicted in Fig. 3.1 where the transfer of angular momentum and energy between the photons and spins is shown. Later it was argued that the amount of absorbed photons was not high enough to give a substantial demagnetization [3]. Also the fact that there is no pump helicity dependence of the demagnetization dynamics was used as an argument to reject this scenario [6].

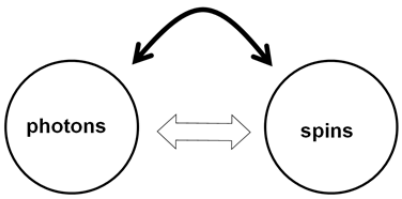

Figure 3.1 | Energy (white arrow) and angular momentum transfer (black arrow) between the light and the spin system for demagnetization due to the spin-photon interaction.

More recently, using a semi-classical approach, it was argued that a light pulse with a relatively weak electric field amplitude can affect the spin-system considerably when one uses photons resonant with the energy level separation in a two-level system [7,8]. Experimental efforts were done to directly investigate this coherent light-matter interaction by looking to the fluence dependence of the rotation of polarization of a single laser pulse in Nickel and $CoPt_3$ films [9]. The authors suggested that there is indeed a coherent light-matter interaction which leads to ultrafast demagnetization. However, the results can be considered as inconclusive because they completely rely on MOKE whereas it is known that there are non-magnetic contributions in the magneto-optical signal at the 100 fs timescale [3].
In the second category one assumes that the laser just acts as a heat pulse which heats the conduction electron sub-system. Energy and angular momentum transfer between the electrons, spins and lattice lead to demagnetization. The fact that the demagnetization proceeds even relatively long after the laser pulse has passed, indicates the importance of incoherent processes. The flow of angular momentum and energy is depicted in Fig. 3.2.

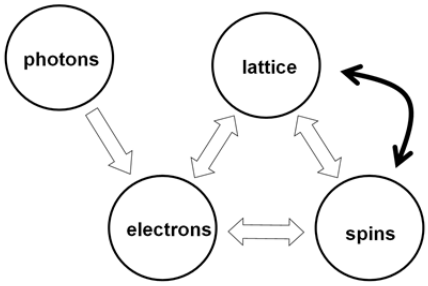

Figure 3.2 | Energy (white arrow) and angular momentum transfer (black arrow) between light, the lattice, electrons and spins. The energy of a photon is absorbed by the electrons after which there is energy transfer to the spins and the lattice. Demagnetization occurs due to various spin-lattice relaxation mechanisms.

In this (second) category, several microscopic demagnetization mechanisms can be distinguished. One is based on spin-flip scattering of (hot) electrons by impurities [10], phonons [11], or by other electrons [12,13]. The latter one will be discussed in more detail later on. The electron-phonon spin-flip mechanism is depicted in Fig. 3.3a: in an electron-phonon scattering process there is a finite probability that the electronic spin is flipped, see also the next section. Another picture involves the angular momentum transfer between the spin and orbital angular momentum in an electron-magnon scattering event and is depicted in Fig. 3.3b [14,15]. Before

photo excitation, the angular momentum is on the spin system (*S*). Because of spin-orbit coupling, angular momentum can be transferred from *S* to the orbital system (*L*) while a magnon is emitted. *L* can be rapidly quenched by the crystal field [14].

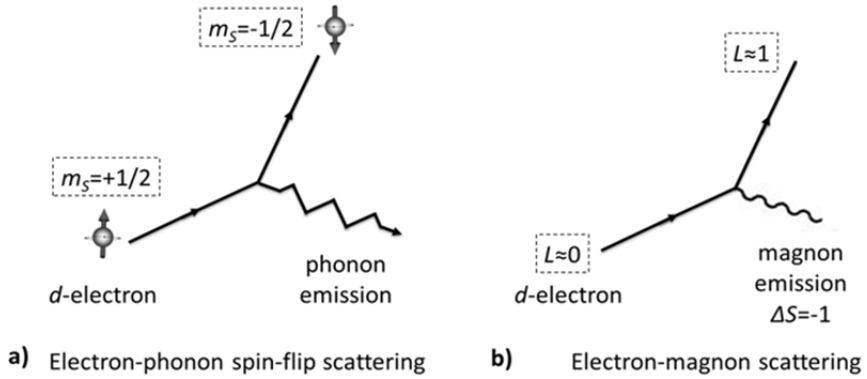

Figure 3.3 | Different spin-flip mechanisms. In a) an electron-phonon spin-flip scattering event is depicted while in b) an electron-magnon scattering event is shown. By the emission of a magnon, the total S is reduced by one (ΔS=-1). In this process angular momentum is transferred to the orbital system (ΔL=+1).

Recently it was also suggested that a mechanism in which hot conduction electron spins diffuse away might play a role. Theoretical papers appeared in which super-diffusive transport was considered to be an important source of ultrafast demagnetization in ferromagnetic metals [16,17]. Recent experimental efforts show the importance of this mechanism at ultrafast timescales [18--22], although it was shown in [20] that they do not dominate the ultrafast demagnetization.

While the discussion on laser-induced demagnetization in Nickel is still ongoing, one can also learn something about ultrafast demagnetization mechanisms by looking at different materials. Several experiments have been performed on ferromagnetic metals, which includes other transition metals and their alloys, rare-earth metals and half-metals [23--26]. A large range of demagnetization times was observed varying from hundreds of femtoseconds to nanoseconds. Apart from metals also diluted ferromagnetic semiconductors (DMS) have been studied [27--29]. In manganese-doped III/V semiconductors the magnetic properties can be tailored by changing the Mn-doping concentration and the hole density. Mn-doped InAs shows two demagnetization times, a fast (< 1ps) and a slower (~100 ps) one [29]. In a recent paper by Koopmans *et al*. [30] it was suggested that *all* these results might be explained in the framework of the microscopic three temperature model (M3TM). In this model a microscopic mechanism based on spin-flip

scattering of conduction electrons upon phonon absorption or emission was implemented in the three temperature model. Both models are discussed in more detail in the next sections.

In the first part of this chapter several models which have been used to explain the observed demagnetization times in different classes of conducting materials (these mechanisms involve conduction electrons) are discussed in more detail. Firstly the phenomenological three temperature model (3TM) is discussed. This model was used to depict the energy flow between the electrons, spins and the lattice in Nickel. After that the so-called microscopic 3TM is introduced. Because of the success in explaining the magnetization dynamics in a wide range of materials, we do this in quite some detail. After that we give an introduction into demagnetization mechanisms which are active in insulators, which does not involve conduction electrons. All these models provide a theoretical framework in which, later on, the results on EuO can be understood.

3.2.1 Demagnetization within the phenomenological three temperature model: energy transfer

In 1996 the so-called three temperature model (3TM) was introduced in order to explain the laser induced demagnetization in metallic Nickel [2]. In this model three sub-systems were defined, the lattice (l), the electrons (e) and the spins (s), which each have their own temperature (T_l, T_e,T_s) and specific heat (C_l, C_e, C_s). Energy transfer between the different sub-systems can be described in a phenomenological manner by three coupled differential equations, see Fig. 3.2. The energy transfer rates depend on the coupling constants between the sub-systems (g_{es}, g_{sp}, g_{ep}). In the simplest case the coupling constants are assumed to be temperature independent.

(3.1) $$C_e(T_e(t))\frac{dT_e(t)}{dt} = -g_{el}[T_e(t) - T_l(t)] - g_{es}[T_e(t) - T_s(t)] + P(t)$$

(3.2) $$C_l(T_l(t))\frac{dT_l(t)}{dt} = -g_{el}[T_l(t) - T_e(t)] - g_{sl}[T_l(t) - T_s(t)]$$

(3.3) $$C_s(T_s(t))\frac{dT_s(t)}{dt} = -g_{es}[T_s(t) - T_e(t)] - g_{sl}[T_s(t) - T_l(t)]$$

The laser action is modeled as a source term $P(t)$ in the differential equation for the electronic temperature. Now the response of the spin temperature on the increased electronic temperature can be simulated if the specific heats and coupling constants are known. While getting a model for the heat capacities is

easy, obtaining the coupling constants involves modeling the electron-lattice-spin interaction in the framework of a microscopic model. The solution of Eq. (3.1)-(3.3) can be fitted to the (magneto) optical data using the coupling constants as fit parameters. Demagnetization can occur due to direct electron-spin energy transfer but also via the electron-lattice-spin channel. For Nickel it is known that the electron-lattice energy transfer takes ~1 ps [2]. Since a demagnetization time of 120 fs is observed [4], the only other available channel in this model, which does not include a direct spin-photon coupling, is the electron-spin channel. Within this model the conclusion is that the spin-electron coupling constant is important. Good agreement with the experiments was obtained for g_{el}/g_{sl}=27 and g_{es}/g_{sl}=20 which reveals that indeed a large electron-spin coupling constant is needed within this model.

The three temperature model was developed for metals where the number of charge carriers is constant and where the thermalized electrons can be fitted with a Fermi-Dirac distribution to obtain an electronic temperature. Next sections introduce the microscopic-3TM and also discuss the applicability of the (M)3TM to EuO, which is a semiconductor.

3.2.2 Demagnetization of conduction electrons by electron-phonon scattering: microscopics

While the 3TM is a powerful model to describe the ultrafast spin dynamics in ferromagnetic metals on a phenomenological level, it does not provide any information on the microscopic level and that is why microscopic models need to be developed. One important question which needs to be answered by this model is where the angular momentum goes during demagnetization. Angular momentum is a conserved quantity and can be either on the spin part of the electronic momentum (S_e), orbital part of the electronic momentum (L_e), the lattice (L_{latt}) or on the photons (L_{phot}).

One such a microscopic model was introduced in [30]; the so-called microscopic three temperature model (M3TM). In this model angular momentum transfer occurs through Elliott-Yafet scattering [30]: due to spin-orbit coupling there is a finite possibility of a spin-flip when an electron scatters with a phonon (or impurity), see also Fig. 3.3a. The direct spin-photon coupling is not included. In this section we will zoom in on the Elliott-Yafet scattering process.

Elliot-Yafet spin-flip scattering can be understood by considering the electronic wavefunction of a conduction electron in a solid. Because of spin-orbit coupling,

the wavefunction is not a pure spin-state but is a mixed state. The wavefunctions can be written as Bloch states with predominantly spin-up or spin-down character [31]:

(3.4) $\psi_{k,\uparrow}(\boldsymbol{r}) = [a_k(\boldsymbol{r})|\uparrow> + b_k(\boldsymbol{r})|\downarrow>]e^{i\boldsymbol{k}\cdot\boldsymbol{r}}$

(3.5) $\psi_{k,\downarrow}(\boldsymbol{r}) = [a^*{}_{-k}(\boldsymbol{r})|\downarrow> + b^*{}_{-k}(\boldsymbol{r})|\uparrow>]e^{i\boldsymbol{k}\cdot\boldsymbol{r}}$

In which $|a|$ is usually close to unity and $|b|$<<1. The potential describing the interaction of an electron with a phonon can be written as [31]:

(3.6) $W_q = W_q^{ordinary} + W_q^{spin-orbit}$

In which $W_q^{ordinary}$ and $W_q^{spin-orbit}$ are the spin-independent and spin-dependent part of the scattering potential. Now the scattering matrix elements are [31]:

(3.7) $M_{k+q,\downarrow;\,k,\uparrow} = \langle\psi_{k+q,\downarrow}|W_q^{ord.} + W_q^{spin-orbit}|\psi_{k,\uparrow}\rangle$

Because of the fact that the electronic states are not pure spin-states, even a spin-independent electron-phonon scattering potential can give rise to spin-flip scattering. The stronger the spin-orbit interaction, the larger is the spin-mixing and the larger is the spin-flip scattering probability.

Apart from electron-phonon spin-flip scattering, electron-electron spin-flip scattering can be a source of demagnetization as well [12,13,32]. One should realize that since the lattice angular momentum is not taken into account, the total angular momentum (*J*) is conserved in electron-electron spin-flip scattering processes [12]. However in these scattering processes, spin-angular momentum can be transferred to orbital momentum after which there can be demagnetization when the orbital momentum is transferred to the lattice. Very often it is assumed that the last process is instantaneous; the lattice is a perfect angular momentum 'sink' [12]. In the following subsection, we discuss the demagnetization within the microscopic 3TM.

3.2.3 Demagnetization within the microscopic three temperature model (M3TM)

The flow of angular momentum and energy in the M3TM is depicted in Fig. 3.4. In [30], the heat capacity of the spin-system was neglected thereby effectively making it a two-temperature model where there is only energy transfer between the electrons and the lattice. In this framework, the demagnetization proceeds as followings. The laser pulse interacts with the electrons after which there is energy

transfer between the hot conduction electrons and the lattice. Demagnetization can occur by means of Elliot-Yafet conduction electron-phonon scattering, see also Fig. 3.3a. In this way, angular momentum is transferred from the spins to the lattice.

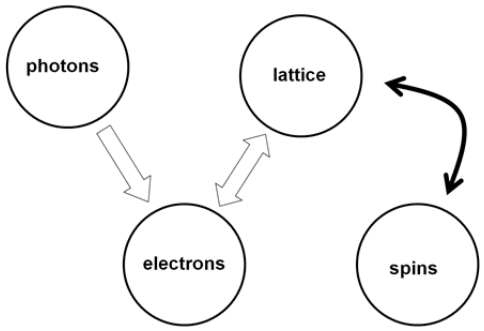

Figure 3.4 | M3TM. Energy (white arrow) and angular momentum transfer (black arrow) between light, the lattice, electrons and spins. The energy of a photon is absorbed by the electrons after which there is energy transfer to the lattice. Demagnetization occurs due to the interaction of the spins with the lattice and the electrons by means of Elliott-Yafet spin-flip scattering. The spins have zero heat capacity.

In [30] a differential equation for the magnetization is derived:

$$\frac{dm}{dt} = Rm\frac{T_l}{T_c}\left(1 - m\,coth\left(\frac{mT_c}{T_e}\right)\right) \tag{3.8}$$

$$R \sim \frac{a_{sf} g_{el} T_C^2}{\mu_{at}} \tag{3.9}$$

$$g_{el} \sim D_F^2\ \lambda_{ep}^2 \tag{3.10}$$

In Eq. (3.8), m is the reduced magnetization, R is the demagnetization rate, T_c is the Curie temperature and T_l, T_e are the lattice and electronic temperatures, respectively. In Eq. (3.9), a_{sf} is the temperature independent spin-flip probability, μ_{at} is the atomic magnetic moment and g_{el} is the electron-lattice coupling constant in the two-temperature model. In Eq. (3.10), D_F is the electronic density of states and λ_{ep} is electron-phonon coupling constant. By looking to Eq. (3.8), one can see that in this model the demagnetization rate is determined by R. In the expression for the demagnetization rate, a_{sf} and g_{el} are difficult to calculate. However T_c and μ_{at} are usually known for a certain material and can be used to make a rough estimation about the demagnetization rate.

When Eq. (3.8) is combined with the differential equations for T_e and T_l in the two temperature model, the model can be fitted to the experimental results. The heat capacity of the lattice (C_l) is taken as a constant while the electronic heat capacity is $C_e=\gamma T_e$. Now, the only fit parameters are g_{el}, C_l/γ and a_{sf}. While g_{ep} and C_p/γ determines the electron-phonon dynamics, the interaction with the spins is determined by the spin-flip probability a_{sf}. Once these parameters are obtained for a certain fluence, they can be treated as constants in the simulations for other fluences. Excellent agreement is obtained when simulations for different fluences are compared with experiments in Nickel [30].

Two very different types of magnetization dynamics can be distinguished depending on the magnitude of the R. For large R (>10 ps^{-1}), demagnetization completes before electron-phonon equilibration is achieved. After that a partial re-magnetization takes place at the electron-phonon equilibration timescale when the electronic temperature decreases. Fast demagnetization can occur due to the high electron-phonon scattering rate of hot electrons. For every scattering event there is a finite probability a_{sf} that the electron will flip its spin due to spin-orbit interaction.

The situation for small R (<0.10 ps^{-1}) is completely different. Fast demagnetization occurs during electron-phonon equilibration but since no quasi- equilibrium between the three sub-systems is achieved, the demagnetization proceeds also at longer time scales. Because of the fact that at this moment the electrons are "cold", this demagnetization component is much slower than the one during electron-phonon equilibration. The case of large R (>10 ps^{-1}) and small R (<0.1 ps^{-1}) were named Type I and Type II dynamics respectively [30]. Later on we will consider the hypothetical case in which the EuO magnetization dynamics can be modeled in terms of the M3TM. A deviation from the standard behavior within the M3TM framework can hint to the presence of novel magnetization dynamics contributions (like for instance magnetic polaron or exciton formation), see Chapter 4 and 5.

Until now we focused mainly on the ultrafast demagnetization in the ferromagnetic metal Nickel. Several demagnetization mechanisms were discussed which involve conduction electrons. The demagnetization of localized magnetic moments proceeds differently, and will be the topic of the next section.

3.3 Demagnetization of localized magnetic moments by spin-phonon scattering

This section focuses on the understanding of the spin-lattice relaxation by the localized spin-phonon scattering mechanism. Based on [33] and [34], we will show that there is a correlation between the magnetic anisotropy energy (MAE) and the spin-lattice relaxation time based on spin-phonon scattering mechanisms. By taking the magnitude of the MAE per atom, we can make an estimate for the AFCF spin-lattice relaxation time. First we start to discuss the origin of the MCA in the rare-earth and transition metals. The mechanisms behind the MCA for rare-earth and transition metals are not the same due to the fact that the ratio between the crystal field and spin-orbit interaction is different.

3.3.1 The origin behind the Magneto crystalline anisotropy (MCA)

The magnetic anisotropy is a measure of how strong the coupling is between the spin angular momentum and the lattice, which in turn is essential in spin-lattice relaxation processes. The nature of the single-ion anisotropy is well studied for transition metals and can be explained as follows [35--37]. In transition metals, there is a strong crystal field, which is much larger than the spin-orbit interaction. Because of this strong crystal field there is a non-spherical charge distribution which is fixed to the lattice. The CF strongly affects the electron orbits. The orbital momentum is quenched, at least without the presence of spin-orbit coupling [38]. With the presence of spin-orbit coupling, *L* is small but non-zero. In this case the expectation value of *L* is orientation dependent, and is maximal along the easy axis of magnetization [36]. The spin-orbit energy ($\propto L \cdot S$) is minimized when *S* is oriented along *L*, which means that at B=0, *S* is aligned with the easy axis [36]. In this way we can understand the reason behind the spin-orbit-lattice coupling, which is the origin behind the MCA as we will see. When an applied magnetic field is applied along a direction different than the easy axis *S* wants to align with the applied magnetic field due to the Zeeman term ($\propto B \cdot S$) in the Hamiltonian. However the spin-orbit energy is minimized when *S* is aligned with *L* along the easy axis [36,37]. The final result is that *S* and L are not fully aligned anymore: *S* is more aligned with the applied magnetic field while *L* is more aligned with the easy axis. Due to the strong crystal field, the anisotropic charge density remains fixed to the lattice, and will not rotate when *L* is not aligned anymore with the easy axis [35]. The line of argumentation is summarized in Fig. A in the appendix.

In [35] it was discussed that for the rare-earth ions the situation is different, since for the localized 4*f* orbitals in the rare earths, the crystal field is much smaller and the spin-orbit coupling is stronger. The MCA can now we explained as follows [35,39]. Without the presence of spin-orbit coupling and a crystal field, the charge distribution of a 4*f* ion with $L \neq 0$ is non-spherical [40]. When there is spin-orbit coupling, the spin is aligned with the orbital moment, and the non-spherical charge distribution is strongly coupled to the total angular momentum (*J*) orientation. The (weak) CF only weakly affects the electron orbits: L is not quenched and is (still) large. However, the CF couples the non-spherical charge distribution to the lattice [35]. Since the non-spherical charge distribution is coupled to L and L is coupled to *S,* we can understand the origin behind the spin-orbit-lattice coupling in this way. When a magnetic field is applied in a direction away from the easy axis J wants to align with the applied field, again due to the Zeeman term. Due the fact that the charge distribution is (strongly) coupled to J, the charge distribution will also rotate when J aligns with the applied field [35,39,40]. The changes in the electro-static energy for the different orientations of the anisotropic charge distribution are the reason behind the MCA energy in the rare-earths. The line of argumentation is summarized in Fig. B in the appendix.

The actual size of the magnetic-anisotropy energy (MAE) is in the order of 1 µeV/ion for Fe[fcc] and Ni [fcc] and can be about 65 µeV/ion for the systems with lower symmetry like (hcp) Co [41]. Because of the unquenched L in rare-earths, the MAE is much larger, typically around 1 meV/ ion [42]. In Tb metal, with *L*=3, for instance the MAE is about 1.1 meV/ion [43]. However since Gd has a *L*=0 configuration ($4f^7$ like Eu^{2+} in EuO), the MAE is much smaller, 35 µeV/ion [42]. The origin of the still relatively large MAE (for a system with L_{4f}=0) can be explained as follows [42]. In Gd metal, the 5*d* conduction electrons carry orbital angular momentum and are therefore coupled to the lattice. Because of the strong 4*f*-5*d* exchange interaction, the 4*f* moments are also coupled to the lattice resulting in a still relatively large MAE for *L*=0 system. In EuO (*L*=0), there are much less conduction electrons, making this mechanism ineffective; the MAE is therefore much smaller, 9.3 meV per atom [44]. In the next subsection we relate the MAE to the (localized spin-phonon) spin-lattice relaxation time.

Table 3.1 | MAE and the corresponding timescales. TM=transition metal, RE=rare-earth, MAE= magnetic anisotropy energy, AFCF=anisotropic fluctuations of the crystal field, calc.= calculated, exp.=experimental. Data taken from Ni [41], Fe [41], Tb [43], Gd [42], EuO [44].

Type	Material	MAE [μeV/ion]	τ=h/MAE	Exp. τ (AFCF)	τ(calc)/ τ (AFCF)
TM	Ni	0.2	21 ns	-	-
TM	Fe	1.4	3.0 ns	-	-
RE	Tb (L_{4f}=3)	1100 (K_2)	3.80 ps	8 ps	0.5
RE	Gd (L_{4f}=0)	35 (K_2)	118 ps	40 ps	3.1
RE	EuO (L_{4f}=0)	9.3 (K_1)	444 ps	-	-

3.3.2 Relating the spin-lattice relaxation time to the MCA energy

Since, as we will see, the spin-orbit-lattice interaction is important in both determining the spin-lattice relaxation time and the single-ion anisotropy (see Fig. B), several authors tried to make a connection between them [23,33]. A theoretical justification of this procedure was given in [33], where the spin-lattice relaxation in rare-earth metals was discussed. In this paper the spin-lattice relaxation time of a single localized spins was calculated by consider Raman spin-phonon scattering processes. In a so-called direct process, transitions between one Zeeman level and another Zeeman level of the spin can be made by the absorption or emission of a single phonon [33,38]. In a Raman process however, transitions between one Zeeman level and another Zeeman level of the spin proceeds via a virtual state. This (Raman) mechanism corresponds to the inelastic scattering of phonons by a localized spin, where the energy is absorbed (Stokes process) or emitted (anti-Stokes process) by the spin-system [33,38]. One can see this as an interaction between the orbital momentum (which is strongly coupled to the spin in rare-earths) and the anisotropic crystal field fluctuations produced by phonons [33]. Following [33] we shall name this localized moment spin-lattice relaxation mechanism, AFCF (Anisotropic Fluctuations of the Crystal Field). Like in the case for the MAE, the spin-lattice relaxation rate is determined by the strength of the spin-orbit-lattice coupling. Moreover it was shown that the spin-lattice relaxation time is inversely proportional to the MAE [33]. Therefore an estimation for the spin-lattice relaxation can be made by calculating τ=h/MAE [23], see the fourth column in Table 3.1. The absence of a very fast (8 ps) direct 4f spin-lattice relaxation time (AFCF) in photo-excited ferromagnetic Gd metal ($4f^7$, L=0) compared to ferromagnetic Tb

metal ($4f^8$, L=3) also supports this idea [26]. Based on this analysis, an AFCF spin-lattice relaxation time of 444 ps can be anticipated for EuO.
In the next section we discuss the demagnetization dynamics in Gd and Tb in some more detail. From this we can extract some interesting information about the dynamics in EuO, based on the fact that there are some similarities in the electronic structure between the different compounds.

3.4 Laser-induced demagnetization in metallic Gadolinium and Terbium

Gadolinium is a ferromagnetic rare-earth metal and has some similarities with EuO. The largest part of the magnetic moment in Gadolinium reside on the localized 4*f* orbitals. The 4*f* shell in Gd is half-filled. According to Hund's rules this gives a $J=S=7/2$; $L=0$ configuration (like Eu^{2+} in EuO) with a total 4*f* magnetic moment of 7.0 μ_B. The metallicity in Gd comes from the partially filled 5*d*/6*s* band. Due to the intra-atomic 4*f*-5*d* exchange interaction, the 5*d*-6*s* band is spin-split, giving a magnetic moment of 0.55 μ_B. This picture is similar to EuO with the big difference that the 5*d*-6*s* band is empty in stoichiometric EuO at T=0K.
Wietstuk *et al.* studied the demagnetization in Gd after excitation of the 5*d*/6*s* electrons by a 100 fs 800 nm laser pulse [25,26]. Demagnetization was probed by XMCD at the $M_{4,5}$ edge which probes directly the localized 4*f* magnetic moments. First a fast demagnetization of 25% was observed at the sub-picosecond time-scale (750 fs). A further decrease of the magnetization occurs with a time-constant of 40 ps towards a demagnetization of about 50% after 200ps. The results can be explained in terms of the microscopic-3TM with small R (Type II dynamics). Here the Elliot-Yafet spin-flip scattering of mobile 5*d*/6*s* electrons provides a channel for demagnetization. Because of the strong exchange coupling between the 4*f* and 5*d*/6*s* moments, also demagnetization occurs in the 4*f* system. From fits to the data, values for g_{el} and a_{sf} were determined from which *R* could be calculated using Eq. (3.9). For μ_{at} a value of 0.55+7.0 μ_B was used. The *R* value is about 187 times smaller than in Nickel and shows that Gd has type II dynamics.
Above we discussed that the M3TM is able to account for the two demagnetization times of ~1 ps and ~40 ps. Based on this one can argue that the Elliot-Yafet scattering can account for the observed demagnetization in Gd. Actually, the longer time constant of 40 ps corresponds to the AFCF spin-lattice relaxation time which has been calculated in [33]. This paper discusses how anisotropic fluctuations of

the crystal field can demagnetize the 4*f* magnetic moment, see the previous section. Therefore it is still not completely clear which of the two is the dominant mechanism for demagnetization at the longer timescales.

Also the dynamics in Tb has been studied experimentally [26]. The amount of 5d/6s conduction electrons is the same for Tb and Gd. However Tb^{3+} has a large orbital momentum (L=3), unlike Gd which has L=0. Tb also shows a two-step behavior. There is a ultrafast 750 fs component, like in Gd. However the slow component is faster in Tb: 8 ps. In [26] this was explained in terms of an AFCF like component due to the fact that the AFCF mechanism (see estimates in Table 3.1) is more effective in Tb due to the large orbital momentum. It might be too easy to make this conclusion since in the end, the electronic structure in both materials is different, which makes a direct comparison challenging. However the 8 ps is similar to the spin-relaxation times we estimate based on $\tau_{AFCF}=h/E_{MCE}$. Another strong indication that the AFCF spin-relaxation for Tb^{3+} ions is fast (~10 ps) comes from measurements on un-doped and 5% Tb-doped EuS: the spin-lattice relaxation time decreases from 120 ps (un-doped) to 12 ps when EuS is doped with Tb (5%) [45], see also the next Chapter. Again this can be explained by an increase of the orbital momentum and the spin-orbit energy when the material is doped with Tb^{3+}[45].

In order to make a clear comparison between demagnetization in Gd and Ni, the flow of angular momentum is shown in Fig. 3.5. In the left panel, the flow of angular momentum in Ni is shown. Neglecting the photons, there are two systems which can carry angular momentum, the lattice and the electrons. In this picture, demagnetization can occur through Elliot-Yafet scattering by conduction electrons (fast in Nickel ~100fs) but also through the interaction of the localized spins with *anisotropic* fluctuations of the crystal field (estimated for Nickel ~21ns, see Table 3.1).

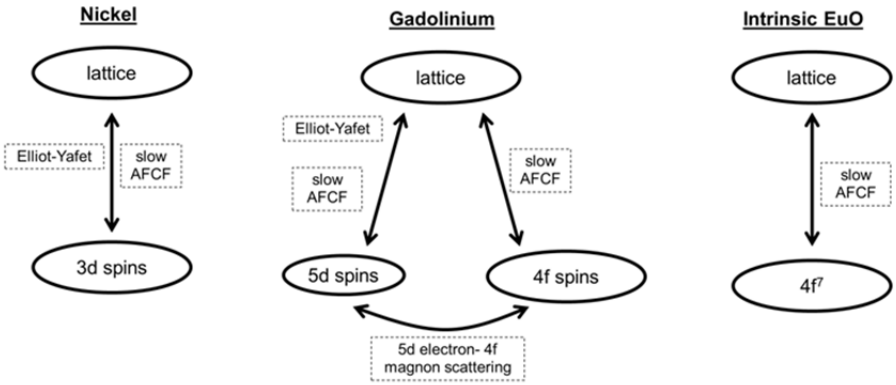

Figure 3.5 | The flow of angular momentum in Nickel, Gadolinium and intrinsic stoichiometric EuO. Different systems which can carry angular momentum are depicted. For Nickel there are the 3*d* spins and the 3d lattice. In Gadolinium there are the 5*d* spins, 4*f* spins and the lattice. In intrinsic stoichiometric EuO there are the 4*f* spins and the lattice. The boxes indicate the different coupling mechanism.

The middle panel of Fig. 3.5 shows the angular momentum flow in Gd. There are three systems which can carry angular momentum: the lattice, the 5*d* electrons and the 4*f* electrons. The 5*d*-4*f* coupling is considered to be so strong, that on the sub-picosecond timescale, the 4*f* and 5*d* system are fully equilibrated. Equilibration occurs due to 5d electron-4f magnon scattering. An example of a 5d electron-4f magnon scattering event is depicted in Fig. 3.6. In the next section we will focus on the magnetization dynamics in EuO en we will ask our self the question: based on the literature, what would be the normal behavior for a ferromagnetic semiconductor. By knowing this, later on it will be easier to recognize novel magnetization dynamics mechanisms.

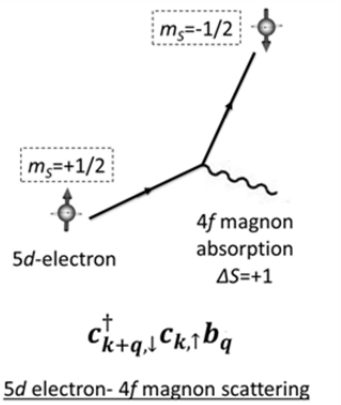

Figure 3.6 | 5d electron-4f magnon scattering event. b_q is the (4f) magnon annihilation operator whereas $c^{\dagger}$ and c are the 5d electron creation and annihilation operators respectively.

3.5 Laser-induced demagnetization in EuO: what can we expect?

3.5.1 EuO in the M3TM framework

In intrinsic stoichiometric EuO, in the ground state at T=0 K, there are no conduction electrons. The angular momentum flow between a hot lattice and the 4f moments is depicted in the right panel of Fig. 3.5. Since there are no 5d conduction electrons, the Elliot-Yafet channel is inactive and the only demagnetization channel is expected to be AFCF. We estimated the AFCF spin-relaxation time to be 450 ps, see Table 3.1.

The situation changes after photo-excitation. After a 4*f* valance band to 5*d* conduction band excitation, the conduction band gets populated. For now we assume that the carriers are long lived and we will neglect the influence of the 4*f* holes. The importance of the 4*f* holes is discussed later on. Within M3TM framework, demagnetization can occur due to Elliot-Yafet scattering of 5*d* conduction electrons like in the case of Gd metal. However, the number of conduction electrons (which is dependent on the laser fluence) in EuO is much smaller than in Gd which will affect the Elliot-Yafet demagnetization rate. A change in conduction electron concentration (n) affects D_F in Eq.(3.10) since D_F is proportional to $n^{1/3}$ in the Sommerfield model of free electrons [38]. From Eq. (3.8)-(3.10) it can be seen that the demagnetization rate R is proportional to $n^{2/3}$. Therefore a smaller n leads to reduced demagnetization rate. Since for free electrons γ is proportional to $n^{1/3}$, also the heat capacity of the electronic system

($C_e=\gamma T_e$) is different. When the electronic specific heat is much smaller than C_{latt}, electrons will cool more rapidly and after photo-excitation, most of the energy flows from the electronic system to the lattice.

We can try to make a very rough estimate of the demagnetization rate in EuO based on the results on Gd and Eq. (3.8)-(3.10) of the M3TM. We will assume that a_{sf} and λ_{ep} are the same for Gd and EuO. For Gd, T_c = 297 K and μ_{at} = 7.6 μ_B whereas for EuO T_c = 69 K and μ_{at} = 6.9 μ_B. In Gd there are three conduction electrons per Gd atom. Now the demagnetization rate (R) of EuO versus doping concentration (n_{EuO}) can be estimated using:

$$R_{EuO}/R_{Gd} \approx \left(\frac{T_{C,EuO}^2 {n_{EuO}}^{2/3}}{\mu_{at,EuO}}\right) / \left(\frac{T_{C,Gd}^2 {n_{Gd}}^{2/3}}{\mu_{at,Gd}}\right) \quad (3.11)$$

R_{EuO}/R_{Gd} for different photo-doping (PD) concentrations is shown in Fig. 3.7. Using Eq. (3.11) it was estimated that the demagnetization rate R is about 160 times smaller than in Gd for n=10%. This indicates that the spin-lattice relaxation (AFCF) rate can become important at the longer time scales and might be the dominant mechanism for demagnetization. We can see that even for high fluences the magnetization dynamics, within our model and approximations, is expected to be much slower than in Gd and will have a Type II dynamics. Also the case is considered when the 4*f* and 5*d* systems are decoupled and only demagnetization occurs in the 5*d* system. In this case a value of $\mu_{at,5d}$ = 1 μ_B is used in Eq. (3.11). For a decoupled 4*f*-5*d* system, the 5*d* electrons demagnetize faster than for a strongly coupled 4*f*-5*d* system due to the fact that the total magnetic moment is smaller.

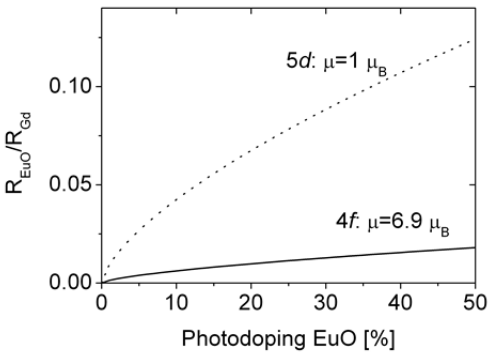

Figure 3.7 | Calculated Elliott-Yafet demagnetization rate R_{EuO}/R_{Gd} in the M3TM. Using Eq. (3.11), the Elliott-Yafet demagnetization rate of EuO is estimated for different atomic magnetic moments.

The applicability of the M3TM model to the EuO case is discussed in the next chapter but there are already some issues which can be addressed right now:

1) When the EY spin-lattice relaxation in the M3TM is slow, it can be comparable with the AFCF spin-lattice relaxation, as was discussed in [23]. The AFCF spin-lattice relaxation is not taken into account in the M3TM model. While the AFCF spin-lattice relaxation for Eu^{2+} ($4f^7$) was estimated to be 450 ps, the AFCF spin-lattice relaxation for 4*f* holes ($4f^6$) with L=3, can be much faster, as was discussed for the Tb case.
2) We do not take into account the different carrier relaxation processes which can occur in semiconductors like for instance trapping, recombination, (magnetic) exciton formation, (magnetic) polaron formation etc. The presence of a large variety of relaxation processes makes the interpretation of the demagnetization data in semiconductors more complex than for metals.
3) The fact that EuO has a fully spin-polarized conduction band at T = 0 K drastically changes the Elliot-Yafet demagnetization rate (R), as was also discussed in [23]. A relation was proposed between the demagnetization rate in half-metals and the spin-polarization P at the Fermi-level. In a perfect half metal the spin polarization at the Fermi level is 100%. Therefore spin-up electrons around the Fermi level cannot scatter adiabatically to spin-down states around the Fermi level since there are no such available spin-down states. This is depicted in Fig. 3.8a where the spin dependent density of states of a half-metal is shown. Whereas it possible for higher energy electrons to spin-flip scatter (process (1) in Fig. 3.8a), the spin-flip scattering channel for electrons around the Fermi level is blocked (process (2) in Fig. 3.8a) resulting in a decrease of the demagnetization rate due to Elliot-Yafet spin-flip scattering. As we will reason later, the degree of spin polarization can also affect the (5d) electron-(4*f)* magnon scattering rate (see also Fig. 3.8c).

In the next section we briefly discuss the magnetization dynamics in a very well-studied class of ferromagnetic semiconductors, the diluted III/V ferromagnetic semiconductors (DMS). Again, this serves as a theoretical framework.

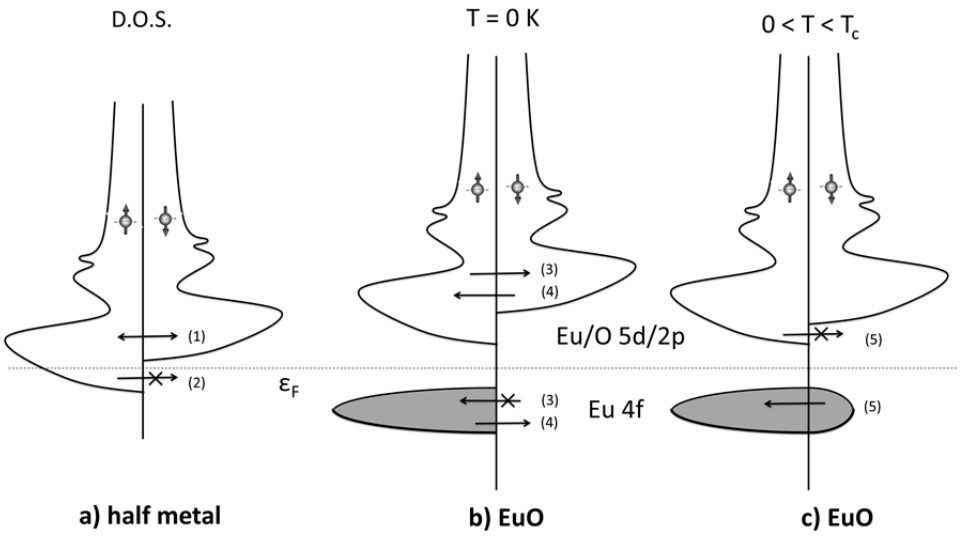

Figure 3.8 | Schematic representation of different spin-flip scattering processes showing the spin dependent density of states (D.O.S.) for a half metal in a), EuO at 0K in b) and EuO at higher temperatures in c). Elliott-Yafet scattering is depicted in a) for different positions in the conduction band. b,c) shows electron-magnon scattering processes. The lower band represents the europium 4*f* valence band while the higher lying band is the europium 5*d* conduction band. Whereas the arrows in the 5*d* band represents 5*d* electronic scattering events, the arrows in the 4*f* band represents magnon creation (arrow pointing to the left) or annihilation (arrow pointing to the right).

3.5.2 Demagnetization in ferromagnetic semiconductors: the well-studied III/V DMS

The localized magnetic moment-conduction electron interaction in a magnetic semiconductor is discussed in [27,28] where the ultrafast laser-induced magnetization dynamics in Mn-doped GaAs was studied. The fast sub-picosecond demagnetization of the localized Mn moments is explained by the efficient hole spin demagnetization (~10fs), followed by hole-Mn spin scattering events. In this way angular momentum is transferred from the localized Mn moments, via the holes, to the lattice. The interaction between the charge carrier spins (*s*) and localized magnetic moments (*S*) can be described by the following Hamiltonian [27,28]:

(3.12) $H_{s-S} \sim J(p)\,\vec{S}\cdot\vec{s} = J(p)\,\{S_z s_z + (S^+ s^- + S^- s^+)\}$

In which $S^{\pm}$,$s^{\pm}$ are the standard raising and lowering operators, *J* is the exchange interaction constant and *p* is the hole concentration. The fast demagnetization of

the Mn moments (~2 ps) is explained by the ($S^+s^- + S^-s^+$) terms. When a spin-down electron scatters to a spin-up state (s^+), a magnon is created (S^-). In this process there is a flow of angular momentum from the Mn to the holes. A simplified energy level diagram, with spin-up and spin-down levels of the localized moments, is shown in Fig. 3.9.

Below T_c, the levels are exchange split by ΔE; there exists an imbalance between the spin-up and spin-down pollutions according to the Boltzmann statistics. AFCF spin-lattice relaxation of the Mn^{2+} moments and the ($S^+s^- + S^-s^+$) term in Eq. (3.12) can cause a decrease of the imbalance. The decrease of the imbalance also leads to a decrease of ΔE (from ΔE to ΔE') due the reduction of the mean (exchange) field. The demagnetization pathway is depicted in Figure 3.9, see arrow 1.

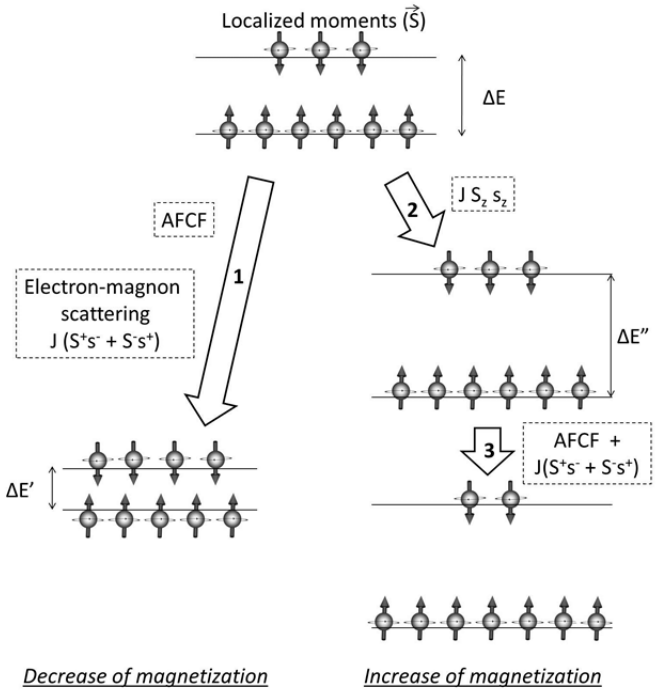

Figure 3.9 | Decrease of magnetization (arrow 1) and increase of magnetization (arrow 2,3) pathways of the localized magnetic moments (S) which are interacting with the spins (s) of the (delocalized) holes. The balls represent the population of the spin-up and spin-down states, which are separated by ΔE.

Let us now discuss the importance of the $J(p)S_zs_z$ in (3.12), as was done in [27]. This term was used to explain the photo-induced slow (~200 ps) increase of the magnetization in Mn-doped GaAs due to a low density of photo-excited holes. In

Fig. 3.9, the increase-of-magnetization-pathway is depicted by arrows 2 and 3. The $J(p)S_zs_z$ term can give an increase of the level splitting ΔE (ΔE$\propto J(p)$) after photo-excitation due to the hole concentration (p) dependent exchange constant $J(p)$; the number of holes increases during photo-excitation. This does not directly lead to an increase of magnetization since the spin imbalance has not changed. However, a subsequent change in the spin imbalance can be caused by AFCF and by the $(S^+s^- + S^-s^+)$ term in Eq. (3.12), thereby leading to an increase of the magnetization. From the results on Mn-doped GaAs, it can be seen that photo-excited carriers can give both an increase and decrease of the magnetization of the localized moments depending on the fluence and pump-probe delay. This is an interesting observation since in EuO the exchange constant is also strongly dependent on the number of conduction electrons, and we will photo-dope the system as well. Very important in the demagnetization or re-magnetization is the localized moment-conduction electron interaction.

3.5.3 Localized moment (4f)-conduction electron (5d) interaction in EuO: different considerations

In this subsection we discuss the electron-magnon scattering rate in EuO, which needs to be high in order to get *ultrafast* magnetization dynamics due to the laser excitation of hot 5*d* conduction electrons. Different electron-magnon scattering processes can be considered which are depicted in Figure 3.8b and c. Whereas the arrows in the 5*d* band represents 5*d* electronic scattering events, the arrows in the 4*f* band represents magnon emission or absorption. When a 5*d* spin-up electron scatters to a spin-down state [see upper arrow (3) in Fig. 3.8b], a low energy magnon is absorbed [lower arrow (3)]. Since there are no magnons at *T*=0 K, this process cannot happen at 0 K. In the reverse process, a 5*d* spin-down electrons scatters to a spin-up state [upper arrow (4)] and a low energy magnon is created [lower arrow (4)]. By this process, the demagnetization of the localized 4*f* moments leads to an increase of the 5*d* electron magnetization. Subsequent demagnetization of the 5*d* electrons can lead to an overall (4*f*+5*d*) demagnetization.

Electron-magnon scattering of (cold) 5*d* electrons at the bottom of the conduction band in magnetically ordered EuO is shown in Fig. 3.8c. A 5*d* spin-up electron scatters to a spin-down state [upper arrow (5)] and a low energy 4*f* magnon is absorbed [lower arrow (5)]. Similar as for the Elliot-Yafet process, there are no available 5*d* spin-down states with the same energy to which a spin-up 5*d* electrons can scatter. Scattering is only possible with magnons which have a higher energy

than the spin-splitting in the conduction band (600 meV [46]). There are no such high energy magnons in EuO; the magnon energy at the X-point of the Brillioun is less than 10 meV [44]. This means that in the picture where we consider 5*d* conduction electrons at the bottom of the spin-split conduction band, the electron-magnon scattering rate for spin-up electrons is very small. The electron-magnon scattering rate for spin-down electrons is much larger, see also [47] where the conduction electron lifetime due to electron-magnon scattering in EuO is calculated.

Concluding, it is expected that the high degree of spin-polarization at the bottom of the conduction band can (apart from suppressing Elliot-Yafet scattering of the 5*d* conduction electrons) also affect the electron-magnon scattering rate. The discussion of this topic is continued in the next chapters.

3.6 Summary

In this Chapter, based on the available literature, we gave an introduction into the laser-induced demagnetization dynamics due to hot conduction electrons is ferromagnets. We discussed different demagnetization dynamics mechanisms which either involve conduction electrons (Elliott-Yafet type) or localized magnetic moments (AFCF type). We also discussed the coupling between conduction electrons and localized moments which is necessary to explain the magnetization dynamics both in rare-earth metals and in ferromagnetic semiconductors. In next chapter we present experimental data on EuO, in which the magnetization is probed by a soft X-ray pulse with an energy corresponding to the M_5 absorption edge of Eu^{2+}.

Appendix A: Magneto-crystalline anisotropy in transition metals

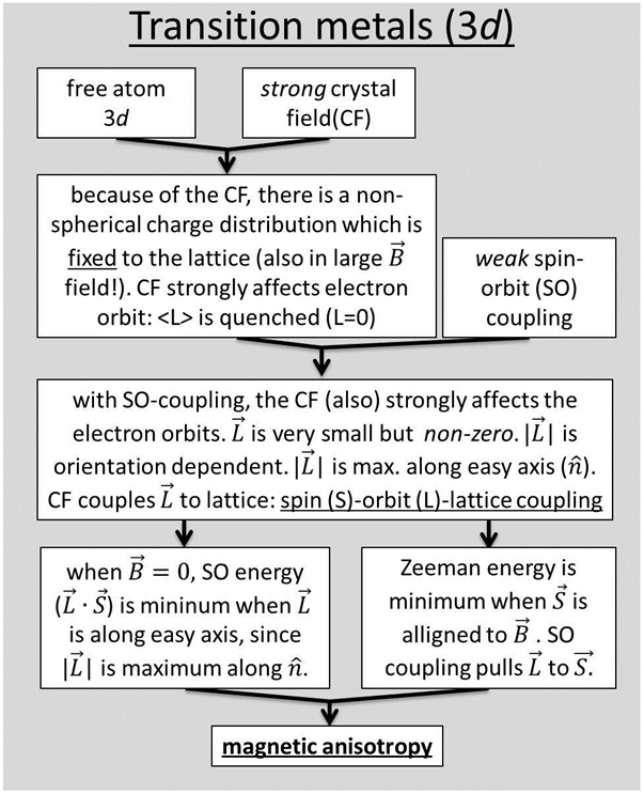

Figure A | Origin of the magneto-crystalline anisotropy in transition metals.

Appendix B: Magneto-crystalline anisotropy in rare earths

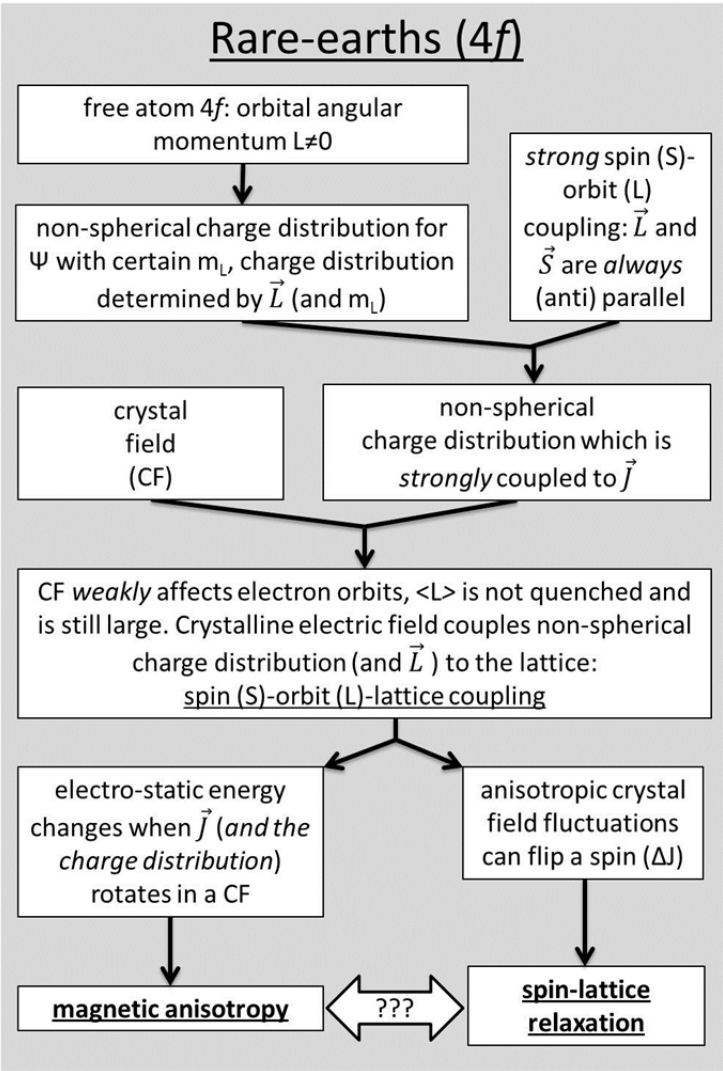

Figure B | Origin of the magneto-crystalline anisotropy and spin-lattice relaxation in rare-earths (4*f*).

References

[1] A. Vaterlaus, T. Beutler, and F. Meier, Phys. Rev. Lett. **67**, 3314 (1991).
[2] E. Beaurepaire, J. C. Merle, A. Daunois, and J. Y. Bigot, Phys. Rev. Lett. **76**, 4250 (1996).
[3] B. Koopmans, M. van Kampen, J. T. Kohlhepp, and W. J. M. de Jonge, Phys. Rev. Lett. **85**, 844 (2000).
[4] C. Stamm, T. Kachel, N. Pontius*, et al*, Nature Materials **6**, 740 (2007).
[5] G. P. Zhang and W. Hubner, Phys. Rev. Lett. **85**, 3025 (2000).
[6] F. Dalla Longa, J. T. Kohlhepp, W. J. M. de Jonge, and B. Koopmans, Physical Review B **75**, 224431 (2007).
[7] G. P. Zhang, Phys. Rev. Lett. **101**, 187203 (2008).
[8] M. S. Si and G. P. Zhang, Journal of Physics-Condensed Matter **22**, 076005 (2010).
[9] J. Bigot, M. Vomir, and E. Beaurepaire, Nature Physics **5**, 515 (2009).
[10] B. Koopmans, J. J. M. Ruigrok, F. D. Longa, and W. J. M. de Jonge, Phys. Rev. Lett. **95**, 267207 (2005).
[11] B. Koopmans, H. H. J. E. Kicken, M. van Kampen, and W. J. M. de Jonge, J Magn Magn Mater **286**, 271 (2005).
[12] M. Faehnle and C. Illg, Journal of Physics-Condensed Matter **23**, 493201 (2011).
[13] B. Y. Mueller, T. Roth, M. Cinchetti, M. Aeschlimann, and B. Rethfeld, New Journal of Physics **13**, 123010 (2011).
[14] E. Carpene, E. Mancini, C. Dallera, M. Brenna, E. Puppin, and S. De Silvestri, Physical Review B **78**, 174422 (2008).
[15] C. Stamm, N. Pontius, T. Kachel, M. Wietstruk, and H. A. Duerr, Physical Review B **81**, 104425 (2010).
[16] M. Battiato, K. Carva, and P. M. Oppeneer, Physical Review B **86**, 024404 (2012).
[17] M. Battiato, K. Carva, and P. M. Oppeneer, Phys. Rev. Lett. **105**, 027203 (2010).
[18] A. Melnikov, I. Razdolski, T. O. Wehling, E. T. Papaioannou, V. Roddatis, P. Fumagalli, O. Aktsipetrov, A. I. Lichtenstein, and U. Bovensiepen, Phys. Rev. Lett. **107**, 076601 (2011).
[19] D. Rudolf, C. La-O-Vorakiat, M. Battiato*, et al*, Nature Communications **3**, 1037 (2012).
[20] E. Turgut, C. La-o-Vorakiat, J. M. Shaw*, et al*, Phys. Rev. Lett. **110**, 197201 (2013).
[21] B. Vodungbo, J. Gautier, G. Lambert*, et al*, Nature Communications **3**, 999 (2012).
[22] B. Pfau, S. Schaffert, L. Mueller*, et al*, Nature Communications **3**, 1100 (2012).
[23] G. M. Mueller, J. Walowski, M. Djordjevic*, et al*, Nature Materials **8**, 56 (2009).
[24] C. Boeglin, E. Beaurepaire, V. Halte, V. Lopez-Flores, C. Stamm, N. Pontius, H. A. Duerr, and J. -. Bigot, Nature **465**, 458 (2010).
[25] M. Wietstruk, T. Kachel, N. Pontius, C. Stamm, H. A. Duerr, W. Eberhardt, A. Melnikov, U. Bovensiepen, C. Gahl, and M. Weinelt, in *International Conference on Ultrfast Surface Dynamics 6, Kloster Banz, Germany, 20-25 July*, 2008).

[26] M. Wietstruk, A. Melnikov, C. Stamm, T. Kachel, N. Pontius, M. Sultan, C. Gahl, M. Weinelt, H. A. Duerr, and U. Bovensiepen, Phys. Rev. Lett. **106**, 127401 (2011).
[27] J. Wang, I. Cotoros, K. M. Dani, X. Liu, J. K. Furdyna, and D. S. Chemla, Phys. Rev. Lett. **98**, 217401 (2007).
[28] J. Wang, L. Cywinski, C. Sun, J. Kono, H. Munekata, and L. J. Sham, Physical Review B **77**, 235308 (2008).
[29] J. Wang, C. Sun, J. Kono, A. Oiwa, H. Munekata, L. Cywinski, and L. J. Sham, Phys. Rev. Lett. **95**, 167401 (2005).
[30] B. Koopmans, G. Malinowski, F. Dalla Longa, D. Steiauf, M. Faehnle, T. Roth, M. Cinchetti, and M. Aeschlimann, Nature Materials **9**, 259 (2010).
[31] D. Steiauf and M. Faehnle, Physical Review B **79**, 140401 (2009).
[32] K. Carva, M. Battiato, D. Legut, and P. M. Oppeneer, Physical Review B **87**, 184425 (2013).
[33] W. Hubner and K. H. Bennemann, Physical Review B **53**, 3422 (1996).
[34] G. M. Mueller, J. Walowski, M. Djordjevic*, et al*, Nature Materials **8**, 56 (2009).
[35] G. van der Laan, E. Arenholz, A. Schmehl, and D. G. Schlom, Phys. Rev. Lett. **100**, 067403 (2008).
[36] H. A. Durr, G. Y. Guo, G. vanderLaan, J. Lee, G. Lauhoff, and J. A. C. Bland, Science **277**, 213 (1997).
[37] H. A. Durr and G. vanderLaan, Physical Review B **54**, R760 (1996).
[38] C. Kittel, *Introduction to Solid State Physics* (Wiley, 1996).
[39] M. Rotter, *Magnetic Properties of Gadolinium Compounds* (Technische Universität Dresden, 2003).
[40] U. Walter, Zeitschrift Fur Physik B-Condensed Matter **62**, 299 (1986).
[41] S. J. Blundell, *Magnetism in Condensed Matter* (oxford university press, 2011).
[42] M. Colarieti-Tosti, S. I. Simak, R. Ahuja, L. Nordstrom, O. Eriksson, D. Aberg, S. Edvardsson, and M. S. S. Brooks, Phys. Rev. Lett. **91**, 157201 (2003).
[43] J. J. Rhyne and A. E. Clark, J. Appl. Phys. **38**, 1379 (1967).
[44] L. Passell, O. W. Dietrich, and J. Alsnielsen, Physical Review B **14**, 4897 (1976).
[45] M. R. Freeman, J. Appl. Phys. **75**, 6194 (1994).
[46] P. Steeneken, *PhD thesis: New light on EuO thin films* (Rijksuniversiteit Groningen, 2002).
[47] R. B. Woolsey and R. M. White, Physical Review B **1**, 4474 (1970).

Chapter 4

Laser-induced Demagnetization Dynamics in EuO probed by XMCD

4.1 Introduction

In this chapter we present the results of XMCD experiments on a class of materials which are called intrinsic ferromagnetic semiconductors. We studied the well-known ferromagnetic semiconductor EuO (and Gd-doped EuO, $Eu_{1-x}Gd_xO$). In our experiments a 100 fs pump pulse excites electrons from the europium 4*f* valence band to the hybridized europium-5*d*/oxygen-2*p* conduction band after which the magnetization dynamics in $Eu_{1-x}Gd_xO$ is probed by a circularly polarized soft-X-ray pulse with a duration of 50 ps (FWHM). The experiments have been carried out at Beamlines UE56/1-PGM and UE56/1-ZPM of the synchrotron facility BESSY II. Due to the limited time resolution in our XMCD measurements, the magnetization dynamics at the ultrafast (100 fs) time scale could not be resolved. The *ultrafast* magnetization dynamics will be discussed in the next chapter which presents a MOKE study of $Eu_{1-x}Gd_xO$. We start with introducing X-ray Magnetic Circular Dichroism (XMCD) spectroscopy.

4.1.1 X-ray Magnetic Circular Dichroism

We focus first on the properties of EuO in the soft X-ray regime. In our experiments we used soft X-rays with a photon energy between 1115 and 1235 eV, which covers the M_5 and M_4 edges in both Eu and Gd [1,2]. These edges correspond to dipole allowed transitions between europium 3*d* core levels and europium 4f levels. In order to describe the absorption peaks in the spectrum it is important to know what the ground state of Eu^{2+} is and which the accessible excited states are. In an

atomic picture, the initial state is in a $3d^{10}4f^{7}5d^{0}$ configuration. By applying Hund's rules this gives a (J=S=7/2, L=0) ground state while higher lying states are far apart and do not need to be considered. See Chapter 2 for more information on this.

The selection rules for electric-dipole allowed transitions in the weak spin-orbit coupling limit are ΔJ=0,±1, ΔS=0, ΔL=0,±1 (not from L=0 to L=0). Therefore it is clear that there are optically allowed transitions to final states with total angular momentum J_{3d+4f}=5/2, 7/2, 9/2 (S=7/2, L=1) [3].

Considering the selection rules, we find that dipole transitions from the ground state to $3d^{9}4f^{8}5d^{0}$final states are allowed [4]. The 3d hole in the final state carries a spin S_{3d}=1/2and orbital angular momentum L_{3d}=2, which can couple to a spin-orbit angular momentum of J_{3d}=3/2 or 5/2. In the final state there is a hole in the 3d shell. This 3d hole has a (S_{3d}=1/2, L_{3d}=2) configuration with possible total angular momentum J_{3d}=3/2 or 5/2. By applying the third rule of Hund one can see that the J_{3d}=5/2 configuration is lower in energy than the J_{3d}=3/2 configuration. The peaks observed in X-ray absorption spectroscopy (XAS) on europium can be grouped by the total angular momentum J of the final state 3d hole [1,2], see Fig. 4.1. Two groups of absorption peaks (edges) are depicted which are named M_5 and M_4 corresponding to the J_{3d}=5/2 and J_{3d}=3/2 3d-hole final states respectively. They are about 30 eV apart in EuO. Both the M_5 and M_4 peaks consist of groups of dipole allowed transitions corresponding to the respective final state multiplets [1].

In a magnetic field the initial and final states are split according to quantum number m_J. The initial state is split in 8 states and the final states in 6, 7, and 8 states for J_{3d+4f} = 5/2, 7/2, and 9/2 respectively. Depending on the polarization, the section rules for m_J (m_L) are 0,+1,-1 for linearly polarized, right circularly polarized (RCP) and left circularly polarized (LCP) light, respectively, while spin flips are not possible, Δm_S=0, for all polarizations [1,2]. Transitions from the ground state to the J_{3d+4f} =7/2 final state at the M_5 peak in a magnetic field are shown in in Fig. 4.2. In the following we explain why there is magnetic dichroism in europium, using the J_{3d+4f} =7/2 final state as an example. The same can be done for the other J final states resulting in a complicated absorption spectrum with many different absorption lines [1,2].

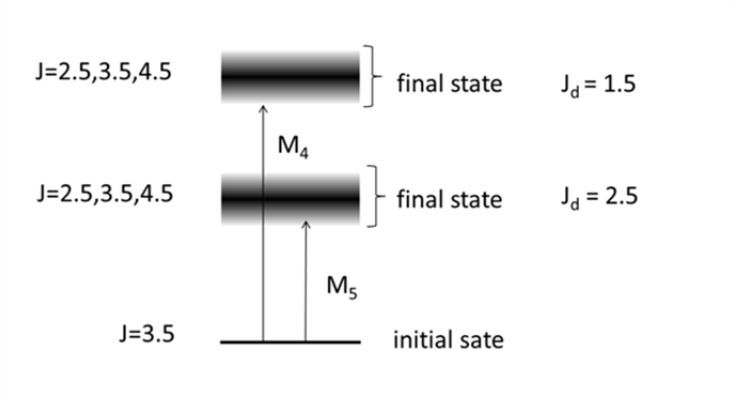

Figure 4.1 | Energy diagram for the optically allowed $3d^{10}4f^{7}5d^{0}$ -> $3d^{9}4f^{8}5d^{0}$ transitions in Eu^{2+}. The transitions can be grouped according to the final state 3*d*-hole configuration (J_d=3/2 or 5/2).

In Fig. 4.2, there are for each circular polarization seven dipole allowed transitions. Each of these transitions can have different oscillator strengths.

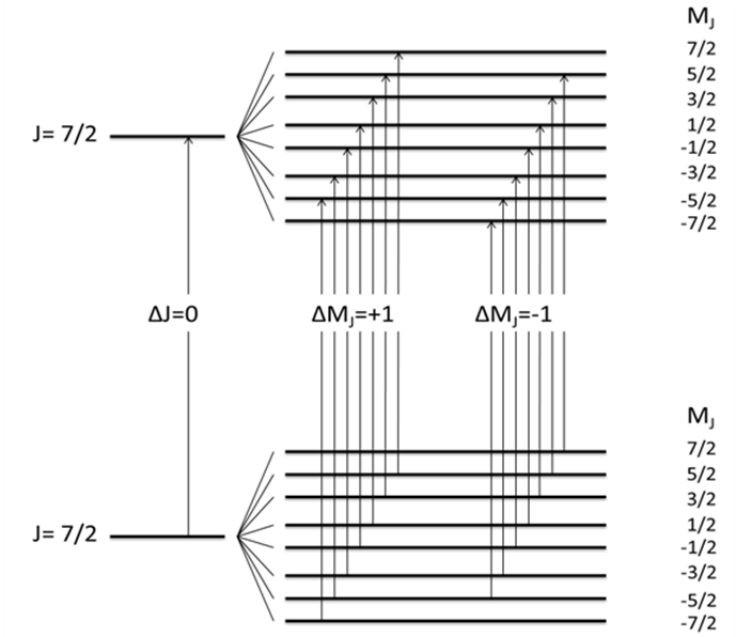

Figure 4.2 | Energy diagram for the $3d^{10}4f^{7}5d^{0}$ -> $3d^{9}4f^{8}5d^{0}$ transitions in Eu^{2+}. Only dipole allowed transitions with either right or left polarized light towards the *J*=7/2 final state are depicted.

In a small magnetic field at room temperature, all the different (ground state) levels are equally occupied and there is no circular dichroism. The situation at 0 K is completely different. At 0 K only the lowest level is occupied which has quantum number M_J=-7/2. From this initial state only dipole allowed transitions with right circularly polarized light are possible. There is large dichroism since there are only RCP transitions. At finite temperature the magnitude of the dichroism is determined by the occupancy of the different M_J levels in the initial sate which is governed by Boltzmann statistics [1]. The energy level splitting is proportional to the applied magnetic field ($g\ \mu_B\ H$). In this way the dichroism is described as an initial state effect. However the magnetic splitting in the final state also determines the exact position of the absorption lines, see Fig. 4.2.

So far a free Eu^{2+} ion a magnetic field was considered. The situation changes for europium atoms in EuO in the ferromagnetic state. In the ferromagnetic state a macroscopic magnetization can exist even without applied magnetic field because of the exchange interaction between the different europium ions. In the mean-field approach this interaction can be modeled as an effective magnetic field. It is this effective field which determines the level splitting of the europium ions in EuO and therefore the dichroism. The effective magnetic field in EuO is ~34 T[5].

After considering all the possible transitions at the M_5 and M_4 edges, the magnitude of the expectation values of the europium 4*f* spin and orbital angular momentum along the *k*-vector of the light can be determined using sum-rules, see Eq. (4.1-4.6) [5]:

(4.1) $\mu(E) = \frac{\mu^+(E)+\mu^-(E)}{2}$ - XAS intensity with + (RCP) or – (LCP) photons

(4.2) $\Delta\mu(E) = \mu^+(E) - \mu^-(E)$ - XMCD intensity

(4.3) $A_5 = \int_{M_5} \mu(E)dE$ - integrated XAS intensity

(4.4) $\Delta A_5 = \int_{M_5} \Delta\mu(E)dE$ - integrated XMCD intensity

(4.5) $L_{4f} = -\frac{(\Delta A_5+\Delta A_4)}{A_5+A_4}\ N_{4f}$ - orbital angular momentum

(4.6) $S_{4f} + \frac{7}{2}T_{4f} = -\frac{(2\Delta A_5-3\Delta A_4)}{2(A_5+A_4)}\ N_{4f}$ - spin angular momentum

In which A_4 and A_5 are the integrated intensities in the X-ray absorption spectrum (μ) at the M_4 and M_5 absorption edge and in which ΔA_4 and ΔA_5 are the integrated

intensities in the XMCD spectrum ($\Delta\mu$) at the M_4 and M_5 absorption edges. N_{4f} is the number of *4f* holes, N_{4f} = 7 in our case. Also the magnetic dipole operator *T* appears in the sum rules. The expectation value of the magnetic dipole moment in EuO is zero because of the cubic symmetry [5]. The possibility of determining *L* and *S* separately from X-ray absorption measurements with different photon helicities makes XMCD spectroscopy a unique tool. Since only the angular momentum component along the *k*-vector of the light is measured, one is also sensitive to the orientation of the magnetization. Another advantage of XMCD spectroscopy is that the magnetic moments of different elements in the same sample can be measured separately as long as the absorption edges do not coincide.
Parts of the measurements that are presented are done at the peak of the M_5 absorption edge. At this edge a combination of L_{4f} and S_{4f} is probed. From Eq. (4.1-4.6) it follows that [5]:

(4.7) $$\Delta A_5 = -\frac{(A_5+A_4)}{N_{4f}}\ (3L_{4f} + 2S_{4f})$$

(4.8) $$\Delta A_4 = \frac{2}{5}\frac{(A_5+A_4)}{N_{4f}}\ (-L_{4f} + S_{4f})$$

Next section focuses on what will happen to the XMCD in EuO after a strong optical excitation.

4.1.2 Time-resolved XMCD

While Chapter 2 has been devoted to the problems in the interpretation of magneto-optical signals, this section focuses on the question why XMCD can be used as a nice tool for probing fast magnetization dynamics. First a comparison of magneto-optics (dichroism) in different parts of the spectrum is made. In EuO there are electric-dipole allowed transitions between the valence band and the conduction band with energies in the visible or near-infrared range. When a macroscopic magnetization appears in the ferromagnetic state, the band structure changes with respect to the paramagnetic state resulting in an unequal absorption and refractive index for left and right circularly polarized light, which is the basis for different magneto-optical effects like the Kerr and the Faraday effect. Both mentioned magneto-optical effects are linearly proportional to magnetization, although the magnetization-induced conduction band splitting complicates the picture, see Chapter 2.

After a strong optical excitation, pump-induced changes in the band structure and populations modify the magneto-optical properties of a material. Although the Kerr and Faraday effects are proportional to the magnetization, this is not automatically true for the pump-induced change in the magneto-optical response. Moreover, one can distinguish the magnetic from non-magnetic contributions to the pump-induced changes of the magneto-optical response.

Several non-magnetic contributions to the magneto-optical signal have been discussed in Chapter 2. Due to the presence of a high density of photo-excited electrons, 5*d* final state filling effects and band gap renormalization can become important which can also affect the magneto-optical properties [6], see also Chapter 5. Because of the difficulties in disentangling the magnetic from the non-magnetic contributions in the magneto-optical signal, a straight forward interpretation of the magneto-optical response becomes problematic. In the soft X-ray region, a simpler atomic picture can be used. The details of the band structure do not have to be considered and Eqs. (4.7-4.8) remain valid even after an optical excitation. This is why XMCD is a useful probe for (ultra) fast magnetization dynamics.

Let us consider how the XMCD signal will change due to an optical excitation (Eu-$4f^7 5d^0$ → Eu-$4f^6 5d^1$) by using a pump beam with a wavelength of 780 nm. The photo-excited atoms have a $3d^{10}4f^6 5d^1$ configuration. In order to describe the XMCD effect in photo-excited EuO, we have to consider transitions from both the $3d^{10}4f^6 5d^1$ and $3d^{10}4f^7 5d^0$ initial states. The difference in the initial state electronic configuration of the excited Eu atoms ($4f^6 5d^1$) compared to the non-excited Eu atoms ($4f^7 5d^0$) may lead to changes in the multiplet structure at the M_5 and M_4 edges. However for the integrated XMCD intensity at the M_5 edge we can write:

$$\Delta A_5 = (1-n)\left(-\frac{(A_5^{(7)}+A_4^{(7)})}{7}\ (3{L_{4f}}^{(7)} + 2{S_{4f}}^{(7)})\right) + n\left(-\frac{(A_5^{(6)}+A_4^{(6)})}{8}\ (3{L_{4f}}^{(6)} + 2{S_{4f}}^{(6)})\right) \quad (4.9)$$

where the superscripts (7) or (6) refer to Eu atoms with a $4f^7 5d^0$ and $4f^6 5d^1$ initial state configuration, respectively, and the subscripts (4) and (5) refer to the different absorption edges. *n* represents the number of optically-excited Eu atoms (Eu-$4f^7 5d^0$ → Eu-$4f^6 5d^1$) and is expected to be roughly constant at least at the sub-nanosecond timescales, see chapter 6. The left part of the right hand side of Eq. (4.9) represents the contribution from the Eu-$4f^7 5d^0$ atoms while the right part represents the contribution from the Eu-$4f^6 5d^1$ ions. For not too high pump fluences, the contribution from the unexcited $4f^7 5d^0$ atoms is much larger than the

contribution from the $4f^6 5d^1$ ions. The pump fluences used in this chapter are high: several percent or several tens of percent of the Eu atoms in EuO are photo-excited by the pump.

From Eq. (4.9) we can see that after optical-excitation, changes in ΔA_5 can occur due to changes in the (optical) parameters $A^{(7,6)}_{5,4}$ or due to the changes in L and S. Because of the atomic character of the transitions at these high energies, the pump-induced changes in $A^{(7,6)}_{5,4}$ are expected to be small. Therefore we are sensitive to changes in the values of the quantum numbers L_{4f}, S_{4f} of both the excited and the non-excited atoms . In the experimental section more details are given on the used samples and on the time-resolved XMCD experimental setup.

4.2 Experimental Methods

4.2.1 Sample preparation

Because of the high absorption coefficients of most materials in the soft X-ray region, we need to work with thin film samples in a transmission setup. As a substrate, 500 nm thick free standing Al films were used. By means of Molecular Beam Epitaxy (MBE), thin films of EuO and Gd-doped EuO were grown on oxidized (Al_2O_3) Al substrates at the University of Cologne. Gd-doped samples were used because Gd-doping increases T_c which makes them easier to study. Details about the synthesis can be found in [4,7,8]. In short, high purity Eu and Gd metal were evaporated from effusion cells while simultaneously oxygen was supplied through a leak valve. The Gd concentration could be varied by changing the temperature of the Gd effusion cell thereby changing the Gd deposition rate. Three different samples were fabricated, an intrinsic sample and two Gd-doped samples with a Gd-concentration of 6%, $Eu_{0.94}Gd_{0.06}O$ (formally we have to speak of substitution rather than doping, however we used the language which is used in the EuO literature) and 24%, $Eu_{0.76}Gd_{0.24}O$ as verified by XAS (cf. sec. 4.3.1). To ensure the correct stoichiometry, the substrate was heated at T=350°C. At this temperature, an excess of Eu at the surface of the samples will evaporate [3]. The prepared samples were polycrystalline with a thickness of about 15-20 nm, see Fig. 4.3. To prevent oxidation of the samples to Eu_2O_3 or Eu_3O_4, the samples are protected by a capping layer of Al with a thickness of about 3 nm. A thicker capping layer reflects too much of the pump light and cannot be used in pump-probe experiments.

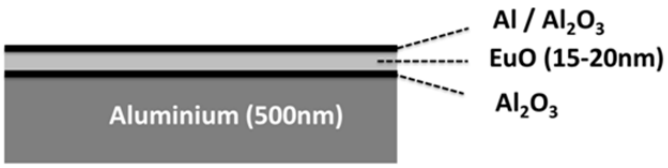

Figure 4.3 | Schematic drawing of the sample design. The Al capping layer is about 3 nm thick and is partially oxidized.

4.2.2 Setup at BESSY

The (time-resolved) XMCD experiments were carried out at the synchrotron facility BESSY II in the Helmholtz-Zentrum für Materialien und Energie GmbH in Berlin. The data was collected in two measurement sessions using the UE56/1-PGM and UE56/1-ZPM beam lines. Both beam lines use the same helical undulator which is capable of generating circularly polarized light in the soft X-ray region. However different types of monochromators were used at both beam lines. PGM stands for Plane Grating Monochromator and is a standard gold grating which disperses the X-ray beam. In this case the soft X-ray photon flux in the pump-probe experiments is small. This is because of the fact that there are large losses in the photon flux after each optical element in the soft X-ray regime. Apart from losses in the dispersion optics, there are additional losses from the focusing optics. The situation can be improved by using a Bragg-Fresnel reflection zone plate monochromator (ZPM) which takes care of both dispersing and focusing the X-ray beam [9]. This results in a higher photon flux. However in this configuration the spectral resolution was worse compared to the PGM case. The Gd- doped samples were measured at the PGM beam line whereas the intrinsic sample was measured at the ZPM beam line.

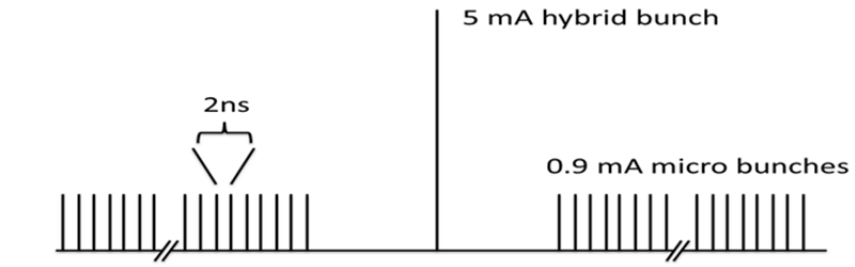

Figure 4.4 | Filling pattern of the storage ring at BESSY II in the multibunch mode of operation. A strong hybrid bunch with a beam current of 5 mA is separated from weaker micro bunches.

For the discussion of the pump-probe measurements it is important to consider the filling pattern of the storage ring. Although BESSY II can operate in different modes, we used only the so-called multibunch mode of operation. The filling pattern is depicted in Fig. 4.4 where the vertical axis represents the number of electrons and the horizontal axis is time. The pattern consists of weak microbunches and one strong hybrid bunch, which is separated in time from the microbunches for the pump-probe experiments. The spacing between the microbunches is 2 ns (500 MHz) while a complete roundtrip of the relativistic electrons bunch is about 800 ns (1.25 MHz). The FWHM of the electron bunches is 50 ps, which is the limiting factor in our time-resolved measurements since it determines the pulse duration of the X-ray pulses.

In order to be able to do pump-probe experiments, the laser which generates the pump pulse needs to be synchronized with the synchrotron. For that the fifth harmonic of the repetition rate of a Ti:Sapphire oscillator was subtracted from the 500 MHz (repetition rate microbunches) generated by the microbunches. The difference frequency was minimized by actively changing the cavity length of the oscillator. The output of the oscillator was amplified in a multipass amplifier yielding pulses of 2 mJ at repetition rate of 3 kHz, a wavelength of 780 nm and a pulse length of 60 fs. A delay line on the pump sets the pump-probe delay. With a frequency of only 3 kHz, the repetition rate in the experiment is limited by the laser. Because of the large average heating of the sample by the pump pulses, in some of the experiments the repetition rate of the laser was reduced to 1.5 kHz by placing a chopper in the pump beam.

In most of the performed pump-probe measurements, the pump pulse arrives before or just after the X-ray pulses generated by the hybrid bunch. Using a delay line, the delay can be changed by about 1.5 ns. In order to check the signal at longer delays, it is also possible to change the timing in such a way that the pump-pulse arrives in the middle of the micro bunches. By monitoring the changes in the train of microbunches using a fast oscilloscope, signals at longer delays can be measured. The time resolution is limited by the spacing between the microbunches (2 ns).

A schematic representation of the setup is depicted in Fig. 4.5. The X-ray beam is parallel to the applied magnetic field while the angle of incidence of the X-ray beam is 30 degrees. In order to determine the XMCD, the transmission (T) of the X-beam is measured at positive and negative magnetic field after which the dichroism can be calculated, $XMCD/d=\alpha_+-\alpha_-=(-\ln T_+/I_0)-(-\ln T_+/I_0)=\ln(T_+/T_-)$, in which d is the

film thickness and I_0 is the incoming intensity. The pump beam makes an angle of about 2 degrees with the X-ray beam. The X-ray beam in the pump-probe measurements is detected by an avalanche photodiode (APD) connected to a boxcar averager and gated integrator. The transmission of the X-rays with and without the presence of the pump-pulse is measured at plus and minus magnetic field after which *ΔXMCD*/*XMCD* can be determined.

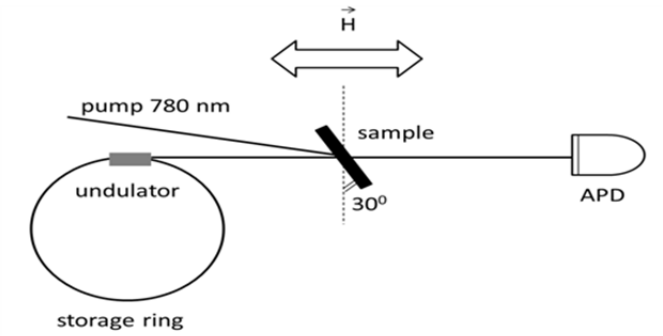

Figure 4.5 | Schematic representation of the experimental configuration in the time-resolved XMCD measurements. When the electron beam passes the undulator, X-rays are emitted which are going to the sample. The X-rays beam is detected by an avalanche photodiode (APD). The applied magnetic field is parallel to the k-vector of the X-ray beam. The surface normal of the sample makes an angle of 30 degrees with the k-vector of the X-ray beam.

In most of the experiments the photon energy is fixed at the maximum of the M_5 XMCD peak and the pump-probe delay is scanned. We refer to the transmission at pump-probe delay τ as (*P*, pumped) and at a very large pump-probe delay of τ+ 167*μ*s as (*U*, unpumped). The boxcar generates two outputs. One is the difference between the signals (*Diff* = *P*-*U*) and one is the sum of them (*Sum* = *P*+*U*). Both signals are measured at positive (+) and negative (-) magnetic field. The unpumped signal *U* can be calculated from the *Diff* and *Sum* signals:

(4.10) $U^{+}(\tau + 167\mu s) = (Sum^{+} - Diff^{+})/2$

(4.11) $U^{-}(\tau + 167\mu s) = (Sum^{-} - Diff^{-})/2$

Since the unpumped signal can be considered as constant in the range of (τ=0-1.2ns), an average value <> can be determined.

(4.12) $U_{mean}^{+} = < U^{+}(\tau + 167\mu s) >$

(4.13) $U_{mean}^{-} = < U^{-}(\tau + 167\mu s) >$

The pumped value *P* was determined as follows:

(4.14) $P^{+}(\tau) = 2\ Diff^{+} + U_{mean}{}^{+}$

(4.15) $P^{-}(\tau) = 2\ Diff^{-} + U_{mean}{}^{-}$

Finally, the *XMCD* value was calculated according Eq. (4.16):

(4.16) $$XMCD(\tau) = ln\left(\frac{P^{+}(\tau)}{P^{-}(\tau)}\right)/d$$

The *XMCD* value at negative pump probe delays is named *XMCD*(neg). *ΔXMCD*/*XMCD* can be calculated using Eq. (4.17):

(4.17) $$\frac{\Delta XMCD}{XMCD}(\tau) = \frac{XMCD(\tau) - XMCD(neg)}{XMCD(neg)}$$

4.3 Results and Discussion

4.3.1 Characterization

Before doing the time-resolved measurements, the (magnetic) properties of the samples were checked by measuring XAS and XMCD spectra and by measuring XMCD hysteresis loops for different samples. By XAS, the doping concentration could be determined. The XAS spectrum of the 24% ($Eu_{0.76}Gd_{0.24}O$) and 6% ($Eu_{0.94}Gd_{0.06}O$) Gd-doped EuO samples are shown in Fig. 4.6.

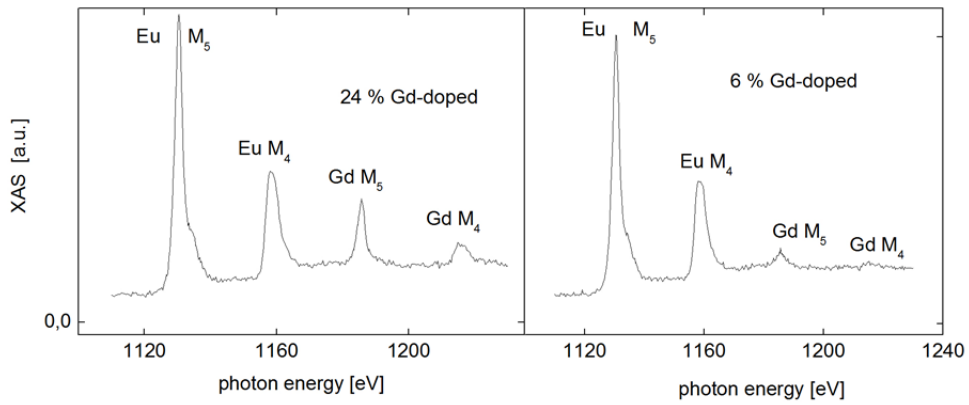

Figure 4.6 | X-ray absorption spectrum of the 24% Gd-doped EuO sample ($Eu_{0.76}Gd_{0.24}O$) and the 6% Gd-doped sample ($Eu_{0.94}Gd_{0.06}O$) at 82K. There is no applied magnetic field.

In Fig. 4.6, the XAS spectra of the 24% and 6% Gd-doped samples at 82 K in zero applied magnetic field are shown. From low to high energy we see the Eu M_5, Eu M_4, Gd M_5 and the Gd M_4 absorption edges. Since Gd^{3+} is also $3d^{10}4f^7$ and has a similar spectral lineshape as Eu^{2+}, the Gd-concentration can be determined by looking to the ratio of the M_5 absorption peaks for Eu and Gd as is described in detail in [4]. The estimated Gd-doping concentrations are 6 ± 1% and 24 ±1%. The XAS spectra can also provide information about the presence of Eu^{3+}. In Eu^{3+} the main absorption peak is shifted by a few eV compared to Eu^{2+} and two additional peaks appear, one at lower energy and one at higher energy of the main peak [10]. Since none of the samples such peaks were observed we can conclude that the samples were not oxidized to Eu_2O_3 or Eu_3O_4 and mostly consist of EuO; we estimate an EuO concentration of at least more than 80%. The XMCD spectrum for the 24% doped sample at 82 K and 485 mT is shown in the right panel of Fig. 4.7. The absorption spectra taken with the magnetic field parallel and antiparallel to the k vector of the X-ray beam are shown in the left panel of Fig. 4.7. The difference gives the XMCD spectrum. The obtained results are similar to results published in [4] indicating the good quality of the samples.

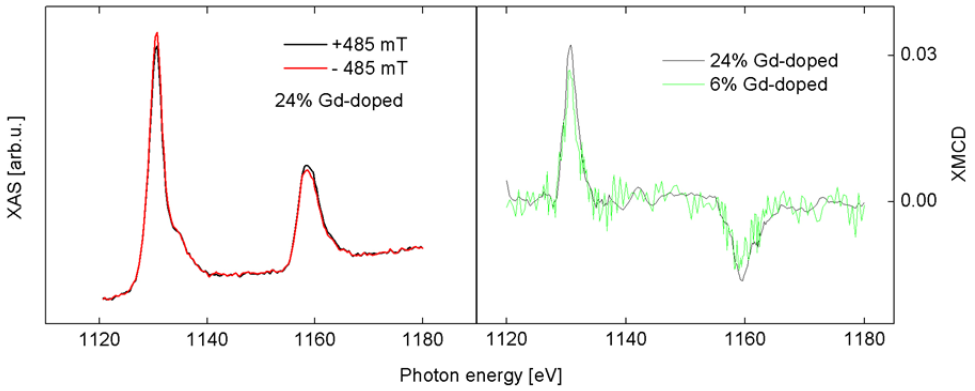

Figure 4.7 | Left panel) X-ray absorption of the 24% Gd-doped EuO sample ($Eu_{0.76}Gd_{0.24}O$) at 86 K. The applied magnetic field is +/- 490 mT. Right panel) XMCD spectrum of the 24% ($Eu_{0.76}Gd_{0.24}O$) and 6% Gd-doped ($Eu_{0.94}Gd_{0.06}O$) EuO sample at 86 K. The applied magnetic field is +/- 485 mT.

The samples were further magnetically characterized by investigating the transmission of the sample at a photon energy which corresponds to the maximum in the XMCD spectrum at the M_5 edge while the applied magnetic field is varied. An

example is shown in the right panel of Fig. 4.8. From the hysteresis loops, the saturation XMCD values can be can be determined. By doing this for different temperatures, Fig. 4.8 can be obtained where the magnetization ($M \propto XMCD$) is plotted versus the temperature. The temperature is given as measured by a temperature sensor close to the sample. In de 24% Gd-doped sample, a maximum in the dichroism of about 15% is obtained at 32K in an applied magnetic field of 485 mT. At the same conditions, the maximum in the dichroism for the 6% Gd-doped EuO sample is about 27%, and is about 5% for the intrinsic sample.

The ordering temperature (vertical line in Fig 4.8 left) of the intrinsic sample is about 93 K while 69 K is expected from the literature for intrinsic stoichiometric samples [11]. A large non-stoichiometry, which can lead to an increased T_c, is excluded because of the growth method [3]. An increase of T_c of 20 K requires an oxygen vacancy concentration of about 2.5% [12], which is very unlikely to be the case. This means that the sample is colder than the temperature sensor. This can be the case since the samples were on the top of the cold finger while the temperature sensor was a bit lower on the sample rod. It is also possible that the temperature sensor has a bad thermal contact with the sample rod. Therefore we can conclude that we have to reduce the measured temperature (sensor) by ~24 K. The same holds for the 24% Gd-doped sample.

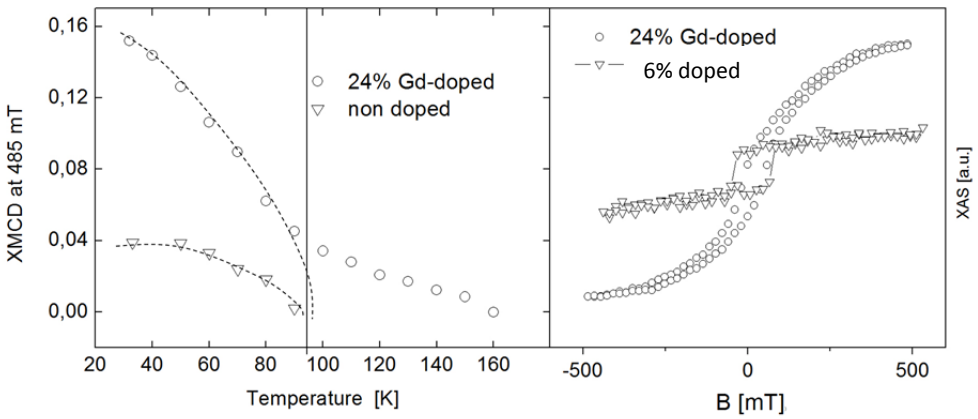

Figure 4.8 | The remanence and saturation values of the 24% Gd-doped ($Eu_{0.76}Gd_{0.24}O$) and intrinsic EuO samples at a photon energy which corresponds to the maximum in the XMCD spectrum at the M_5 edge (this is *not* the integrated value of the XMCD M_5 peak). The saturation value was taken at +/- 485 mT. The right panel shows the hysteresis loop of the 24% and 6% Gd-doped ($Eu_{0.94}Gd_{0.06}O$) samples at 32K. On the vertical axis the X-ray absorption of right circularly polarized light is shown.

In Fig. 4.9 the SQUID magnetization data and saturation XMCD values are shown for the 6% Gd-doped sample. The SQUID and XMCD data nicely overlap for this sample indicating that the actual sample temperature for the 6% Gd-doped sample was correctly determined.

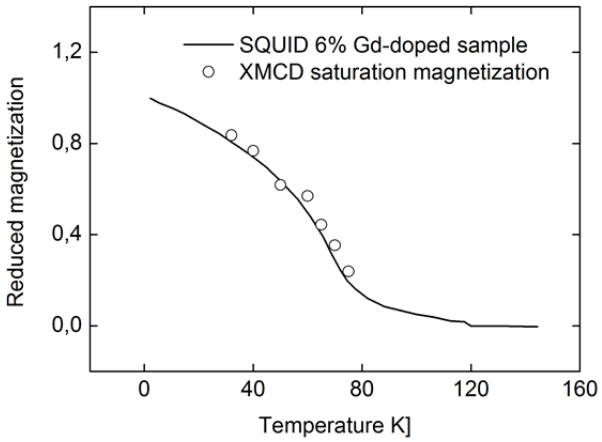

Figure 4.9 | SQUID magnetization data and XMCD saturation (490 mT) data on the 6% Gd-doped sample ($Eu_{0.94}Gd_{0.06}O$). The reduced magnetization and XMCD values are plotted versus temperature.

Based on XMCD measurements (Fig. 4.8) and SQUID data (Fig. 4.9) one can see that the Gd-doped samples have two different ordering temperatures. One is about 120 K (= 140K in Fig. 4.8) and one is the normal one at 69 K. The increase in ordering temperature is discussed in chapter 1, and involves (mobile) conduction electrons via a RKKY like mechanism. The substitution of Eu with Gd increases the conduction electron concentration. It is believed that at lower doping concentrations (< 8%), in between 69 K and 120 K, there are ferromagnetic domains (or regions) generated in a paramagnetic background [8]. At about 8% the material is rather magnetically homogeneous while at higher doping concentration there is an instability of the ferromagnetic configuration against a spiral configuration along the [111] direction [4,8].

The data presented in Figs. 4.8 and 4.9 is important later on in this chapter where we discuss pump-probe experiments in which the pump pulses heat up the sample. In this case the temperature given by the temperature sensor might be different from the actual (dynamical) temperature in the sample. When the pump beam is

turned on, the following can happen. The first pump pulse heats the sample and if the heat diffusion is not efficient enough, the sample is still warm before the next pulse arrives. By looking at negative delays, where the probe pulse arrives just before the pump pulse, the temperature of the sample can be probed by measuring the XMCD value and by comparing it with the magnetization versus temperature graph without pump. The obtained temperature needs to be subtracted by 20 K. By doing this we know the temperature of the sample just before the next pump pulse arrives.

4.3.2 Gd-doped EuO

In order to measure the photo-induced demagnetization in Gd-doped EuO, we performed time-resolved XMCD experiments on the Gd-doped samples on the UE56/1-PGM beam line. Before doing so, we tested the setup with Nickel, which also gave us the possibility to determine the time-zero in these experiments, see Fig. 4.10. A pump-probe experiment was performed at the L_3 edge of Nickel using an 800 nm pump beam (~80 fs FWHM). The data could be fitted by a step function which is convoluted with a Gaussian. From this measurement also the time-resolution was determined which is 50 ps. Because of the fast rise time due to the limited time resolution, the signal starts already at negative delays (~ -25 ps).

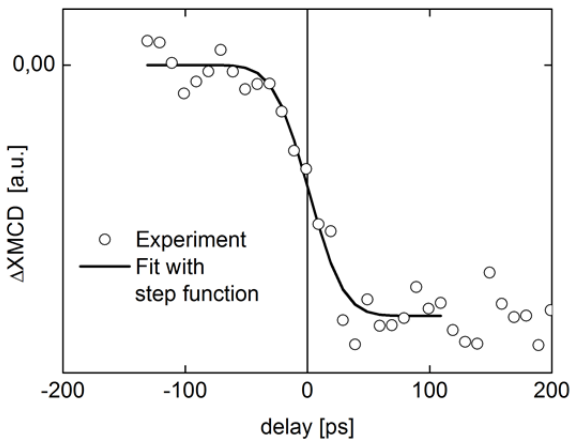

Figure 4.10 | Time-resolved XMCD measurement on Nickel at the L_3 edge at room temperature. The line represents the fit of the data with a step function which is convoluted with a Gaussian.

The pump induced changes at the maximum of the M_5 absorption edge of Europium for the 6 and 24% Gd-doped samples are shown in Fig. 4.11. In these experiments the pump beam was focused down to a spot of 1.2x0.5 mm. The applied magnetic field was 150 mT (x = 6%) and 490 mT (x=24%). The temperature was set to 32 K in all the measurements The estimated temperature of the sample at small negative delays was determined by measuring the XMCD and by comparing this with the XMCD values in Fig. 4.8. The results for the Gd-doped samples are shown in Figure 4.11. The exact experimental conditions are shown in Table 4.1.

Table 4.1 | Experimental conditions for the data as presented in Figure .

Curve	Gd-doping	B [mT]	Estimated temp.	Fluence	Photo-doping
Red	6 %	150	52 ± 10 K	5.1 mJ/cm^2	10%
Black	6 %	150	52 ± 10 K	1.9 mJ/cm^2	4%
Green	24 %	490	50 ± 10 K	3.6 mJ/cm^2	7%

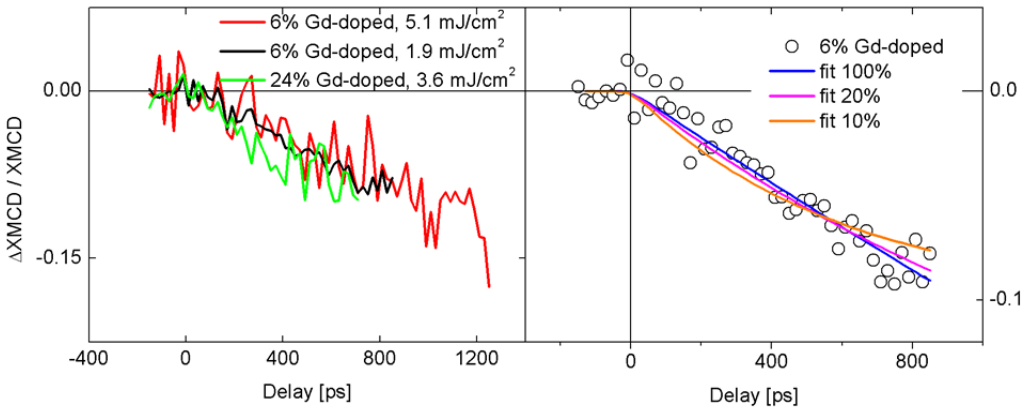

Figure 4.11 | Time-resolved XMCD measurements on the 24% ($Eu_{0.76}Gd_{0.24}O$) and 6% ($Eu_{0.94}Gd_{0.06}O$) Gd-doped EuO samples at a temperature of about 50 K. We measured the pump induced changes at the maximum of the M_5 absorption edge. The exact used conditions are described in Table 4.1. The right panel shows the fits for the black line in the left panel. Fits for different demagnetization amplitudes are shown.

The data was taken below the second magnetic ordering temperature ($T < T_c$= 69 K) for both samples with a photo-doping (PD) concentration ranging from 4-10%. The high fluence measurement of the 6% doped sample has a lower temperature at negative delays than the lower fluence experiment. This can be explained by a

sample spot dependent cooling efficiency. The free standing Al film is mounted on a metal ring which in turn is mounted on a cold finger. The film is more efficiently cooled closer to the edges of the film where there is a better thermal contact with the ring. No clear fluence and Gd-doping concentration was observed. In all the data the demagnetization amplitude (*A* in Eq. (4.18 below) is about 8% at +650 ps. Assuming that the demagnetization is exponential, the data could be modeled by an exponential which is convoluted with a Gaussian:

(4.18) $\frac{\Delta XMCD}{XMCD}(t) = G(t-t_0) * \left[H(t-t_0) \cdot \left\{A(1-e^{-(t-t_0)/\tau_A})\right\}\right]$,

where *G* is a Gaussian and *H* is a Heavyside step function. A Gaussian with a FWHM of 50 ps was used which describes the temporal resolution of the setup. The component proportional to *A* corresponds to an exponential decay. The simulated results are shown in the right panel of Fig. 4.11 for different demagnetization times τ_A and amplitudes A and are compared with the 6% Gd, 4% PD measurement. Reasonable fits could be obtained for demagnetization amplitudes of 20-100 % and corresponding demagnetization times ranging from 1.3 - 9.0 ns.

In order to determine the long time demagnetization amplitude, the pump pulse timing was changed in such a way that it arrives in the microbunches. The XMCD results for the 24% Gd-doped EuO sample ($Eu_{0.76}Gd_{0.24}O$), as determined from the oscilloscope traces, is shown in Fig. 4.12. The applied field is 490 mT while the photo-doping (PD) is 7%. The estimated temperature at negative delay is 95 K. The separation of the different micro bunches is 2 ns. However due to the limited time-resolution of the electronics no separate pulses could be observed.

The right panel shows a zoomed-in version of the left panel including a fit with Eq. (4.19) to the response of the system to a single hybrid bunch pulse (green line):

(4.19) $\Delta XMCD/XMCD(t) = G(t) * [H(t) \cdot C]$,

In which C is a constant. After the fast rise time there is a much slower decay in the signal (not shown). From the rise time the temporal resolution of the setup was determined. The width of the Gaussian is determined to be σ=0.72. The red line corresponds to a fit of Eq. (4.18) to the XMCD experiment using a Gaussian with *σ*=0.72, giving a time constant of τ= 1.5±0.2 ns and a demagnetization amplitude of 54%.

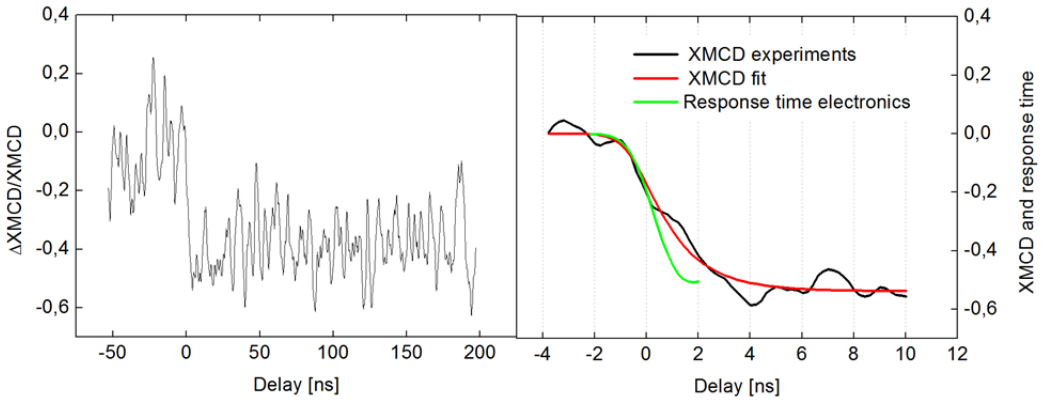

Figure 4.12 | Time-resolved XMCD as measured on the oscilloscope for the 24% Gd-doped EuO sample ($Eu_{0.76}Gd_{0.24}O$). We measured the pump induced changes at the maximum of the M_5 absorption edge. The photo-doping concentration is 7% and the applied magnetic field is 490 mT. The left panel shows a close up around time-zero. The green curve shows the response time of the electronics on a 50 ps X-ray pulse. The red curve represents a fit of (4.18) to the experimental data.

Apart from measurements at the M_5 peak in the XMCD spectrum also time-resolved XMCD spectra were taken at -150 ps and +950 ps. These spectra can give information about changes in the multiplet structure and changes in the spin to orbital angular momentum ratio. The results on the 6% Gd-doped EuO sample is shown in Fig. 4.13. The measured temperature is 57 K, while the PD concentration is 4% and the applied magnetic field is 490 mT. The signal S in the left panel represents the change in the XMCD signal with respect to a reference measurement which is taken 167 µs after/before the pump pulse:

$$S(\tau, \hbar\omega) = \frac{XMCD[\tau,\hbar\omega] - XMCD\,[\tau+167\mu s,\hbar\omega]}{XMCD[\tau+167\mu s, M_5\ max]} \quad (4.20)$$

Since at + 167 μs the sample is warmer than at -150 ps, the XMCD signal at -150 ps is larger than at + 167 μs. After the pump pulse, the magnetization decreases and therefore also $\Delta XMCD$ at +950 ps. The difference between -150 ps and 950 ps is plotted in the right panel of Fig. 4.13.

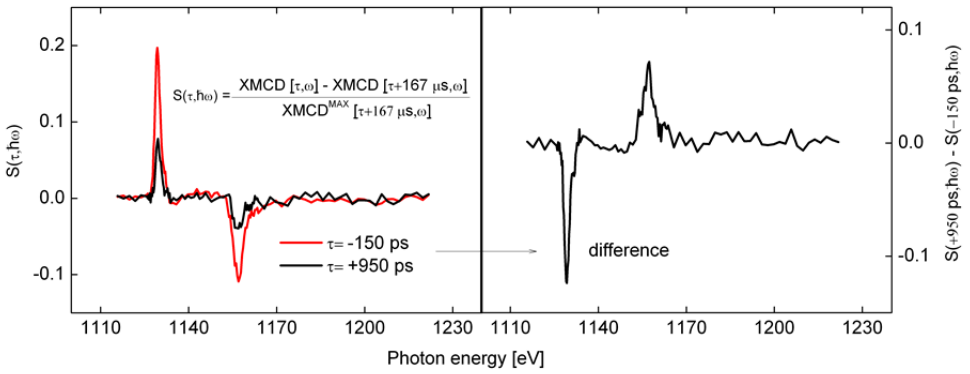

Figure 4.13 | Time-resolved XMCD spectra of the 6% Gd-doped sample ($Eu_{0.94}Gd_{0.06}O$). The measured temperature is 57 K, while the PD concentration is 4% and the applied magnetic field is 490 mT. In the left panel $S(\tau, \hbar\omega)$ is plotted for differen delays, while in the right panel $S(+950\ ps, \hbar\omega) - S(-150\ ps, \hbar\omega)$ for different photon energies.

Within the noise, no changes in the integrated intensities of M_5 and M_4 were observed indicating that the *L* to *S* ratio is constant. Also no changes in the line shape in the XAS or XMCD were observed. This means that the magnetization can be probed by just looking to the maximum of the M_5 peak. Before discussing the results in more detail, the data on the intrinsic samples is presented in the next section.

4.3.3 Intrinsic EuO

The data on the intrinsic samples is taken on the UE56/1-ZPM beam line. The resolution was about 4 eV which almost covers the whole M_5 peak. Since the repetition rate was 1.5 kHz instead of 3 kHz, higher fluences could be used. The set temperature for all the data is 32 K and the applied magnetic field is 490 mT. The results are shown in Fig. 4.14 while the experimental conditions are shown in Table 4.2. For all the fluences, the measured temperature is lower than T_c.

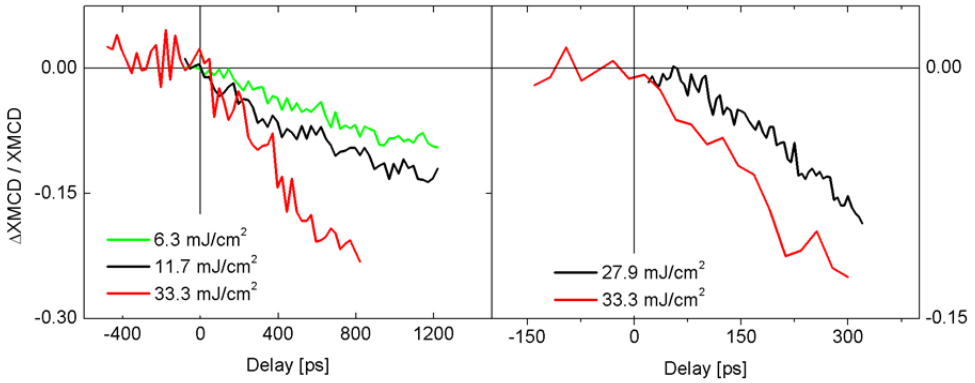

Figure 4.14 | Time resolved XMCD measurements on an intrinsic sample at the M_5 edge. The XMCD probe almost covers the whole M_5 peak. The exact used conditions are described in Table 3.

Table 4.2 | Experimental conditions for the data as presented in Figure 4.14. (L) is left panel in Fig. 4.14, (R) is the right panel.

Curve	Gd-doping	B [mT]	Estimated temp.	Fluence	Photo-doping
(L) green	0 %	485	25 ± 10 K	6.3 mJ/cm^2	10%
(L) black	0 %	485	30 ± 10 K	11.7 mJ/cm^2	18%
(L) red	0 %	485	56 ± 10 K	33.3 mJ/cm^2	52%
(R) black	0 %	485	64 ± 10 K	27.9 mJ/cm^2	44%
(R) red	0 %	485	61 ± 10 K	33.3 mJ/cm^2	52%

From Fig. 4.14 we can see that the amplitude at +650 ps is 5% and 20% for fluences of about 6 and 33 mJ/cm^2 respectively. The measurement at 33 mJ/cm^2 was fitted with an ingrowing exponential, see Eq. (4.18), giving a demagnetization amplitude of 50% and a demagnetization time of 1.2 ± 0.4 ns, see Fig 4.15.

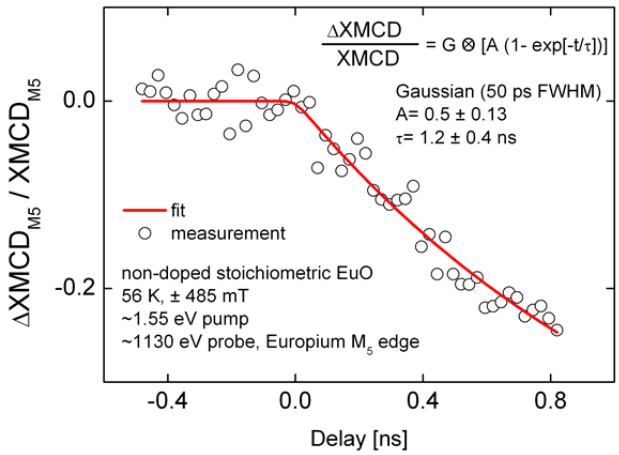

Figure 4.15 | Time-resolved XMCD measurements on an intrinsic EuO sample at the M_5 edge. The XMCD probe almost covers the whole M_5 peak. The pump fluence is 33 mJ/cm^2. The data is fitted with equation which is depicted in the graph.

In Fig. 4.16, the data in Fig. 4.14 is normalized to the pump fluence. An increase of the pump fluence leads to a decrease of the normalized amplitude (ΔXMCD/Fluence) at +800 ps. When we assume that the demagnetization amplitude *A* in Eq. (4.18) increases linearly with pump fluence, then we can conclude that the demagnetization time decreases with pump fluence. However the photo-doping concentration might not be linear in the pump fluence at high fluence. Also the estimated temperatures in the measurements are different and a temperature effect cannot be excluded.

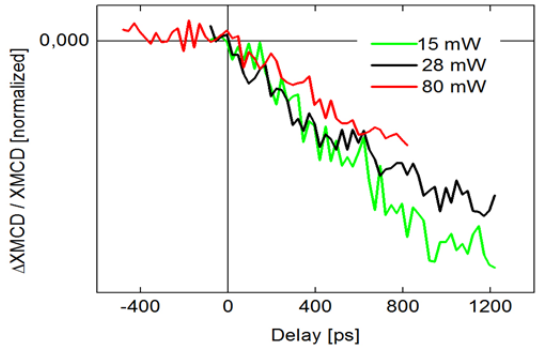

Figure 4.16 | Time-resolved XMCD measurements on the intrinsic EuO sample. The data shown is the same as in the left panel of Fig. 4.14 with the difference that it is normalized to the pump fluence. The pump fluences are: green (6.3 mJ/cm^2), black (11.7 mJ/cm^2), red (33.3 mJ/cm^2).

4.4 Discussion

Based on the time-resolved XMCD measurements on EuO we can conclude that within the noise level there is no considerable demagnetization amplitude (or integrated demagnetization, $\int_0^{+50\,ps} \Delta M(t)dt$) during the first 50 ps, which is completely different from Gd metal where there is a fast component (~1 ps) with an amplitude of 25% [13]. In the following we will discuss why there is no such large fast demagnetization component and briefly discuss what the mechanism behind the observed slow demagnetization component is. The discussion is continued in Chapter 5, where the magnetization dynamics data (probed with magneto-optics) with a better temporal resolution (200 fs) are presented. Before discussing the data, we will present some (theoretical) consideration, which are important for the understanding of the data.

4.4.1 Photo-excitation in semiconductors: the role of the gap

First we point to one of the differences in photo-excitation between a semiconductor and a metal (for instance Gd). In EuO, using light with a photon energy of 1.55 eV, electrons are excited from the valence to the conduction band. After electron-electron thermalization (typically ~100 fs in semiconductors), the distribution of the photo-excited electrons can be described by a Fermi-Dirac distribution with an electronic temperature which differs from the lattice temperature. This hot electron gas cools down by phonon emission after which the electrons and the lattice become in thermal equilibrium at the electron-phonon equilibration timescale (typically hundreds of fs in semiconductors). Since light with a photon energy of 1.55 eV was used and the band gap is about 1.2 eV, only a fraction (0.35 eV=1.55-1.2eV) is used to heat up the electrons and lattice at the electron-phonon equilibration timescale. Therefore for every absorbed photon only 23% of its energy is transferred to the conduction band-lattice system at the picosecond time scale.

4.4.2 Different (electronic) magnetic sub-systems in EuO

Photo-excited EuO is also a complicated system because there are different (electronic) magnetic sub-systems. Three different (electronic) magnetic systems can be distinguished: 1) the $4f^7$ magnetic moments of Eu and Gd 2) the 5*d* electrons and 3) the $4f^6$ magnetic moments. All the sub-systems interact with each other. The $4f^7$ moments have a (J=S=7/2) configuration and the 5*d* electrons can be modeled as S=1/2 electrons. At T=0 K all the 4*f* moments are aligned. After photo-excitation,

demagnetization in 1) or 2) can occur due to changes in the orientation of the different $4f^7$ and 5*d* atomic magnetic moments in the sample leading to a decrease of the samples macroscopic magnetization.

For the $4f^6$ magnetic moments the picture is less clear. From a Hund's rule analysis, the ground state of a $4f^6$ ion is *S*=*L*=3 with J=0. In the excited states *J* can range from *J*=0 to 6, depending on the angle between $(\vec{S},\vec{L})$. Although it is easy to determine the ground state configuration, it is not clear what the value of *J* is right after photo excitation since the ions are in an excited state configuration. Therefore demagnetization in system 3) can occur due to i) changes in the orientation of the different atomic moments but also due to ii) changes in the magnitude of a single $4f^6$ magnetic moment (due to changes in the angle between $(\vec{S},\vec{L})$).

In Fig. 4.17 the contributions of the different magnetic subsystems right after photo-excitation in magnetically ordered EuO are shown for different pump fluences, assuming that there are no spin-flips during photo excitation. The magnetic moment of EuO at 0 K is 6.9 μ_B. If one considers a spin-only magnetic moment in the $4f^6 5d^1$ excited state, the magnetic moment of the $5d^1$ system is $g\cdot \mu_B \cdot S$, which equals μ_B for *S*=1/2,*g*=2. Now the $4f^6$ moments are assumed to have a magnetic moment of 6.9 -1 = 5.9 μ_B. The percentage of the magnetization (M) of the different sub systems to the total magnetization is shown in Fig. 4.17 for different photo doping (PD) concentrations. A more detailed picture is given in the next chapter.

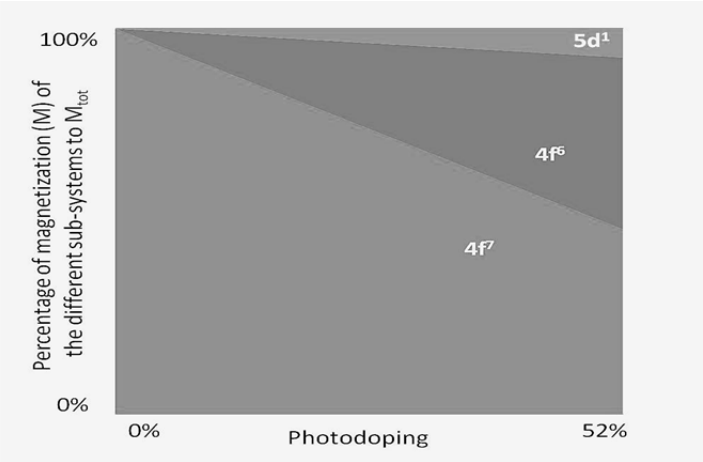

Figure 4.17 | Percentage of the magnetization of the different sub-systems to the total magnetization.

From Fig. 4.17 can be seen that even for the highest pump fluences in this picture, the contribution of the 5*d* moments is only 13%. The fact that the 5*d* contribution to the magnetization is small, does not means that it could be neglected. The 5*d* moments can still play a crucial role in the demagnetization of the $4f^{6,7}$ moments, as was observed in Tb and Gd, and as we will see later for EuO as well.

4.4.3 The interaction between different magnetic sub-systems in EuO

After we have distinguished different magnetic sub-systems, we also have to discuss the coupling between them. In Figure 4.18, the transfer of angular momentum between the sub-systems is shown. In the 'standard model', demagnetization occurs because of a flow of angular momentum to the lattice through the AFCF mechanism for localized moments, or due to Elliot-Yafet (EY) spin-flip scattering of conduction electrons, see Chapter 3 and for instance [14,15]. Moreover, there are also interactions between the different (electronic) magnetic systems which can be the described by electron-magnon scattering processes (see Chapter 3) or an inter-atomic 4*f*-4*f* Heisenberg exchange interaction (see also Chapter 7).

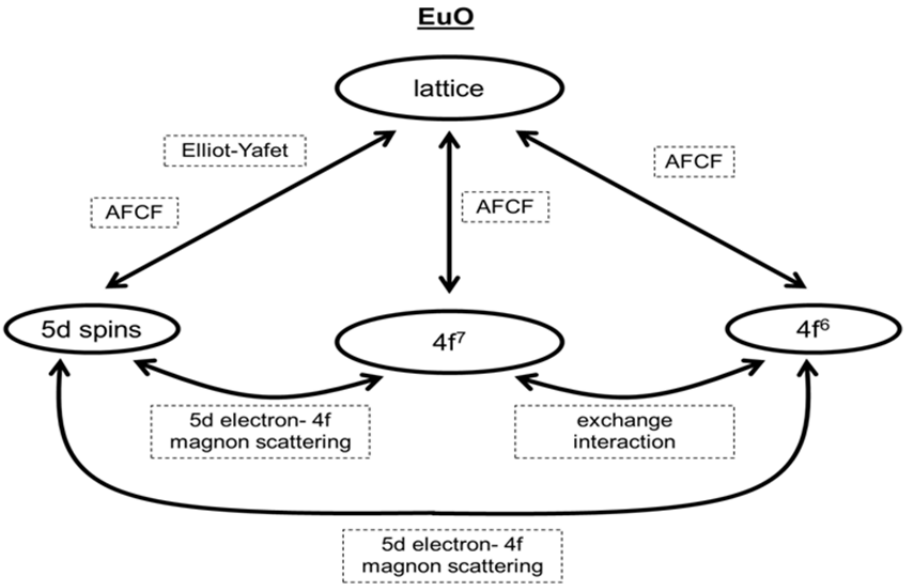

Figure 4.18 | Transfer of angular momentum between different sub-systems: $4f^7$ (Eu^{2+}, S=7/2, L=0), $4f^6$ (Eu^{3+}, S=3, L=3) and $5d^1$ spins. The interaction with the lattice is described by AFCF and Elliot-Yafet scattering while the interaction between the different magnetic sub-systems is described by 4f-4f exchange interaction and 4f-5d magnon-electron scattering.

Below we focus on the different electronic magnetic sub-systems separately, and make theoretical estimations for the AFCF and EY spin-lattice relaxation times which we compare with literature results:

- $4f^7$ (Eu^{2+}, L=0) AFCF: in Chapter 3 we estimated the AFCF spin-lattice relaxation time to be 450 ps, based on the Magnetic Anisotropy Energy [16,17]. The spin-lattice relaxation time has already been studied in EuS [18], which is also a ferromagnetic semiconductor (T_c=16K) and has an electronic structure which is very similar to EuO. In order to determine the spin-lattice relaxation, a MOKE measurement was performed by exciting the system with short magnetic field pulses and by probing the system with optical pulses . The observed spin-lattice relaxation time in EuS of 120 ps at 5 K is in the same order of magnitude as our theoretical estimate for EuO.
- 5*d* EY: the EY spin-lattice relaxation rate *R* (in Eq. 3.9) is (even for very high photo-doping concentrations, 30% Eu atoms excited) more than 10 times smaller than for Gd, based on our very crude estimation that we made in Chapter 3. Therefore according to this estimation and by neglecting other mechanisms, EuO should have so-called Type II dynamics (see Chapter 3) in which there are two steps in the demagnetization dynamics: one fast component before electron-phonon equilibration, and a slower component after electron-phonon equilibration. In the case that R in EuO is 10 times smaller than in Gd [14], the amplitude of the fast component is expected to be small.
- $4f^6$ (Eu^{3+}, L=3) AFCF: Now the AFCF spin-lattice relaxation of $4f^6$ moments is discussed. After photo-excitation some of the Eu atoms are in a $4f^6$ configuration. As mentioned, *S*=3 and *L*=3 while *J* can range from J=0-6. A big difference with the $4f^7$ moments is the presence of orbital angular momentum (*L*=3). The presence of ions with large orbital angular momentum and spin-orbit interaction can reduce the spin-lattice relaxation time drastically, as was demonstrated by doping EuS with 5% Tb ($4f^8$, *J*=6, *S*=3, *L*=3) [18,19]. In this case the spin-lattice relaxation time of 5% Tb-doped EuS was reduced from 120 to 12 ps. Since the Tb ions interact with the Eu ions by exchange interaction, this opens a faster spin-lattice relaxation channel of the (Eu) 4*f* system.

  For the AFCF spin-lattice relaxation of $4f^6$ moments we considered two different cases. As discussed before, case i) involves transitions between J_{4f6} final states (J_{4f6}=0-6) which are separated by large energy differences (~100meV [3]). Case ii) involves transitions between different M_J Zeeman levels which are separated by a much smaller energy gap ($g\ \mu_B\ H$). The large energy difference between

different J_{4f6} final states might reduce the spin-lattice relaxation rate in process i) because these energy differences are larger than typical phonon energies in EuO (< 40 meV). Process ii) is expected to be fast due to the fact that the Zeeman level splitting are smaller than typical optical phonon frequencies.

4.4.4 Discussion of the time-resolved XMCD measurements and Conclusion

With a temporal resolution of 50 ps, we observed a slow demagnetization with time-constants between 1-9 ns (demagnetization amplitude 20%-100%), when the sample is pumped with fluences between 2 and 33 mJ/cm^2. From the data no strong statements about the fluence and Gd-doping concentration dependence on the demagnetization time can be made. But there are indications that the demagnetization time decreases with pump fluence, based on the intrinsic EuO sample measurements. Also no changes in the *L* to *S* ratio were observed.

The slow nanosecond demagnetization time is not surprising when we compare this time with the AFCF spin-lattice relaxation time of the $4f^7$ moments; we estimate this time to be in the order of 440 ps which is a bit slower than in are our estimations. Also we reasoned that the EY spin-lattice relaxation process (involving 5d electrons) in EuO should be much slower than for instance in Gd metal, due to the fact that there are much less conduction electrons, see Chapter 3. The high degree of spin-polarization in the conduction band reduces the EY spin-lattice relaxation rate even more. Therefore also from this point of view, the absence of a fast (< 50ps), large (integrated, $\int_0^{+50\ ps} \Delta M(t)dt$) demagnetization component is not surprising.

The small nanosecond demagnetization time comes as a surprise when we compare it with the estimated AFCF spin-lattice relaxation time of the $4f^6$ moments (~10 ps), see the discussion in the previous subsection. We can explain the observed slow nanosecond demagnetization in different ways:

- There are not many $4f^6$ moments in the sample: there is ultrafast electron-hole recombination
- The $4f^6$ moments are weakly coupled to the surrounding $4f^7$ moments: the exchange scattering rate between $4f^6$ moments and $4f^7$ moments is small
- The $4f^6$ moments end up in a J_{4f6}=0 final state and therefore there is no AFCF spin-lattice relaxation of the $4f^6$ moments.
- Our model or framework is wrong, and we should include other novel effects like for instance magnetic exciton or magnetic polaron formation.

The discussion will be continued in the next chapter in which the laser-induced magnetization dynamics is studied by the Faraday and magneto-optical Kerr effect using short pump and probe pulses (<200 fs). This allows us to probe the magnetic ordering in EuO on the short timescales, which will help us in the understanding of the XMCD data.

References

[1] J. B. Goedkoop, J. C. Fuggle, B. T. Thole, G. Vanderlaan, and G. A. Sawatzky, J. Appl. Phys. **64**, 5595 (1988).
[2] J. B. Goedkoop, B. T. Thole, G. Vanderlaan, G. A. Sawatzky, F. M. F. Degroot, and J. C. Fuggle, Physical Review B **37**, 2086 (1988).
[3] P. Steeneken, *PhD thesis: New light on EuO thin films* (Rijksuniversiteit Groningen, 2002).
[4] H. Ott, S. J. Heise, R. Sutarto, Z. Hu, C. F. Chang, H. H. Hsieh, H. J. Lin, C. T. Chen, and L. H. Tjeng, Physical Review B **73**, 094407 (2006).
[5] V. V. Krishnamurthy, D. J. Keavney, D. Haskel, J. C. Lang, G. Srajer, B. C. Sales, D. G. Mandrus, and J. L. Robertson, Physical Review B **79**, 014426 (2009).
[6] B. Koopmans, M. van Kampen, J. T. Kohlhepp, and W. J. M. de Jonge, Phys. Rev. Lett. **85**, 844 (2000).
[7] R. Sutarto, S. G. Altendorf, B. Coloru*, et al*, Physical Review B **79**, 205318 (2009).
[8] R. Sutarto, S. G. Altendorf, B. Coloru*, et al*, Physical Review B **80**, 085308 (2009).
[9] C. Stamm, N. Pontius, T. Kachel, M. Wietstruk, and H. A. Duerr, Physical Review B **81**, 104425 (2010).
[10] B. T. Thole, G. Vanderlaan, J. C. Fuggle, G. A. Sawatzky, R. C. Karnatak, and J. M. Esteva, Physical Review B **32**, 5107 (1985).
[11] A. Mauger and C. Godart, Physics Reports-Review Section of Physics Letters **141**, 51 (1986).
[12] M. Barbagallo, N. D. M. Hine, J. F. K. Cooper, N. -. Steinke, A. Ionescu, C. H. W. Barnes, C. J. Kinane, R. M. Dalgliesh, T. R. Charlton, and S. Langridge, Physical Review B **81**, 235216 (2010).
[13] M. Wietstruk, A. Melnikov, C. Stamm, T. Kachel, N. Pontius, M. Sultan, C. Gahl, M. Weinelt, H. A. Duerr, and U. Bovensiepen, Phys. Rev. Lett. **106**, 127401 (2011).
[14] B. Koopmans, G. Malinowski, F. Dalla Longa, D. Steiauf, M. Faehnle, T. Roth, M. Cinchetti, and M. Aeschlimann, Nature Materials **9**, 259 (2010).
[15] G. M. Mueller, J. Walowski, M. Djordjevic*, et al*, Nature Materials **8**, 56 (2009).
[16] W. Hubner and K. H. Bennemann, Physical Review B **53**, 3422 (1996).
[17] G. M. Mueller, J. Walowski, M. Djordjevic*, et al*, Nature Materials **8**, 56 (2009).
[18] M. R. Freeman, J. Appl. Phys. **75**, 6194 (1994).
[19] M. Faehnle and C. Illg, Journal of Physics-Condensed Matter **23**, 493201 (2011).

Chapter 5

Laser-induced Demagnetization Dynamics in EuO probed by Magneto-Optics

5.1 Introduction

Whereas the previous chapter has been devoted to laser-induced demagnetization dynamics which was probed by time-resolved XMCD spectroscopy with a temporal resolution of about 50 ps (FWHM), in this chapter results are presented in which the magnetization dynamics was probed by short (<300fs) optical (1.55 eV or 3.10 eV) probe pulses. The improved time-resolution allows us to investigate the laser-induced *ultrafast* magnetization dynamics in EuO and Gd-doped EuO. In Chapter 3 an introduction into the field of magnetization dynamics has been given. Therefore for a general introduction, we refer to Chapter 3.

This chapter presents three experimental sections presenting different types of experiments. The first section discusses optical pump (1.55 eV)/ optical probe (1.55 eV) measurements on the same 6% Gd-doped EuO sample which was used in the time-resolved XMCD experiments. Since the experimental conditions (temperature/applied magnetic field) in both experiments (XMCD/optical probe) were similar, the results allow a direct comparison in order to address the question what is exactly being probed by the magneto-optical probe. The samples used in the XMCD experiments are grown on a rather wobbly Al foil substrate, causing undesired scattering of the optical pump and probe beams. Therefore, we used EuO samples grown on flat MgO substrates for more detailed time-resolved magneto-optical studies. The results of these studies are presented and discussed in the remainder of this chapter. The results show the presence of a large (~10%)

and fast (sub-picosecond) in-growing demagnetization component, in addition to the nanosecond 4*f* spin-lattice relaxation component. Since this fast component decays in tens of picoseconds, it is not surprising that this component has not been observed in XMCD with a time-resolution of 50 ps (ΔXMCD/XMCD). The first two sections focus on the dynamic magnetization processes in the high pump-fluence regime (>1 mJ/cm^2) showing always an optically induced *demagnetization*. In contrast, the last section shows that it is also possible to optically induce a dynamical *increase* of the magnetization in EuO, provided that experiments are performed in a low fluence regime (0.2 mJ/cm^2). Before presenting the experimental results, we first discuss what is exactly probed by magneto-optics in the NIR/VIS/UV range, and how the changes in the polarization state are measured.

5.2 Magneto-optical and XMCD signal analyses

5.2.1 Magneto-optics (NIR/Vis/UV range) compared to XMCD (M_5 edge)

Whereas it is well established that XMCD is a good probe for magnetism (angular momentum), time-resolved magneto-optical measurements may suffer from non-magnetic components [1]. In this section a comparison is made between both techniques in order to identify how magnetically clean the magneto-optical signal is. As was discussed in Chapter 2, we can assume that the magneto-optical signal in EuO (Eu^{2+} $4f^7$) is proportional to the magnetization resulting from the $4f^7$ magnetic moments; at least when the magnetic-field (or short-range order) dependent absorption edge shift is considered to be zero. The magneto-optical signal can therefore be expressed as

(5.1) M.O. signal = $a\,\vec{M}_{4f^7}$,

in which *a* is a proportionally constant. Now, the optical pump pulse cannot only change the $4f^7$ magnetization but also the proportionality constant:

(5.2) M.O. signal (t) = $a\,\vec{M}_{4f^7} + a\,\Delta\vec{M}_{4f^7}(t) + \Delta a(t)\,\vec{M}_{4f^7} + \Delta a(t)\,\Delta\vec{M}_{4f^7}(t)$.

The last term in Eq. (5.2) can be neglected when the pump-induced changes are small. From Eq. (5.2) we can see that the M.O. signal may contain magnetic and non-magnetic (N.M.) terms. The $\Delta a(t)\,\vec{M}_{4f^7}$ and $\Delta a(t)\Delta\vec{M}_{4f^7}$ components, we shall later on name $O_{N.M}$. For EuO, this is actually not the full story. As described in

Chapter 3, after photo-excitation (using 800 nm light pulses) Eu 5*d* electrons and Eu 4*f* holes (4f^6 moments) are created. We write the M.O. signal as a summation over different contributions:

(5.3) M.O. signal(t) = $a\,\vec{M}_{4f^7} + a\,\Delta\vec{M}_{4f^7}(t) + b\,\vec{M}_{4f^6}(t) + c\,\vec{M}_{5d^1}(t) + O_{N.M.}(t)$,

in which the third and fourth term represent pump-induced changes in the magnetization resulting from the valence band holes (4f^6) and the 5*d* conduction electrons, respectively; each of them with its own proportionality constant (*b* and *c*). These terms can be important in the high fluence regime. Based on the fact that the spin-orbit energy of the 5*d*-electrons is much smaller than the spin-orbit energy of the 4*f*-electrons [2] we anticipate:

(5.4) a, b >> c.

Because of this, and because of the fact that the major part of the magnetization is in the 4*f*-system ($\vec{M}_{4f} \gg \vec{M}_{5d}$, see Chapter 3), large changes in the M.O. signal should be ascribed to changes in the 4*f*-system, or to a possible non-magnetic component. Therefore, in this limit, we can write for the pump-induced changes in the M.O. signal:

(5.5) ΔM.O. signal(t) $\cong a\,\Delta\vec{M}_{4f^7}(t) + b\,\vec{M}_{4f^6}(t) + O_{N.M.}(t)$.

Now we can write for the relative changes in the rotation θ and ellipticity ε:

(5.6) $\Delta\theta/\theta \cong \frac{\Delta\vec{M}_{4f^7}(t)}{\vec{M}_{4f^7}} + \frac{b\,\vec{M}_{4f^6}(t)+O_{N.M.}(t)}{a\vec{M}_{4f^7}}$,

(5.7) $\Delta\varepsilon/\varepsilon \cong \frac{\Delta\vec{M}_{4f^7}(t)}{\vec{M}_{4f^7}} + \frac{d\,\vec{M}_{4f^6}(t)+O_{N.M.}(t)}{c\vec{M}_{4f^7}}$.

In which *a*,*b*,*c*, and *d* are proportionality constants and $O_{N.M.}(t)$ are the non-magnetic terms. We can see that Δθ/θ and Δε/ε can be nonequivalent when either $b/a \neq d/c$ or $O_{N.M.}/a \neq O_{N.M.}/c$. In the former case, the signal is of magnetic origin and rated to changes in $\vec{M}_{4f^6}(t)$. It is actually very reasonable to assume that $b/a \neq d/c$ based on the fact that the rotation and ellipticity spectra are different (but Kramers-Kronig related), see chapter 2. In the latter case $O_{N.M.}/a \neq O_{N.M.}/c$ meaning that the signal is of non-magnetic origin.

Now we want to compare the magneto-optical signal with the XMCD signal at the peak europium M_5 edge. As discussed in chapter 3, the integrated XMCD intensity at the M_5 edge can be written as:

$$XMCD_{M_5} = -\frac{3}{7} XAS_{M_5+M_4} \left(L_{4f^7} + \frac{2}{3} S_{4f^7}\right) - \frac{3}{8} XAS_{M_5+M_4} \left(L_{4f^6} + \frac{2}{3} S_{4f^6}\right). \quad (5.8)$$

In which *XAS* is the integrated X-ray absorption over both the M_5 and M_4 edge and *L* and *S* are the orbital and spin angular momenta, respectively. Also in this case we are not sensitive to the 5*d* magnetization; we are the M_5 edge (Eu 3*d* to Eu 4*f*). When we assume (based on Hund's rules) that the orbital momentum of the Eu^{2+} $4f^7$ moments is zero, we can write for the pump-induced changes of the XMCD and M.O. signal [3]:

$$\Delta XMCD_{M_5}(t) \cong \alpha\, \Delta S_{4f^7}(t) + \beta \left(\Delta L_{4f^6}(t) + \frac{2}{3}\Delta S_{4f^6}(t)\right), \quad (5.9)$$

$$\Delta\text{M.O. signal(t)} \cong a\, \Delta S_{4f^7}(t) + b \left(\Delta L_{4f^6}(t) + 2\Delta S_{4f^6}(t)\right) + O_{N.M.}(t), \quad (5.10)$$

where we used the fact that $\mu = (L + 2S)\mu_B$ (μ is the atomic magnetic moment). By comparing Eq. (5.9) and Eq. (5.10), we can see that in both measurements we are sensitive to angular momentum (projection) changes in the 4*f* system ($4f^7$ and $4f^6$). However in Eq. (5.9) there is also a (possible) non-magnetic component. We can also see that the *L* to *S* ratio is different for the $4f^6$ moments in both methods. Magneto-optics is more sensitive to the spin-angular momentum whereas XMCD at the M_5 edge is more sensitive to the orbital angular momentum. Next section focusses on the used magneto-optical experimental setup.

5.2.2 Polarization state analysis

In order to measure the magnetization dynamics in EuO, the change in polarization state upon reflection or transmission has to be measured. In our experiments the incoming light is linearly polarized. Because of magneto-optical effects, the polarization of the reflected or transmitted light is rotated with respect to the polarization of the incoming light. At wavelengths where the absorption in EuO is negligible, the transmitted light is linearly polarized while it is elliptical at wavelengths where there is absorption. The ellipticity is defined as the ratio of the minor to the major axis of the ellipse. The rotation is defined as the angle between the major axis of the ellipse and a reference direction, for instance the x-axis. The MO experiment can conveniently be described using the Jones formalism, in which we will use the ellipticity angle ψ, defined through $\varepsilon = \tan\psi$, to describe the

ellipticity ε. Elliptical light, with the main axes along the x- and y-direction, can be represented by the following Jones vector [4,5]:

(5.11) $$\begin{pmatrix} E_x \\ E_y \end{pmatrix} = \begin{pmatrix} cos\psi \\ i\ sin\psi \end{pmatrix},$$

where E_x and E_y are the electric field components of the light. In order to get the Jones vector of a rotated ellipse, the Jones vector needs to be multiplied by a rotation matrix. In this way the major axis of the ellipse is rotated by an angle θ:

(5.12) $$\begin{pmatrix} E_x \\ E_y \end{pmatrix} = \begin{pmatrix} cos\theta & -sin\theta \\ sin\theta & cos\theta \end{pmatrix} \begin{pmatrix} cos\psi \\ i\ sin\psi \end{pmatrix} = \begin{pmatrix} cos\theta\ cos\psi - i\ sin\theta\ sin\psi \\ sin\theta\ cos\psi + i\ cos\theta\ sin\psi \end{pmatrix}_{rotated\ ellipse}.$$

The experiential configuration for the rotation measurements is shown in Fig. 5.1. Before the sample, the incoming light is linearly polarized (ψ=0) and has a polarization angle θ=C_θ. After passing through the sample, the polarization is rotated (θ=C_θ+δ_θ) and the light has become elliptically polarized (ψ=δ_ψ) due to the magneto optical effects. The measured magneto-optical rotation (δ_θ) and ellipticity (δ_ψ) angles are small in our case, maximally a few degrees. After the sample, the light passes a birefringent phase retarder, a Half Wave Plate (HWP). The optical axis (angle α) of the HWP is set in such a way that the major axis of the ellipse becomes θ=45 degrees. When C_θ=0, the HWP needs to set to α=22.5 degrees. After the HWP, the light passes a Wollaston prism (WP) which splits the beam in two beams which have orthogonal polarization.

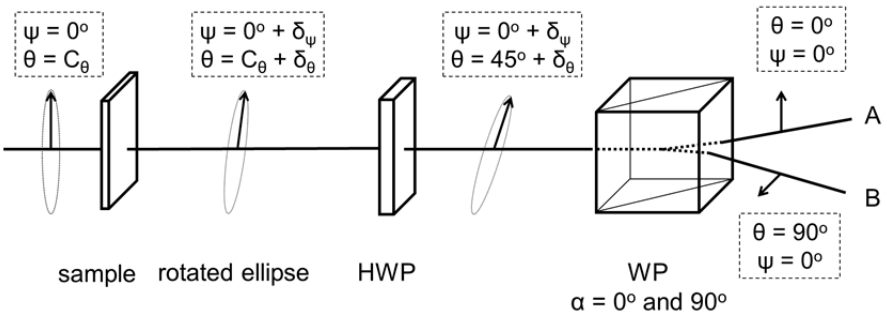

Figure 5.1 | Experimental configuration for the rotation measurements. The polarization state at every point is described by the rotation and ellipticity angle, θ and ψ respectively. HWP and WP stand for half wave plate and Wollaston prism respectively.

The optical axis of the two prisms in the WP are orthogonal to each other but are both perpendicular to the wave-vector of the incoming beam (when the angle of incidence is 0 degrees). In our case, a α=90/0 degrees configuration is used for the

WP. Beams A (x-polarized) and B (y-polarized) are detected by photodiode A and B respectively. The action of the HWP and WP on the polarization state can be described by Jones matrices [4,5]. For the case C_θ=0, the electric field of the x-polarized beam (A) after the WP is:

(5.13) $$\begin{pmatrix} E_x \\ E_y \end{pmatrix}_{detector\ A} \propto WP_{\alpha=\frac{\pi}{2}/0}\, HWP_{\alpha=\frac{\pi}{8}} \begin{pmatrix} E_x \\ E_y \end{pmatrix}_{rotated\ ellipse\ before\ HWP},$$

(5.14) $$\begin{pmatrix} E_x \\ E_y \end{pmatrix}_{A} \propto \begin{pmatrix} 1 & 0 \\ 0 & 0 \end{pmatrix} \begin{pmatrix} 1 & -1 \\ -1 & -1 \end{pmatrix} \begin{pmatrix} cos\theta\ cos\psi - i\ sin\theta\ sin\psi \\ sin\theta\ cos\psi + i\ cos\theta\ sin\psi \end{pmatrix}.$$

The intensity on photodiode A can be calculated using:

(5.15) $$I_A = E_{x,A}E^*_{x,A} + E_{y,A}E^*_{y,A}.$$

The same can be done for beam B:

(5.16) $$\begin{pmatrix} E_x \\ E_y \end{pmatrix}_{B} \propto \begin{pmatrix} 0 & 0 \\ 0 & 1 \end{pmatrix} \begin{pmatrix} 1 & -1 \\ -1 & -1 \end{pmatrix} \begin{pmatrix} cos\theta\ cos\psi - i\ sin\theta\ sin\psi \\ sin\theta\ cos\psi + i\ cos\theta\ sin\psi \end{pmatrix}.$$

Now it can be shown that:

(5.17) $$\frac{I_A - I_B}{I_A + I_B} = sin2\theta\ cos2\psi \cong 2\theta(1 - 2\psi^2) \cong 2\theta.$$

In this way, to first order, we are linearly proportional to the rotation angle. But when the ellipticity is large, there is also a contribution from the ellipticity. The ellipticity is measured in a different way, as is shown in Figure 5.2. Again, before the sample the incoming light is linearly polarized (ψ=0, θ=C_θ) and because of magneto-optical effects, the polarization state becomes θ=C_θ+δ_θ, ψ=δ_ψ. A HWP rotates the major axis of the ellipse in such a way that it coincides with the x-axis. After that, a Quarter Wave Plate (QWP), in which the optical axis makes an angle of α=45 degrees with respect to the x-axis, makes the light circularly polarized. In the case that C_θ=0, the electric field of beam A becomes:

(5.18) $$\begin{pmatrix} E_x \\ E_y \end{pmatrix}_{detector\ A} \propto WP_{\alpha=\frac{\pi}{2}/0}\, QWP_{\alpha=\frac{\pi}{4}} \begin{pmatrix} E_x \\ E_y \end{pmatrix}_{rotated\ ellipse\ before\ QWP},$$

(5.19) $$\begin{pmatrix} E_x \\ E_y \end{pmatrix}_{A} \propto \begin{pmatrix} 1 & 0 \\ 0 & 0 \end{pmatrix} \begin{pmatrix} 1 & i \\ i & 1 \end{pmatrix} \begin{pmatrix} cos\theta\ cos\psi - i\ sin\theta\ sin\psi \\ sin\theta\ cos\psi + i\ cos\theta\ sin\psi \end{pmatrix}.$$

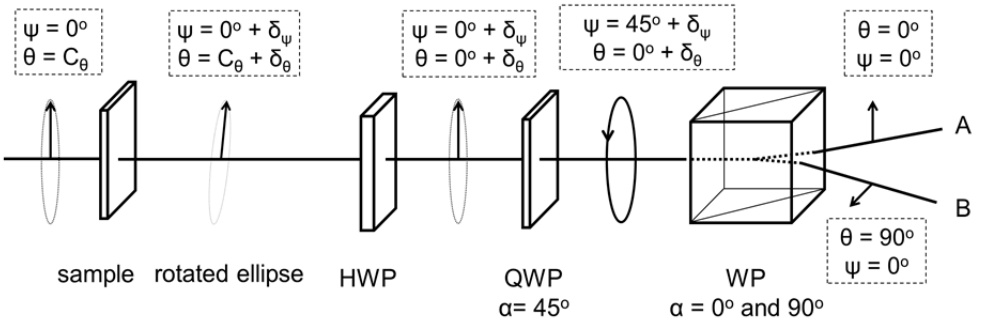

Figure 5.2 | Experimental configuration for the ellipticity angle measurements. The polarization state at every point is described by the rotation and ellipticity angle, θ and ψ respectively. QWP and WP stand for quarter wave plate and Wollaston prism respectively.

The same can be done for beam B after which it can be shown that:

(5.20) $\frac{I_A - I_B}{I_A + I_B} = sin2\psi \cong 2\psi \cong 2\varepsilon.$

To first order, we are linearly proportional to the ellipticity angle and therefore also to the ellipticity. In order to measure linear magneto-optical effects (θ_{MO}, ψ_{MO}) in EuO, I_A-I_B and I_B are measured from which I_A+I_B can be constructed. I_A-I_B and I_A+I_B are named D (difference) and S (sum) respectively. Both are measured at positive (+) and negative (-) applied magnetic field. The linear magneto-optical effects are calculated as follows:

(5.21) $\theta_{MO}(M) \equiv \theta(\vec{M}) - \theta(-\vec{M}) = \frac{D^+}{2S^+} - \frac{D^-}{2S^-},$

(5.22) $\psi_{MO}(M) \equiv \psi_{MO}(\vec{M}) - \psi_{MO}(-\vec{M}) = \frac{D^+}{2S^+} - \frac{D^-}{2S^-}.$

If the transmittance or reflectance is magnetic field independent (S^+=S^-=S), which is usually the case, this can be rewritten to:

(5.23) $\theta_{MO}(M) = \frac{D^+ - D^-}{2S}.$

In the pump-probe experiments, the pump can induce changes in the magneto-optical signal: *D* and *S* can change to *D*+*ΔD* and *S*+*ΔS,* respectively. If one assumes that the transmittance or reflectance is magnetic field independent, the pump-induced change in the rotation can be written as:

(5.24) $\Delta\theta_{MO}(M) \equiv \Delta\theta(\vec{M}) - \Delta\theta(-\vec{M}) = \left(\frac{\Delta D^+ - \Delta D^-}{2(S+\Delta S)}\right) + \left(\frac{D^+ - D^-}{2(S+\Delta S)} - \frac{D^+ - D^-}{2S}\right).$

From which we can see that when the changes in the reflection or transmission are large, we have to correct for this in order to get the right *magneto-optical* rotation. For the relative pump-induced changes we can write (in the case that $D^+ - D^- \neq 0$):

(5.25) $\frac{\Delta\theta_{MO}(M)}{\theta_{MO}(M)} = \frac{1}{1+\frac{\Delta S}{S}}\left(\frac{\Delta D^+ - \Delta D^-}{D^+ - D^-} - \frac{\Delta S}{S}\right)$.

In the last term in Eq. (5.25), $\Delta S/S$ represents the transient reflectance ($\Delta R/R$) or transmittance ($\Delta T/T$).

5.3 Nanosecond 4*f* spin-lattice relaxation probed by magneto-optics

5.3.1 Experimental setup

For the pump-probe experiments, an amplified Ti:sapphire laser system was used providing pulses with a wavelength of 800 nm and a pulse duration (FWHM) of about 150 fs at a repetition rate of 1 kHz. Weak p-polarized probe pulses where focused on the sample after which the polarization state (rotation/ellipticity) of the reflected probe pulses was analyzed, see for more details the next section. The sample was placed in a cryostat in which the sample was in contact with cold helium gas. The cryostat in turn was placed in between the poles of an electromagnet. The orientation of the sample is such that the angle between the surface normal of the film and the applied magnetic field is 45^0. The angle of incidence is 45^0 whereas the wave vector of the incident probe beam is parallel to the applied magnetic field; see Fig. 5.3.

The wavelength of the intense linearly polarized pump pulses is 800 nm. The polarization angle of the pump-pulses could be changed by a HWP. The pump-probe pulse delay was set by a mechanical delay line which was on the pump arm. The pump beam was chopped at 500 Hz by a laser-synchronized optical chopper after which the pump pulse-induced changes of the probe pulse intensity and polarization state were detected at a frequency of 500 Hz using a lock-in amplifier referenced to the optical chopper.

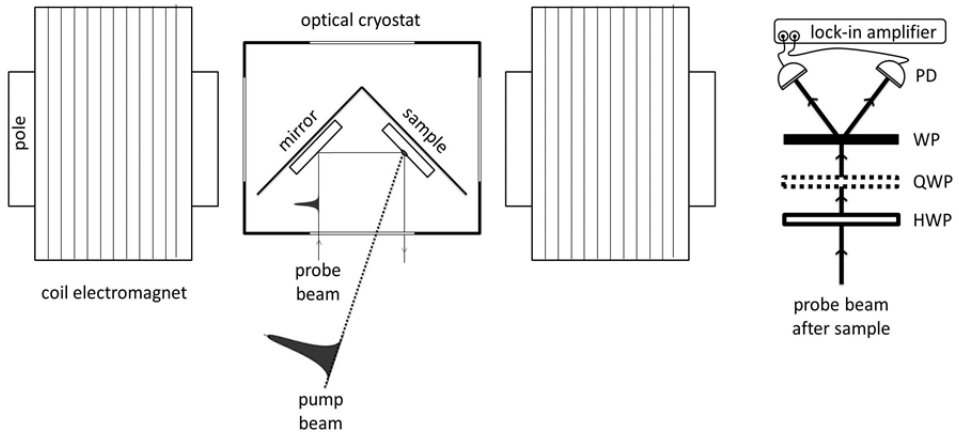

Figure 5.3 | Experimental setup for magneto optical pump probe spectroscopy. For details, see text.

5.3.2 Sample characterization

We performed magneto-optical Kerr effect (MOKE) measurements on the 6% Gd-doped EuO sample (20 nm $Eu_{0.94}Gd_{0.06}O$, grown on a 500 nm thick Al substrate, the Al capping layer is about 3 nm thick, see the previous chapter for more information) at a wavelength of 800 nm. Kerr rotation hysteresis loops at 25 K and 65 K are shown in the left panel of Fig. 5.4.

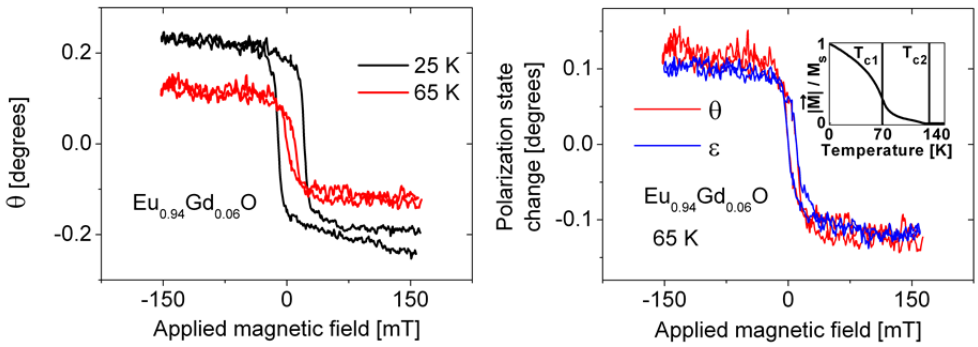

Figure 5.4 | Kerr rotation and ellipticity hysteresis loops for the 6% Gd-doped sample measured at a wavelength of 800 nm. Left panel: Kerr rotation for different temperatures; Right panel: Kerr rotation and Kerr ellipticity at *T*=65K. The inset in the right panel shows the reduced magnetization versus temperature as measured by SQUID magnetometry in an applied magnetic field of 1000 Gauss.

The magnitude of the Kerr rotation signal as well as the coercivity is decreasing with temperature, as expected. The coercivity at 25 K is about 30 mT, whereas the coercivity decreases at 65 K to about 10 mT.
Apart from the rotation, also the Kerr ellipticity has been measured at 65 K, see the right panel of Fig. 5.4. As one can see the rotation and ellipticity hysteresis loops are very similar in size and hysteresis shape. In the inset of the figure, the reduced magnetization versus temperature is shown as measured by SQUID magnetometry in an applied magnetic field of 1000 Gauss. Two ordering temperatures were identified, T_{c1} and T_{c2}. Whereas the first one represents the ferromagnetic ordering of pure EuO, the second was interpret as the ferromagnetic ordering of the Gd-moments and its nearest-neighbors [6,7]. Due to the additional 5*d* electron of Gd, the nearest–neighbor exchange interaction is enhanced. The XMCD and MOKE measurements have been performed at about 65 K, just below T_{c1}.

5.3.3 Results

The time-resolved magneto-optical (MO) measurements at 65 K on the 6% Gd-doped EuO films are shown in Fig. 5.5. The probe wavelength was 800 nm while the applied magnetic field is ±130 mT. The pump fluence is 6.2 mJ/cm^2. At this applied magnetic field, the magnetization is close to saturation and the magnetization vector lies in the film plane. The relative change in the MO rotation and ellipticity was calculated using Eq. (5.25). In the lower right panel of Fig. 5.5, the MO rotation is compared with the time-resolved XMCD measurements (M_5 edge, time-resolution FWHM=51 ps) on the same sample, at roughly the same temperature. The pump wavelength was 800 nm (4*f* to 5*d* transition) in all cases.

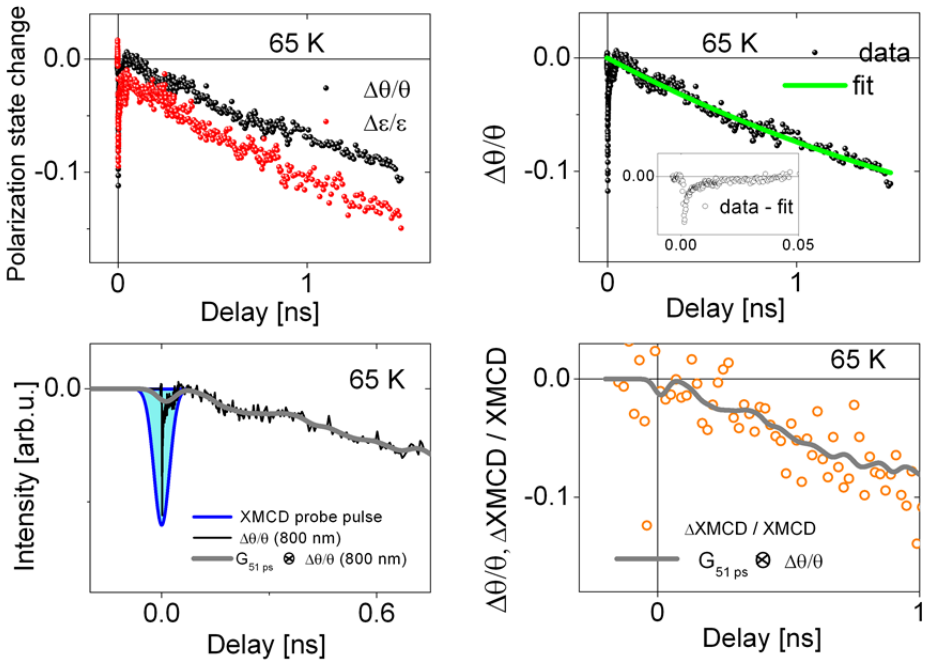

Figure 5.5 | Comparison of the pump (800nm)-probe measurements at 65 K and ±130 mT using different probes. Upper left: pump-induced changes in the MO rotation and ellipticity at a probe wavelength of 800 nm. Upper right: fit of the slow (nanosecond) component in the MO rotation. The inset shows the fit residuals. Lower left panel: Un-convoluted and convoluted MO rotation data. The convolution was done with a Gaussian (FWHM=51.3 ps) which represents the temporal resolution of the time-resolved XMCD setup. Lower right panel: XMCD (M_5-edge) probe experiments compared with the convoluted MO rotation experiments.

In the upper left panel of Fig. 5.5, the Kerr rotation and ellipticity are shown. Although both signals are not identical, they are very similar in magnitude and behavior. At negative delays, the pump-induced signal is zero, indicating that the film which is in direct contact with cold helium gas, has completely cooled down within 1 ms (repetition rate = 1 kHz). After the pump pulse hits the sample, there is an exponentially in-growing negative signal with a picosecond time constant (τ_1= 0.6±0.1 ps). After that the signal is increasing exponentially (τ_2= 6.9±1.3 ps) and approaches zero around 50 ps. Subsequently, the negative signal is growing again. When in the 100-1400 ps range, the nanosecond component in the MO rotation is fitted (right upper panel Fig. 5.5) with an in-growing exponential, we obtain a time constant of τ_3= 2.5±0.02 ns while the (demagnetization) amplitude is -0.12±0.01. When this component is subtracted from the MO rotation signal, we obtain a graph

which is shown as an inset in the upper right panel of Fig. 5.5. In the lower panels the MO rotation is compared with time-resolved XMCD measurements (see Chapter3). Since the temporal resolution in the XMCD measurements was 51 ps (FWHM), the MO rotation is convoluted with a Gaussian having FWHM=51 ps. We obtain the grey curve in the left lower panel of Fig. 5.5 while the blue line/area represents the Gaussian. Due the fast time constants (τ_1 and τ_2), the large peak at about 1 ps is much less visible in the convoluted data.
In the lower right panel, the convoluted MO rotation is compared with the time-resolved XMCD data, taken at similar fluence and temperature. With our XMCD time-resolution and signal to noise ratio it is apparently not possible to observe the ultrafast negative peak in the XMCD data. Therefore, the comparison to XCMD data does not allow for conclusive statement on the magnetic or non-magnetic origin of the fast component in the magneto-optical data. We will return to this issue in the discussion section, later on.

5.3.4 Conclusion

Based on the comparison between the MO experiments and the XMCD data we can conclude that the MO signal at longer timescales (ns) is predominantly magnetic in origin and reflects the nanosecond 4*f*-spin-lattice relaxation component previously observed in the XMCD experiments. To get a better understanding of the early time magnetization dynamics, and the processes responsible for them, the remainder of this chapter focusses on the ultrafast MO response of EuO.

5.4 *Ultrafast* 4*f* spin-lattice relaxation in EuO

5.4.1 Experimental setup and configuration

The experiments described in this section were performed on a setup similar as the one described in the previous section. The pump wavelength is 800 nm while the probe beam is frequency doubled in BBO (second harmonic generation) to 400 nm; the probe beam photon energy is higher than the pump beam photon energy, see also Fig. 5.6. We used this configuration ($\omega_{probe} > \omega_{pump}$) in order to reduce the possibility of non-magnetic effects (due to for instance state filling effects) in the pump-induced rotation or ellipticity signal, see Eq. (5.10). Both initial (4*f*) and final state (5*d*) filling effects can give rise to non-magnetic contributions [1]. By choosing the energy of the probe that is much higher than the energy of the pump, we

anticipate that the (non-magnetic) 5*d*-final-state filling effect signal is much smaller. An additional advantage of choosing different pump and probe wavelengths is that we can easily reduce the size of the signal coming from pump-light scattering: by placing a colored glass filter in front of the photo-detectors the pump beam was blocked while the probe beam was transmitted.

The penetration depth, (defined as 1/α, where α is the absorption coefficient), is about 150 nm for both the pump and the probe beam, indicating that the same volume is pumped and probed. Within a film of 50 nm, about 28% of the pump light is absorbed (1-exp[-α·d]).

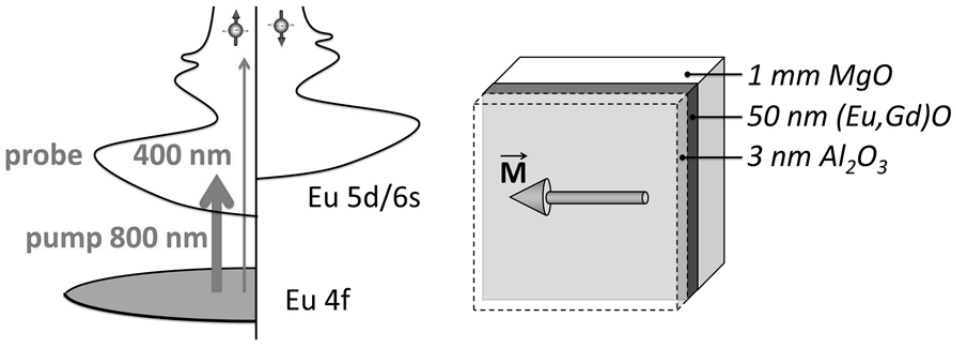

Figure 5.6 | Left: spin-dependent density of states of EuO at T=0K. The vertical arrows represent the pump and probe energy. Right: Gd-doped EuO sample grown on MgO and protected from oxidation by an Al_2O_3 capping layer. The thin (Eu,Gd)O film has an in-plane magnetic anisotropy. For a magnetic field of B≤90 mT applied at an angle of 45 degrees with respect to the surface normal, the magnetization vector is in-plane with a negligible out-of-plane component.

A cross correlation of the pump and probe beam yields a temporal resolution of $447/\sqrt{2} = 316$ fs (FWHM). The angel of incidence (AOI) of the probe beam on the sample is 45 degrees, see the inset of Fig. 5.7, and the AOI of the pump is 57 degrees. The wave vector of the probe is perpendicular to the applied magnetic field (see the left panel of Fig. 5.1) while the angle between the surface normal of the films and the applied magnetic field is 45 degrees. In contrast to the previously described MO experiments, here the intensity and polarization state of the *transmitted* probe beam is monitored in order to probe the sample's magnetization dynamics. The experiments where performed in the (nearly fully) ordered ferromagnetic phase at a temperature of 25 K in relatively small applied magnetic fields, B≤90 mT. For a magnetic field of B≤90 mT applied at an angle of 45 degrees

with respect to the surface normal, the magnetization vector is mostly in-plane with a negligible out-of-plane component, as we will see in the next section.

5.4.2 Sample characterization

A hysteresis loop for a p-polarized probe beam (400 nm) at 25 K is shown in Fig. 5.7. The grey lines are a guide for the eye.

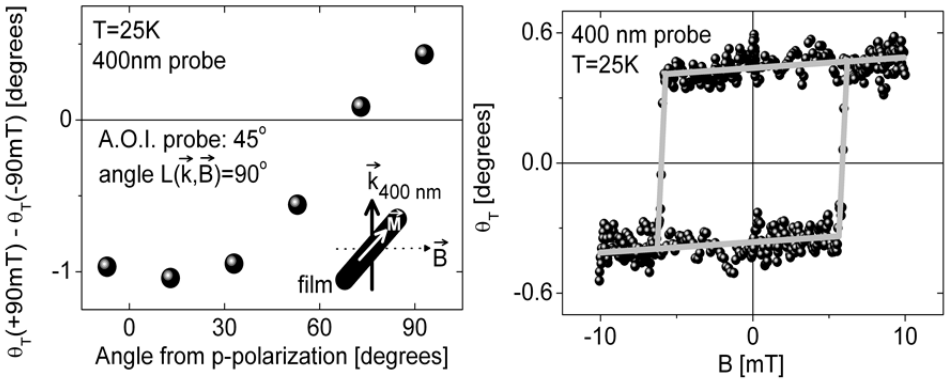

Figure 5.7 | Left panel: probe (400nm) polarization dependence of the MO rotation measured in transmission at 25K in an applied magnetic field of 90 mT. The inset shows the used configuration. The A.O.I. was 45 degrees, the wave vector ($\vec{k}_{400\,nm}$) of the incoming probe beam is orthogonal to the applied magnetic field. The thick black line represents the sample. The angle between the surface normal and the applied magnetic field is 45 degrees. The magnetization at 90 mT is (almost) in the sample-plane due to the large in-plane anisotropy of the film. Right panel: MO rotation of the transmitted probe (400nm) beam at 25K for a p-polarized probe beam. The grey lines are a guide for the eyes.

The hysteresis loop shows a step-like behavior with a small linear component. The sample has an in-plane magnetic anisotropy and the hysteresis shape suggests a coherent magnetization vector rotation within the sample plane [8]. Since the remanence is almost the same as the saturation magnetization, the sample behaves effectively as a single domain particle and no domain wall effects are observed [9]. The in-plane component of the applied magnetic field is large enough to switch the magnetization whereas the perpendicular component of the applied magnetic field is not large enough to create a considerable out-of-plane component, as we can see form the hysteresis shape. The coercivity is about 6.5 mT.

The left panel of Fig. 5.7 shows the saturation magnetization (at 90 mT) versus probe polarization angle. Since the Faraday rotation in the bulk of the EuO film is

proportional to $\vec{k}_{400\,nm} \cdot \vec{M}$ [5,10], where $\vec{k}_{400\,nm}$ is the wavevector of the refracted probe beam, one would not expect a polarization dependence, in contrast to what is observed. This indicates that the main contribution of the rotation is coming from magneto-optical Kerr reflection and transmission Fresnel coefficients, which is not surprising because the AOI is 45 degrees. This means that we are most sensitive the EuO/MgO and EuO/Al_2O_3 interface (surface) and less to the "bulk" of the sample. We get a maximum MO rotation for a polarization which is close to p-polarization. In all the pump-probe experiments we therefore used a p-polarized probe beam.

5.4.3 Results: the pump-induced dynamics of the rotation and ellipticity

The pump-induced changes in the magneto-optical rotation and ellipticity (defined by Eq. 5.18) versus pump-probe delay (τ) are shown in Fig. 5.8: T=25K, B=±10 mT, pump= 800nm, probe =400 nm, pump fluence= 5.3 mJ/cm^2.The signals can be divided in different zones. The first three zones are shown in the upper left panel while the fourth and fifth zone are presented in the upper right and lower left panel, respectively. We define the zones as follows:

1. The signal at negative delays (τ<0). The probe arrives before the pump and probes the effect of the previous pump pulse, 1 ms before. The signal at τ=-2 ps is zero indicating that there is no long-lived electronic effect or thermal signal.
2. The positive peak occurring during pump-probe overlap (τ≈0).
3. The sub-picosecond decrease (τ=0-2 ps) of the MO signal.
4. The subsequent picosecond (2-50 ps) increase of the MO signal.
5. And finally the nanosecond decrease (50-750 ps) of the MO signal.

In the following we will describe zone 2-5 in detail, starting from the pump-induced signal at pump-probe overlap.

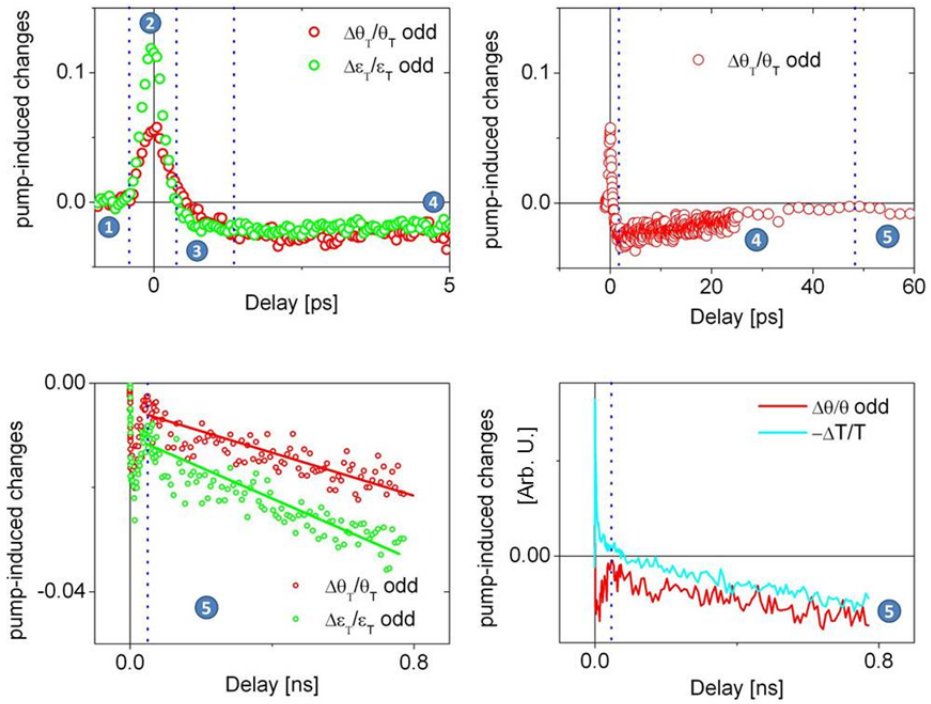

Figure 5.8 | Pump induced changes in the transmitted intensity and polarization state of the probe beam (400nm) after an intense pump pulse (800 nm, 4*f* to 5*d*). Upper panels and lower left panel: pump-induced changes of the MO rotation and ellipticity for different pump-probe delays. Lower right: Δθ/θ en -ΔT/T signals in arbitrary units. Both signals have a slow nanosecond component.

5.4.4 Results: Pump-probe overlap (zone 2)

In order to identify where the signal at pump-probe overlap comes from, we performed pump-polarization dependent measurements in zero applied magnetic field at 25 K. The probe is p-polarized while the AOI is 45 degrees. The results are shown in Fig. 5.9. We have observed that the sign and magnitude of the signal is pump polarization dependent. The amplitude of the signal at τ=0 is plotted in the right panel of Fig. 5.9. The behavior is sinusoidal with maxima at ± 45 degrees.

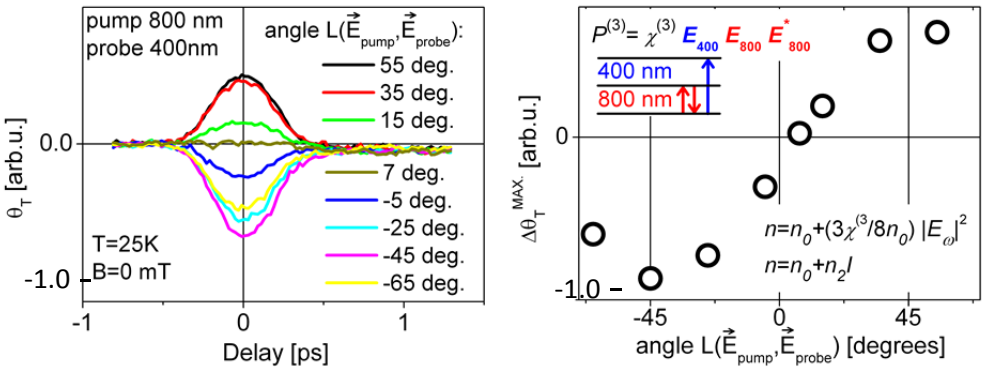

Figure 5.9 | Left panel: pump-polarization dependence of the rotation of polarization of the probe (θ_T) at B=0 mT, T= 25K. Right panel: The amplitude of θ_T at τ=0 ps. The origin of the observed effect is explained in terms of the electro-optical Kerr effect, see inset. $\chi^{(3)}$ is the third-order susceptibility. n_0 and n_2 are the linear and nonlinear components to the refractive index.

The origin of the observed effect is explained in terms of the ac electro-optical Kerr effect (EOKE), which is a $\chi^{(3)}$ process [11]. We can obtain a third order polarization at ω=h c/400nm by considering three interacting electric fields: the electric field of the pump, the complex conjugate of the electric field of the pump and the electric field of the probe beam.

(5.26) $$P^{(3)}(400\,nm) = \chi^{(3)} E_{400\,nm} E_{800\,nm} E_{800\,nm}{}^{*}.$$

The transitions at 800 nm and 400 nm are resonant in EuO. In the ac EOKE, the pump-beam (800 nm) modulates the refractive index at 400 nm. In this case we can write for the refractive index [11]:

(5.27) $$n = n_0 + \left(\frac{3\chi^{(3)}}{8n_0}\right)|E_\omega|^2 = n_0 + n_2 I_{pump},$$

in which n_0 and n_2 are the linear and nonlinear components to the refractive index, respectively, and I_{pump} is the pump intensity. The pump-induced birefringence causes the polarization of the 400 nm probe beam to rotate. The EOKE provides a good measurement of the pump-probe cross correlation in the sample. The FWHM of the cross correlation is 447 fs.

The normal EOKE is not sensitive to an applied magnetic field and is therefore even in B. However we have also seen a component in the rotation which is odd in B. In order to identify this component, we made a pump-induced hysteresis loop at τ=0 ps for a p-polarized pump and probe beam. The result is shown in Fig. 5.10.

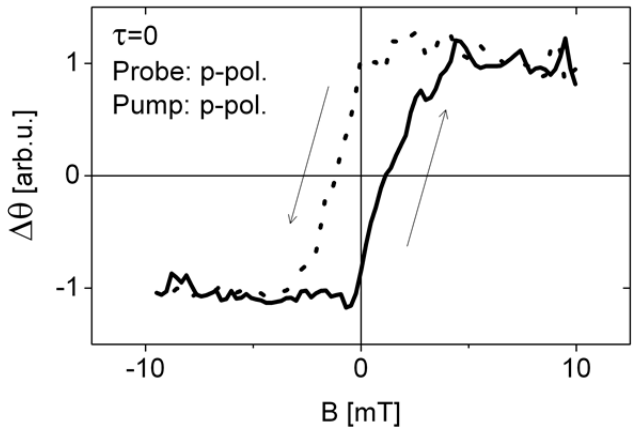

Figure 5.10 | Pump-induced change in the rotation versus the applied magnetic field (B). T=25K. The full line represents the curve for up going fields whereas the dotted line is for down going fields.

From Fig. 5.10 we can see that the there is a pump-induced component which is sensitive to the magnetization of EuO. The fact that there is hysteresis indicates that this component is really coming from the EuO film and not from the MgO substrate. For a detailed discussion on the pump-induced hysteresis loops we refer to the end of this chapter.

Pump-probe transients in the [-1,+4] ps range in an applied magnetic field of 10 mT are shown in Fig. 5.11. The component of rotation which is even in the applied magnetic field $(\Delta\theta_{even}/\theta_{even})$ is compared with the pump-induced changes in the transmittance; see the left panel of Fig. 5.11. The data is scaled to the minimum value (and normalized to -1). The $\Delta\theta_{even}/\theta_{even}$ signal consists of a negative peak at overlap and slower picosecond decaying component. The negative peak is fitted with a Gaussian (FWHM=447 fs), see the red curve. When we integrate the Gaussian, we obtain an error like function: $\mathrm{erf}(\tau) \equiv -1/2\left(1/2 + \int_{-3\ ps}^{\tau} G(\tau)d\tau\right)$, see the black line. When this function is compared with the changes in the transmittance, we can see that the ingrowth of the $\Delta T/T$ signal is proportional to the amount of photo-excited carriers, see Chapter 6 for more information. The signal appears to be instantaneous within our time-resolution.

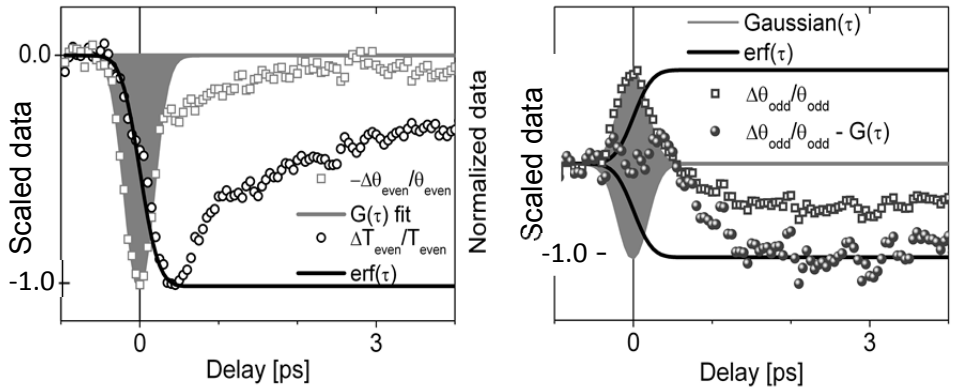

Figure 5.11 | Left: scaled components of $\Delta\theta_{even}/\theta_{even}$ (squares) and $\Delta T/T$ (circles) which are even in the magnetic field. T=25 K, B=10 mT. The area represent the Gaussian (G(τ)) fit of $\Delta\theta_{even}/\theta_{even}$ during pump-probe overlap whereas the black line is the integrated Gaussian: $\mathrm{erf}(\tau) \equiv -1/2\left(1/2 + \int_{-3\ ps}^{\tau} G(\tau)d\tau\right)$. Right: odd component of θ. $\Delta\theta_{odd}/\theta_{odd}$ (squares) scaled to the maximum of G(τ) and $\Delta\theta_{odd}/\theta_{odd} - G(\tau)$ is scaled to the level at 3 ps.

The component of the rotation which is odd in the applied magnetic field $(\Delta\theta_{odd}/\theta_{odd})$ is plotted in the left panel of Fig. 5.11. The contribution to the signal around zero delay has the same characteristics as the non-magnetic component observed in the experiments at 0 mT. The question now is whether the pump induced changes around τ=0 originate from a change in the magnetization or from non-magnetic changes in the refractive index, see Eq. (5.8). Based on the following two arguments, we attribute the signal to the presence of a non-magnetic component:

- The MO rotation and ellipticity are in-equivalent, see Fig. 5.8. The relation $\Delta\theta/\theta \sim \Delta\epsilon/\varepsilon \sim \Delta M/M$ does not hold which means that there are changes in the magneto-optical proportionality constants [1].
- EuO at T=25 K is (almost) in the fully ordered ferromagnetic state. It is therefore not possible to get a substantial increase in the magnetization. The fact that the sign is positive, and the magnitude is large (up to about 50% at τ=0 at a fluence of 20 mJ/cm^2), shows that most, if not all, of the signal is non-magnetic.

5.4.5 Results: Dynamics during the first few picoseconds (zone 3)

Before we discuss the MO response in the first few picoseconds we return to the observed changes in the transmission (see Fig. 5.8, lower left panel). We saw that

$\Delta T/T$ is proportional to the amount of photo-excited carriers. The question now is where the ultrafast ΔT/T signal originates from. One candidate one usually has to consider is state-filling: when (due to pump excitation) the amount of final states is reduced, the absorption is also reduced. This will in turn lead to an increase in the transmission. Since we observed a negative $\Delta T/T$ signal, this picture is not consistent with the measurements as expected since our probe energy is substantially higher than the pump energy. Another candidate that we have to consider is the response from the free electrons after pump-excitation. To do so, we calculate the pump-induced changes in the transmission. The static dielectric function at 400 nm is $\varepsilon(400\ \mathrm{nm}) = 3.3 + 0.8i$ [2]. The free electron response can be calculated in the Drude model. We consider the effective mass to be the same as the mass for a free electron (m_e). $\Delta T/T$ can then be calculated as follows [12]:

(5.28) $$\varepsilon(400\ \mathrm{nm}) + \Delta\epsilon(400\ \mathrm{nm}) = 3.3 + 0.8i - \frac{N e^2}{\epsilon_0 m_e} \frac{1}{\omega^2 + i\frac{\omega}{\tau_e}}$$

(5.29) $$\frac{\Delta T}{T} = \frac{T\left(\varepsilon(400\ \mathrm{nm}) + \Delta\epsilon(400\ \mathrm{nm})\right) - T(\varepsilon(400\ \mathrm{nm}))}{T(\varepsilon(400\ \mathrm{nm}))}$$

In which τ_e is the scattering time and N is the photo-induced free electron concentration. For the calculation of $\Delta T/T$ we considered the sample structure shown in Fig. 5.6. The reflective index of MgO at 400 nm was taken to be 1.76. A calculation of $\Delta T/T$ for different scattering times is shown in Fig. 5.12. The grey area represents the experimental scattering times which has been found for different sample (stoichiometric and Eu-rich EuO) and different temperatures (4K and 298K) [13]. As we can see from the figure, there is no strong scattering time dependence in the grey area. We can also see that the sign is negative, like in the experimental data. Based on Fig. 5.12 we can make an estimate for the free electron concentration.

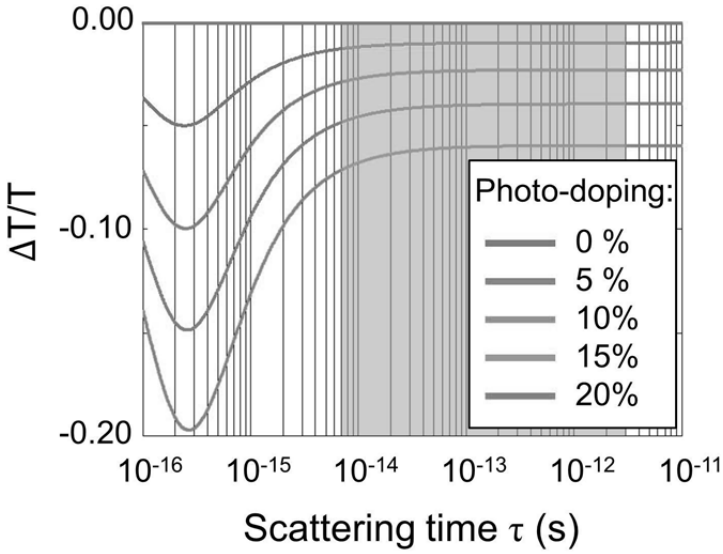

Figure 5.12 | Free electron scattering time dependence on Δ*T*/T(400 nm) for different free carrier (photo-doping) concentrations (upper curve is 0%, lower curve is 20%) for a sample structure as is shown in Fig. 5.6.

The maximum experimental amplitude of Δ*T*/*T* is about 1% for a fluence of 5.3 mJ/cm^2. Using τ=10^{-13} s, we find a free electron concentration of about 6.2%. From the absorption coefficient we estimate a photo-excitation of about 3.9%. Given the crudeness of the method, we consider this a good agreement. A more reliable way of getting information on the free carrier concentration can be obtained using THz probe pulses looking more directly at the Drude response. Optical-pump THz-probe experiments are presented in the next chapter of this thesis.

When the Δ*T*/*T* data is fitted by two exponentials and a constant (in the range of 0.5-25 ps), relaxation times of τ=510±70 fs and τ=4.6±0.3 ps were obtained. This multi-exponential decay can be partially be explained by a change in the number of *free* electrons by for instance trapping and/or recombination processes, but partially might also originate from magnetic-exciton formation, as we will discuss later on.

Now we return to the MO measurements. $\Delta\theta_{odd}/\theta_{odd}$ is plotted and compared with Δ*T*/*T* in Fig. 5.13. The red area corresponds to the Gaussian, the dashed blue line indicates the time delay of the maximum in -Δ*T*/*T*. -Δ*T*/*T* is vertically shifted to be able to compare the rise time of $\Delta\theta_{odd}/\theta_{odd}$ with the decay time in Δ*T*/*T*. From this we can see that both time-scales are comparable. It seems that $\Delta\theta_{odd}/\theta_{odd}$

starts to decrease after pump-probe overlap, at the maximum of -Δ*T*/*T*. However, very likely this component already starts before, but due to the large non-magnetic effects during pump-probe overlap, this component is not clearly visible.

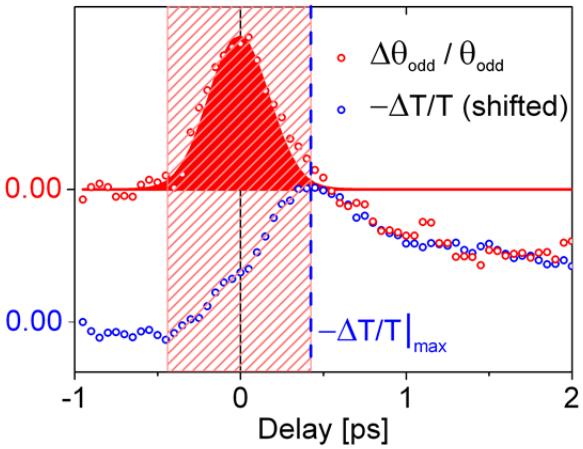

Figure 5.13 | A comparison of -Δ*T*/*T* and $\Delta\theta_{odd}/\theta_{odd}$ at T=25K. The red area corresponds to a Gaussian, the dashed blue line is the maximum in -Δ*T*/*T*. The hatched area corresponds to the region where there is pump-probe overlap. The *y*-axis zero-crossing for -Δ*T*/*T* and $\Delta\theta_{odd}/\theta_{odd}$ are shifted.

At the minimum (at about 2 ps), the MO signal has an amplitude of about -2.0%. In order to understand the origin behind this decrease, we consider three different magnetic sub-systems, see also Chapter 4. Before photo-excitation, the $4f^7$ europium atoms have a magnetic moment of gxS=2x3.5=7.0μ_B (7 aligned Eu 4*f* spins). Photo-excitation creates $4f^6$ valence band holes and 5*d* conduction electrons. The magnetic moment of the (ferromagnetically aligned) 5*d* conduction electron is 1μ_B (S=1/2). The $4f^6$ moment is: gxS=2x3.0=6.0μ_B (which is μ_{4f7}-μ_{5d1}).
At the used fluence, the relative amount of excited Eu atoms is N=3.9%. When we anticipate that the changes in the MO signal are due to a complete demagnetization of the $4f^6$ magnetic subsystem, we expect a reduction of the total magnetization of (6.0 μ_B/7 μ_B) x3.9%=3.4%. Here we assume that the magneto-optical proportionality constants *a* and *b* (in Eq. (5.3), $a = b$) are the same for the $4f^7$ and $4f^6$ magnetizations. These considerations indicate that it is possible that the 2% demagnetization observed during the first few picoseconds is due to a demagnetization of the $4f^6$ magnetic subsystem. Later on we will come back to this issue. We mentioned before (see also the introduction) that the 5*d* contribution is negligible.

5.4.6 Results: Dynamics during the first 50 ps and nanosecond dynamics (zone 4, 5)

Starting from about 2 ps, the magnetization is increasing and reaches a maximum at about 50 ps, see Fig. 5.8. Though the recovery dynamics is nearly equivalent for the MO rotation and the ellipticity, there are some minor differences indicating the presence of a small non-magnetic contribution to the MO signal, or indicating the presence of a significant contribution from the $4f^6$ moments. After the signal reaches a maximum at about 50 ps, it linearly decreases and reaches an amplitude of about 2% at a pump-probe delay of +750 ps. An important observation is that the amplitude at long delays (nanosecond) is larger than the initial demagnetization minimum, which is happening at the picosecond timescale.

5.4.7 Results: Pump power dependence

The pump-fluence dependence of the MO rotation at T=25K for different pump-probe delays is shown in Fig. 5.14. The green line represents the linear fit of the signal during pump-prove overlap. The blue line is the linear fit for +45 ps whereas the red line is the fit for +774 ps. The right panel of Fig. 5.14 shows the fluence dependence of the response at 774 ps over a wider fluence range (0-20 mJ/cm^2). Even in the high fluence regime, the demagnetization at +774 ps is linear in the fluence. Assuming that this is a thermal effect, we can conclude that even for high fluence, the absorbed power is linearly proportional to the pump-fluence; there is no pronounced two or three photon absorption. Therefore we conclude that although the pump-fluence was reasonably high, we were still in the linear regime.

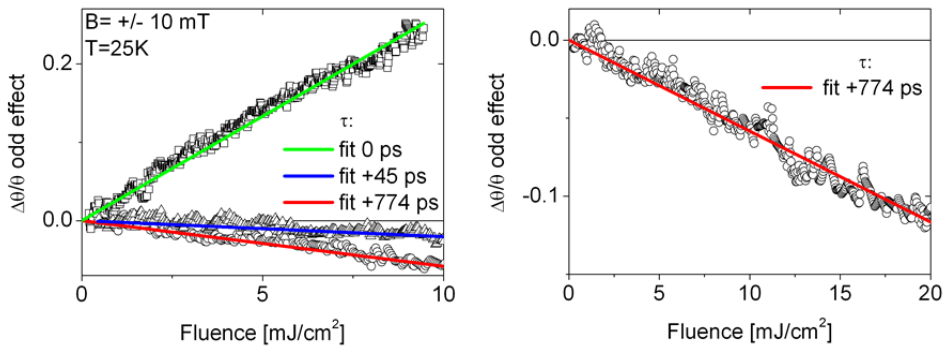

Figure 5.14 | Left: pump (800nm) fluence dependence of the MO rotation in the 0-10 mJ/cm^2 for different pump-probe delays. The colored lines represent linear fits. Right: in this graph the fluence dependence for τ=+774ps in the 0-20 mJ/cm^2 range is shown.

5.4.8 Results: Pump-induced changes in the magnetic hysteresis loop

More about the system can be learned from pump-induced hysteresis loops. The left panel of Fig. 5.15 shows a hysteresis loop at measured at *T* = 25 K when the pump beam is closed (red curve).

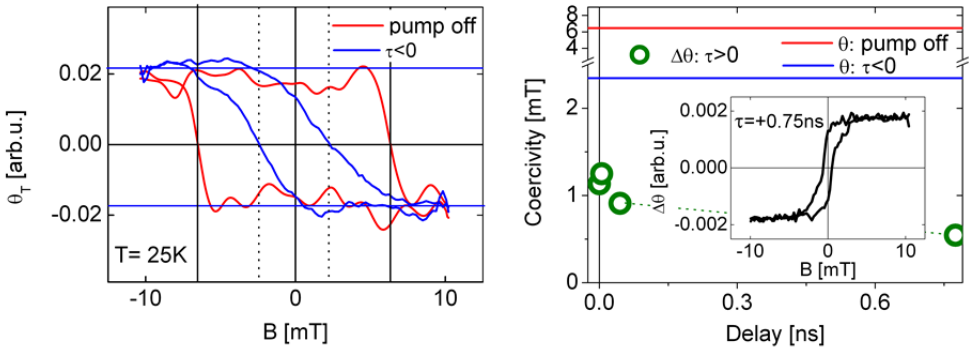

Figure 5.15 | Left: MO rotation (θ) with the pump closed (red) and pump open (blue) measured at the repetition rate of the probe beam (1 kHz) using a lock-in amplifier. The pump fluence is about 20 mJ/cm^2, T= 25K. Right: coercivity in the pump-induced rotation signal (Δθ, measured at the pump repetition rate; 500 Hz) versus pump-probe delay. The inset shows the Δθ hysteresis loop for a delay of +0.75 ns.

The curve has been measured using a lock-in amplifier referenced with the 1 KHz repetition rate signal (laser) of the probe beam. The blue line represents the signal (at 1000 Hz as well) for a pump fluence of 20 mJ/cm^2 at a delay of -25 ps. At -25 ps, the probe pulse arrives before the pump pulse. Or, at -25 ps, the probe beam arrives 2 ms after the previous pump pulse (the pump frequency is 500 Hz).

From a comparison between the pump-off saturation magnetization (B=±10 mT) and the pump-on saturation magnetization at τ<0, one can see that the pump pulse does not cause a substantial overall heating of the sample; the samples has cooled down within 2 ms.

The pump-induced changes in the remanence and coercivity during optical excitation are more difficult to understand but do provide interesting information about what is happening in the sample. In order to understand this, we have to consider the details of the pump-probe scheme; the measurements are done in a stroboscopic way [14,15]. In the upper graph in Fig. 5.16 we show, in a cartoonish way, how the heating/cooling down cycle looks like when the applied field is strong enough to saturate the magnetization. In this figure only the slow nanosecond demagnetization component has been drawn. After the arrival of the pump pulse,

the sample heats up and we observe a decrease in the magnetization at the spin-lattice relaxation timescale. After the magnetization reaches a minimum after a few nanoseconds (=> spin-lattice relaxation time), heat diffusion and other relaxation processes causes the sample to relax to the ground state. Before the next probe pulse arrives after 1 ms, the sample has already cooled down to the equilibrium temperature, as we can conclude by looking at the saturation magnetization. Even for a complete ultrafast demagnetization, the applied field causes the magnetic moments to re- align completely as the sample cools down, in a similar fashion to a field-cooled SQUID magnetization measurement.

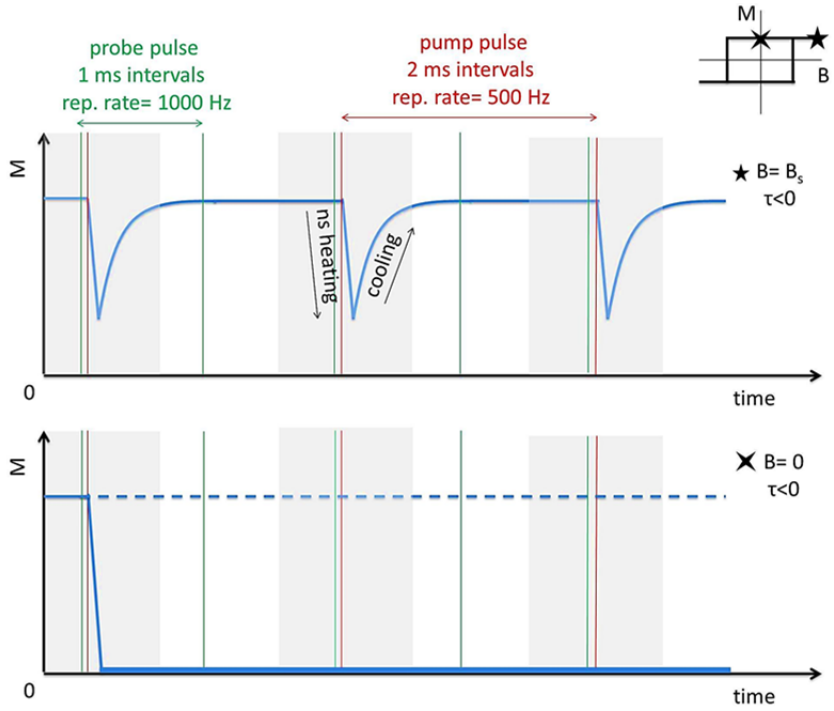

Figure 5.16 | Upper panel: *z*-component of the magnetization in a static applied magnetic field $B=B_{saturation}$. The red and green vertical line represents the timing of the pump and probe pulses respectively. The pump and probe repetition rate (rep. rate) is 500 Hz and 1000 Hz respectively. The pump probe delay is negative $\tau<0$. We only depict the pump-induced demagnetization and subsequent cooling of the sample. The gray areas indicate the time intervals where the optical chopper in the pump beam is open. In the upper right, a hysteresis loop is shown in which we define the saturation field (five-point star) and the remanence field (four-point star). Lower panel: pump-induced magnetization at remanence in the (hypothetical) case the demagnetization is 100%. After the first pulse, the magnetization remains zero.

The situation is different in zero applied field (B=0). In this case when there is a complete demagnetization, the sample cannot remagnetize since there is no field (B=M=0) to align the magnetic moments. This means that after the first pump pulse demagnetizes the sample the magnetization will remain zero indefinitely (Fig. 5.16, lower panel). In this case the measured remanence at 0 mT will be zero, unlike what we observe in Fig 5.15 (left). The fact that the measured remanence with pump pulse is almost the same as in the unexcited sample indicates that the demagnetization is not 100%, and that there are not a lot of irreversible magnetic domain boundary replacements during the demagnetization/ remagnetization cycle. If there would have been a large number of irreversible boundary replacements [9], we would have had observed a remanence (with pump on) which is much smaller than the remanence with the pump off (which is not the case).

We will now discuss the origin behind the pump-induced decrease of the coercivity. The coercivity is the magnitude of the negative applied magnetic field needed in order to completely quench the magnetization previously saturated by magnetic field in the opposite direction. When the magnetization is positive after it has been statured by a positive applied magnetic field, it will remain positive in a negative magnetic field larger than coercive field of -6.9 mT. When the pump-beam causes the coercivity to decrease, the magnetization can flip in a field larger than -6.9 mT. The coercivity in the case that the pump is on was found to be |2.3| mT. This means that somewhere in the heating/cooling cycle in our stroboscopic pump-probe measurements, the pump-induced coercivity is 2.3 mT. One requirement for this is that the time-duration that the coercivity is diminished, should be long enough to allow the magnetization to flip. A typical timescale for longitudinal magnetization switching is <200 ns, which is based on the Gilbert damping coefficients in ferromagnetic dielectrics (YIG) [16,17].

Assuming that the reduction of the coercivity is a thermal effect which is caused by a single pump pulse, and that the cooling of the sample is slow compared to the longitudinal magnetization switching time, we can conclude from the pump-induced changes in the coercivity in Fig. 5.15 (left), that the sample reaches a maximum temperature of about 65 K. This temperature is determined by comparing the pump-induced changes in the coercivity with the coercivity versus temperature behavior for a non-pumped sample. The magnetization at 65 K is about 50% of the magnetization at T=25K. This is an upper limit for the demagnetization amplitude since the effect of multiple pump pulses (the experiment is done in a stroboscopic way, see Fig. 5.16) and a possible pump-

induced *electronic* softening (non-thermal effect, see for instance [18]) may also lead to a decrease of the coercivity with respect to the non-pumped situation.
We also measured the influence of the pump on the hysteresis loops for different pump-probe delays. We did not observe any pump-induced changes in the θ magnetic hysteresis loop (measured at 1 kHz) when the pump-probe delay was changed. However, apart from the θ hysteresis loop, we also measured the pump-induced Δθ magnetic hysteresis loop (at 500 Hz), which is sensitive to the pump-probe delay. Like in the case of θ, the interpretation of Δθ hysteresis loop is very challenging but we can still make some interesting observations. A typical Δθ hysteresis loop is shown in the inset of the right panel in Fig. 5.15. The coercivity in the Δθ hysteresis loop for different pump-probe delays is plotted in the right panel of Fig. 5.15. The Δθ signal at negative delays is zero. At pump-probe overlap, the coercivity has dropped to about 1.1 mT. At t=0.75 ns the coercivity decrease further to about 0.5 mT.
Note also that the coercivity of Δθ at τ=0 is much smaller than the coercivity of θ at τ<0. This is consistent with the picture in which there are two different phases in the sample after photo-excitation, see for more information the discussion section. One phase consist of the non-photo-excited Eu atoms ($4f^7$) while the other phase consist of the photo-excited Eu atoms ($4f^6$) and its nearest neighbors. In the θ hysteresis loop at τ<0 we probe the $4f^7$ phase (with a coercivity of 2.3 mT) while in Δθ (pump-induced change) we *mainly* probe the $4f^6$ phase (with a coercivity < 2.3 mT). In the next section we propose a qualitative model for the increase of the magnetization (the so-called remagnetization) and demagnetization dynamics in EuO.

5.5 Discussion

The left panel of Fig. 5.17 shows the data on a logarithmic time scale. The horizontal lines in Fig. 5.17 refer to particular induced rotations values: 1 refers to the level at negative delays; 2 refers to the minimum after a few picoseconds; 3 to the maximum after the (partial) recovery at several tens of picoseconds and 4 (no line) refers to the minimum in the pump-induced rotation after a few nanoseconds.

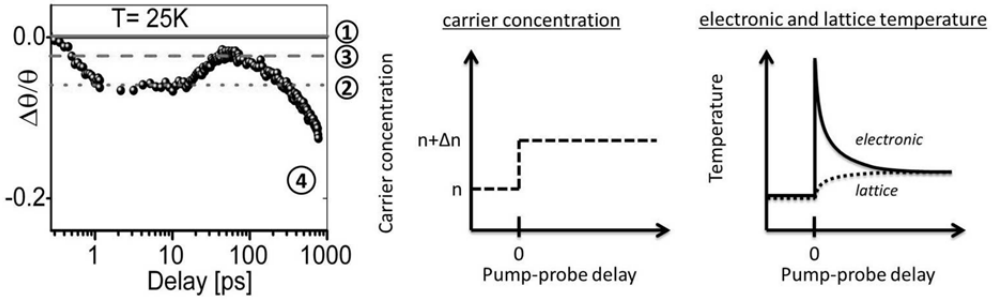

Figure 5.17 | Left) Pump induced (800 nm) changes in the rotation of polarization of the transmitted probe (400nm) at a fluence of 20 mJ/cm^2. 1) level before excitation. 2) level after 2 ps demagnetization. 3) level after (partial) magnetization recovery. 4) level after ns demagnetization processes. Middle/right) Carrier concentration versus pump-probe delay (middle) and electronic temperature and lattice temperature in the 2TM (right).

This complicated behavior is interesting, but also very challenging, from a modeling point of view. However even from some very basic argumentation, one can say something about the observed behavior. We consider the case where the conduction electron concentration is more or less constant after photo-excitation (at least during the first nanosecond, we will come back at this point later where we will present evidence that this is indeed the case), and where the conduction electrons and lattice are in thermal equilibrium after a few picoseconds (this is usually the case in semiconductors), see Fig 5.17 (middle and right). In this case, within the framework of the three temperature model [19,20], it is not possible to obtain the magnetization recovery (after tens of ps) and subsequent slow nanosecond demagnetization, see also Chapter 1 and 7. Therefore it looks like that there is not one magnetic system, but that there are two magnetic subsystems [21,22]. In this discussion section, we will try to answer the following two questions:

- What are the two different magnetic 4*f* subsystems and how are they coupled?
- What is mechanism behind the angular momentum transfer between the lattice and the 4f spins?

The second question can help to answer the first question and we will start with this. After that we will present (literature) results from which we can conclude that the life-time of the 5*d*-conduction electrons and 4*f* holes ($4f^6$) is long: longer than 1 ns (this will be confirmed later in the chapter discussing THz pump-probe

experiments). In the Discussion section E-F, we will present a qualitative model, based on the discussion in section A-D.

5.5.1 Discussion A: angular momentum transfer between the lattice and the 4f spins

One important question we have to answer is what the mechanisms are behind the angular momentum transfer between the lattice and the 4*f* spins. By comparing the experimentally observed timescale in EuO with other experiments and theoretical estimations, we can get information about the spin-lattice angular momentum transfer mechanisms. For EuO several possible candidates, each with its own typical timescale, can be sorted out (see also Chapter 3 for more information):

i. Ultrafast (sub ps - tens of ps), 5*d* conduction electrons: one mechanism which can account for the ultrafast demagnetization in the metallic Nickel and Gd is the Elliott-Yafet mechanism [19,23], in which there is demagnetization because of conduction electron spin-flip scattering with phonons. In EuO there are also conduction electrons (5d) and therefore the EY mechanism is also active. The demagnetization of the 5*d* conduction electrons will also lead to a demagnetization of the 4*f*-spins when the 4*f*-spins and the 5*d*-conduction electrons are strongly coupled (like in Gd [19]).
   The EY process can provide for an efficient demagnetization pathway in the case that the spin-flip probability is large and the conduction band electron temperature (T_e) temperature is high compared to the spin temperature, before electron-phonon equilibration [19]. After electron-phonon equilibration this channel is less efficient but can still contribute to the demagnetization. The lattice temperature influences only the speed of demagnetization while it does not affect the final amplitude of de/re-magnetization (in the M3TM, see Chapter 3).
ii. Fast (tens of ps), $4f^6$ holes (L=3): one mechanism which can account for the ultrafast re/de-magnetization at the 8-50 ps timescale is the direct 4*f* AFCF spin-lattice relaxation channel (AFCF= anisotropic crystal field fluctuations, [23--25]). For this to happen, the lattice needs to have an elevated temperature compared to the 4*f* spins. The lattice temperature (T_l) can increase by means of different electronic relaxation processes. The spin temperature (T_s) reaches a new quasi-equilibrium value with a characteristic time, the 4*f* spin-lattice relaxation time. In the case of an ion with large

orbital momentum, like the 4*f* hole (L=3), the AFCF channel can be as fast as 8 ps [23], see also chapter 3 and 4.

iii. Slow (sub-nanosecond or nanosecond), $4f^7$ moments (L=0): in the case of an ion with zero or very small orbital momentum, like the $4f^7$ moments (L=0), the AFCF channel is slow. In Chapter 3 we estimated the AFCF spin-relation time for the $4f^7$ moments in EuO to be in the order of 450 ps.

iv. Unknown timescale, magnetic excitons and magnetic polarons: we do not know how exactly the magnetic polaron or exciton formation influences the angular momentum transfer timescale of the $4f^7$ moments and the $4f^6$ holes. In the discussion section D, based on very general arguments, we reason that magnetic exciton formation can slow down the spin-lattice relaxation of the $4f^6$ holes.

Mechanism i), ii) and iii) are well-established *universal* angular momentum transfer mechanisms which have been observed in different compounds (metals/half metals/semiconductors). Therefore we will also try to explain the magnetization dynamics in EuO in terms of these angular momentum transfer mechanisms, but we will consider the effects of magnetic exciton and magnetic polaron formation on the spin-lattice relaxation time as well. Since the demagnetization is observed after pump-probe overlap, coherent light-4*f* spin interaction mechanisms (in which angular momentum is transferred to the pump-pulse) are not considered. Because of the importance of the 4*f* holes and the 5*d* conduction electrons, as we will see later, we first discuss the life-time of the carriers (electrons/holes).

5.5.2 Discussion: life-time of the 4f hole ($4f^6$) and the 5d conduction electrons after photo excitation

The literature gives some more information on the electron-hole lifetime (before recombination). The electron-hole lifetime in EuO, EuTe and Eu^{2+} doped salts has been measured or estimated by means of different techniques:

- Luminescence of Eu^{2+} atoms in different salts: Luminescence (5*d* to 4*f*) of Eu^{2+} at 78 K in different salts ($BaCl_2$, $SrCl_2$, $CaCl_2$, SrF_2, CaF_2) after photo-excitation (λ=254 nm) is in the 0.4-0.8 μs range with a quantum efficiency of 34-80% [26].
- Luminescence in EuTe: The decay time of the radiative recombination (5*d* to 4*f*) channel in antiferromagnetic EuTe is greater than 2 ns as was determined from luminescence experiments in [27] by Heiss *et al.*, see also Chapter 7. In these luminescence experiments, the Eu moments in EuTe were partially

ferromagnetically aligned by applying a magnetic field. The photo-excitation wavelength was λ = 400 nm. The larger the total magnetization, the slower the radiative process. Therefore, in ferromagnetic EuO, we also expect the radiative channel to be slow (>ns).

- Decay of the photoconductivity in EuO from electrical transport measurements: The decay of the photoconductivity in stoichiometric EuO (no Metal Insulator Transition MIT) and non-stoichiometric EuO (with MIT) after 4*f* to 5*d* photo-excitation below T=100 K is in the range of 10-30 ms, both for thin films and EuO single crystals [2,28,29]. This slow decay was interpreted in [28,29] in terms of trapping of the conduction electrons.

Based on these findings we do not expect any considerable recombination or trapping in EuO thin films during the first few nanoseconds. In the next section we consider the intra-atomic angular momentum relaxation within a single 4*f* hole ($4f^6$, $J_{4f6}\neq 0$) towards the $J_{4f6}=0$ Hund's rule ground state. This is important since this intra-atomic angular momentum relaxation may affect the stability and formation rate of magnetic excitons.

5.5.3 Discussion: intra-atomic relaxation of a $4f^6$ magnetic moment

In an intra-atomic angular momentum relaxation process, the relative orientation of spin and orbital angular momentum is changing, resulting in a change of the *z*-component of the total angular momentum. There can be intra-atomic angular momentum relaxation when the 4*f* hole interacts with the lattice (phonons), neighboring $4f^7$ moments (magnons), or with 5*d* conduction electrons. In these processes angular momentum needs to be transferred from the 4f hole to the lattice, 5d electrons, or to neighboring $4f^7$ moments (since the total angular momentum is a conserved quantity). Concerning the intra-atomic angular momentum relaxation time (J_{4f6}=5 to J_{4f6}=0) *within* a single Eu^{3+} ion we know from experimental papers and different (theoretical) considerations:

- Resonant Magnetic X-ray Diffraction on EuTe: by time-resolved resonant X-ray magnetic diffraction on EuTe, the antiferromagnetic order parameter was probed after a 4*f* to 5*d* optical excitation (Photo-Doping (PD) = 6%), as was done in [30] by Holldack *et al*. After an initial sub-picosecond decay, the AFM order parameter (l) recovers to $\Delta l/l=0$ at 50 ps; the AFM order has been completely restored after 50 ps. This means that during the first 50 ps there is no angular

momentum relaxation (J=5 to J=0) *within* a single Eu^{3+} ion. Assuming that this intra-*atomic* angular momentum relaxation process is the same for EuO, we conclude that the intra-atomic angular momentum relaxation time is > 50 ps.

- 5*d* electron-4f^6 localized moment scattering: in our first point in this subsection we reasoned that there is no intra-atomic angular momentum relaxation time during the first 50 ps. Now we discuss what we expect to happen after 50 ps by considering 5*d* electron-4f^6moment scattering processes (see for more information on 5*d* electron-4f^7 magnon scattering, Chapter 3 and 7). After 50 ps, we expect the conduction electrons to be ferromagnetically aligned with the localized 4*f* moments; they occupy the spin-up states at the bottom of the spin-split 5*d* conduction band. The spin-splitting at low temperatures (0.6 eV) is much larger than the energy difference between the different J_{4f6} states ($\Delta E=E_{J+1}-E_J$), see also Fig. 5.18. This means that when the electrons are at the bottom of the conduction band, the 5*d* electron-4f^6moment scattering channel is blocked and no exchange of angular momentum between the 5*d* electrons and the 4f^6 moments can occur via this channel. Therefore we expect that the intra-atomic angular relaxation because of 5*d* electron-4*f* magnon scattering is slow (let us say, slower than 1 ns).
- 4f^6 spin-phonon AFCF scattering: by comparing the energy scale for 4f^6 intra-atomic angular momentum relaxation (J=6 to J=5, J=5 to J=4 , etc. Fig. 5.18, right) with phonon energy scale (Fig. 5.18 left) we can see that intra-atomic angular momentum relaxation can only happen by multiple phonon scattering processes. Multiple phonon scattering processes are expected to be much slower than single phonon processes. As stated before, in Tb metal (with L=3) the single phonon AFCF relaxation is about 8 ps[23]. We expect the AFCF relaxation by 10 phonon processes to be much slower than 8 ps; let say slower than 1 ns.
- 4f^6 spin-4f magnon scattering: the energy scale for 4f^6 intra-atomic angular momentum relaxation is larger than the magnon energy scales, indicating that one-magnon scattering processes cannot happen. Since multiple magnon scattering processes are slow, we anticipate that 4f^6 spin-4*f* magnon scattering time is > 1 ns.
- Destabilization of ferromagnetism in $Eu_{1-x}O$: in Eu-deficient EuO, a portion of the Eu atoms have a 3+ valency (Eu^{3+}). In this case Hund's rule predicts a J_{4f6}=0 (L_{4f6}=S_{4f6}=3) ground state configuration. SQUID measurements on $Eu_{1-x}O$ (x>0), presented in [31] by Wicks *et al.* reveal that a small amount of Eu^{3+} can lead to a

drastic suppression of the ferromagnetism: a 20% increase in the partial oxygen pressure during MBE film growth leads to a complete quenching of the magnetization: (M_{Eu1-xO}/M_{EuO})<0.03. Since we observe that $\Delta M/M$ is smaller than 50% (for a very large photo-doping concentration of 15%), we conclude that the $4f^6$ moments will not relax to the Hund's rule ground state within a few nanoseconds.

Based on these findings we do not expect a considerable intra-atomic angular relaxation (within a single Eu^{3+} atom). In addition we expect that the carriers are long lived (> 1 ns).

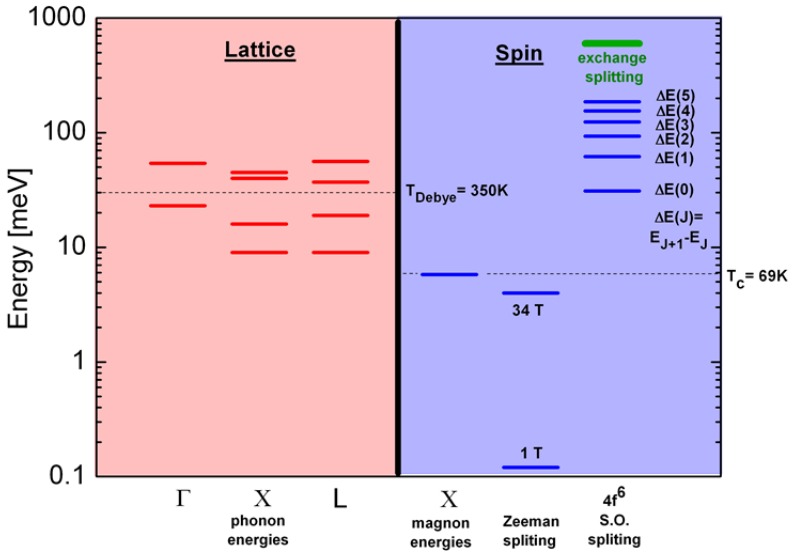

Figure 5.18 | Energy scales in EuO based on data in [2,32--39]. Left: the phonon energies at different points in the Brillouin zone. The dotted line is the Debye temperature. Right: the Zeeman ($4f^7$ ion), magnon, spin-orbit ($4f^6$ ion, L=S=3, λ=34 meV) and exchange (exchange splitting conduction band, green) energies in EuO. The blue dotted line is T_c.

5.5.4 Discussion: angular momentum transfer between the lattice and the $4f^6$ moments, the role of magnetic excitons.

The long lifetime of photo excited carriers opens the possibility of the formation of magnetic excitons in EuO. In a magnetic exciton the 5*d* electron is bound to the 4f hole ($4f^6$) by the Coulomb (and exchange) interaction but the exciton is also stabilized by the exchange interaction of the 5*d* electron with the nearest neighbors and possibly by lattice deformations [40--44]. In order to understand the

role of magnetic excitons on the spin-lattice relaxation time of $4f^6$ moments, we first consider the magnetic energy in the case where there are no 5*d* electrons: the $4f^6$ moments only interact with its 12 nearest $4f^7$ neighbors, see Fig. 5.19A. The magnetic energy of the ferromagnetic configuration is:

(5.30) $E_{NN,4f-4f} = -12J_{NN}S_{4f^6}S_{4f^7}$,

whereas energy of the antiferromagnetic configuration is

(5.31) $E_{NN,4f-4f} = +12J_{NN}S_{4f^6}S_{4f^7}$.

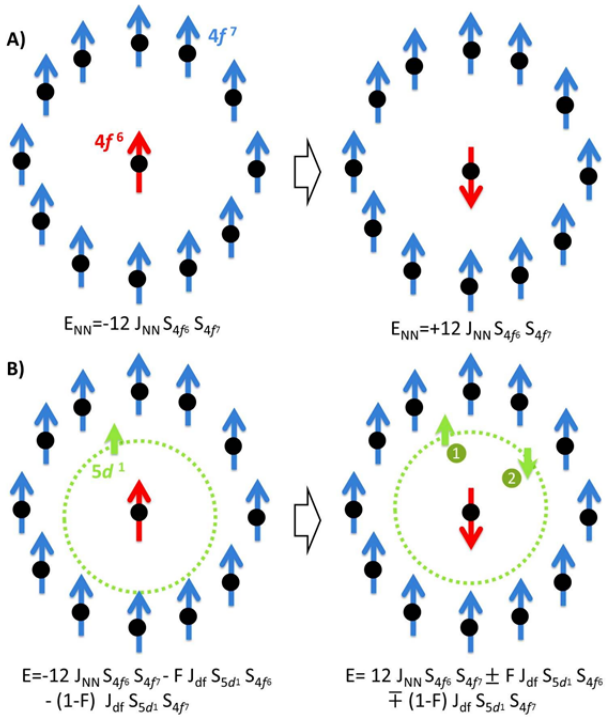

Figure 5.19 | A) Demagnetization of $4f^6$ ions (S_{4f6} =3), only considering nearest neighbor (S_{4f7} =3) exchange interaction (J_{NN}=0.052 meV). The energy cost of a spin flip is: $24J_{NN}\ S_{4f6}\ S_{4f7}$. B) The same as in A) but now we are also considering the intra-atomic *d-f* exchange (J_{df}=150 meV). Note that J_{df}>> J_{NN}. *F* (value between 0 and1) is the spatial overlap of the 5*d* wave function to its nearest neighbors. For *F*=1, the 5*d* electron is on the center; *i.e.* on the $4f^6$ ion. If F=0, the 5*d* electron is fully delocalized over the nearest neighbors. Two cases can be distinguished: 1) the 5*d* spin remains aligned with the S_{4f7} moments after the S_{4f6} spin-flip. 2) the 5*d* spin remains aligned with the S_{4f6} moments during the S_{4f6} spin-flip. The energies of the different states are indicated in the pictures.

In EuO, $J_{NN} = 0.0522$ meV [2]. The energy difference between the AFM and FM state is$\Delta E_{NN,4f-4f} = 24J_{NN}S_{4f^6}S_{4f^7}$. Let now see what happens when there is a

5*d* conduction electron which is bound to the 4*f* hole ($4f^6$). In the ferromagnetic configuration, additionally, there are now the following terms in the energy of the system:

(5.32) $E_{5d-4f} = -FJ_{df}S_{5d^1}S_{4f^6} - (1-F)J_{df}S_{5d^1}S_{4f^7}$,

in which *F* is the probability that the 5*d* electron of the magnetic exciton is on the central $4f^6$ atom, and J_{df} is the 4f-5d exchange constant. See also Fig. 5.19 B. The first and second term in Eq. (5.32) represents the *d-f* exchange interaction between the 5*d* electron and the $4f^6$ and $4f^7$ moments, respectively. We assume that J_{df} is the same in both terms; $J_{df} = +150$ meV in EuO [2,35] (note that $J_{df} \gg J_{NN}$). In the case that *F*=1, the electron is on the central $4f^6$ atom whereas in the case *F*=0, the 5*d* electron is delocalized over its nearest neighbors.

Next, we consider the antiferromagnetic configuration in which the S_{4f^6} moment and the 12 nearest neighbors (S_{4f^7}) are anti-parallel. Here we distinguish two different situations for the 5*d*-electron spin (S_{5d^1}): i) In this case S_{5d^1} remains ferromagnetically aligned with S_{4f^7} . ii) In this case S_{5d^1} is ferromagnetically aligned with S_{4f^6}. The energy difference ΔE between the antiferromagnetic case (S_{4f^6}parallel to S_{4f^7}) and the ferromagnetic case (S_{4f^6}antiparallel to S_{4f^7}) for different *F* values is shown in Fig. 5.20.

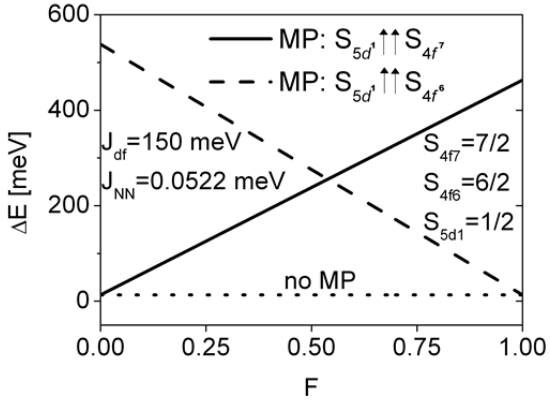

Figure 5.20 | Energy difference between antiferromagnetic (S_{4f6}, S_{4f7} antiparallel) and ferromagnetic alignment (S_{4f6}, S_{4f7} parallel) of the central S_{4f6} and its 12 S_{4f7} nearest neighbors for different *F*, see also Fig. 5.23. *F* is the probability that the 5*d* electronic wavefunction of the magnetic exciton is on the central $4f^6$ atom. The 'no MP' dotted line (MP= magnetic polaron) represent the case where there is no 5*d* conduction electron. Next, we consider the situation where there is a 5*d* electron and *d-f* exchange. Here we distinguish two cases: Case 1) In this case S_{5d^1} remains ferromagnetically aligned (denoted as ↑↑) with S_{4f^7}. Case 2) In this case S_{5d^1} is ferromagnetically aligned with S_{4f^6}.

Case i) is represented by a straight line whereas case ii) is represented by the dashed line. Depending of the value of F, either case i) or case ii) is lower in energy ΔE. The dotted line is ΔE when there are no 5*d* electrons involved; in this case $\Delta E = 24 J_{NN} S_{4f^6} S_{4f^7}$.

When *F*=1, the wavefunction is localized on the central $4f^6$ atom. However this localization costs kinetic energy and therefore the 5*d* electron has the tendency to partially delocalize over its nearest neighbors. The delocalization will be larger when the nearest neighbors are ferromagnetically aligned since then the *d-f* exchange energy is minimized. In the limit that *F*=0, the Coulomb energy with the hole ($4f^6$) is reduced. The result of this competition between kinetic and potential energy causes *F* to be in between 0 and 1. In our model we neglect the option of a possible lattice deformation which can be another stabilizing factor of a magnetic exciton.

From this simple model one can see that the magnetic energy cost for a flip of the $4f^6$ moments increases dramatically when a magnetic exciton is formed (and F is not close to 0 or 1). This has important consequences for the spin-lattice relation time of the $4f^6$ moments. We consider the demagnetization time of the $4f^6$ moments in two different scenarios:

- ***F=0, F=1:*** Both in the fully delocalized case (*F*=0) and in the fully localized case (*F*=1), the spin-flip energy *ΔE* for single S_{4f^6} magnetic moment is small and for this case we expect the demagnetization of an *L*=3 moment to be in the order of 8 ps; based on what we known from AFCF-spin relaxation time in Tb or Tb-doped EuS [23].

  Because of the strong 4*f*-4*f* exchange (S_{4f^6}-S_{4f^7}), we expect the S_{4f^7}moments and the S_{4f^6}moments to be strongly coupled. The timescale for the exchange of angular momentum between the process can be estimated to be in the order of $\hbar/J_{NN}$=80 ps. Therefore the S_{4f^7} demagnetization time (in a two-step process) is expected to be rate-limited by the second 80 ps step. The estimated demagnetization time from this process is much faster than the nanosecond S_{4f^7} demagnetization time that we have observed. Therefore the described scenario (F=0 or F=1) is not consistent with the experimental observations.
- ***0<F<1 (F is not close to 0 or 1):*** In this case, because of the *d-f* exchange interaction, the energy cost of flipping a single S_{4f^6} magnetic moment is large (>100 meV), thereby stabilizing the ferromagnetic alignment within the magnetic exciton. Therefore in this case we have to consider the spin-flip of a

complete magnetic exciton, instead of a single S_{4f^6} magnetic moment. The question is what we can expect for the demagnetization time of a complete magnetic exciton. Whereas the demagnetization time for a single S_{4f^6} ion (*L*=3) was expected to be around 8 ps, the situation for the magnetic exciton is more difficult since it consist of twelve *L*=0 ions and one central *L*=3 ion. For the spin-orbit coupling strength λ of a magnetic exciton we can write: $\lambda_{SO}^{magn.exc.} = (1-F)\lambda_{SO}^{4f7} + F\,\lambda_{SO}^{4f6}$. In this approximation the spin-orbit coupling strength is in between λ_{SO}^{4f7} (spin-orbit coupling strength $4f^7$ moment) and λ_{SO}^{4f6} (spin-orbit coupling strength $4f^6$ moment). Therefore the demagnetization time is expected to be in between 8 ps (L=3, estimation based on Tb-metal) and 450 ps (*L*=0, from AFCF estimation, see chapter 3).

To conclude, when a magnetic exciton is formed, we expect the demagnetization time of the $4f^6$ moments to substantially slow down compared to the free $4f^6$ moment value.

5.5.6 Discussion: sub-picosecond and picosecond magnetization dynamics in EuO

Using the information from the previous subsections, we now will look again to the magnetization dynamics during the first few picoseconds. We know that at negative delays (point 1 in Fig. 5.17) the electrons, spins and the lattice are in thermal equilibrium. We also know that only after a few nanoseconds (at point 4), the electrons, spins and the lattice are in equilibrium again: the different sub-systems (lattice, spins, electrons) have the same temperature but the temperature is higher than the temperature at negative delays. At this point the system is in quasi-equilibrium.

Within the first 2 ps the system undergoes a substantial demagnetization. However the amplitude of this initial demagnetization is smaller than the amplitude at point 4 (after a few nanoseconds). This ultrafast demagnetization is consistent with mechanism i) (EY, see discussion section A), and requires the presence of *free* 5*d* conduction electrons. Because of the strong 4*f*-5*d* exchange, the demagnetization of the 5*d* conduction electrons in turn can also lead to a demagnetization of the 4*f* moments (like in Gd and Tb metal). We will see in the next chapter that most of the conduction electrons are free, at least during the first few picoseconds at high fluences. This means that during the first few picoseconds, no magnetic excitons are involved.

By phonon-emission, the conduction electron temperature decreases during the first few picoseconds, based on what is known for typical semiconductors [45]. This reduction in the conduction electron temperature leads to a slowing down of the spin-lattice relaxation rate by EY processes [19]. The high degree of spin-polarization at the bottom of the conduction band also leads to a slowing down of the EY demagnetization rate [25]. This means that after electron-lattice equilibration (after a few ps), the EY demagnetization rate is expected to be slow. Note that for the (sub) picosecond demagnetization mechanism:

- We are not considering Elliott-Yafet spin-flip scattering of holes due to the fact that they are localized and that therefore the momentum scattering rate (τ_p) is very low. Since according to the Elliott-Yafet relation $1/T_1 \sim \tau_p$ [46], the EY-contribution from the holes can be neglected.
- We are not considering AFCF mechanisms ii) and iii) because the rate is too fast for direct AFCF spin -lattice relaxation, see also Chapter 3.
- We are also not considering the mechanism ii) and iii) because during the first picosecond, before considerable electronic energy relaxation took place, the lattice is cold which means that AFCF mechanism is not active yet.

The fact that there is a substantial demagnetization at the picosecond time-scale comes as a surprise. In the M3TM [47], taking the spin-flip probability of Gd but the conduction electron concentration of photo-excited EuO, the demagnetization rate *R* is small and therefore the demagnetization time is expected to be long (tens of picoseconds to nanoseconds). See Chapter 3 for more information. This means that the spin-flip probability of an electron in EuO is much higher than in Gd and that ultrafast demagnetization is possible in EuO.

5.5.7 Discussion: sub-nanosecond and nanosecond magnetization dynamics in EuO

Now we turn to the sub-nanosecond and nanosecond dynamics. As discussed in subsection A, the observed behavior hints to the presence of two magnetic 4*f* sub-systems. In this sub-section we propose a model which can account for the re-magnetization/demagnetization behavior and which includes two magnetic 4*f* sub-systems. One of the sub-systems, most likely, is the $4f^7$ sub-system, which is the largest sub-system. For the other 4*f*-subsystem, there are three candidates: 1) $4f^6$moments (photo-excited 4*f* holes). 2) $4f^7$moments in magnetic polarons. 3) $4f^6$moments plus their nearest neighbor $4f^7$moments in magnetic excitons.

By looking at the re-magnetization timescale (tens of ps), we can get information about the nature of the second magnetic sub-system. We mentioned before that after a few picoseconds, the EY demagnetization rate is slow. Therefore the spin-lattice angular momentum transfer process is most likely an AFCF mechanism (mechanism ii or mechanism iii). Based on the timescale (tens of ps), we expect that $4f^6$ moments are involved: the AFCF-SLR of $4f^6$ moment is faster than the AFCF-SLR of $4f^7$ moments and the estimated timescale corresponds to the observed remagnetization time. Therefore we expect that the second magnetic $4f$ subsystem is formed by the $4f^6$moments 1).

Based on the discussion in the previous subsections, we propose the following picture. During the first few picoseconds, angular momentum is transferred from the $4f^6$ system, via the 5d electrons, to the lattice (Fig. 5.21 A, EY-process). After that angular momentum is transferred from the lattice (directly) back to the $4f^6$ system (Fig. 5.21 B, AFCF-process).

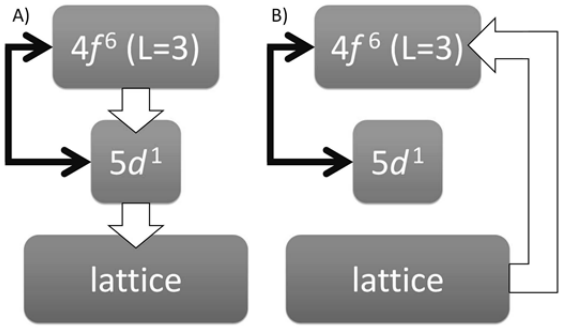

Figure 5.21 | Angular momentum transfer (white arrows). A) Going from point 1 to point 2 in Fig. 5.17. B) Going from point 2 to point 3 Fig. 5.17. The black arrows represent the exchange coupling between the different magnetic systems. A) and B) show the 2 ps demagnetization and 20 ps re-magnetization processes, respectively.

The previous discussions raise a few interesting questions:

- Why mostly the $4f^6$ system demagnetizes during the first few picoseconds.
- Why and during what timescale the two magnetic subsystems are decoupled.
- What is the origin behind the remagnetization of the $4f^6$ system.

The first question can be answered by considering the $4f^6$moment as charged "impurities" in EuO. By EY spin-flip scattering processes, the 5d conduction electrons will demagnetize. Now, when the scattering rate between the 5d conduction electrons and these "impurities" is much higher than the scattering rate

with the $4f^7$ lattice, than the $4f^6$ system will demagnetizes much faster than the $4f^7$ system.

In order to answer the second question, we have to look at the exchange constant between a $4f^6$ moment and a neighboring $4f^7$ moment. The strength of this interaction is unknown, but we do know the nearest neighbor exchange interaction in EuO: J_{NN}/k_B=0.6 K [2] corresponding to a timescale of $\hbar/J_{NN}$=80 ps. Based on this estimate, we can say that it is indeed possible that during the first tens of picoseconds, both systems are weakly coupled.

Let us now turn the third question. We explained the re-magnetization in terms of an AFCF mechanism involving $4f^6$ moments (see Fig. 5.21). The situation after a few picoseconds is as follows: after a few picoseconds the surrounding $4f^7$ is still cold while the lattice and the $4f^6$ system are hot, see Fig. 5.22 left.

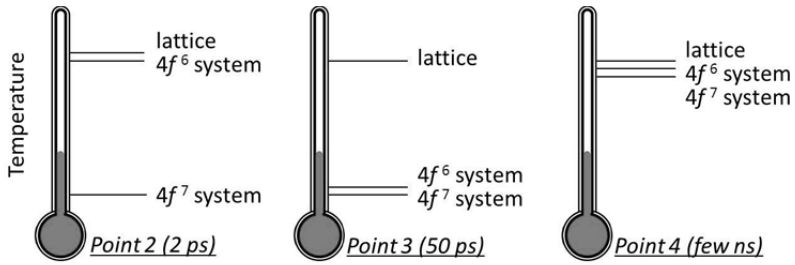

Figure 5.22 | Temperature of the different magnetic subsystems at different delays (see Fig 5.17).

We propose that because of magnetic exciton formation (after tens of picoseconds), the nearest neighbor $4f^6$-$4f^7$exchange constant is increasing (due to 5*d* conduction band electron mediated $4f^6$-$5d^1$-$4f^7$ exchange) and the ferromagnetic order is (partially) restored. By considering the Boltzmann destitution of the Zeeman $4f^6$-levels, one can convert the magnetization to a temperature. In this way an increase of the magnetization corresponds to a drop in the $4f^6$ temperature (Fig. 5.22 middle). We can understand this when due to magnetic exciton formation the internal energy of the system is lowered while this is (apparently) not compensated by a considerable decrease of the entropy (*F=U-TS*).

From Fig. 5.22 we can see that at point 3, the $4f^6$, $4f^7$ and $5d^1$ spin systems are in equilibrium with each other but out of equilibrium with the lattice. However at point 4, all the systems ($4f^6$, $4f^7$,$5d^1$, lattice) are in quasi equilibrium. This change can be explained in terms of demagnetization of magnetic excitons, see Fig. 5.23.

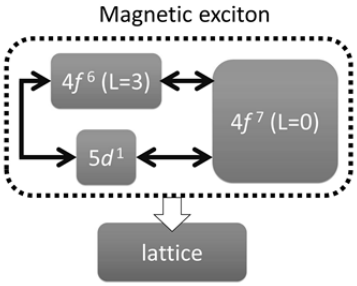

Figure 5.23 | Angular momentum transfer (white arrows) between the lattice and magnetic excitons, going from point 3 to point 4 in Fig. 5.17 and 5.22.

Remember, we reasoned in subsection *Discussion D* that once a magnetic exciton is formed, the spin-flip energy of a single $4f^6$ is high while the spin-flip energy of a complete magnetic exciton is much lower. The slow demagnetization timescale (ns), although a bit slower, fits well to the estimated AFCF spin-lattice angular momentum transfer rate for magnetic excitons. This explains why the magnetization dynamics slows down after 50 ps, when magnetic excitons has been formed. In the next section we will summarize our qualitative model.

5.5.7 Discussion: the qualitative model summarized

Depicted in another way, the different demagnetization/remagnetization steps are shown in Fig. 5.24. 1) represents the non-photo-excited sample. After photo-excitation, there are mobile electrons (5*d*) and localized holes ($4f^6$). After EY-scattering, the 5*d* electrons become demagnetized. The demagnetization is transferred to the holes by 4*f*-5*d* exchange scattering, which is depicted in B). The demagnetized holes are shown in 2). Re-magnetization of the holes by the AFCF mechanism leads restores the short-range magnetic order around the hole. The electron becomes bound to the hole in a magnetic exciton, see Fig. 5.24-3). Finally the slow nanosecond demagnetization component can be explained by the demagnetization of magnetic excitons, see Fig. 5.24-4)

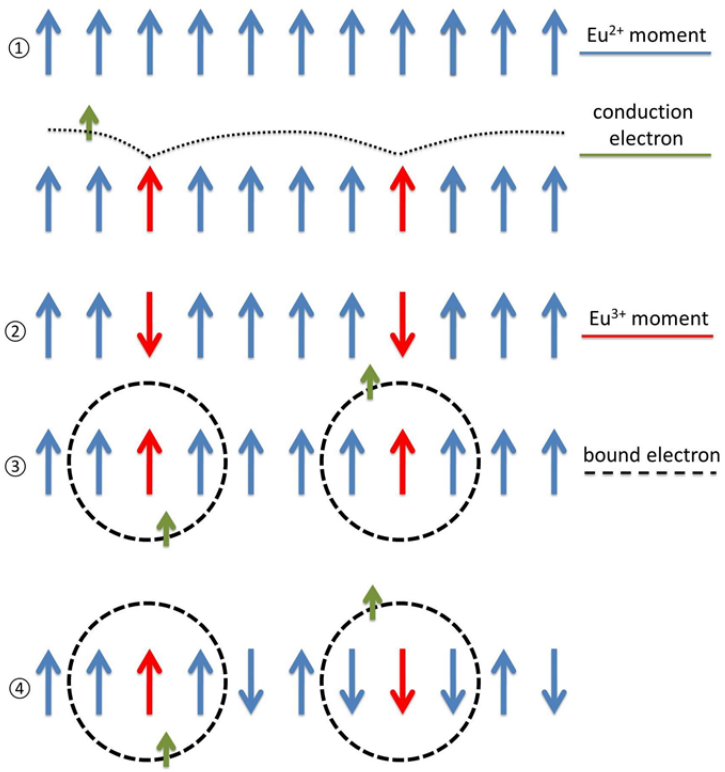

Figure 5.24 | Demagnetization in EuO in several steps. ①-④ refer to the points in Fig. 5.17. 1) Eu^{2+} magnetic moments (blue) in unexcited EuO (point ①). Photo-excitation leads to the presence of 5*d*-spins (green) and Eu^{3+} moments (red). EY scattering of 5*d* spins leads to a demagnetization of the Eu^{3+} moments due to 5*d*-4*f* exchange scattering. 2) The Eu^{3+} moments become demagnetized, point ②. 3) AFCF spin-lattice relaxation of the Eu^{3+} moments restores the short-range magnetic order, point ③. The 5*d* electron becomes bound to the Eu^{3+} ion (magnetic polaron formation). 4) AFCF spin-lattice relaxation of magnetic polarons and isolated 4*f* spins leads to a demagnetization on the ns timescale (towards point ④).

5.6 Optically induced magnetization in EuO in the low fluence regime

5.6.1 Experimental setup and configuration

Whereas the previously described experiments were done using amplified Ti-sapphire laser systems with a repetition rate in the kHz range (1-3 kHz), the experiments described in this section where done using a cavity-dumped system.

The used repetition rate was 800 kHz and the pulse duration was 80 fs. The high repetition rate allows us to get a good signal to noise even in the low fluence (*Fl*) regime, which we define as: *Fl*<1 mJ/cm^2. The cryostat used is equipped with a helium cooled superconducting magnet (up to B=7 T). The wavelength of the linearly polarized pump and probe pulses was 800 nm, in contrast to the experiments described in the previous section where the probe wavelength was 400 nm. The wavevector of the p-polarized probe is parallel to the applied magnetic field. The angle of incidence is 45 degrees, see Fig. 5.25 The polarization state (rotation) of the reflected probe was determined using a half wave plate, a Wollaston prism and a balanced photodiode. For the details, see Fig. 5.25.

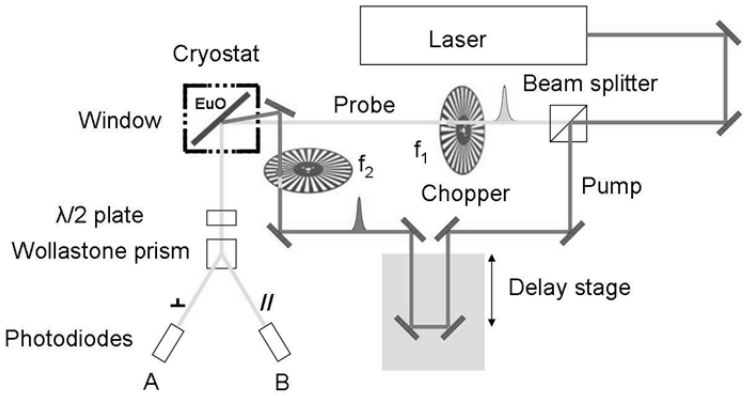

Figure 5.25 | Experimental setup. For the details, see text.

To reduce the effect of pump beam scattering, a double modulation scheme was used in which both the pump and the probe were chopped using a single optical chopper [48]. The probe and pump were chopped at frequencies f_1 and f_2 respectively; $f_2 = {}^5/_7 f_1$. The pump-probe delay could be varied by using a mechanical delay stage on the pump beam arm of the setup. If the high repetition rate laser beam is considered as a quasi cw source (cw=continuous wave), the effect of the chopper can be modeled as a periodic heavy side step function. By doing this for both the pump and the probe beam and by analyzing the Fourier coefficients in the Fourier series, we can write for the pump induced changes in the reflectivity:

(5.32) $$\frac{\Delta R}{R} = \pi \frac{I_R(f1-f2)}{I_R(f1)}$$

In which $I_R(f_1)$ is the reflected intensity at the probe chopper frequency f_1 when the pump beam is closed and $I_R(f_1 - f_2)$ is the reflected intensity at the difference

frequency f_1-f_2 when the pump beam is open. Both signals are detected using a lock-in amplifier. The reference frequency was taken from the optical chopper controller (f_1 or f_1-f_2). The same analysis can be made for the change in the rotation of polarization θ_K:

(5.33) $$\Delta\theta_K = \frac{\pi}{2}\frac{I_{R,H}(f1-f2)-I_{R,V}(f1-f2)}{I_{R,H}(f1)+I_{R,V}(f1)} = \frac{\pi}{2}\frac{I_{R,H}(f1-f2)-I_{R,V}(f1-f2)}{I_R(f1)}$$

In which $I_{R,H}$ and $I_{R,V}$ are the horizontal and vertical components of the intensity after the Wollaston prism. The relative change in the rotation can be written as:

(5.34) $$\frac{\Delta\theta_K}{\theta_K} = \pi\frac{I_{R,H}(f1-f2)-I_{R,V}(f1-f2)}{I_{R,H}(f1)-I_{R,V}(f1)}$$

5.6.2 Sample preparation

The EuO films were grown by Molecular Beam Epitaxy (MBE) in the group of Prof. L.H. Tjeng at the University of Cologne. See for more information [49,50]. High purity Eu metal was evaporated from an effusion cell. Molecular oxygen was added simultaneously through a controlled leak valve. In order to prevent the formation of higher oxides Eu_2O_3 and Eu_3O_4 and Eu metal clusters, a recipe from Steeneken was used [2]. In this method there is an excess of Eu and the substrate temperature (T_s) was kept at 350^{o}C. The oxygen atoms can react with Eu in order to form EuO while the excess of Eu atoms is re- evaporated into the vacuum. The sample was grown on a double-side epi-polished (100) MgO substrate. Before the growth, the substrates were annealed for one hour in a 1 x 10^{-7} mbar oxygen atmosphere. Eu metal was evaporated at 515 ^{o}C resulting in a growth rate around 9 Å/min as was checked with a quartz crystal thickness monitor. The oxygen partial pressure near the substrate during the growth was 5 x 10^{-8} mbar as was determined with a mass spectrometer. In this way a 25 nm thick EuO film was synthesized. The samples were protected from oxidation by a 23 nm thick MgO capping layer. For making the MgO capping, the T_s was kept at 225^{o}C and Mg was evaporated at 296^{0}C giving a flux rate of about 4.1 °A/ min. The oxygen atmosphere during the capping was about 2.7 x 10^{-7} mbar.

5.6.3 Sample characterization

The sample's Kerr rotation magnetic hysteresis loops, SQUID magnetization hysteresis loops and absorption spectrum are shown in Fig. 5.26. The Kerr rotation versus applied magnetic field, for different temperatures, is shown in the upper left panel. The width of the hysteresis loop(the coercivity) is about 10 mT at 10 K. The

Kerr rotation at 100 mT (close to saturation) and 0 mT (remanence) is shown in the lower left panel. As expected for non-doped stoichiometric EuO, T_c is around 70 K. This conclusion is based on the drop in the saturation Kerr rotation measurements at 70 K. In the upper right panel, SQUID magnetization measurements are shown for different orientations of the applied magnetic field (*B*) and the surface normal vector (*n*); the sample has an in-plane anisotropy. The lower right panel shows the absorption spectrum for EuO at room temperature whereas the red curve represents the pump and probe spectrum. The absorption peak corresponds to a 4*f* to 5*d* transition, as was described in Chapter 2. Based on these results we can conclude the film quality is good.

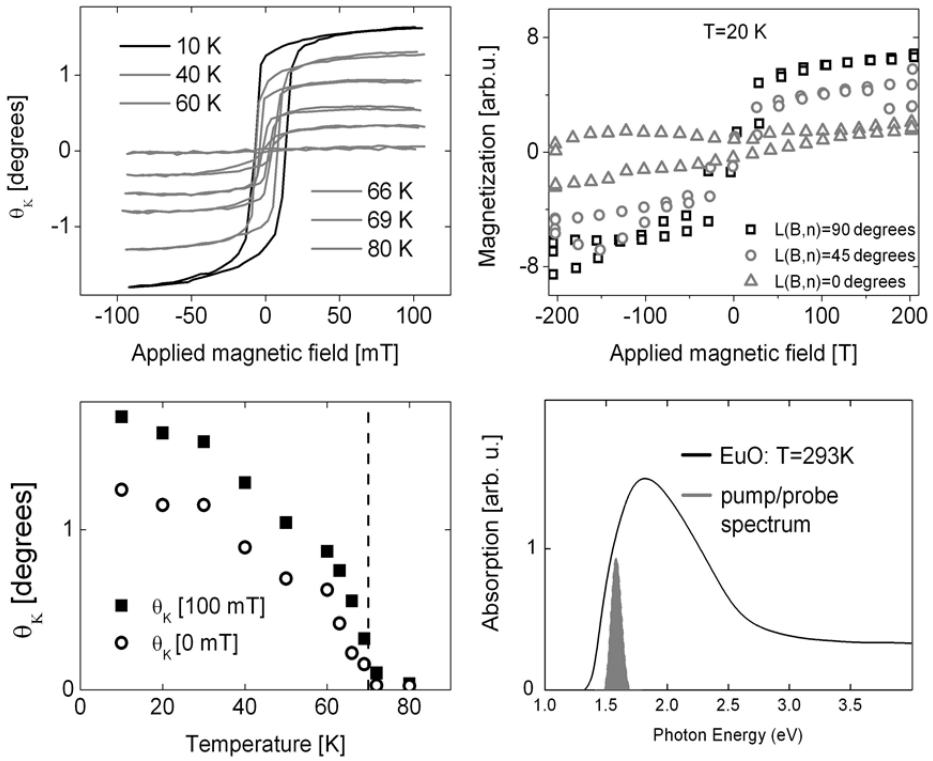

Figure 5.26 | Sample characterization. The Kerr rotation versus applied magnetic fields is shown in the upper left panel. The Kerr rotation at 100 mT (close to saturation) and 0 mT (remanence) are shown in the lower left panel. In the upper right panel, SQUID magnetization measurements are shown for different orientations of the applied magnetic field (B) and the surface normal vector (n); the sample has an in plane anisotropy. The lower right panel shows the absorption spectrum for EuO at room temperature. The gray area represents the pump and probe spectrum.

5.6.4 Results and discussion

The pump-induced changes in the MO Kerr rotation (Δθ) versus applied magnetic field for different pump-probe delays (τ) are shown in the upper panels of Fig. 5.27. The "transient hysteresis" loops (TH) at negative delays (τ =-10ps) represents the average heating signal by the pump pulse train; the pump beam was modulated by an optical chopper with a frequency of $5/7$x2000≈1426 Hz whereas the probe beam was chopped at 2000 Hz. The demagnetization signal at the difference frequency ($2/7$x2000≈571Hz) at pump-probe overlap (τ =0 ps) is larger than the signal at negative delays. After pump-probe overlap there is an increase in Δθ which reaches a maximum at τ =+5 ps. After that the magnetization is decreasing again, see the transient hysteresis loop at τ =+1000 ps. Δθ/θ versus pump-probe delays for different applied magnetic fields is shown in the middle panels of Fig. 5.27. In these graphs Δθ/θ[τ]-Δθ/θ[-10ps] is plotted, which is determined from transient hysteresis measurements for different pump-probe delays (τ). We can describe the observed behavior as follows:

1) Heating signal at negative delays (τ=-10ps). The effect of the pump-pulse train leads to an average heating of the sample.
2) Ultrafast temporal resolution limited decrease of Δθ/θ.
3) Fast picosecond (750 fs) recovery of Δθ/θ.
4) Slower picosecond (6.2 ps) increase of Δθ/θ. Δθ/θ changes sign after a few ps.
5) Slow nanosecond (0.9 ns) decrease of Δθ/θ.

There is a clear difference in Δθ/θ for B=80 mT and B=0 mT. The difference between the value of Δθ/θ close to saturation (80 mT) and Δθ/θ at remanence (0 mT) is shown in the lower left panel. After a fast initial decay, Δθ/θ[80mT]-Δθ/θ[0mT] remains constant over time in the 1-1000 ps range, see the dotted line. In the lower right panel, the pump-induced changes in the reflectance (ΔR/R) are shown. After an instantaneous decrease, the ΔR/R signal remains more or less constant over time. The dynamics of ΔR/R is completely different from the Δθ/θ dynamics. In Fig. 5.28, Δθ/θ at T=66 K is compared with experiments at T=20K.

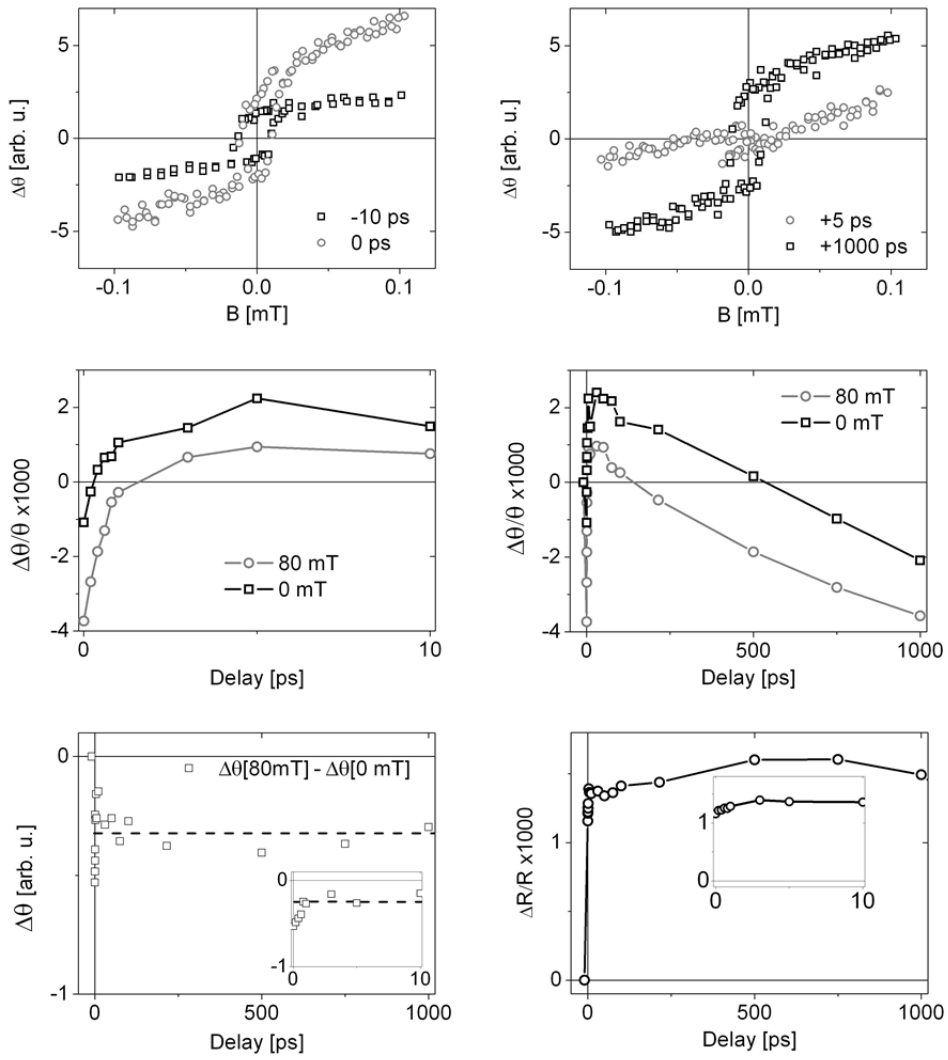

Figure 5.27 | Upper panels) the pump-induced (λ_{pump}= λ_{probe} = 800 nm) changes in the MO-Kerr rotation (Δθ) versus applied magnetic field for different pump-probe delays (τ) at T=20K. Middle panels) the pump-induced changes (Δθ/θ) in the MO-Kerr rotation versus pump-probe delay for different applied magnetic fields, at T=20K. We subtracted the value of Δθ/θ at negative days (τ=-10 ps). Left lower panel) Δθ[80mT]- Δθ[0mT]. The inset shows the first 10 ps. The dotted black line represents the constant value of Δθ[80mT]-Δθ[0mT] in the range of 0.8 ps -1000 ps. Right lower panel) pump-induced change in the reflectance (ΔR/R) versus pump-probe delay at T=20K. The inset shows the first 10 ps.

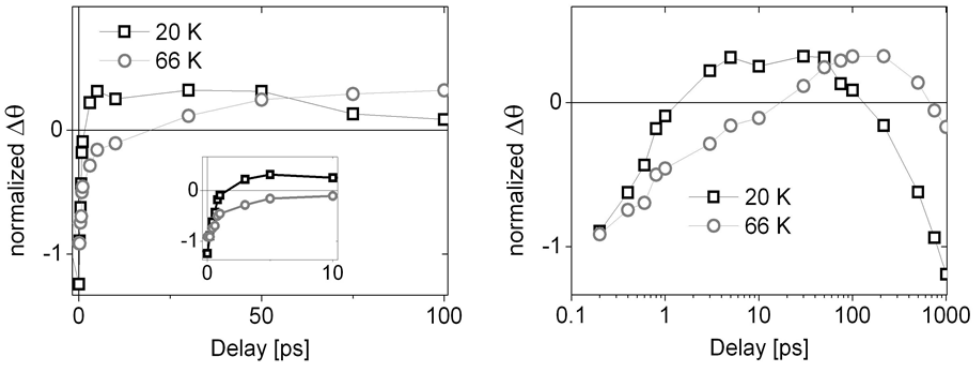

Figure 5.28 | The pump-induced (λ_{pump}= λ_{probe} = 800 nm) changes in the MO-Kerr rotation (Δθ at B=80 mT) versus pump-probe delay for different temperatures. The curves are scaled to the positive maximum in Δθ. In the left graph the first 100 ps and first 10 ps (inset) is shown. The right graph shows the first 1000 ps.

In order to quantify the differences, the data in Fig. 5.28 can be modeled by either of the mathematically equivalent Eq. (5.35) or (5.36).

(5.35) $\frac{\Delta\theta}{\theta}(t) = D_f e^{\frac{-t}{\tau_f}} + D_m e^{\frac{-t}{\tau m}} + I_s\left(1 - e^{\frac{-t}{\tau_s}}\right) + C$ *D_f<0, D_m<0, I_s<0, C>0*

(5.36) $\frac{\Delta\theta}{\theta}(t) = I_f\left(1 - e^{\frac{-t}{\tau_f}}\right) + I_m\left(1 - e^{\frac{-t}{\tau m}}\right) + I_s\left(1 - e^{\frac{-t}{\tau_s}}\right) + C$ *I_f>0, I_m>0, I_s<0, C<0*

In Eq. (5.35) and (5.36), $\tau_{f,m,s}$ stands for fast (f), medium (m) and slow (s) relaxation processes, respectively. Both equation are mathematically equivalent but by explicitly writing them in terms of in-growing (I) or decaying (D) components, we want to stress the fact the that there can be different physical interpretations (demagnetization or remagnetization) of the different components. We will come back to this later. The fitted time constant are shown in Fig. 5.29, where $\tau_{f,m,l}$ for two different temperatures is shown. The sign of the amplitudes is stated on the right side of Eq. (5.35) and (5.35).

We can see that both equations (5.35/5.35) contain a constant and slow in-growing exponent. We chose for this functional form because we observed this slow component in all our experiments; the slow component correspondents to the AFCF spin-lattice relaxation time of magnetic excitons and/or $4f^7$ magnetic moments, see the previous sections. The situation is more unclear for the fast and medium components and the constant: is the fast/medium component an ingrowing component (5.36), or is it a decaying component (5.35). In the case of Eq.

(5.36), the amplitude at t=0 is *C* whereas the amplitude at t=0 is D_f+D_m+*C* for Eq. (5.35). We come back to this later soon.

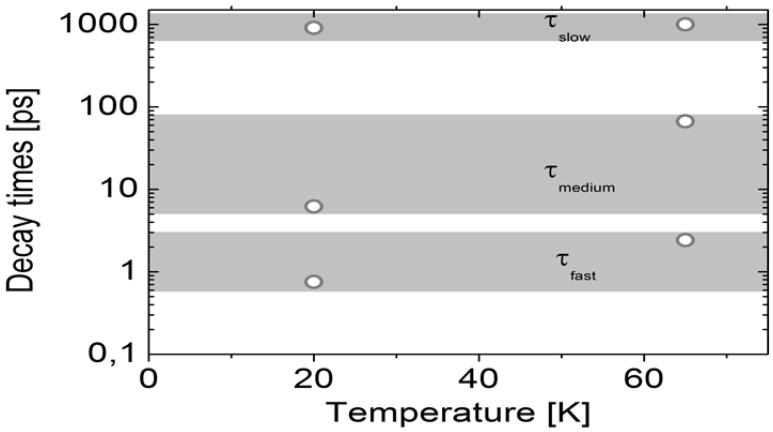

Figure 5.29 | Decay times obtained by fitting Eq. (5.35) to different data sets at different temperature. The used data is shown in the upper panels of Fig. 5.27. The fast decay time, which corresponds to an increase of Δθ/θ, is in the order of 700-2000 fs whereas the slower decay time is in the order of 6-66 ps. The slow in-growing exponent, which corresponds to a decrease of Δθ/θ is in the 0.9-1.1 ns range.

From Fig. 5.29 we can see that the fast time constant (τ_f) is of the order of 700-2500 fs whereas the slower time constant (τ_m) is of the order of 6-66 ps. The slow negative in-growing exponent (τ_s) is in the 0.9-1.1 ns range. The time constants for the 20 K data (0.7 ps, 6 ps, 0.9 ns) are smaller than the time constants for the 66 K data (2.5 ps, 66 ps, 1.1 ns). For the data obtained at T=66 K, the amplitudes of the decaying exponents (D_f, D_m) are similar. However, for *T*=20 K, $|D_f|>|D_m|$.
Let us now discuss the origin of temporal resolution limited component: (D_f+D_m+*C)* in Eq. (5.35) and C in Eq. (5.36). There are two different scenarios that we discuss:

magnetic interpretation: the Elliot-Yafet (EY) spin-flip scattering of the 5*d* electrons could in principle lead to a decrease of the 4*f* magnetization (after 4*f*-5*d* scattering) with a time constant of τ<<190 fs. This is however very unlikely since the EY demagnetization time in other systems with localized 4*f* moment and a much higher density of itinerant 5*d* electrons (Gd and Tb) is in the order of 750 fs [23]. It is also in contradiction with the high fluence experiments on EuO.

non-magnetic interpretation: the fact that both the rise time of Δθ/θ and ΔR/R is temporal resolution limited, suggests that both processes could be related. Since

ΔR/R probes the carrier dynamics and carrier relaxation processes, we have indications that the ultrafast (<115 fs) component in Δθ/θ is non-magnetic and is related to carrier dynamics.

We conclude that the temporal resolution limited component is most likely non-magnetic. Let's now come back to the fast and medium component. A comparison with the pump-induced changes in the reflectance shows that the timescales are completely different. This give hints that the fast and medium components are of magnetic origin and that Eq. (5.36) is the right functional form. τ_f and τ_m are in the same order as we observed in the high fluence experiments which we presented in the previous section. However, the sign of fast component (sub-picosecond) is different than we observed in section 5.4 (decrease of magnetization), although it has the same sign as in the results that we presented in section 5.3 (increase of magnetization).

5.6.5 Discussion and conclusions

Based on the discussion in section 5.4 we explain the m-component in terms of an increase of the magnetization because of magnetic exciton formation. The slow τ_s component, that we have observed in all the MO experiments throughout this chapter can be explained in terms of AFCF spin-lattice relaxation of the 4*f* magnetic moments.

The (microscopic) interpretation of the $\tau_{f,}$ components is more challenging: what is the origin of the sign change of the (ultra)fast component in the different experiments? If the τ_f component in the low fluence data is indeed magnetic, it would correspond to an increase of the magnetization. As reasoned earlier, the only well-established *ultrafast* angular momentum transfer process which can be responsible for this is the EY scattering of 5*d* electrons, and the subsequent demagnetization of the $4f^6$ moments (due to 4*f*-5*d* electron scattering). Generally, in several materials including ferromagnetic semiconductors, metals and half metals, EY scattering of hot itinerant electrons leads to *demagnetization*. Therefore, an ultrafast increase in the magnetization because of EY spin-flip scattering of (hot) itinerant electrons [25,47] would come as a big surprise and we cannot completely rule out that this component is non-magnetic (although it has a different timescale as the transient reflectance). Of course it is also possible that a magnetic component is competing with a nonmagnetic component with the same timescale. In this scenario the nonmagnetic component ($d\theta/dt > 0$) would be

predominant with respect to the magnetic one ($d\theta/dt < 0$) and that would explain the observed increase in $\Delta\theta/\theta$.

The fact that we did not see this, possible non-magnetic, component (τ_f) in the 6% Gd-doped sample (high fluence, section 5.4) might be related to the differences in the probe wavelength. Whereas the probe wavelength is 400 nm in the high fluence experiments (pump= 800 nm), the probe wavelength is 800 nm in the low fluence experiments. Therefore it might be that probing at a wavelength of 400 nm gives a more magnetically-clean MO signal compared to the experiments in which a probe beam with a wavelength of 800 nm is used.

References

[1] B. Koopmans, M. van Kampen, J. T. Kohlhepp, and W. J. M. de Jonge, Phys. Rev. Lett. **85**, 844 (2000).

[2] P. Steeneken, *PhD thesis: New light on EuO thin films* (Rijksuniversiteit Groningen, 2002).

[3] V. V. Krishnamurthy, D. J. Keavney, D. Haskel, J. C. Lang, G. Srajer, B. C. Sales, D. G. Mandrus, and J. L. Robertson, Physical Review B **79**, 014426 (2009).

[4] E. Hecht, *Optics* (Pearson Education, 2003).

[5] A. K. Zvezdin and V. A. Kotov, *Modern Magnetooptics and Magnetooptical Materials* (Taylor & Francis, 2010).

[6] R. Sutarto, S. G. Altendorf, B. Coloru*, et al*, Physical Review B **80**, 085308 (2009).

[7] R. Sutarto, S. G. Altendorf, B. Coloru*, et al*, Physical Review B **79**, 205318 (2009).

[8] S. J. Blundell, *Magnetism in Condensed Matter* (oxford university press, 2011).

[9] C. Kittel, *Introduction to Solid State Physics* (Wiley, 1996).

[10] A. Kirilyuk, A. V. Kimel, and T. Rasing, Reviews of Modern Physics **82**, 2731 (2010).

[11] R. W. Boyd, *Nonlinear Optics* (Academic Press, 2003).

[12] M. Fox, *Optical Properties of Solids* (Oxford University Press, 2004).

[13] Y. Shapira, S. Foner, and T. B. Reed, Physical Review B **8**, 2299 (1973).

[14] X. R. Wang, Modern Physics Letters B **24**, 2215 (2010).

[15] T. Roth, D. Steil, D. Hoffmann, M. Bauer, M. Cinchetti, and M. Aeschlimann, Journal of Physics D-Applied Physics **41**, 164001 (2008).

[16] B. Heinrich, C. Burrowes, E. Montoya, B. Kardasz, E. Girt, Y. Song, Y. Sun, and M. Wu, Phys. Rev. Lett. **107**, 066604 (2011).

[17] B. Koopmans, J. J. M. Ruigrok, F. D. Longa, and W. J. M. de Jonge, Phys. Rev. Lett. **95**, 267207 (2005).

[18] A. H. M. Reid, G. V. Astakhov, A. V. Kimel, G. M. Schott, W. Ossau, K. Brunner, A. Kirilyuk, L. W. Molenkamp, and T. Rasing, Appl. Phys. Lett. **97**, 232503 (2010).

[19] B. Koopmans, G. Malinowski, F. Dalla Longa, D. Steiauf, M. Faehnle, T. Roth, M. Cinchetti, and M. Aeschlimann, Nature Materials **9**, 259 (2010).

[20] E. Beaurepaire, J. C. Merle, A. Daunois, and J. Y. Bigot, Phys. Rev. Lett. **76** (1996).
[21] A. Mekonnen, A. R. Khorsand, M. Cormier, A. V. Kimel, A. Kirilyuk, A. Hrabec, L. Ranno, A. Tsukamoto, A. Itoh, and T. Rasing, Physical Review B **87**, 180406 (2013).
[22] A. J. Schellekens and B. Koopmans, Physical Review B **87**, 020407 (2013).
[23] M. Wietstruk, A. Melnikov, C. Stamm, T. Kachel, N. Pontius, M. Sultan, C. Gahl, M. Weinelt, H. A. Duerr, and U. Bovensiepen, Phys. Rev. Lett. **106**, 127401 (2011).
[24] W. Hubner and K. H. Bennemann, Physical Review B **53**, 3422 (1996).
[25] G. M. Mueller, J. Walowski, M. Djordjevic*, et al*, Nature Materials **8**, 56 (2009).
[26] T. Kobayasi, S. Mroczkowski, J. Owen, and L. Brixner, J Lumin **21**, 247 (1980).
[27] W. Heiss, R. Kirchschlager, G. Springholz, Z. Chen, M. Debnath, and Y. Oka, Physical Review B **70**, 035209 (2004).
[28] C. Llinares, L. Gouskov, C. Duchemin, and G. Bordure, Journal of Physics and Chemistry of Solids **36**, 567 (1975).
[29] C. Llinares, E. Monteil, G. Bordure, and Paparodi.C, Solid State Commun. **13**, 205 (1973).
[30] K. Holldack, N. Pontius, E. Schierle, T. Kachel, V. Soltwisch, R. Mitzner, T. Quast, G. Springholz, and E. Weschke, Appl. Phys. Lett. **97**, 062502 (2010).
[31] R. Wicks, S. G. Altendorf, C. Caspers, H. Kierspel, R. Sutarto, L. H. Tjeng, and A. Damascelli, Appl. Phys. Lett. **100**, 162405 (2012).
[32] L. Passell, O. W. Dietrich, and J. Alsnielsen, Physical Review B **14**, 4897 (1976).
[33] J. Alsnielsen, O. Dietrich, and L. Passell, Physical Review B **14**, 4908 (1976).
[34] P. Boni and G. Shirane, Physical Review B **33**, 3012 (1986).
[35] P. Steeneken, L. Tjeng, I. Elfimov, G. Sawatzky, G. Ghiringhelli, N. Brookes, and D. Huang, Phys. Rev. Lett. **88**, 047201 (2002).
[36] A. B. Henriques, M. A. Manfrini, P. H. O. Rappl, and E. Abramof, Physical Review B **77**, 035204 (2008).
[37] A. B. Henriques, G. D. Galgano, B. L. Diaz, P. H. O. Rappl, and E. Abramof, Journal of Physics-Condensed Matter **19**, 406234 (2007).
[38] A. B. Henriques, A. Wierts, M. A. Manfrini, G. Springholz, P. H. O. Rappl, E. Abramof, and A. Y. Ueta, Physical Review B **72**, 155337 (2005).
[39] R. Zeyher and W. Kress, Physical Review B **20**, 2850 (1979).
[40] T. Kasuya and A. Yanase, Reviews of Modern Physics **40**, 684 (1968).
[41] T. Kasuya, J Magn Magn Mater **195**, 141 (1999).
[42] M. Umehara, Physical Review B **52**, 8140 (1995).
[43] M. Umehara, Physical Review B **67**, 035201 (2003).
[44] R. Akimoto, M. Kobayashi, and T. Suzuki, Journal of the Physical Society of Japan **63**, 4616 (1994).
[45] R. Ulbricht, E. Hendry, J. Shan, T. F. Heinz, and M. Bonn, Reviews of Modern Physics **83**, 543 (2011).

[46] Steiauf D., Illg C., and F ahnle M., Journal of Physics: Conference Series **200**, 042024 (2010).
[47] B. Koopmans, G. Malinowski, F. Dalla Longa, D. Steiauf, M. Faehnle, T. Roth, M. Cinchetti, and M. Aeschlimann, Nature Materials **9**, 259 (2010).
[48] D. A. Mazurenko, *Ultrafast optical swiching in three-dimensional photonic crystals* (University of Utrecht, 2004).
[49] R. Sutarto, S. G. Altendorf, B. Coloru*, et al*, Physical Review B **79**, 205318 (2009).
[50] S. G. Altendorf, A. Efimenko, V. Oliana, H. Kierspel, A. D. Rata, and L. H. Tjeng, Physical Review B **84**, 155442 (2011).

Chapter 6

Ultrafast conductivity dynamics in EuO: signatures of magnetic excitons and magnetic polarons

6.1 Introduction

In this chapter we study the conductivity dynamics in EuO after an optical excitation with sub-picosecond temporal resolution, using an excitation wavelength of 800 nm, which corresponds to a 4*f* to 5*d* electronic transition. The optical conductivity is probed in the THz range using single cycle, optically-generated electric field pulses. The *dc* conductivity in EuO has been studied extensively [1--5], but a full understanding of the metal insulator transition (MIT) and colossal magneto resistance (CMR) is still lacking [3]. By studying the conductivity dynamics, the nature of the optical transition can be determined (4*f*-5*d* exciton or band). In particular, from its relaxation dynamics information can be obtained about the microscopic nature of the conductivity in EuO, about magnetic exciton and polaron formation, and about electron-hole recombination.

This chapter is organized as follows. We start with an introduction in which we discuss the transport properties of EuO, and in which we introduce three different models for the optical conductivity such as the Drude, Lorentz and Drude-Smith models. We also explain how the electrical conductivity can be obtained from THz transmission experiments and give a general introduction to the time-domain THz spectroscopy methods employed in the present experiment.

In the experimental section we describe our THz setup, and outline how the data is obtained. In the results section we characterize the setup and the EuO sample, and we present ultrafast conductivity dynamics experiments on EuO. The ultrafast conductivity dynamics so obtained is fitted with a phenomenological model at different temperatures and pump fluences to extract a few numerical parameters from the data. Finally in the discussion and conclusion section the fitted

parameters are modeled to obtain information about carrier dynamics, magnetic excitons and magnetic polarons in EuO.

6.1.1 The conductivity of EuO thin films and the metal-insulator transition

The resistivity versus temperature curve for a stoichiometric 25 nm thick EuO film is shown in Fig. 6.1 left (see the uppermost black curve [3]). The resistivity is decreasing with increasing temperature, like for any normal nonmagnetic semiconductor. The behavior changes for Eu-rich EuO ($Eu_{1+x}O$, x>0), (see the other curves in Fig. 6.1 left [3]). In Eu-rich EuO there is a metal insulator transition (MIT) around the magnetic ordering temperature, T_c=69 K. Apart from that, the resistivity of Eu-rich EuO is strongly magnetic field dependent (see Fig. 6.1 middle [3]).

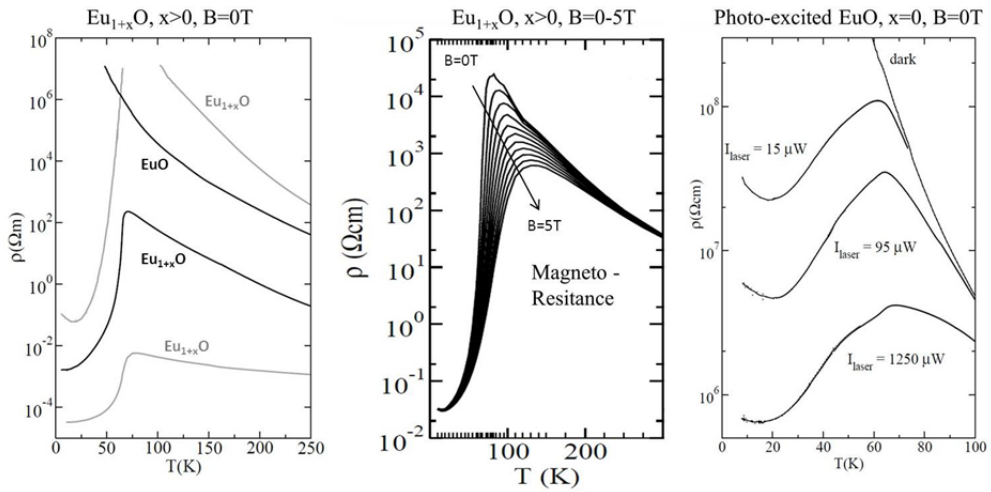

Figure 6.1 | Magnetic properties of $Eu_{1+x}O$ films (20-35 nm). Left: with x>0 at B=0T (left), with *x*>0 and B=0-5T (middle, negative magneto-resistance) and photo-excited (*λ*=632.8 nm) EuO (right, *x*=0, B=0mT). The graphs has been taken from [3], with permission.

We can summarize the results presented in the left and middle panel of Fig. 6.1 as follows:

- Stoichiometric EuO shows activated behavior in the whole temperature range (T=10-250K), typical of a semiconductor.
- Eu-rich EuO (at B= 0T) has a metal-insulator transition around T_c.
- Eu-rich EuO shows negative colossal magneto resistance (MR) with the maximum MR around T_c. At very low temperatures, the MR effect is close to zero.

- Using the mean field model for the magnetization, the Eu-rich EuO (ρ,T) data in the middle panel of Fig. 6.1 can be converted to (ρ,M) [3]. This can done, since in the mean field model, the magnetization M(B,T) can be calculated when the temperature and the applied magnetic field is known. When this procedure is done for (ρ,T) data in the T=10-100 K range, all the data can be superimposed on a universal curve [3]. For the data shown in middle panel of Fig. 6.1 it was shown that $\sigma(M_r) \propto e^{b\,M_r}$, with $b \approx 13.3$ [3]. M_r is the reduced magnetization. Surprisingly, the conductivity in this range dependent solely on the magnetization, and not on the temperature or applied magnetic field (other than the field and temperature dependence of *M*).
- The fact that Eu-rich EuO (ρ,T) curves below T=100 K can be superimposed on each-other when (ρ,M) is plotted using the mean field model suggests that that there should be a macroscopic magnetization in the sample in order to see the MIT and MR effects. This is however not the case since the MIT is also happening at B=0T in a sample which has not been magnetized. At B=0T, the spins are aligned *within* the magnetic domains, but the magnetization direction of *different* magnetic domains is random, leading to a zero macroscopic magnetization. The reduced magnetization in $\sigma(M_r) \propto e^{b\,M_r}$ refers to the average magnetization of a magnetic domain. The fact that the overlapping works so well by using the mean field model, and not by using the spin-spin nearest neighbor correlation function (which deviate considerably around T_c, see chapter 2), shows that the conductivity is mainly induced by, and sensitive to, spin correlations on a length scale larger than several unit cells (>1 nm).
- Recently it was shown the the MIT transition in 65 nm thick Eu-rich EuO films is induced by mobility changes. At the same time carrier concentration (*n*) is nearly temperature independent [4]. The mobility is around 3 $cm^2/V\,s$ at 90 K and increases towards 70 $cm^2/V\,s$ at 5 K for B=0T. The observed size of the MR is small compared to the data shown in Fig. 6.1 [3]: the resistivity decreases only one order of magnitude (T= 70K, B=8T). In another experiment also a change in *n,* during the MIT, has been observed in EuO bulk samples [2]. This unsolved contradiction makes the interpretation of the MIT problematic.

Several microscopic models have been proposed to explain the above mentioned experimental observations. The simplest model is based on the concept that in Eu-rich EuO (with a low off-stoichiometry), the electrons might be "trapped" by the electrostatic potential of the oxygen vacancy [3,5]. The vacancy electronic levels are just below the conduction band with a large binding energy, i.e. several 100 of meV. Promotion to the conduction band is thermally activated. The emerging 4*f* magnetic order causes the spin polarized conduction band to shift, because of the d-f exchange interaction. Now, the down shifted spin-up conduction band can cross the vacancy levels, leading to a delocalization of the trapped electrons. The MIT is then purely explained by a change of the number of *free* (delocalized) electrons. In the simplest model, in which the vacancy states are not spit by the effective magnetic field, we can write for the conductivity:

$$\sigma = ne\mu = e\,\mu\,n_0 e^{\frac{\Delta E}{k_B T}} = e\,\mu\,n_0 e^{-\frac{a-cM}{k_B T}} \qquad \text{for } a - cM > 0 \;\; (a > 0, c > 0) \tag{6.1}$$

$$\sigma = e\,\mu\,n_0 \qquad \text{for } a - cM \leq 0 \;\; (a > 0, c > 0)$$

In which ΔE is the energy difference between the conduction band and the vacancy levels. *a* is the energy difference when *M*=0 in the paramagnetic phase, and *c* is the proportionality constant which relates the conduction band shift to the reduced magnetization *M*. n_0 is the conductivity at high temperatures ($k_B T \gg a - cM$). Here we assume that the conductivity shows an activated behavior due to the energy gap between the vacancy state and the conduction band.

This simple model is in contradiction with the experimental observation in two ways: firstly it explains the MIT in terms of change in the carrier concentration, while in the experiments on thin films is shown that it is related to changes in the mobility [4]. Secondly, in this case the conductivity is not only dependent on the magnetization, but also on the temperature (other than the field and temperature dependence of *M*).

A more detailed version of this model was made in reference [3], which takes into account: 1) the number of vacancy states *N;* 2) the number of free electrons n_c; 3) the number of trapped electrons n_i; 4) charge neutrality, $n_c+n_i=N$; 5) the fact that one vacancy can bind two electrons; 6) the Coulomb interaction between different vacancies; 7) the conductivity is calculated by $\sigma=n_c e\mu$, where the mobility is taken as a constant (53 cm^2/V s, not temperature dependent). This model could reproduce the data in Fig. 6.1 using *N*=0.5 % and it could also reproduce its reduced magnetization dependence, $\sigma(M_r) \propto e^{b\,M_r}$. This model is in contradiction with the

data in the sense that it explain the MIT in terms of a change in the free carrier concentration, while the experiments on thin films show that this is not the case.
In literature, also models were made which explain the MIT in terms of a change both the mobility and the free carrier concentration, see reference [6]. For an overview of the different models which are used to explain the MIT, we refer to references [3] and [1]. However, due to the contradiction in the mobility and carrier concentration data between films and bulk samples, no definite conclusion can be made about the mechanisms which are responsible for the MIT.
The photo-resistivity of a stoichiometric EuO film is shown in the right panel in Fig. 6.1 [3]. Without photo-excitation, the resistivity shows an activated behavior. After photo-excitation using a continuous-wave Helium-Neon laser (λ=632.8 nm), a MIT appears similarly to the one observed in Eu-rich EuO. The origin of this MIT is the matter of subject in this chapter and will be discussed intensively in the discussion section.

6.1.2 Relating the transient changes in the THz transmission to the optical conductivity

In this section we want to make a connection between an optical quantity that we can measure, the amplitude THz transmission coefficient, and the material property which we are interested in: the (optical) conductivity (at THz frequencies), following [7--13]. We consider the sample structure shown in Fig. 6.2, in which we depict the optical transmission trough a MgO/EuO/MgO sample.

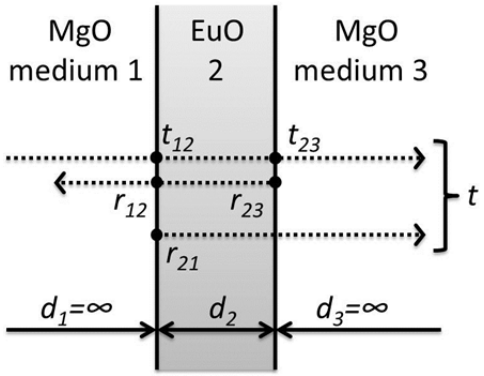

Figure 6.2 | Sample structure and the definition of the amplitude reflection and transmission coefficients for a THz beam coming from the left at normal incidence. In this case the capping layer and substrate are considered to be of infinite thickness.

The MgO substrate and capping layer are considered to be of infinite thickness while the EuO film is tens of nanometers. Later we elaborate more about the assumption that the capping layer is of infinite thickness; the actual thickness of the capping layer is about 20 nm. The normal incidence transmission through the structure which is shown in Fig. 6.2, including an infinite amount of multiple reflections within the film (medium 2) is:

(6.2) $t = \frac{t_{12}t_{23}e^{i\varphi}}{1-r_{23}r_{21}e^{i2\varphi}}$ - Fabry-Perot interferometer amplitude transmission

In which t, r and φ are defined in the usual way:

(6.3) $r_{ij} = \frac{N_i - N_j}{N_i + N_j}$ - amplitude reflection coefficient at boundary i/j

(6.4) $t_{ij} = \frac{2N_i}{N_i + N_j}$ - amplitude transmission coefficient at boundary i/j

(6.5) $\varphi = \frac{N_2 \omega d_2}{c}$ - complex phase in medium 2 with thickness *d*

(6.6) $N_i = n_i + i\kappa_i$ - complex refractive index in medium *i*

In our case, $N_1 = N_3 = n = 3.08$ (MgO at ν=1 THz). Now, we can write for Eq. (6.2):

(6.7) $t = \frac{4N_2 n}{(N_2+n)^2 e^{-i\varphi} - (N_2-n)^2 e^{+i\varphi}}$

For free electrons in the THz regime generally holds that $\sigma_r \gg \sigma_i$, in which σ_r and σ_i are the real and imaginary part of the optical conductivity. In this case we can write for the phase: $\varphi = \frac{N_2 \omega d_2}{c} \approx \sqrt{\frac{\sigma_r \omega}{2\varepsilon_0}} \frac{d_2}{c}(1+i)$. Using parameters for our EuO thin film, $\omega = 1$ THz, d_2=60 nm and σ_r <2x10^5 [1/Ωm], we can see that the phase is small φ<<1 and we can approximate $e^{\pm i\varphi}$ as: $1 \pm i\varphi$. Now we can write for Eq. (6.7):

(6.8) $t = \frac{2N_2 n}{2N_2 n - i\varphi({N_2}^2 + n^2)} = \frac{2n}{2n - i\left(\frac{\omega d_2}{c}{N_2}^2\right) - i\left(\frac{\omega d_2}{c} n^2\right)}$ $\varphi \ll 1$

from now on we indicate which working approximation the equation is obtained from in a shaded box on the equation right. Now, by using the following identities:

(6.9) $\varepsilon_2 = {N_2}^2$ - dielectric function ε_2

(6.10) $\varepsilon_2 = 1 + \frac{i\sigma_2}{\varepsilon_0 \omega}$ - optical conductivity $\sigma_2 = \sigma_r + i\,\sigma_i$

(6.11) $Z_0 = \frac{1}{\varepsilon_0 c} = 377\ \Omega$ - free space impedance

We can write Eq. (6.8) as:

(6.12) $t = \frac{2n}{2n+\sigma_2 Z_0 d_2 - i\frac{\omega d_2}{c}(n^2+1)}$ $\varphi \ll 1$

From now on we will always work within the assumption that: $\varphi \ll 1$. Therefore we will omit these assumptions behind the equations. If we include the vacuum/MgO reflections, and the propagation in MgO, the transmission becomes:

(6.13) $t = \frac{2n}{2n+\sigma_2 Z_0 d_2 - i\frac{\omega d_2}{c}(n^2+1)} \cdot \frac{4n}{(n+1)^2} e^{i\frac{n\,\omega(d_1+d_3)}{c}}$.

The transmission in vacuum is

(6.14) $t_V = e^{i\frac{\omega(d_1+d_2+d_3)}{c}}$,

from which we can see that the transmission ratio is:

(6.15) $\frac{t}{t_V} = \frac{2n}{2n+\sigma_2 Z_0 d_2 - i\frac{\omega d_2}{c}(n^2+1)} \frac{4n}{(n+1)^2} e^{i\frac{n\,\omega(d_1+d_3)}{c} - i\frac{\omega(d_1+d_2+d_3)}{c}}$.

Noting that in our case d_1 =24 nm d_2 =60 nm, d_3 =1 mm, ω = 1 THz, *n*=3.08, we can approximate Eq. (6.15) as:

(6.16) $\frac{t}{t_V} \cong \frac{E}{E+\sigma_2} \cdot A \cdot e^{iB}, \quad \sigma_2 = E\left(\frac{A \cdot e^{iB}}{\frac{t}{t_V}} - 1\right)$ $i\frac{\omega d_2}{c}(n^2+1) \ll 1, \quad (d_1, d_2) \ll d_3$

(6.17) $A \equiv \frac{4n}{(n+1)^2}, \qquad B \cong \frac{(n-1)\,\omega d_3}{c}, \qquad E \equiv \frac{2n}{Z_0 d_2}$

The argument and the phase shift in [fs] for the case that σ_i<<$(\sigma_r + E)$ becomes:

(6.18) $arg(t/t_V) \cong atan\left(\frac{-\sigma_i}{E+\sigma_r}\right) + B$ $\frac{\omega d_2}{c}(n^2+1) \ll 1, \quad \sigma_i$<<$(\sigma_r + E), \quad (d_1, d_2) \ll d_3$

(6.19) $\Delta\phi[fs] = \frac{1000}{\omega[THz]} arg(t/t_V)$ see Eq. 6.18

In which σ_r and σ_i are the real and imaginary part of the optical conductivity in EuO (σ_2, medium 2), respectively and $\Delta\phi$ is the phase shift in femtosecond (fs). In our case E is a reasonable large number; 2.72x10^5 [1/Ω m]. The absolute value of t/t_V we can write as:

(6.20) $|t/t_V| = A\ \frac{E}{E+\sigma_r}$ $i\frac{\omega d_2}{c}(n^2+1) \ll 1, \quad \sigma_i$<<$(\sigma_r + E), \quad (d_1, d_2) \ll d_3$

After inversion we see that we can determine σ_r and σ_i as follows:

(6.21) $\sigma_r = E\left(\frac{A}{|t/t_V|} - 1\right)$ $\quad i\frac{\omega d_2}{c}(n^2+1) \ll 1, \quad \sigma_i << (\sigma_r + E), \quad (d_1, d_2) \ll d_3$

(6.22) $\sigma_i = [-\tan(arg(t/t_V) - B)] \cdot [E + \sigma_r]$ $\quad$ see Eq. 6.21

Eq. (6.16), (6.21) and (6.22) will be used later on to calculate σ_r and σ_i from t/t_V. Once we determined σ_r from $|t/t_V|$, we can determine σ_i from the phase: $arg(t/t_V)$. Now we will see what will happen when we optically change the optical conductivity with a laser. If the optical conductivity, because of the effect of the laser, changes from σ_2 to $(\sigma_2 + \Delta\sigma_2)$, we can write for the ratio of the transmission:

(6.23) $\frac{t(laser\ on)}{t(laser\ off)} = \frac{\Delta t(\omega)}{t(\omega)} + 1 = \frac{2n+\sigma_2 Z_0 d_2 - i\frac{\omega d}{c}(n^2+1)}{2n+(\sigma_2+\Delta\sigma_2)Z_0 d_2 - i\frac{\omega d_2}{c}(n^2+1)}$

As before, we can neglect the small $i\frac{\omega d_2}{c}(n^2+1)$ term in our case. We can calculate the complex $\Delta\sigma(\omega)$ from the complex $\Delta t/t$ as follows:

(6.24) $\Delta\sigma(\omega) = -\frac{\frac{\Delta t(\omega)}{t(\omega)}}{\frac{\Delta t(\omega)}{t(\omega)}+1}[E + \sigma(\omega)]$ $\quad \frac{\omega d_2}{c}(n^2+1) \ll 1$

From now on we will always work within the assumption that: $\frac{\omega d_2}{c}(n^2+1) \ll 1$. Therefore we will omit this assumption behind the equation. Within our assumption, we can relate the real and imaginary component of $\Delta\sigma$ directly with the pump induced changes $\Delta t/t$:

(6.25) $\Delta\sigma_r(\omega) = -\frac{\frac{|\Delta t(\omega)|}{|t(\omega)|}}{\frac{|\Delta t(\omega)|}{|t(\omega)|}+1}[E + \sigma_r(\omega)]$ $\quad (\sigma_i, \Delta\sigma_i) \ll (\sigma_r + E), \quad \Delta\sigma_r \gg \Delta\sigma_i$

(6.26) $arg(\Delta t/t) = \operatorname{atan}\left(\frac{\Delta\sigma_i}{\Delta\sigma_r} - \frac{\sigma_i+\Delta\sigma_i}{E+\sigma_r+\Delta\sigma_r}\right)$ $\quad (\sigma_i, \Delta\sigma_i) \ll (\sigma_r + E), \ \Delta\sigma_r \gg \Delta\sigma_i$

(6.27) $\Delta\sigma_i \cong \tan[arg(\Delta t/t)] \cdot (E + \sigma_r + \Delta\sigma_r) + \sigma_i$ $\quad (\sigma_i, \Delta\sigma_i) \ll (\sigma_r + E), \ \Delta\sigma_r \gg \Delta\sigma_i$

Eq. (6.25) will be used in order to calculate $\Delta\sigma_r(\omega)$ from $|\Delta t|/|t|$in optical-pump THz-probe experiments where the pump induced phase shift is very small, see the experimental section. Note that Eq. (6.25) differs slightly from the equation which is used very often in the literature (see for instance [11,13]) for a vacuum/film/substrate system; see the nominator of the second term:

(6.28) $\Delta\sigma_r \cong \left(\frac{1}{\left|\frac{\Delta t}{t}+1\right|} - 1\right)\frac{1+n}{Z_0 d_2}$ $\quad (\sigma_i, \Delta\sigma_i) \ll \frac{1+n}{Z_0 d_2}, \ \Delta\sigma_r \gg \Delta\sigma_i, \ \sigma_r = 0$

In the derivation of this equation medium one is vacuum instead of MgO. The difference between Eq. (6.28) and Eq. (6.25) for n=3.08 is -34%. Using Eq. (6.28) with n=3.08 (MgO at 1 THz), d_2=60 nm, and $\sigma_r = 0$, $\Delta\sigma_r$ is plotted against $-|\Delta t|/|t|$, see Fig. 6.3. Having, generally, a signal to noise better than 0.5% ($\Delta t/t$), we can probe an increase of the optical conductivity in the range of 10^3-10^7 $\Omega^{-1}m^{-1}$. We can also see that for small $\Delta t/t$ the optical conductivity change is proportional to $\Delta t/t$.

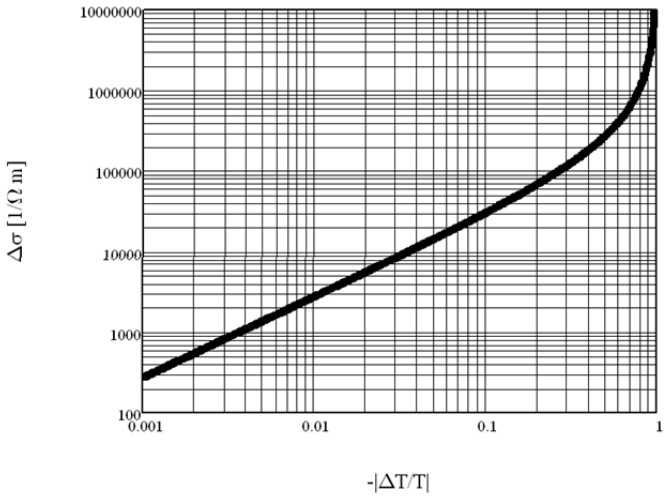

Figure 6.3 | The optical conductivity $\Delta\sigma_r$ is plotted against $\frac{-\Delta t}{t}$ for n=3.08 (MgO at 1 THz) and d_{EuO}=60 nm for a sample structure shown in Fig. 6.2.

6.1.3 Conductivity models

Later on in this chapter, the photo-induced increase of the conductivity is interpreted in the framework of the Drude model and other conductivity models. In this section we will discuss these models. In the Drude model, where the electrons are modeled as damped harmonic oscillators with a resonance frequency of zero, the optical conductivity is [7]:

(6.29) $\sigma = \frac{\sigma_0}{1-i\omega\tau} = ne\mu_{Drude}$ - Drude conductivity

(6.30) $\sigma_0 = \frac{n_c e^2 \tau}{m}$ - (real part) optical conductivity at (ω=0, ϵ_∞=1)

where the frequency dependent Drude mobility is defined as [14]:

(6.31) $\mu_{Drude} = \frac{e\tau}{m}\frac{1}{1-i\omega\tau}$, - frequency dependent Drude mobility

which at ω=0 reduces to the classical formula for the static mobility $\frac{e\tau}{m}$. When the free electrons are in a medium with dielectric constant ϵ_∞, we can write for the real and imaginary part of the conductivity:

(6.32) $\sigma_r = \frac{\sigma_0}{1+\omega^2\tau^2}$ - real part optical conductivity

(6.33) $\sigma_i = \omega\varepsilon_0(1-\epsilon_\infty) + \frac{\omega\tau\sigma_0}{1+\omega^2\tau^2}$ - imaginary part optical conductivity

Where ϵ_∞ is the dielectric function at ω=0 and n_c is the carrier concentration. In vacuum ϵ_∞=1. For this case, the real and imaginary part of the optical conductivity, divided by σ_0, are plotted in Fig. 6.4.

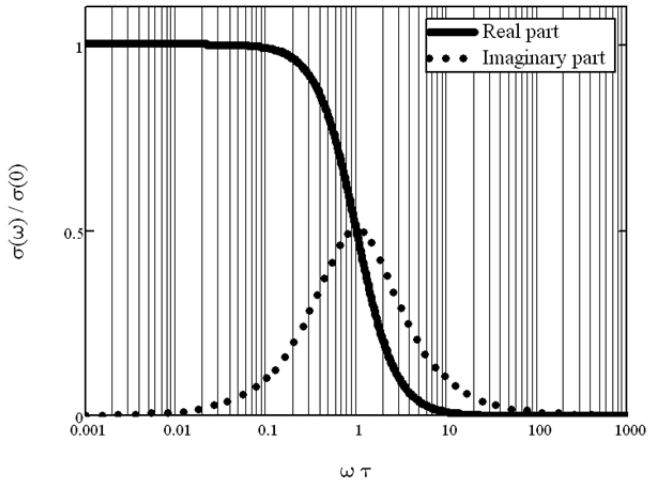

Figure 6.4 | The optical conductivity σ_r/σ_0 and σ_r/σ_0 are plotted against ω for τ=1 and ϵ_∞=1.

From Fig. 6.4 we can see that in the ωτ<<1 limit, which is very often the case in the THz regime, σ_r can be considered as frequency-independent while σ_i is small. In the case of EuO, however, ϵ_∞=26.5. $\sigma_r(\omega)$ and $\sigma_i(\omega)$ for ϵ_∞=26.5, n_c=0.1%, and different scattering times τ (we do not know τ for our samples, and in the literature a wide range of scattering times has been observed) is shown in Fig. 6.5.

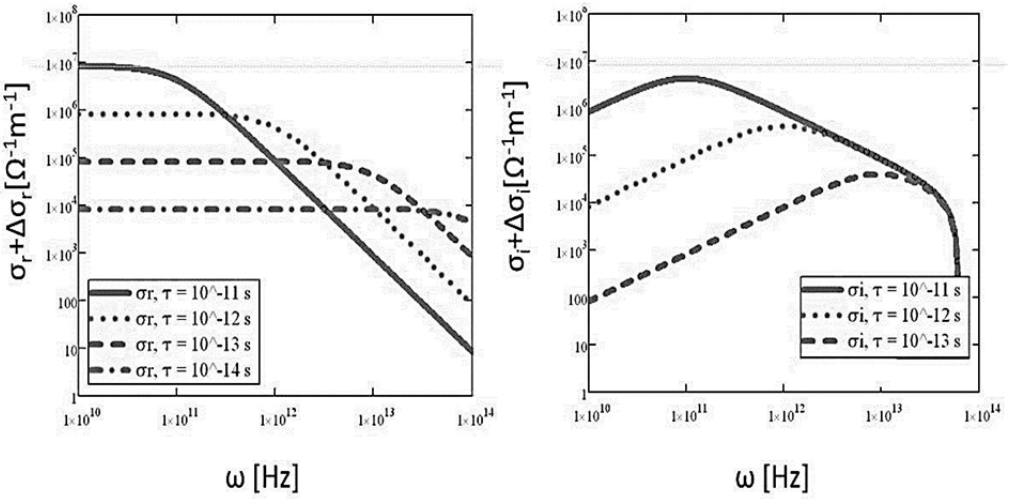

Figure 6.5 | The optical conductivity σ_r and σ_i, calculated within the Drude model framework, are plotted against ω for ϵ_∞=26.5 and different scattering times τ. n_c=0.1% Note that it is a double log plot.

As we can see, depending on the scattering time, σ_r is flat or is decreasing with frequency in this frequency range shown while σ_i is increasing with increasing frequency in the low frequency range; after reaching a maximum at 1/ τ it decreases with increasing frequency. The magnitude of σ_i is increasing with increasing scattering time τ in the frequency range shown. Since we experimentally observe a relatively flat conductivity in the THz range, we can say that the scattering time is shorter than about 100 fs and that $\sigma_r >> \sigma_i$. We expect τ not to be much shorter than 10 fs, based on literature values [2]. A frequency independent σ_r (in the depicted range) will also result in a frequency independent $|\Delta t/t|$.

Using Eq. (6.23) with n=3.08 (MgO at ω= 1THz) and d=60 nm, we can make a plot of $|\Delta t/t|$ and $\frac{arg(\Delta t/t)}{\omega}$ versus n_c for different scattering times, see Fig. 6.6 (ϵ_∞=26.5). From this we can estimate how large the pump-induced amplitude change will be and how large the pump-induced phase is. Here we took for the non-photo-excited conductivity: $\sigma_r = 0, \sigma_i = \omega\varepsilon_0(1-\epsilon_\infty)$. n_c is in between 10^{24}-10^{28}m^{-3}, which corresponds to doping concentrations in between 0.0033% and 33% respectively. $|\Delta t/t|$ is increasing with increasing frequency and saturates to one at high n_c; the saturation point depends on the scattering time. The pump-induced phase shift (Δ(Δϕ)) in fs is plotted in the right graph of Fig. 6.6. Δ(Δϕ) is more or less constant for low carrier concentrations but decreases for high carrier concentrations. For large scattering times, Δ(Δϕ) is close to 1 ps, whereas for small scattering times,

Δ(Δϕ) is about 10 fs for low n_c. A phase shift of more than 100 fs, should be definitely visible is our experiments. Therefore the magnitude of the phase shift at low n_c can give us valuable information about the frequency dependent Drude mobility.

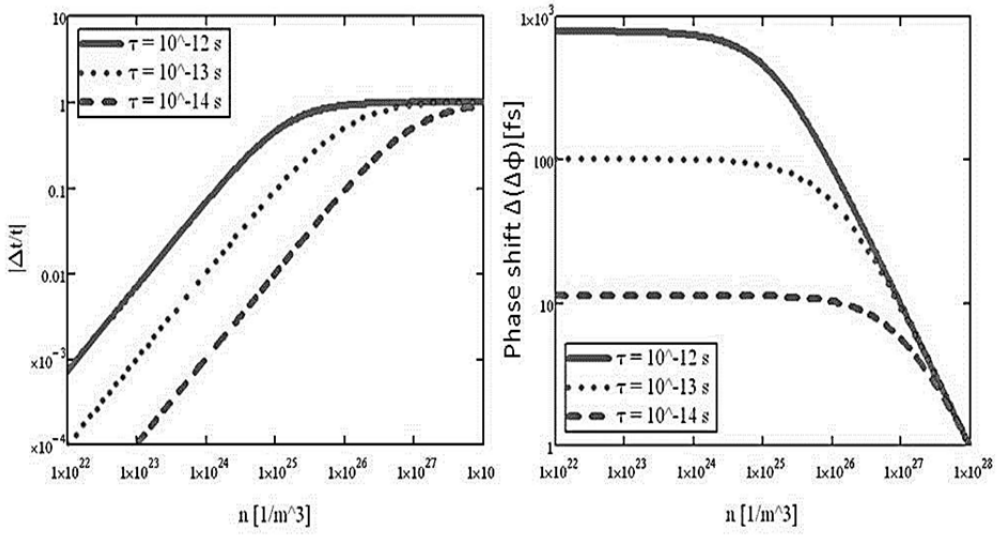

Figure 6.6 | $|\Delta t/t|$ and $arg(\Delta t/t)/\omega$ in [fs] are plotted against the carrier concentration for ϵ_∞=26.5, ω=1 THz, n_{MgO}=3.06, d_{EuO}=60 nm and different scattering times. The unpumped conductivity is taken as $\sigma_r = 0, \sigma_i = \omega\varepsilon_0(1-\epsilon_\infty)$.

Having derived a simple expression in which we can calculate $\Delta\sigma_r$ from $\Delta t/t$, later on, we have to deduce whether the changes in the conductivity are related to changes in the carrier concentration (n_c), or changes in the mobility:

(6.34) $\Delta\sigma_r = (n_c + \Delta n_c)e(\mu + \Delta\mu) - n_c e\mu = \Delta n_c e\mu + n_c e\Delta\mu + \Delta n_c e\Delta\mu$

The pump excitation can lead to an increase in the amount of free electrons n_c, and therefore also for an increase in the conductivity. After this the conductivity will relax back to the equilibrium value. In semiconductors there exists different general relaxation mechanisms of $\Delta\sigma_r$. One of them is electron-hole recombination. This lead to a drop in the amount of free electrons n_c and therefore also to a drop in $\Delta\sigma_r$. Another reason for a drop in $\Delta\sigma_r$ can be the fact the free electrons becomes bounded, for instance because of exciton formation or trapping (by deep traps). The bound electrons can be described by the Lorentz model [7]:

(6.35) $\sigma = A\ \frac{1}{1 - i\tau\omega + i\tau\frac{\omega_0^2}{\omega}}$ - conductivity in Lorentz model

(6.36) $A = \frac{n_c e^2 \tau}{m} f$ - amplitude for an oscillator with strength (f).

(6.37) $\mu_{Lorentz} = \frac{e\tau}{m} \frac{1}{1 - i\tau\omega + i\tau\frac{\omega_0^2}{\omega}}$ - frequency dependent mobility

in which A is the amplitude and ω_0 is the resonance frequency. As we will see later, in our experiments there are no sharp features in the conductivity spectrum indicating that we are probing either free electrons or bound electrons with a high resonance frequency: $\omega_0 >> \omega$ (when $\omega_0=0$, the equations are the same as in the Drude model). When we are in the limit $\omega_0 >> \omega$ (large binding energy), the real and imaginary part of the mobility becomes:

(6.38) $Re(\mu_{Lorentz}) = \frac{e\tau}{m} \frac{1}{1+\tau^2 \left(\frac{\omega_0^4}{\omega^2}\right)}$, $Im(\mu_{Lorentz}) = \frac{e\tau}{m} \frac{-\tau \left(\omega_0^2/\omega\right)}{1+\tau^2 \left(\frac{\omega_0^4}{\omega^2}\right)}$

From which we can see that real part of the mobility is 0 at ω=0 in contrast to the Drude mobility:

(6.39) $Re(\mu_{Drude}) = \frac{e\tau}{m} \frac{1}{1+\tau^2 (\omega^2)}$, $Im(\mu_{Drude}) = \frac{e\tau}{m} \frac{\tau (\omega)}{1+\tau^2 (\omega^2)}$

In the limit that the resonance frequency a much higher than THz frequencies, $\omega_0 >> \omega_{THz}$, we can see the real part of the Drude mobility is much higher than the Lorentz mobility. This means we will see a drop in the real part of the conductivity when the free electrons becomes bound and $\omega_0 >> \omega_{THz}$. The Lorentz (left) and Drude (right, c=0 curve) conductivities are shown in Fig. 6.7. We can see that for small ω, σ_r is much larger for free electrons.

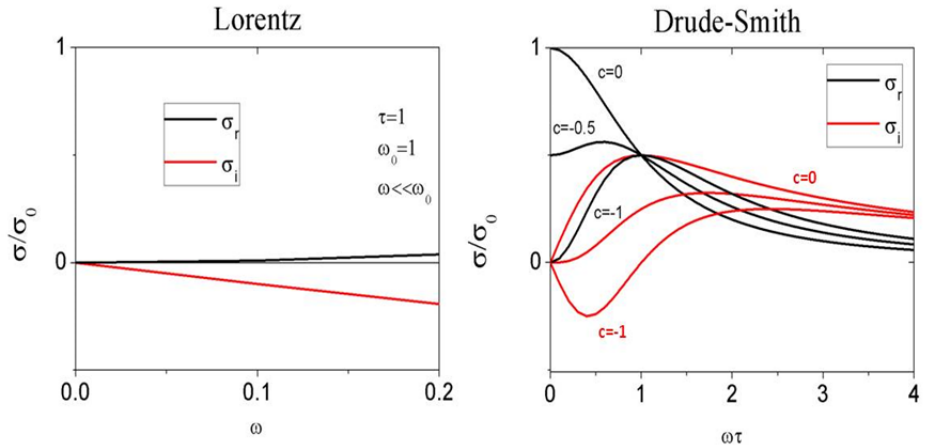

Figure 6.7 | Real and imaginary part of the conductivity in the Lorentz (left) and Drude-Smith (right) model. In the Lorentz model we took $\tau=\omega_0=1$ and we are in the limit $\omega<<\omega_0$, the oscillator strength we took as one. In the Drude-Smith model [15], the conductivity for different c values is shown. From top to bottom: c=0, c=-0.5, c=-1. σ_0 is defined as $n_c e^2 \tau / m$.

When we see a drop in the conductivity because of the fact that the electrons become strongly bound, we interpret the dynamics in terms of a change in the *free* carrier concentration. The conductivity, however, can also change due to changes in the free carrier mobility. In the framework of a pump probe experiment and the Drude model, this means that the scattering time τ can be time-dependent (pump-probe delay dependent). This can be the case for instance due to pump induced changes in the lattice temperature, which affects the electron-phonon scattering rate, but also due to changes in the spin temperature. In the CMR manganites a drop in the conductivity has been observed due to an increased spin-temperature [16]. Apart from that, in semiconductors, also carrier localization effects have been considered [14]. Disorder (by impurities, defects or other random potentials) can induce strong localization of charge carriers. Localization can strongly reduce the *dc* conductivity while the optical conductivity has a maximum at finite frequencies [15]. Smith made a model which can describe materials in which long-range transport is suppressed by disorder [15]. The so-called Drude-Smith model has been used to describe the conductivity spectra in a wide range of materials: polymers, poor metals and semiconductors (nanostructures) [12,14]. The modified Drude model becomes:

$$(6.40)\quad Re(\mu_{Drude-Smith}) = \frac{e\tau}{m}\ \frac{1}{1+\omega^2\tau^2}\left[1+\frac{c\left(1-\omega^2\tau^2\right)}{1+\omega^2\tau^2}\right]$$

$$(6.41)\quad Im(\mu_{Drude-Smith}) = \frac{e\tau}{m}\ \frac{\omega\tau}{1+\omega^2\tau^2}\left[1+\frac{2c}{1+\omega^2\tau^2}\right]$$

In which *c* is the *persistence of velocity* parameter which can be in between -1 and 0 and which tells how much of the velocity is retained after one scattering event [12]. With *c*=0, the carriers scatter isotropically, thereby randomizing the momentum completely. When *c*=-1, charge carriers are allowed to scatter anisotropically (reflection). For *c*=0, the Drude model is recovered and the carriers are delocalized. For *c*=-1, there is full localization. For intermediate values there is a partial localization. The conductivity spectra for different *c* values are shown in the right graph of Fig.6.7. From this graph we can see that there is a maximum at finite frequencies and that $\sigma_r(0)/\sigma_0$ changes from 1 (c=0, Drude) to 0 (c=-1). We can also see that for c=-1, σ_r/σ_0 has a positive slope for $\omega\tau<<1$ and that there is a maximum at ωτ. Note that in the THz frequency range one very often is in the $\omega\tau<<1$ regime. The *large* positive slope of σ_r/σ_0 is indicative for strong localization effects (in the Lorentz model with $\tau=\omega_0=1$ and $\omega<<\omega_0$ the slope is also positive but very small).

From this analysis we can see that changes in the conductivity can be also ascribed to change the localization.

Summarizing, in semiconductors the conductivity variations in the conductivity can ascribed to changes in free carrier concentration n_D, isotropic scattering time τ_D, localization c, bound electron concentration n_L, bound electron scattering time τ_L and bound electron resonance frequency ω_0, see Fig. 6.8, where the equation for the real part of the conductivity is depicted. When $\omega << \omega_0$, the second term in the equation in Fig. 6.8 is small (Lorentz term) and is smaller than the first term. This means that in this case in a typical semiconductor, the variations in the conductivity (σ_r) should be mainly ascribed to the time-dependence of $n_D(t)$, $c(t)$ and $\tau_D(t)$.

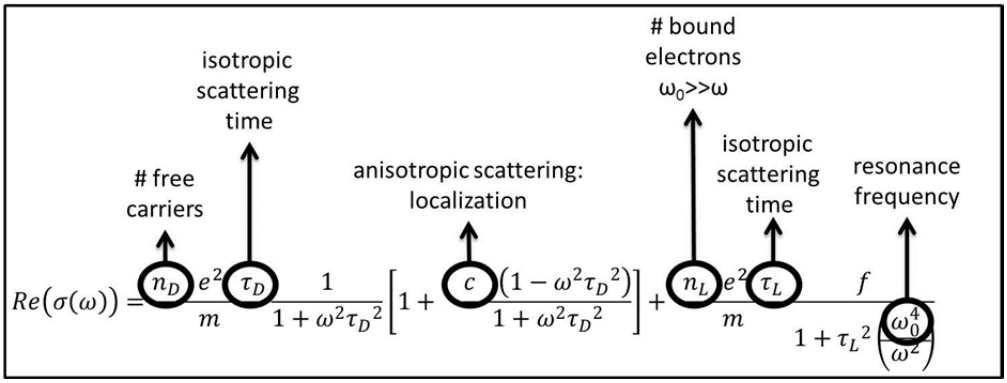

Figure 6.8 | Equation for the real part of the optical conductivity in terms of the Drude-Smith and Lorentz model ($\omega_0 >> \omega$). #= number of, f= oscillator strength.

6.2 Experimental setup

In this chapter we show and discuss measurements in which the sample is excited by a strong short (≈100 fs) optical laser pulse with a wavelength of 800 nm after which the conductivity is probed using weak, short (≈1 ps), single cycle coherent THz-pulses. In this section we first discuss how we generate single-cycle THz pulses, and how they are detected. Since the used setup is a very standard THz setup and because of the fact that the details of our setup are described in [17,18], we will discuss this only briefly. A schematic picture of our setup is shown in Fig. 6.12.

6.2.1 THz generation

In our setup we use a Ti:sapphire regenerative laser amplifier , providing ≈100 fs long pluses at a repetition rate of 1 kHz and a central wavelength of 800 nm. In order to create THz pulses by the process of optical rectification, a collimated laser

beam is steered though a [110]-oriented, 1 mm-thick ZnTe crystal [17,18]. ZnTe has no inversion symmetry, and therefore second order non-linear processes (like optical rectification) are allowed. ZnTe is a good generation crystal due to its high second-order non-linear optical constant $\chi^{(2)}(800nm)$= 1.6 x 10^{-7} esu [18], and due to the small group velocity mismatch between the 800 nm THz generation beam and the THz beam [18]. Also the fact that the ZnTe bandgap (E_g=2.28 eV [18]) is large is favorable because this means that the absorption at 800 nm is small. The bandwidth of our 800 nm pulses is around 10 nm. Having a bandwidth of 10 nm, the maximum frequency which can be generated by difference frequency generation is 4.7 THz. This is an upper limit for the frequency, set by the laser bandwidth. After the ZnTe crystal, a 2 mm think Teflon plate is placed in order to block the 800 nm beam; the THz beam is transmitted by the Teflon plate. The cone of THz light which is emitted from the ZnTe "point source" is collimated by a 45 degrees off-axis parabolic mirror. A second 45 degrees off-axis parabolic mirror focusses the beam on the sample in the cryostat. Due to the fact that THz light is absorbed by air, the THz generation, the sample and the THz detection is done in a vacuum box which is pumped by a diffusion pump.

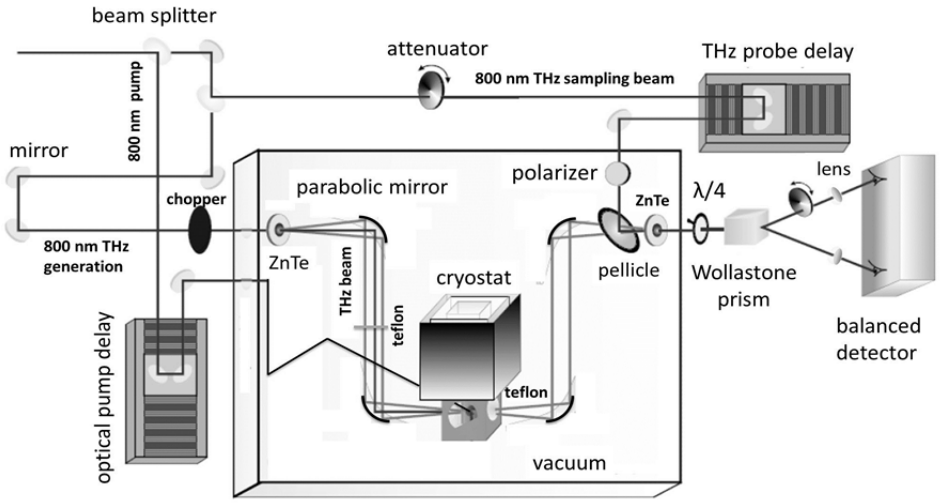

Figure 6.12 | Schematic picture of our optical-pump THz-probe setup. For details, see the text. This figure is adapted from [18].

6.2.2 THz detection

THz electric field detection (amplitude + phase) by means of standard electronics is challenging due to the very high frequencies involved (compared to typical

electronic frequencies). A relatively simple optical technique was developed based on a (THz) pump- (optical) probe scheme which does not require helium cooled THz detectors [17,18]. Moreover, by using a pump-probe scheme, we can overcome the problem of measuring processes (changes in the electric field in this case) with frequencies >>1 GHz; we will have the desired THz bandwidth. THz detection is performed by the so-called free-space electro-optic sampling (FSEOS) method [18]. In this technique, the low frequency (compared now to optical frequencies which are $>10^{14}$Hz) THz electric field induces birefringence at optical frequencies (λ=800 nm) in a [110] oriented ZnTe THz detection crystal, in a similar way as in the Pockels effect [17,18]. In the Pockels effect, a *dc* electric field can induce changes to the birefringence at optical frequencies in materials with non-zero second-order non-linear effects (materials without inversion symmetry). The induced birefringence is proportional to the electric field amplitude. In our case, the slow varying THz electric field modifies the birefringence in ZnTe; the birefringence at λ=800 nm directly follows the THz electric field amplitude. The changes in the birefringence, which are happening at the ps timescale, are observed by sending a linearly polarized, so-called, THz sampling beam through the ZnTe detection crystal and by monitoring the (THz pulse-induced) changes in the polarization state of the sampling beam. The THz sampling beam has a wavelength of λ=800 nm and a pulse duration of FWHM≈140fs, which is much shorter than one period of a THz pulse. The THz-sampling pulse can be time-delayed with the THz pulse, after which we can measure the THz pulse induced-birefringence changes in ZnTe versus delay (τ)[1].

The ZnTe THz detection crystal needs to be thin: due to the group velocity mismatch between the THz pulse and the 800 nm sampling pulse, which is 0.4 ps/mm, a thicker crystal results in a larger probing time-window, thereby decreasing the time-resolution of the THz detection. In our case the thickness of the [110] oriented ZnTe detection crystal was 0.2 mm. The influence of the THz probing resolution on the spectrum is depicted below, Fig. 6.13. In this graph a THz pulse is convoluted with a Gaussian (red lines), which represents the temporal resolution of the THz detector (THz probing). The THz pulse here is “generated” by

[1] The THz pulse detection scheme is similar to a standard pump-probe technique. The THz “pump” beam changes the birefringence in ZnTe after which the optical “probe” beam with λ=800 nm, probes the birefringence changes at different delays. The THz pulse induced-birefringence changes at λ=800 nm at time *t* is linearly proportional to the THz electric field amplitude at time *t*. This means that if we can measure the birefringence changes at λ=800 nm versus the (THz pulse)-(THz sampling pulse) delay, we can deduce the THz electric field versus time.

taking the second derivative of a Gaussian. The un-convoluted pulse is the blue line whereas the black lines represent the convoluted pulses. By taking the Fourier transform of the THz pulse, we can obtain the THz spectrum. The normalized spectra are shown in the right graph of Fig. 6.13. For Gaussians with a larger FHWM (in the time domain), the maximum in the THz spectrum is red-shifted, see the inset. This graph shows that one needs to have either a very good THz probing temporal resolution, or one needs to correct the spectrum for the limited temporal resolution. One can do this as follows. When we name the real un-convoluted THz pulse in the time domain $R(t)$ and the Gaussian $G(t)$, the Fourier transform gives: $FT[R(t)*G(t)]=FT[R(t)]\ FT[G(t)]$, in which * represents the convolution operator. This means that the convoluted spectrum $FT[R(t)*G(t)]$ needs to be divided by the Fourier transform of the temporal resolution $FT[G(t)]$, which is represented by a Gaussian $G(t)$, see the inset in the right graph of Fig. 6.13. For a Gaussian of 100 fs, $FT[G(t)]$ is more flat in the frequency domain (0-3 THz) than for a 500 fs Gaussian. The THz probing temporal resolution G(t) is limited by the 800 nm pulse duration and the group velocity mismatch between the THz pulse and the 800 nm sampling pulse. The latter origin favors thin ZnTe THz detection crystals. Due to the fact that we do relative measurements (sample vs. no sample; pump vs. unpumped), the effect of the limited THz probing temporal resolution on the spectra is divided out: $FT[R_{pumped}(t)*G(t)]/\ FT[R_{unpumped}(t)*G(t)]= FT[R_{pumped}(t)]/\ FT[R_{unpumped}(t)]$.

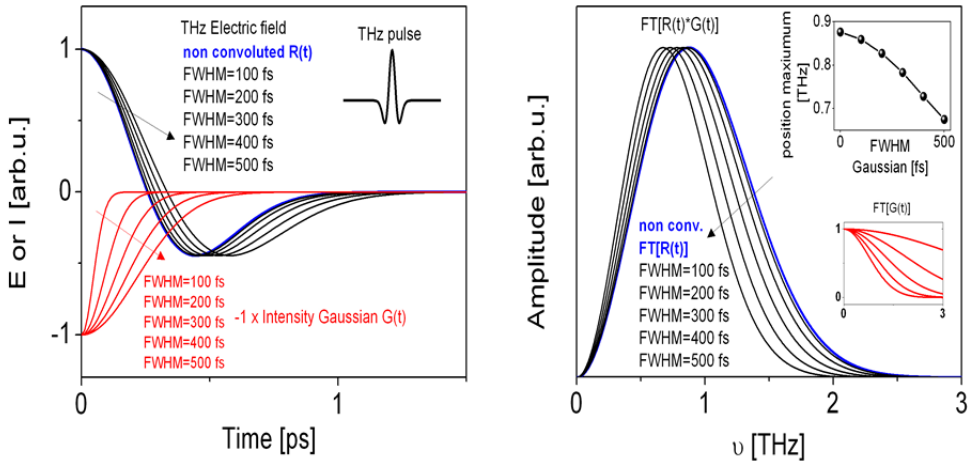

Figure 6.13 | THz pulse (blue line) convoluted with different Gaussian (red lines). The normalized THz spectrum is shown in the left graph. The inset shows the maximum of the THz peak.

The fact that a thin ZnTe crystal is used also has disadvantages: due to multiple reflections within the thin ZnTe crystal, small replicas of the THz pulse will appear at different delays. Depending on whether the weak reflection is resulting from the sampling pulse or from the THz pulse, the replicas can precede or succeed the main THz signal in time. To overcome this problem, the [110] oriented ZnTe detection crystal is mounted on a [100] oriented ZnTe crystal of 0.5 mm. In the thick [100] oriented ZnTe crystal, due to phase matching conditions, no Pockels effect will take place [18]. However, due to the fact the refractive index of the [110] oriented and [100] oriented ZnTe are very similar, there are no reflections from the [110] - [100] boundary. This means that the reflections are delayed by (0.5 mm x 2 x v_g) in which v_g is the group velocity of the 800 nm pulse or the THz pulse.

As said before, the THz light and the 800 nm beam are parallel and overlapping in the ZnTe THz detection crystal. This is done in the following way. The focused THz beam at the sample is collimated by a 45 degrees off-axis parabolic mirror after which it is focused to the ZnTe detection crystal by another 45 degrees off-axis parabolic mirror. In order to make the 800 nm beam collinear with the THz beam, a pellicle beam splitter is placed before the ZnTe THz detection crystal which transmits the THz beam, but reflects (part of) the THz sampling beam (with λ=800 nm). The THz beam and the sampling beam are overlapped on the pellicle after which they are send collinearly to the ZnTe THz detection crystal. The linearly polarized sampling beam is collimated (and not focused) before the ZnTe THz detection crystal. After the ZnTe detection crystal, the sampling beam (λ=800 nm) leaves the vacuum box. Since the THz detection happens by the non-linear mixing of the THz beam and 800 nm beam in the ZnTe crystal, the polarization state measurement of the sampling pulse can be done in air.

Without the presence of the THz pulse, the sampling beam is linearly polarized. With the presence of the THz pulse, the polarization state becomes elliptical. The ellipticity is measured by a half wave plate (HWP), Wollaston prism (WP) and two balanced photodiodes. The method of measuring the ellipticity has been discussed in detail in Chapter 5. The optical axis of the HWP makes an angle of α=45 degrees with respect to the sampling beam polarization in the case there is no THz light. The optical axis of the two prisms of the WP are at α=90/0 degrees. The ellipticity is calculated from the intensities of the two photodiodes as follows:

(6.42) $\frac{I_A - I_B}{I_A + I_B} = sin2\psi \cong 2\psi \cong 2\varepsilon$

In which $I_{A,B}$ are the horizontal and vertical intensity components of the 800 nm sampling beam, measured by photodiode A and B respectively. ψ, ε are the ellipticity angle and the ellipticity, respectively. It can be shown that the ellipticity is linearly proportional to the THz electric field amplitude (E_{THz}) in the ZnTe detection crystal, in the case that the THz electric field amplitude is small [19]:

(6.43) $\frac{I_A - I_B}{I_A + I_B} \cong 2\varepsilon = \frac{\omega n^3 E_{THz} r_{41}}{2c}(cos(\alpha)\sin(2\varphi) + 2\sin(\alpha)\cos(2\varphi))$

In which n is the refractive index of ZnTe at 800 nm and α is the angle between $\vec{E}_{THz}$ and the (001) axis of ZnTe. φ is the angle between the optical electric field ($\vec{E}_{opt}$) and the (001) axis of ZnTe [19]. r_{41} is the only nonzero coefficient of the electro-optic tensor of ZnTe: r_{41} = 4.04 pm/V [18]. The highest detection efficiency can be achieved with both parallel or crossed, (E_{THz}, E_{opt}) polarizations for α=90 and 270 degrees [19].

In our experiments, the THz generation beam is modulated by an optical chopper with frequency (f_1); therefore the THz beam is also modulated at f_1. The THz beam modulation, in turn, will lead to a polarization state modulation of the sampling beam at f_1. Since $I_A - I_B \sim \varepsilon \sim E_{THz}$, the THz electric field amplitude can be determined by measuring the difference signal $I_A - I_B$ at f_1 using a lock-in amplifier.

6.2.3 THz spectra and optical pump-THz probe measurements

The THz electric field can be probed by changing the relative delay (τ_{ts}) between the THz generation beam and the THz sampling beam. After having obtained the THz electric E(t), with and without sample, we can determine the transmission amplitude spectrum by performing a Fourier Transform (FT):

(6.44) $\frac{t(\omega)}{t_V(\omega)} = \frac{|t(\omega)|}{|t_V(\omega)|}\frac{e^{i\,\varphi_t(\omega)}}{e^{i\,\varphi_{t_V}(\omega)}} = \frac{FT\left(E(\tau_{ts})\right)_{sample}}{FT\left(E(\tau_{ts})\right)_{no\ sample}}$

The Fourier transform gives us the amplitude $|t|/|t_V|$ and phase difference $arg(|t|/|t_V|) = \varphi_t(\omega) - \varphi_{t_V}(\omega)$. The accumulated (unwrapped) phase difference is used to determine the imaginary part of the optical conductivity, see Eq. (6.21). See for more details appendix.

We also performed experiments in which the sample was first excited by an optical pump pulse, and in which the changes in the conductivity of the sample was probed by a THz pulse. We first consider the optical-pump induced changes in the

transmission for a fixed optical pump-THz probe delay (τ_{pt}). The optical pump will change the transmitted THz electric field from $E(t)$ to $E(t)+\Delta E(t)$. Then we can write:

$$\frac{t_{on}}{t_{off}}(\omega) = 1 + \frac{\Delta t}{t}(\omega) = \frac{FT\left(E(\tau_{ts})+\Delta E(\tau_{ts})\right)_{optical\ pump\ on}}{FT\left(E(\tau_{ts})\right)_{optical\ pump\ off}} = 1 + \frac{FT\left(\Delta E(\tau_{ts})\right)}{FT\left(E(\tau_{ts})\right)} \quad (6.45)$$

$$\frac{\Delta t}{t}(\omega) = \frac{FT\left(\Delta E(\tau_{ts})\right)}{FT\left(E(\tau_{ts})\right)} \quad (6.46)$$

In our case, the optical pump mainly affects the amplitude of the $E(\tau_{ts})$ without any large optical-pump-induced phase shift ($\Delta(\Delta\phi)[fs]$). In order to measure the pump-induced changes in the transmission spectrum ($\Delta t/t(\omega)$) at a fixed optical pump-THz probe delay (τ_{pt}), the optical pump was chopped at frequency f_2. The optical pump, in turn, modulates the THz beam at f_2 due to the fact that the optical pump affects the conductivity of the film. Because of this, the polarization state of the sampling beam is also modulated at f_2. We determine $\Delta t/t(\omega)$ as follows:

$$\frac{\Delta t}{t}(\omega) = \frac{FT\left(\frac{I_A-I_B}{I_A+I_B}(\tau_{ts}) \rightarrow chopper\ at\ optical\ pump\ beam\ (f_2),\ optical\ pump\ beam\ open\right)}{FT\left(\frac{I_A-I_B}{I_A+I_B}(\tau_{ts}) \rightarrow chopper\ at\ THz\ beam\ (f_1),\ optical\ pump\ beam\ closed\right)} \quad (6.47)$$

After we verified that the pump induced phase shift $\Delta(\Delta\phi)[fs]$ is small, we did most of the experiments in a different way. Instead of measuring THz spectra by scanning τ_{ts} at fixed pump-probe delays τ_{pt}, we were scanning τ_{pt} for a fixed THz pulse-sampling pulse delay τ_{ts}. The THz pulse-sampling pulse delay τ_{ts} was set to the maximum of the THz pulse. In this way, we used a standard pump probe configuration where $\Delta t/t$ versus the pump-probe delay (τ_{pt}) was measured.

6.3 Results

In this section we will present the following experimental results which include sample/substrate characterization and setup characterization:

- *EuO sample preparation and characterization.*
- *THz source spectrum.*
- *The THz conductivity in (non-photo excited) EuO.*

After we characterized the setup and the sample, the optical pump-THz probe spectra and transients, fitting results and fluence dependences are presented:

- *Optical pump induced conductivity changes in EuO: spectra at fixed pump-probe delays.*
- *Pump induced conductivity changes: low fluence (0.16-0.23 mJ/cm^2) pump-probe transients.*

- *Temperature dependence of the amplitude Δσ for low fluences.*
- *Mobility and free carrier generation efficiency: fluence dependence in the paramagnetic phase ($T>T_c$).*

Based on this data we try to solve our research questions. The experimental data is discussed extensively in the discussion section.

6.3.1 EuO sample preparation and characterization

The EuO film was grown by Molecular Beam Epitaxy (MBE) at the university of Cologne. High purity Eu metal was evaporated from an effusion cell (for more information on the growth method see also [3,20]). Molecular oxygen was added simultaneously through a leak valve. The MgO substrate temperature (T_s) was kept at 300°C, in order to make Eu-rich EuO. The sample was grown on a double-side epi-polished (100) MgO substrate. Before the growth, the samples were annealed for one hour in a 1 x 10^{-7} mbar oxygen atmosphere. Eu metal was evaporated at 515 °C resulting in a growth rate around 9.2 °A/ min as was checked with a quartz crystal thickness monitor. The oxygen partial pressure near the substrate during the growth was 5 x 10^{-8} mbar as was determined with a mass spectrometer. In this way a 60 nm thick EuO film was synthesized. The samples were protected to oxidation by a 24 nm thick MgO capping layer. For making the MgO capping, the T_s was kept at 225°C and the Mg was evaporated at 298 °C with a growth rate of about 4.3 Å / min. The oxygen atmosphere during the capping layer growth was about 2.5 x 10^{-7} mbar. The magneto-optical Kerr rotation hysteresis loops (reflection, A.O.I. =45 degrees, λ=800nm, p-polarized, $\vec{B} \perp \vec{k}_{in}$) are shown in Fig. 6.14. From this we can see that T_c is around 70 K and that the samples are of good quality. The oxygen vacancy concentration is not high enough to see a second T_c around 130 K, see Chapter 1 and [21].

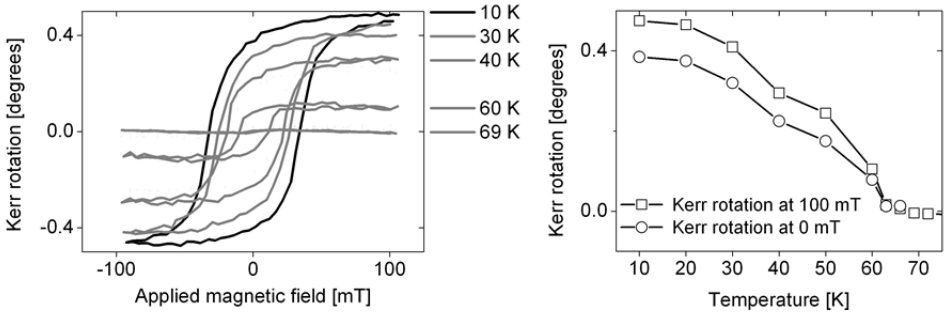

Figure 6.14 | Left) Kerr hysteresis loops: reflection, A.O.I. = 45 degrees, λ=800 nm, p-polarized. Right: the Kerr rotation versus temperature for B=100 mT and B=0 mT.

6.3.2 THz source spectrum

A typical THz pulse which is generated and detected in ZnTe, and which was propagating in vacuum is shown in Fig. 6.14. The delay line was in the step-mode and the lock-in amplifier time-constant was 300 ms. The bandwidth was limited by the THz generation and THz detection in ZnTe, and by the laser bandwidth (10 nm) and is about 3 THz. Therefore the Nyquist frequency is 6 THz. In the shown example, the electric field is oversampled: f_s =100 THz. The signal to noise ratio is about 250 and can be easily achieved in one scan. The amplitude spectrum (not corrected for the limited probing temporal resolution) was generated by performing a FT, see the right graph in Fig. 6.14. The spectrum has a maximum around 0.5 THz has a bandwidth of 3 THz. The frequency resolution can be calculated by f_s/N, where N is the number of data points. In our case the frequency resolution is f_s/N=81 GHz.

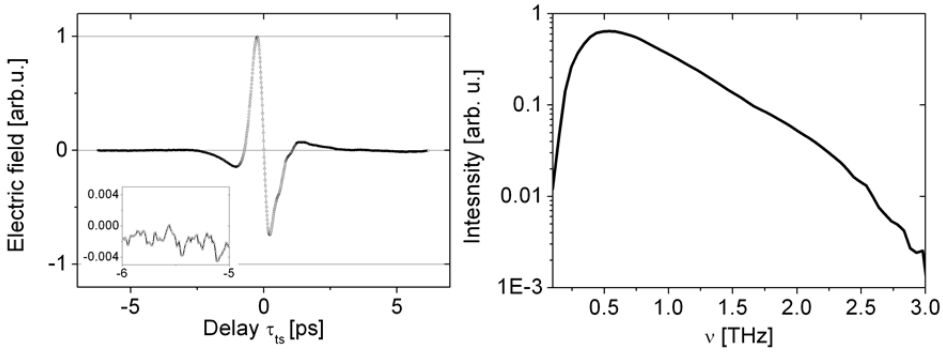

Figure 6.15 | Left) Typical THz pulse electric field in vacuum which is generated in ZnTe by optical rectification and is also detected in ZnTe by FSEOS [17,18]. Right) amplitude spectrum obtained after performing a FFT.

6.3.3 The THz conductivity in (non-photo excited) EuO

Now we will characterize the transport properties of non-photo-excited EuO. The EuO films was grown on a MgO substrate. Based on (our) THz measurements on the substrate we can conclude that the substrate is mostly transparent and that the properties are not significantly changing with temperature. The results are in agreement with literature [26]. This means that MgO is a suitable substrate for THz measurements in a wide temperature range. The transmission spectrum at T= 30 K and T=295 K for the EuO sample (+ substrate) is shown in Fig. 6.16. From Eq. (6.21), $\sigma_r(\omega)$ was calculated, see the right graph in Fig. 6.16.

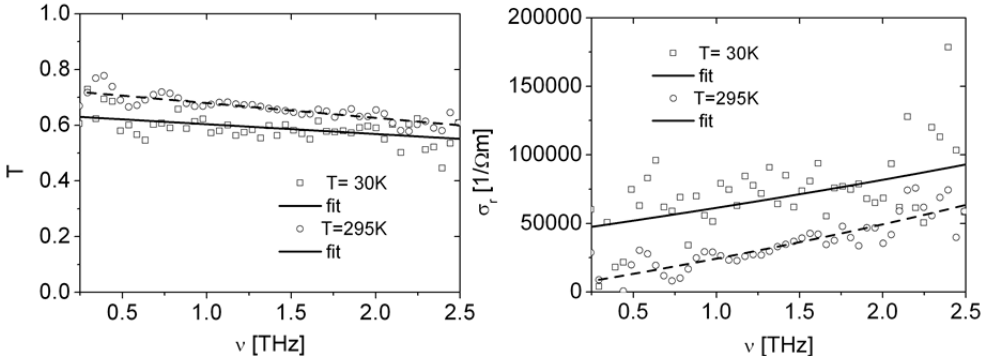

Figure 6.16 | Left) Transmission of the 60 nm EuO sample. Right) Calculated real part of the optical conductivity.

We observed a positive slope in $\sigma_r(\omega)$, both at 30 K and 295 K. The origin of the positive slope is surprising. From normal Drude behavior, a negative slope is expected. A positive slope in $\sigma_r(\omega)$ is known to occur in materials where localization caused by disorder causes non-Drude behavior: see the discussion on the Drude-Smith model before [12,14,15]. However it is also possible that the positive slope is due to the onset of a higher lying broad absorption peak. On top of that, there is then the Drude contribution, which is expected to have a flat frequency dependence in this regime (ωτ<<1). In order to be more sensitive to the temperature dependence of $\sigma_r(T)$, we set the (800 nm sampling pulse-THz pulse) delay to the maximum of the THz peak, and then we changed the temperature (T). The result is shown in Fig. 6.17.

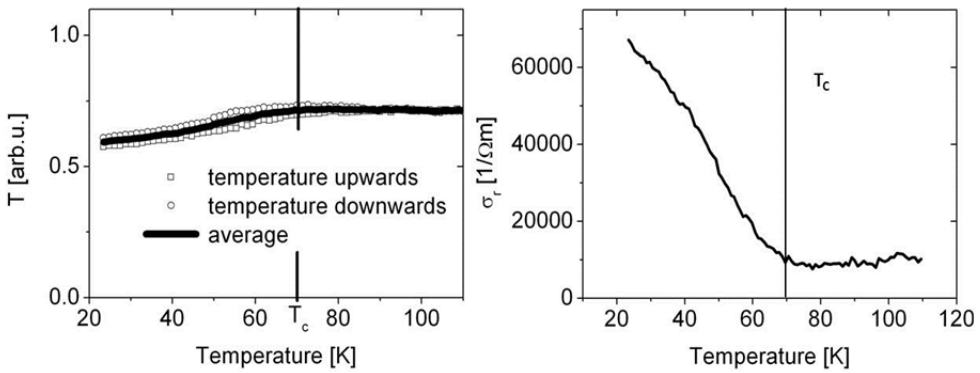

Figure 6.17 | Left) transmission at the THz peak versus temperature. The squares represent the data when the temperature was swept form 120 K towards 25 K (downwards). The dots represent the data when the temperature was swept form 25 K towards 120 K (upwards). The black line is the average. Right) the optical conductivity versus temperature.

We can clearly see a MIT around T_c. Above the transition temperature; the conductivity has a steep negative slope, typical for a metal. Above T_c, the slope is small but positive, typical for a normal semiconductor. If the conductivity is extrapolated to T=0 K, we obtain a conductivity of approximately 80000 Ω^{-1} m^{-1}. Using scattering times in the range of 10-1000 fs, a free carrier concentration (n_f=# free electrons/N_{Eu} x 100%) in the range of n_f= 0.009-0.9% is obtained by using $\sigma = n_f e^2\tau/m_0$. In the framework in which the MIT is explained by a change in n_f, this means that the estimated oxygen vacancy concentration (N_V=# vacancies/N_{Eu} x100%) is also in the N_V=0.009-0.9% range. Here we assume that at T= 0 K, all the electrons are free (vacancy level energy crosses the conduction band) and that there are no other compensating acceptor levels in the crystal; at T=0 K, $n_f = N_V$. The free carrier concentration versus temperature for different scattering times in shown in Fig. 6.18. One should realize that in reality the scattering time is expected to be temperature dependent.

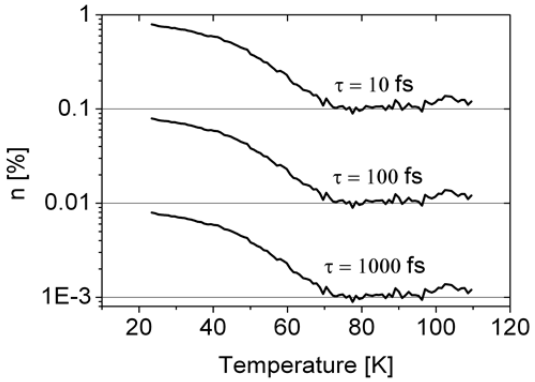

Figure 6.18 | The calculated free carrier concentration n_f versus temperature for different scattering times using the conductivity data presented in Fig. 6.16 and equation $\sigma = n_f e^2\tau/m_0$.

We can see that for 80 K, the estimated free carrier concentration is low, in the n_f=0.001-0.1% range while at 26 K n_f=0.008-0.8%. At 26 K, 81% (n_f/N_V x 100%) of the electrons are free and 19% ([1- n_f/N_V] x 100%) of the electrons are trapped in the vacancy levels. This means that the empty trap concentration is in between 0.008-0.8% at 26 K (# empty traps/N_{Eu} x100%). At 80 K the situation is different; 89% of the taps are filled. In this case the empty trap concentration is in between 0.001-0.1% (# empty traps/N_{Eu} x100%). One should realize that this analysis only works in case that the MIT is explained in terms of a free carrier concentration change and not when the MIT is explained in terms of a mobility change. However,

from our analysis in this section we at least got an idea about the maximum vacancy concentration in this EuO sample.

The imaginary part the conductivity can be obtained by looking to the relative phase shift between the [≈1 mm MgO substrate 1 + 60 nm EuO thin film] sample and the [≈1mm MgO substrate 2, no EuO film] sample. Due to the error in the thickness and the refractive index of the thick MgO substrate, it was not possible to determine the phase shift of the thin film with high accuracy, which means that we could not determine $\sigma_i(\omega)$. In the next section we measure the conductivity with the presence of a pump pulse.

6.3.4 Optical pump induced conductivity changes in EuO: spectra at fixed delays

The transmitted THz electric field amplitude, without (*E*) and with (|*ΔE*|) the presence of the pump pulse is shown in the left graph of Fig. 6.19 for temperature *T*= 26 K and fluence *Fl*=2.5 mJ/cm^2. The pump-probe delay is +0.86 ps; as we will see later this corresponds to the maximum of |*ΔE*|.

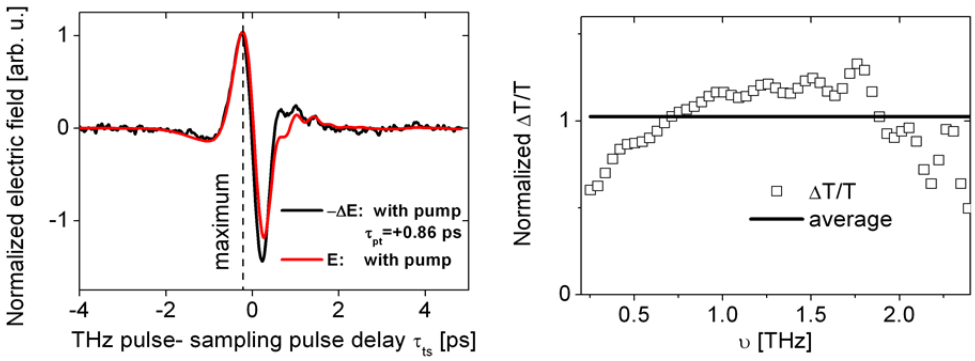

Figure 6.19 | Left) Normalized transmitted THz electric field amplitude at 26 K. The black line is *ΔE* while the red line is *E*. Right) Normalized ΔT/T in order to have an average around 1.

As we can see, even at very large fluence, there is no large phase shift of the positive maximum of the THz peak. Due the small thickness of the film, we are less sensitive to the imaginary part of the optical conductivity (which will lead to a THz pulse phase shift). This means that we can do pump-probe experiments where we fix the THz pulse-sampling pulse delay while we are scanning the optical pump-THz probe delay, as discussed before. By measuring the changes in the maximum of the THz pulse, we are mostly sensitive to the real part of the optical conductivity. This is true at all the temperatures, pump-probe delays, and fluences we use. The frequency response of the real part of the optical conductivity changes are not completely flat, see the right graph in Fig. 6.19. The black line represents the

average value of the transmission. The frequency response in the 0.8-1.7 THz range is flat. However above and below this range, there is a drop in the transmission. In the optical pump- THz probe measurements at fixed sampling pulse delay, we measure the weighted average THz pulse transmission in the 0.2-3 THz range. In next section we present the pump-probe transients in the low(er) fluence regime: *Fl*=0.16-0.23 mJ/cm^2.

6.3.5 Pump induced conductivity changes: low fluence (0.16-0.23 mJ/cm^2) pump-probe transients

Using Eq. (6.25), we determined the conductivity changes (real part) from the pump-induced transmission changes. The conductivity change for different temperatures is shown in Fig. 6.20; the fluence is *Fl*=0.23 mJ/cm^2. In the upper left graph the un-normalized data is shown whereas in the lower graphs the data is scaled to the maximum. In the upper right graph, the temperature dependence of the maximum $\Delta\sigma_{MAX}$ is shown.

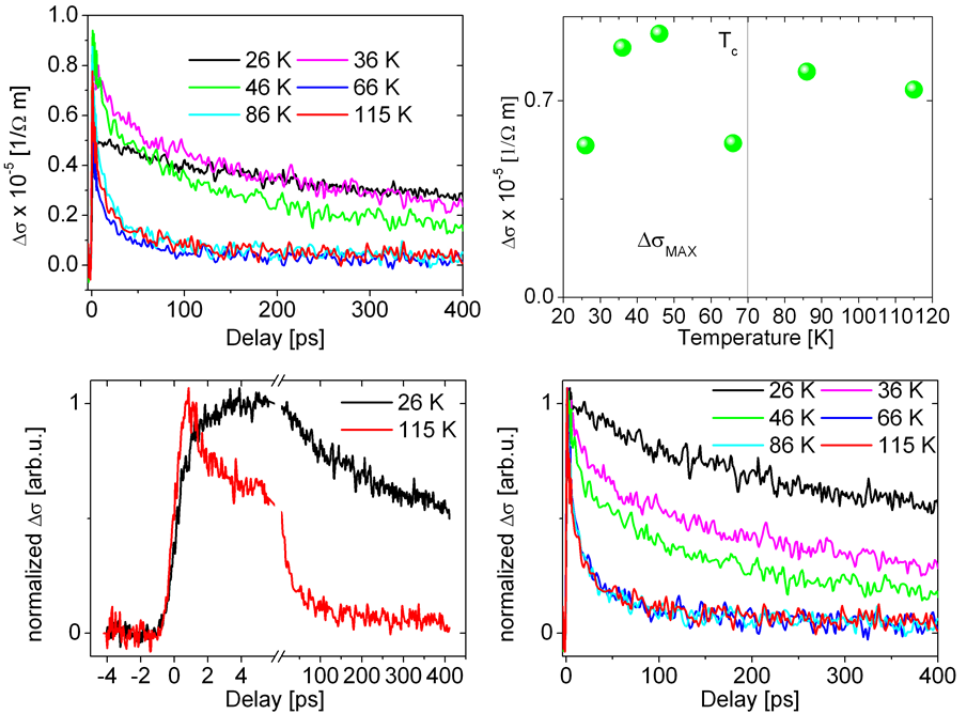

Figure 6.20 | Upper left) Δσ versus pump probe delays for different temperatures, Fl=0.23mJ/cm^2. Upper right) $\Delta\sigma_{MAX}$ versus temperature for the same fluence. Lower left) Normalized Δσ versus pump probe delays for 26 K and 115 K. Lower right) Normalized Δσ versus pump probe delays for different temperatures.

From Fig. 6.20 we can see that the decay of Δσ (for t>5 ps,) is strongly temperature dependent. We can see that at 400 ps, Δσ is large below T_c and that Δσ is small and temperate independent above T_c. The increase of Δσ at long timescale does not follow the behavior what we expect from an average temperature increase: $\partial\sigma(T)/\partial T < 0$ (see Fig. 6.17) for T<T_c. Based on this we can conclude that Δσ at long timescales is due to an electronic effect and not due to average heating. Apart from the very long-time scale (>250 ps) dynamics, there is more happening when the temperature is changed. Upon increasing the temperature starting from 26 K, the amplitude of a decaying component with a time constant of about 20 ps starts to increase. Above T_c this component is large and more or less temperature independent whereas this component is small at 26 K. Now we have a closer look to the dynamics at the first 6 ps. Whereas at 26 K we observed an ingrowing signal which is slower than the experimental temporal resolution, at 115 K the signal rise time seems to be close to temporal resolution limited.

In order to identify the different contributions to the signal, the signal is fitted with exponentials which are convoluted with a Gaussian (which represents the THz pulse). The 26 K and 115 K data was fitted with:

$$\Delta\sigma(t)/\sigma_{MAX} = G(FWHM, t_0) * \left[H(t_0) \cdot \left(X e^{-\frac{t}{\tau_X}} + Y\, e^{-\frac{t}{\tau_Y}} + Z\, e^{-\frac{t}{\tau_Z}}\right)\right], \quad (6.48)$$

In the fitting procedure, $G(FWHM, t_0)$ was obtained by fitting the high temperature and high fluence data. The obtained FWHM of 1.2 ps is much longer than the cross correlation between the optical pump and THz sampling beam which is <350 fs. We can compare this with the results on a reference sample: Si. In the Si experiments, the FWHM of the Gaussian was about FWHM=0.5 ps, indicating that the rise time even for T>T_c, might not be temporal resolution limited. However we use Eq. (6.48) and fix the FWHM of Gaussian to 1.2 ps for all the measurements. The obtained value for the rise time for the T<<T_c data is than a lower limit. Eq. (6.48) could *mathematically* describe all the data very well. Later on we will discuss the physics behind the different components *X*,*Y*,*Z*).

At 26 K *X*<0 (τ_X=0.8 ps) and *Y*,*Z*>0 (τ_Y=93.5 ps, τ_Z=971 ps). We observed that the dynamics far below T_c=69 K and above T_c is completely different. At 115 K data *X*,*Y*,*Z*>0 . The time constants in this case were τ_X=0.8 ps, τ_Y= 20 ps, τ_Z= 287 ps. The fitting results are shown in Fig. 6.21. The different (*X*, *Y*, *Z*) are depicted by thin black lines.

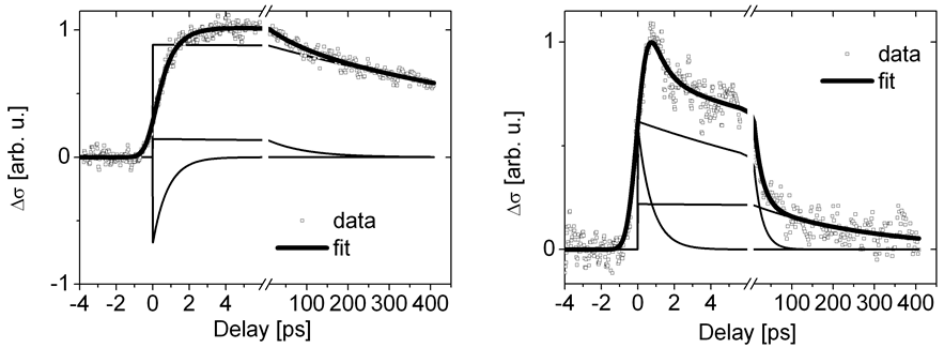

Figure 6.21 | Left) fit results of the 26 K data (*Fl*=0.16 mJ/cm^2) with Eq. (6.31). Right) fit results of the 115 K data (*Fl*=0.14 mJ/cm^2) with Eq. (6.31). The different components (X, Y, X) are depicted by thin black lines.

To convince ourselves that the rise time at low temperatures is not temporal resolution limited, we plot the fits of the low and high fluence data for 26 K and 115 K, see Fig. 6.22. The dotted lines represent the high fluence data (Fl=2.5 mJ/cm^2). We can see that the signal at T>T$_c$ grows faster than $G_{THz}(t_0=0,\sigma)*H(t_0=0)$ (green line) due to the presence a fast positive decaying exponential. The blue curve represents the Gaussian pump pulse with a FWHM of 115 fs. The situation is different for the low fluence data (Fl≈0.15 mJ/cm^2) at T<<T$_c$. Whereas the 115 K data has a fast rise time similar to the high fluence data, the 26 K data has a slow rise time; much slower than $G_{THz}(t_0=0,\sigma)*H(t_0=0)$.

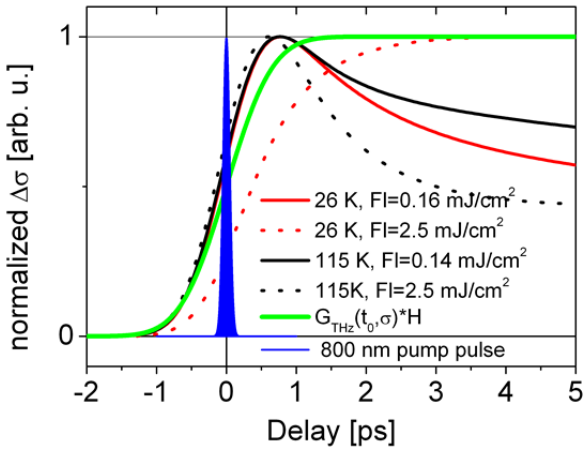

Figure 6.22 | Fit results of the 26 K and 115 K data (*Fl*≈0.15 mJ/cm^2 or 2.5 mJ/cm^2) using Eq. (6.31). The green line represents $G_{THz}(t_0=0,\sigma)*H(t_0=0)$ whereas the blue curve represents the Gaussian pump pulse with a FWHM of 115 fs.

After we convinced our self the low fluence data at 26 K and 115 K can be described by Eq. (6.48), we fitted also the other data in the 26-115 K range using Eq. (6.48). The result is shown in Fig. 6.23. The red curve represents the 26 K data with a fluence of 0.15 mJ/cm^2. The thick black lines are the normalized Δσ data at different temperatures. The green line represents the fits using Eq. (6.48). The thin black lines are the different exponents (X, Y, Z) in the fit.

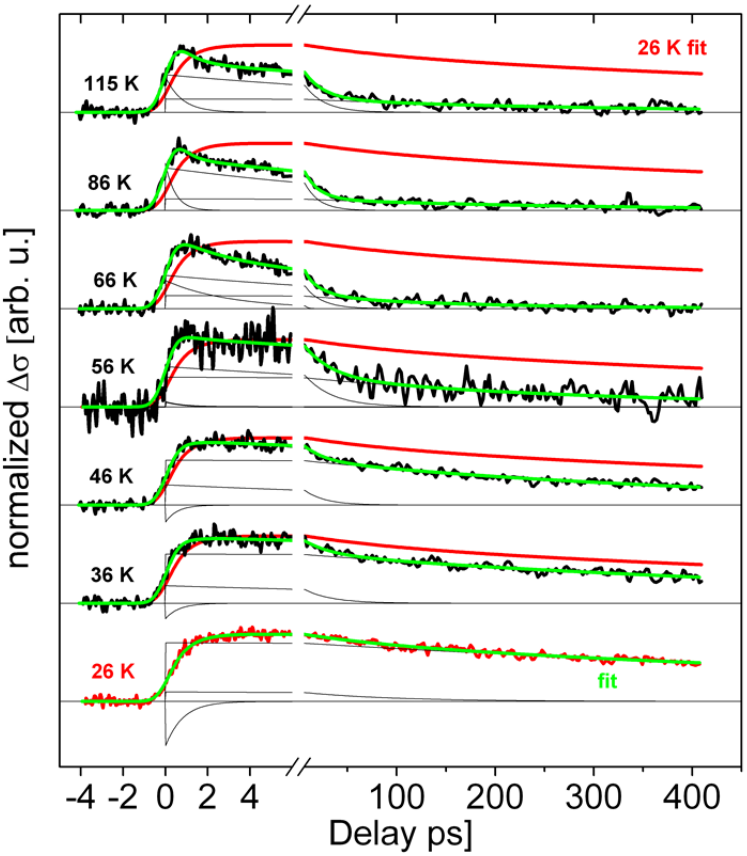

Figure 6.23 | The red curve represents the 26 K data with a fluence of 0.15 mJ/cm^2. The thick black lines are the normalized Δσ data at different temperatures. The green line represents fits using Eq. (6.48). The thin black lines are the different exponents (X,Y,Z) in the fit.

We observed that all the data in the 26-115 K range could be well described by three exponents. We also can see that the amplitudes and decay times of the different terms are temperature dependent. The temperature dependence of the different fitting parameters in Eq. (6.48) are shown in Fig. 6.24. X, Y and Z are the short, medium, and long timescale exponents, respectively. The amplitudes are divided by the maximum in Δσ. The lower graphs shows the temperature

dependence of the decay times (τ). The dotted horizontal line is the average value of the 86 and 115 K data. The straight vertical line represents T_c. The red lines are guides to the eye. The sum of the amplitudes (X+Y+Z) is shown in the lower right graph.

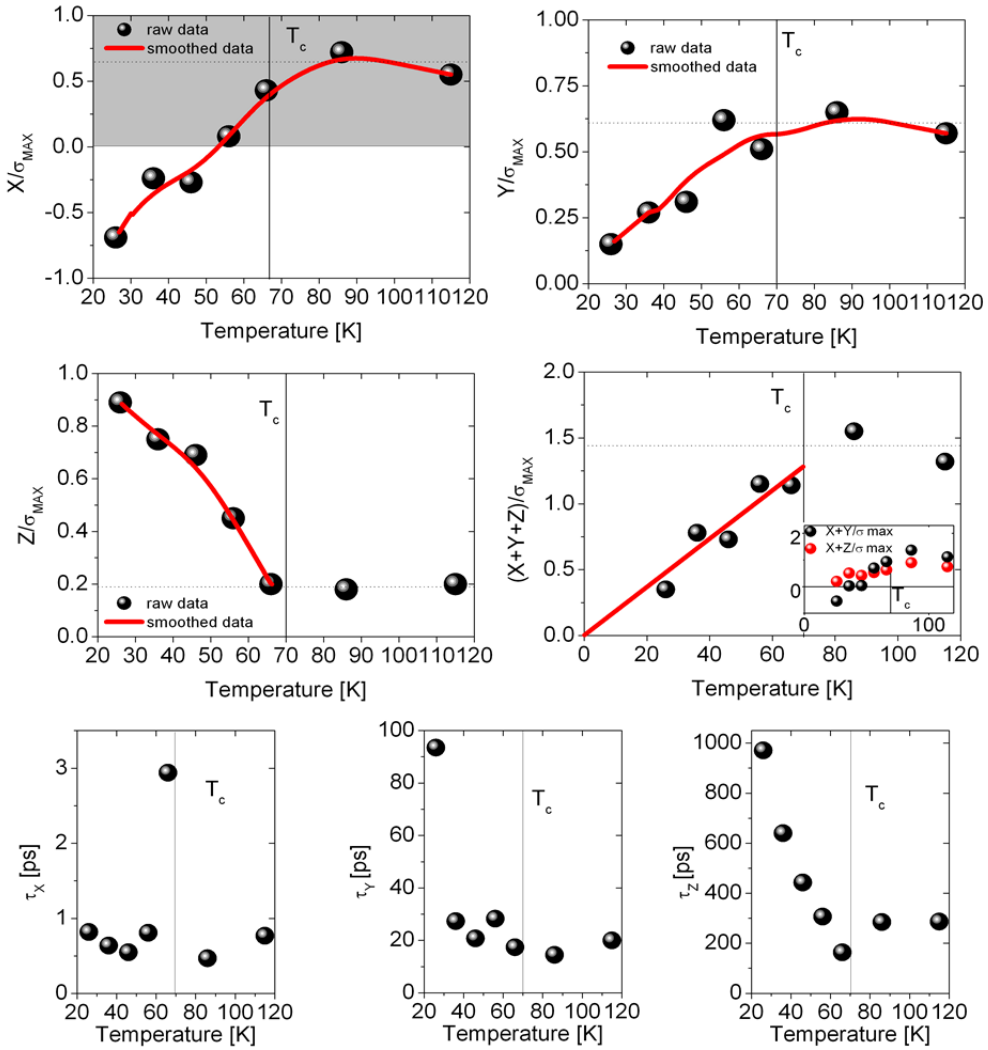

Figure 6.24 | The temperature dependence of the different fitting parameters in Eq. (6.48) in the fit of the Fl≈0.15 mJ/cm^2 data. X, Y and Z are the short, medium, and long timescale exponents, respectively. The amplitudes are divided by the maximum in Δσ. In the lower graphs, the decay times are shown. The dotted horizontal line is the average value of the 86 K and 115 K data. The straight vertical line represents T_c. The red line is the smoothed data. The sum of the amplitudes (X+Y+Z) is shown in the lower right graph. In the inset of the right middle graph, $(X+Y)/\sigma_{MAX}$ and $(X+z)/\sigma_{MAX}$ are plotted.

We observed that the amplitudes *X* and *Y* show an increase below T_c which flattens above T_c. In contrast, the amplitude *Z* is increasing with decreasing temperature below T_c. Apart from a temperature independent constant, amplitude *Z* seems to follow the magnetization below T_c to become about zero above T_c. *X* changes sign around 56 K. The decay time τ_X seems to be not very temperature dependent (except for one point at 66 K) while the decay time τ_Y is decreasing with increasing temperature. The anomalous behavior (of τ_X) for the point at 66 K might be related to critical effects at the phase transition, however more data is needed to confirm this. The most spectacular temperature depend changes in the decay time were observed for decay time *Z*, which increases dramatically upon decreasing the temperature below T_c. The normalized total amplitude (*X*+*Y*+*Z*) at t=0 is shown in the lower right graph. Although we normalized the maximum of $\Delta\sigma$ to one, the total amplitude at 85 K and 115 K exceeds one. This is due to the fact that there is a ultrafast decaying exponent which has a decay time shorter than the THz pulse width. The total amplitude at t=0 is decreasing with decreasing temperature.
In order to understand the physics behind this, we have to look to the origin of the signal. Here we distinguish two cases: 1) the paramagnetic phase $T>T_c$ and 2) the ferromagnetic phase $T<<T_c$. In the paramagnetic phase, the rise time is fast (<< 1ps) and there are mainly two fast decaying component (≈0.7 ps fs and ≈20 ps). At $T<<T_c$, the situation is different: the rise time is slower (≈700 fs) and there is mainly one slow decaying component (≈1000 ps). The situation is summarized in Fig. 6.25. The (sub) picosecond increase in $\Delta\sigma$, can be understood by the process of free carrier generation from a bound state; the photo-excited carriers are bound at t=0. The decay of $\Delta\sigma$ can be understood by a decrease in the free carrier concentration or by an decrease in the mobility. See for the details, the discussion section where we will discuss different models which can explain the temperature dependence of $\Delta\sigma(t)$.

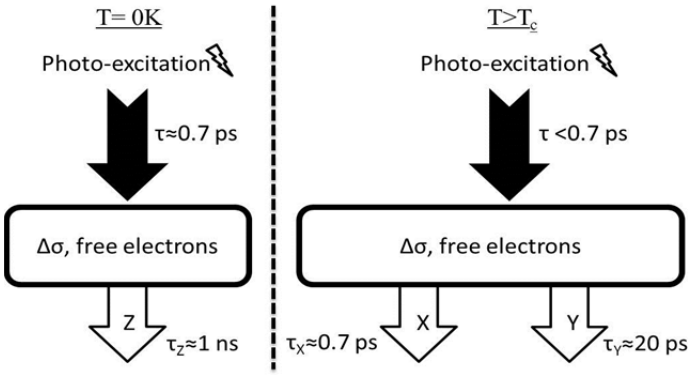

Figure 6.25 | Dynamics of Δσ(t) for $T<<T_c$ and $T>T_c$. X,Y,Z refer to the different components from the fit using Eq. (6.60).

6.3.6 Temperature dependence of the conductivity amplitude Δσ (t) for low fluences

More clues about what is the physical origin behind the mechanisms can be obtained by looking to the temperature dependence of the *magnitude* of Δσ for a fixed pump-probe delay; see Fig. 6.26. In the right graph $\sigma+\Delta\sigma_{MAX}$ (red) is shown whereas in the left graph σ+Δσ(+163 ps) is shown (grey). The data is compared with the un-pumped case σ (black). In the inset, $\Delta\sigma_{MAX}$ is shown (grey).

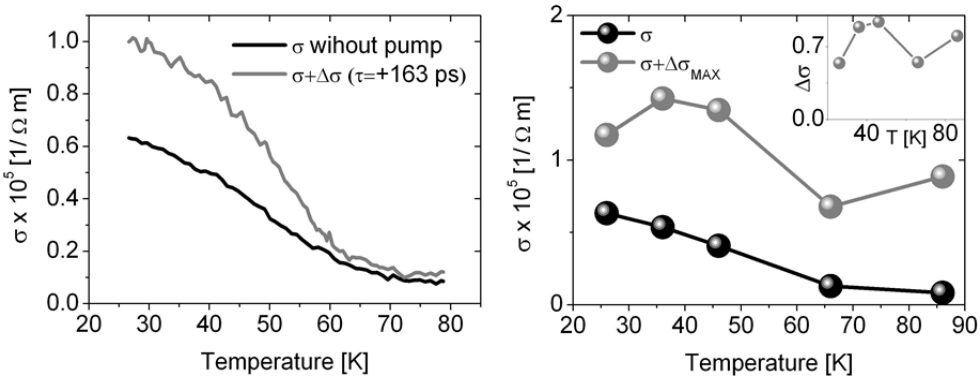

Figure 6.26 | Left) Temperature dependence of the conductivity at a fixed pump-probe delay of τ=+163 ps without (black line) and with pump (grey line). Right) Same as the left graph but than at the maximum of σ(τ).

We observed that there are no large temperature changes in $\Delta\sigma_{MAX}$. If the mobility would be temperature independent, we expect $\Delta\sigma_{MAX}$ to follow the absorbance since the absorbance determines the total amount of free electrons ($n_{calc.}$). The

absorbance for a 60 nm EuO film is shown in the left graph of Fig. 6.27. To correct $\Delta\sigma_{MAX}$ for the change in the absorbance, we divide $\Delta\sigma_{MAX}$ by the absorbance (*A*), see the inset. If the mobility is not temperature dependent (and if there are no short term relaxation processes), we expect $\Delta\sigma_{MAX}(T,\omega)/A(T,\omega)$ to be constant. This is actually what we observed; the points are scattered around the average. Based on this we conclude that the mobility of the hot photo-excited free carriers in the conduction band, after 1 ps, is not strongly temperature dependent.

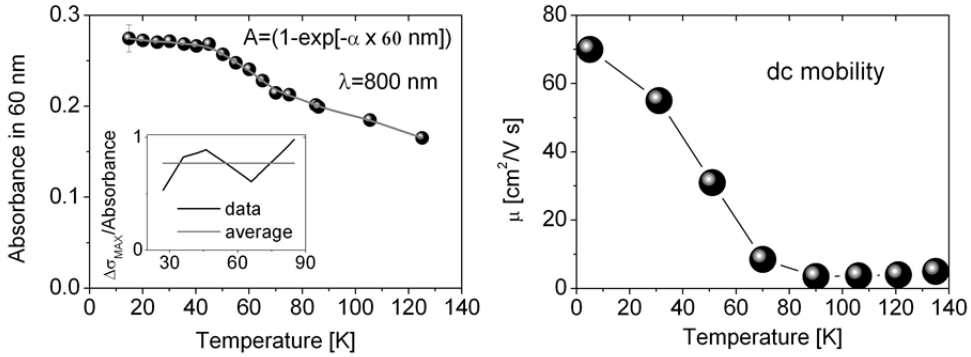

Figure 6.27 | Left) Temperature dependence of the absorbance (A) in an EuO film of 60 nm. In the inset $\Delta\sigma_{MAX}/A$ is depicted. Right) mobility versus temperature in a EuO thin film as was reported in [4].

Now we turn back to the σ+Δσ data at a pump-probe delay of +163 ps, see the left figure in Fig. 6.26. Unlike $\Delta\sigma_{MAX}$, Δσ (+163 ps) is strongly temperature dependent and shows the same behavior as the non-pumped data (σ): there is a MIT transition in σ+Δσ(+163 ps) around T_c. At +163 ps we probe the long term exponent (*Z*), see Eq. (6.48)). The physical origin of these components will be discussed later on.
We can conclude this section by saying that the conduction band mobility (right after photo excitation) is not much temperature dependent.

6.3.7 Mobility and free carrier generation efficiency: fluence dependence in the paramagnetic phase ($T>T_c$)

The last experimental results we present here is the fluence dependence of Δσ in the paramagnetic phase at 115 K. Based on this results we extract an estimate for the free carrier generation efficiency and mobility. We discuss the fluence dependence at 115 K and not at $T<<T_c$ for the following reasons. Due to the large pump powers involved, the pump pulse can cause the sample to heat up which

means that the temperature at negative delays (after 1 ms) will be higher than the 115 K base temperature. In XMCD measurements on thin EuO films with a pump fluence of 33 mJ/cm^2, the temperature increase can be up to 40 K. In the THz experiments the maximum fluence is 2.5 mJ/cm^2, therefore the expected pump-induced temperature increase is much smaller but can still be a few degrees. Above T_c, this temperature increase of a few degrees does not cause very drastic changes in the conductivity, see Fig. 6.17; furthermore there is no drastic change in absorbance at T> 90 K, see Fig. 6.27. This means that the fluence dependence at 115 K can give a clean result. The 115 K data was fitted with Eq. (6.49) in the (– 4 ps, +60 ps) range:

$$\Delta\sigma(t) = G(FWHM, t_0) * \left[H(t_0) \cdot \left(Xe^{-\frac{t}{\tau_X}} + Y\, e^{-\frac{t}{\tau_Y}} + Z\right)\right], \quad (6.49)$$

in which the last term is a constant now. $\Delta\sigma_{MAX}$ and $\Delta\sigma_{X+Y+Z}$ are shown in the left graph of Fig. 6.28. The fit of the 0.14 and 2.5 mJ/cm^2 data is shown in Fig. 6.29. From the fit we obtain X,Y,Z>0. Both $\Delta\sigma_{MAX}$ and $\Delta\sigma_{X+Y+Z}$ are non-linear in the pump fluence.

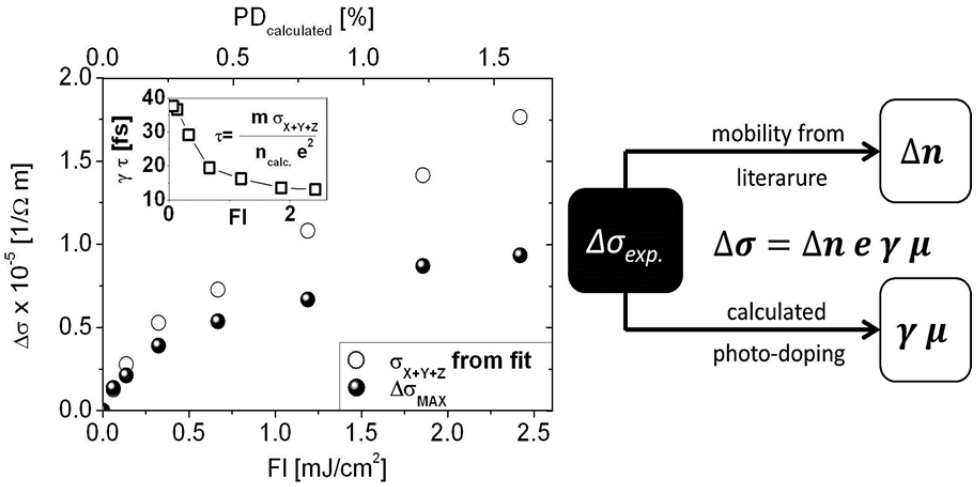

Figure 6.28 | Left) Δσ versus pump fluence. The black dots is σ_{MAX} whereas the white dots is σ_{X+Y+Z} from the fits using Eq. (6.47). In the inset τ·γ versus fluence is shown: $\tau\cdot\gamma = (\sigma\cdot m_0)/(e^2\cdot n_{calc.})$. Right) Δn can be estimated by using literature values of the mobility. τ·γ can be calculated by using $n_{calc.}$, with can be calculated from the pump fluence.

The photo-doping percentage (upper scale) is calculated assuming that every photo-excited electron becomes free; the free electron generation efficiency (γ, 0< γ <1) is taken one in this case. When γ=1, all the exited carrier are free electrons

while when γ=0, there are no free electrons after photo-excitation (bound carriers). The free carrier concentration within this assumption we shall name $\Delta n_{calculated}$ and $PD_{calculated}$. The difference in fluence dependence between the experimental $\Delta\sigma_{MAX}$ and the fitted $\Delta\sigma_{X+Y+Z}$ is caused by the fact that τ_X is shorter than $FWHM_{THz}$ and that τ_X is fluence dependent. However, even $\Delta\sigma_{X+Y+Z}$ shows a non-linear fluence dependence. The scattering time multiplied by the free electron generation efficiency, $\tau\cdot\gamma = (\sigma\cdot m_0)/(e^2\cdot n_{calc.})$, is depicted in the inset of Fig. 6.28. $n_{calc.}$ can be calculated from the pump fluence when the dielectric function is known. For this estimation we used a *dc* mobility expression in the Drude model framework. This can be done when one is in the $\omega\tau<<1$ limit. For high fluences, $\tau\cdot\gamma$ becomes smaller indicating that the mobility is fluence dependent or that the free electron generation efficiency becomes small. $\tau\cdot\gamma$= 40 fs at low fluences. Since $0<\gamma<1$, this is a lower limit for the scattering time: $\tau>40$ fs.

We can learn more about the generation efficiency by calculating Δn, using literature values for the maximum (*dc*) scattering time at 115 K, according to equation: $\Delta n_{experimental} = (\sigma\cdot m_0)/(e^2\cdot\tau_{literarture})$. Now, the generation efficiency can be determined by: $\gamma = \Delta n_{experimental}/\Delta n_{calculated}$. The generation efficiency for different scattering times is shown in Fig. 6.29 (upper right). A real lower limit (red line) is based on a scattering time of 210 fs with is the highest τ which could be found in the literature at 4.2 K [2]. At 115 K the scattering time is usually one order of magnitude smaller [2]. Taking τ=21 fs, we obtain a lower limit of γ at 115 K (blue line). Based on this limit we can conclude that the generation efficiency is in between 64-100% and that most of the excited electrons becomes free electrons after 1 ps.

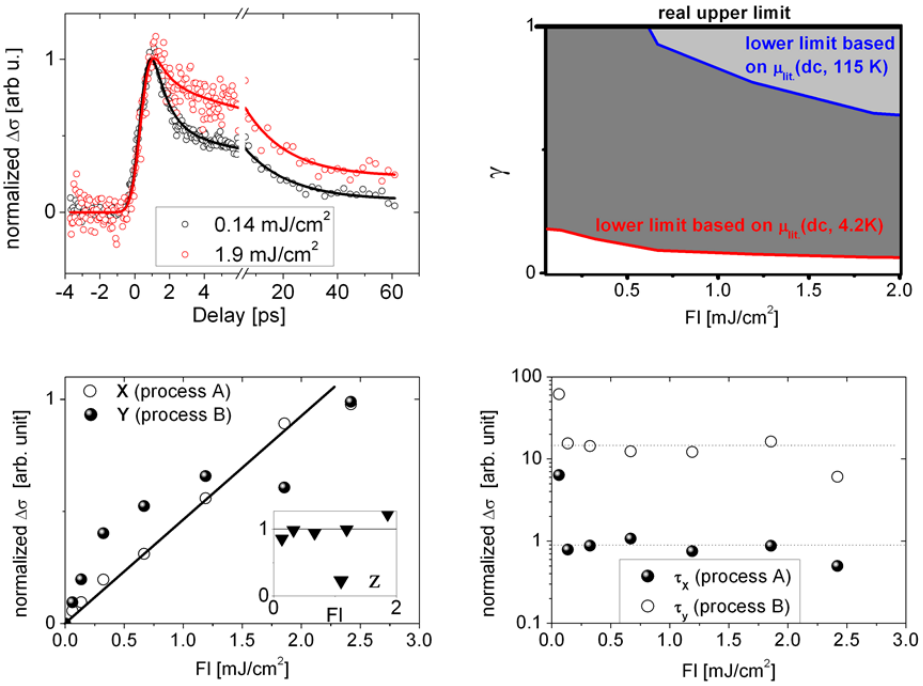

Figure 6.29 | Upper left) fit of the 0.14 and 1.9mJ/cm^2 data for T=115K . Upper right) The generation efficiency for different fluences and scattering times for T=115K. Lower left) The fluence dependence of the amplitudes (X,Y,Z) for T=115 K. Lower right) The fluence dependence of the relaxation times (τ_X, τ_Y).

The fluence dependence of the amplitudes (*X* ,*Y*, *Z*) and relaxation times (τ_X, τ_Y) is shown in the lower left and lower right graph in Fig. 6.32. Whereas *X* has a (more or less) linear fluence dependence, the fluence dependence of *Y* is highly non-linear. Above 0.14 mJ/cm^2, τ_X and τ_Y are weakly decreasing with increasing fluence. The most important conclusion from this section is that most photo-excited electrons become free electrons.

6.4 Discussion

6.4.1 The first picoseconds: evidence for magnetic exciton creation and dissociation

The 4*f* to 5*d* optical transitions in the Europium Chalcogenides have been studied extensively [3,27--29] in order to get information about the 5*d* conduction band, the bandwidth, the interaction with the 4*f* localized moments and the 4*f*-5*d* exchange. See for details Chapter 2. Although the nature of the initial states is pretty clear ($4f^7$, Eu localized moments, small bandwidth W_{4f} [3]), the nature of the

final state ($4f^6$ $5d^1$) is less clear and is still debated [3,29,30]. The expected 5*d* conductivity in the final state ($4f^6$ $5d^1$) can be based on different models describing the optical properties of EuO in the NIR-visible range, see also Chapter 2. In the hypothetical case that the 5*d* bandwidth is small and comparable to the intra-atomic 4f-5d exchange energy, the conductivity is expected to occur due to hopping between different *Eu* sites. Above T_c, where there is no long range magnetic order, the effective charge carrier transfer integral t_{eff} is expected to be small since it costs energy to hop from one side to another side when the moments are not aligned [31]; since $W \propto t_{eff}$, W is small [32]. Far below T_c, when the moments are aligned, t_{eff} (and W) is large and the system is a better conductor. In this hopping model, the conductivity is activated: $\sigma \propto \exp[t_{eff}]$ [32], and t_{eff} is effectively proportional to the reduced magnetization M: $W \propto t_{eff} \propto M$ [3,32].

In the case where the 5*d* bandwidth is larger than the intra-atomic 4f-5d exchange energy, a more band-like (instead of hopping) conduction is expected, even for $T>T_C$. For metallic band-like conduction one would expect $\sigma \propto t_{eff}$ [32]. For both cases we can see that the conductivity is large at low temperature ($T<<T_c$) and that the conductivity is small at higher temperatures ($T>>T_c$) due the fact that $t_{eff} \propto M$.

In other models the optical absorption spectra are explained in terms of magnetic excitons [33], where the 5*d* electrons are bound to the 4*f* hole by Coulomb and exchange interactions. The exciton is stabilized by the 4*f*-5*d* exchange interaction with the nearest neighbor $4f^7$ moments. When the nearest neighbors are ferromagnetically aligned, the stabilization is large whereas in the case that there is no correlation between the localized moments of the nearest neighbors, this stabilization is not present. In this model the 5*d* bandwidth can be large since the narrow absorption peak is explained in terms of an exciton [33].

Let us now look at the optical data. The experimental red shift of the optical (4*f*-5*d*) absorption edge occurring upon entering the magnetically ordered state has been shown to be proportional to the nearest neighbor spin correlation function and starts already above T_c, where short-range magnetic order sets in. This can understood in two different ways. Either the carriers are localized after excitation and therefore sensitive to short-range magnetic order, or the carriers are delocalized but there is strong exchange scattering between (delocalized) conduction electrons and two exchange coupled nearest neighbor 4*f* moments, which leads to a renormalization of the conduction electron energy, see Fig. 6.30. The latter model for the red shift was proposed by Takahashi *et. al.* [34].

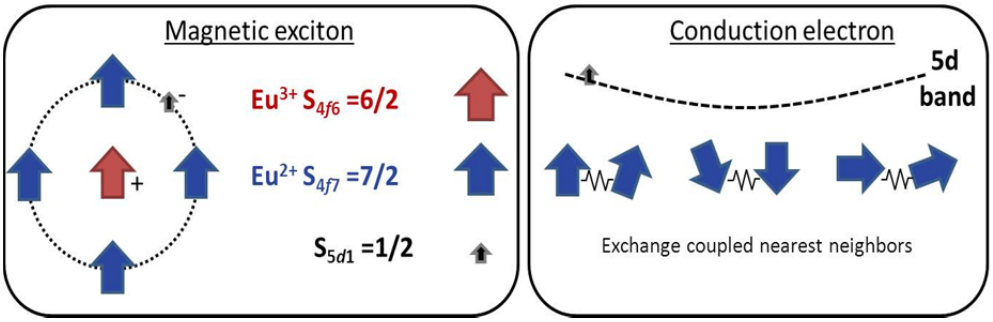

Figure 6.30 | Origin of the optical absorption edge shift for $T>T_c$. Left: Magnetic exciton formation leads to a stabilization and is sensitive to shot range magnetic order. Right: conduction electron scattering with exchange coupled nearest neighbors for $T>T_C$: M=0, $\langle S_i S_j \rangle \neq 0$.

When the localization is happening due to exciton formation, the 5*d* conductivity right after photo-excitation is expected to be low at all temperatures; the exciton has no net charge and the 4*f* hole is localized (the transfer integral is small). If the localization is happening due the very small 5*d* bandwidth (bandwidth comparable to the intra-atomic 4f-5d exchange energy), the conductivity is expected to be high at lower temperatures ($T<<T_c$), where the magnetic moments are aligned, and to be low at higher temperature ($T>T_c$), where there is no long range magnetic order. Table 6.1 summarizes the different models and the expected theoretical conductivity for the 5*d* conduction electrons.

Table 6.1 | optical absorption models and the expected 5*d* conductivity

Model	**$T<<T_c$**	**$T>T_c$**
narrow 5*d* band ($W_{5d} \leq E_{4f\text{-}5d\ exchange}$)	high conductivity, $\sigma \propto \exp[t_{eff}]$ hopping, localized	low conductivity, $\sigma \propto \exp[t_{eff}]$ hopping, localized
broader 5*d* band ($W_{5d} > E_{4f\text{-}5d\ exchange}$)	high conductivity, $\sigma \propto t_{eff}$ band, delocalized	low conductivity, $\sigma \propto t_{eff}$ band, delocalized
4*f*-5*d* magnetic exciton (broad 5d band)	low conductivity exciton, localized	low conductivity exciton, localized

Note that in Chapter 2 the optical absorption spectrum was calculated considering a conduction band and not a magnetic exciton. The estimated FWHM of the 5*d*

conduction band is 675 meV while the exchange splitting is in the order of 600 meV [3]; therefore $W_{5d} \approx E_{4f\text{-}5d\ exchange}$. From this point of view, we expect a hopping conductivity.

Now we will turn to our optical pump-THz probe experiments, which will reveal more about the nature of the 5*d* conduction band. Because of our limited temporal resolution, we could not resolve dynamics much faster than 1 ps. However at $T \ll T_c$, the rise-time of the conductivity is about 700 fs and is not limited by our temporal resolution. Assuming no additional ultrafast processes (<< 1ps) that change the conductivity, we can conclude that the conductivity right after photo-excitation (t=0) at $T \ll T_c$ in the low fluence regime is very small; such a value is consistent with the presence of a magnetic exciton which is derived from the 5*d* conduction band. The conductivity increase (rise time 700 fs), then can be explained by exciton ionization in which the 5*d* electrons dissociates in the 6*s* conduction band, as was suggested in [35]. LLinares *et al*. [36], however, proposed a model in which after exciton ionization the free conduction electron ends up at the X-point of the 5*d*-band, which is lower than the Γ-point. For clarification, the two cases are depicted in Fig. 6.31. We do not have evidence to distinguish between the two cases.

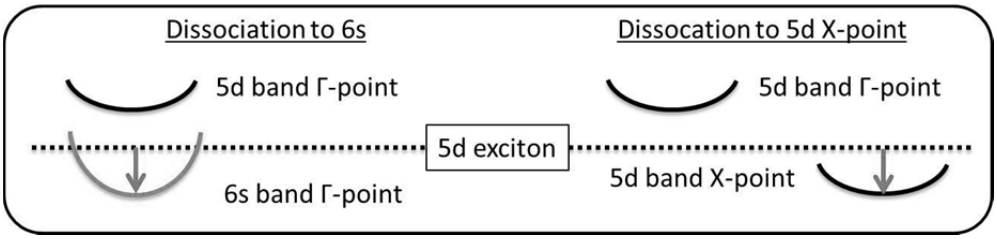

Figure 6.31 | Free carrier generation mechanisms. A schematic view of the momentum resolved band structure is shown. Left: exciton dissociation into the 6*s* band (direct relaxation). Right: exciton dissociation into the 5*d* band at the *X*-point.

The 700 fs time scale corresponds to typical electron-phonon or electron-magnon scattering times in magnetic semiconductors. Therefore for the mechanism of exciton ionization we suggest that exciton-phonon and/or exciton-magnon scattering are important.

We did not discuss yet the 700 fs *decay* of Δσ, which we observed for $T > T_c$. A drop in Δσ can be either explained in terms of a mobility $\Delta\mu$ drop or a drop in the free carrier concentration n_C, for instance due to trapping. When we assume an ingrowing exponential for Δn_C and $\Delta\mu$ and $n_C=0$, we can write for Δσ:

(6.50) $\Delta\sigma \propto \left(1 - e^{-\frac{t}{\tau_D}}\right)\left(1 + \frac{\Delta\mu}{\mu}\left[1 - e^{-\frac{t}{\tau_\mu}}\right]\right)$ - mobility drop

(6.51) $\Delta\sigma \propto \left(1 - e^{-\frac{t}{\tau_D}}\right)\left(1 + T\, e^{-\frac{t}{\tau_T}}\right)$ - trapping

In which τ_D is the exciton dissociation time and the constant T determines how much carriers are trapped with trapping time τ_T. τ_μ is the time constant for the mobility drop. Because of our limited temporal resolution, our limited signal to noise ratio, and our un-precisely determined t_0 (because our characterization experiments using Si cannot be simply described by a temporal resolution limited step-function), it did not make sense to fit Eq. (6.50) and (6.51) to our data since there are too many free parameters to determine. To draw some conclusions we look instead to the general trend of the data. The normalized $\Delta\sigma$ for $\tau_T = \tau_\mu = \tau_D = 700\ fs$ and different T and $\Delta\mu/\mu$ is shown in Fig. 6.32.

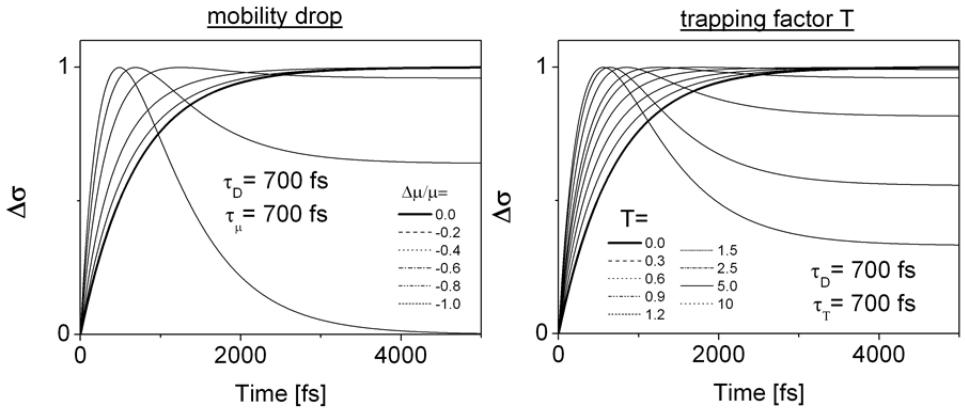

Figure 6.32 | Δσ during the first picoseconds in different models, see the text for more information.

In the left graph of Fig. 6.32, the $\Delta\sigma$ for different $\Delta\mu/\mu$ is shown. In order to model trend of the data by a change in $\Delta\mu/\mu$, $|\Delta\mu/\mu|$ needs to become larger with increasing temperature. The conductivity change in the CMR manganites was related to a temperature induced change of the condcutivity [16]. In [16], the change in the conductivity was written as:

(6.52) $\Delta\sigma(t, T_s, T_p) = \frac{\partial\sigma(T_p,T_s)}{\partial T_p}\Delta T_p + \frac{\partial\sigma(T_p,T_s)}{\partial T_s}\Delta T_s = ne\left(\frac{\partial\mu(T_p,T_s)}{\partial T_p}\Delta T_p + \frac{\partial\mu(T_p,T_s)}{\partial T_s}\Delta T_s\right)$

Which means that an increase of the lattice (T_p) or spin temperature (T_s), can lead to a change in the conductivity. Let us now have a closer look to the temperature dependence of $\Delta\mu/\mu$.The mobility can be described, by Eq. (6.65):

(6.53) $\Delta\mu(T_s,T_p) = \frac{\partial\mu(T_p,T_s)}{\partial T_p}\Delta T_p + \frac{\partial\mu(T_p,T_s)}{\partial T_s}\Delta T_s = \frac{\partial\mu(T_p,T_s)}{\partial T_p}\Delta T_p + \frac{\partial\mu_0 e^{b\,M(T_S)}}{\partial T_s}\Delta T_s$

In here we assume that the MIT in EuO is also due to a mobility change (which is debatable) and the mobility can be described by $\mu_0 e^{b\,M(T_S)}$, see the introduction and [3,32]. We also assume that the relation $\Delta\mu \propto \Delta T_p$ also holds for EuO. Using the chain rule we can write Eq. (6.65) as:

(6.54) $\Delta\mu(t,T_s,T_p) = \frac{\partial\mu(T_p,T_s)}{\partial T_p}\Delta T_p(t) + C(T_s)\Delta T_s(t); \qquad C \equiv b\,\mu_0 e^{b\,M(T_S)}\frac{\partial M(T_S)}{\partial T_s}$

The first term in Eq. (6.66) represents the mobility change due to an increased lattice temperature. The lattice temperature in a semiconductor can increase due to electron relaxation (phonon emission) within the conduction band. In semiconductors this is typically happening at the (sub) picosecond time scale. The second term represents the mobility change due to an increased spin temperature. The scaled $C(T_s)$ versus temperature curves for different *b*'s is shown in Fig. 6.33. In here we modeled the reduced magnetization simply as $\sqrt{69\,K - T}/\sqrt{69}$. The value of *b* in the example in the introduction was *b*=13. However, in our sample, the change in the resistivity (at the MIT) is much smaller than in this example. Therefore we expect *b* to be smaller than 13 (b≈2, as we will determine later on).

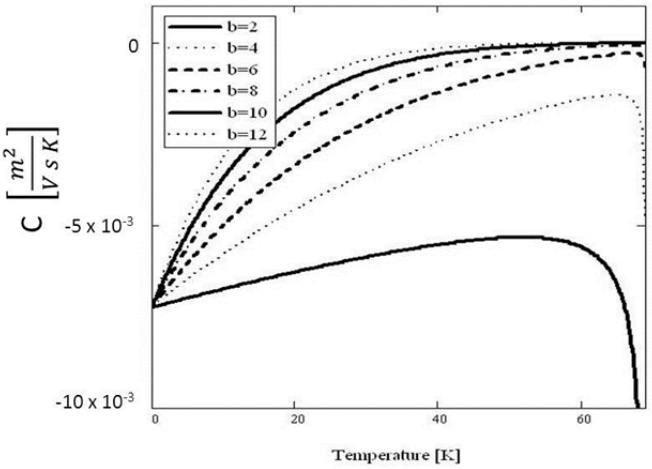

Figure 6.33 | *C* versus (spin) temperature for different *b* values. See Eq. (6.66) and see the text.

From Fig. 6.33, we can see that (for T<65K) |C| is larger at low temperatures (compared to T=60K), which means that we expect $|-\Delta\mu/\mu|$ to be large at low temperatures. Apart from that, ΔT_s is expected to be smaller at higher temperature

due to the fact that the heat capacity is larger at higher temperatures. The same holds for ΔT_p. Therefore in our model (change in $\Delta\mu/\mu$) we expect an opposite trend from what is needed to explain the temperature dependence of $\Delta\sigma$ (see Fig. 6.25-6.26). Our magnetization dynamics experiments (previous chapter) do no reveal very large changes in ΔT_s during the first picoseconds anyways, and therefore we have to look for other models in order to find the *main* origin of the change in the dynamics.

In the right graph of Fig. 6.32, $\Delta\sigma$ for different T is shown. The constant T determines how much carriers are trapped or bound. The temperature dependence of $\Delta\sigma$ can be modeled by an increase of T with increasing temperature. At low temperature T is small (no trapped carriers) and for high temperatures, T is large. More clues whether this scenario is correct can come from the fluence dependence at low temperatures, see Fig. 6.22. For low fluence, we observed an ingrowing exponential with a time constant of 700 fs, whereas for high fluences, there is a decaying exponential with a time constant of 700 fs. This means that the dynamics gets faster with increasing fluence. In our model, we actually expect T to be smaller with increasing fluence (the traps are getting filled), which is the opposite from what we see. Therefore we need to look for another reason in order to explain the observed trend.

Until now we assumed that the decay times are constant $\tau_T = \tau_D = 700\,fs$. We can actually also model the data by considering a temperature dependent τ_D (the exciton dissociation rate can be for instance related to the Boltzmann population factor n(E,T)+1 with E=energy, T=temperature), while we take T and $\tau_T = 700\,fs$ as a constant. In Fig. 6.34, $\Delta\sigma$ for different τ_D is shown for T=1.

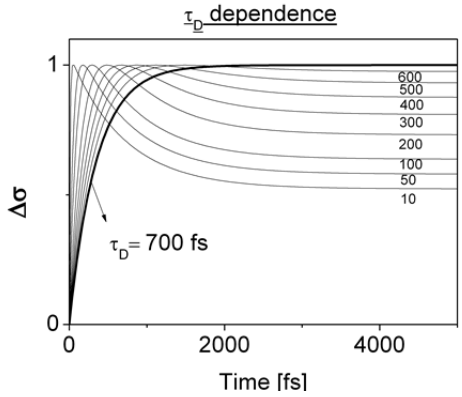

Figure 6.34 | Δσ during the first picoseconds for different τ_D and T=1, see the text for more information.

From Fig. 6.34, we can see that a change in τ_D can account for the observed behavior of $\Delta\sigma(T)$. The temperature dependent dynamics of $\Delta\sigma$, essentially can be explained by a change in τ_D. τ_D gets shorter with increasing temperature: it is around 700 fs at 26 K and is a few hundred femtosecond for $T>T_c$. The trapping time τ_T is constant and is around 700 fs while *T* is around 1 for $T>T_c$. An decrease of τ_D with increasing temperature is physical: there are more phonons and magnons at higher temperature which means that there is more exciton-phonon or exciton-magnon scattering. For higher fluences τ_D gets shorter as well, which can be explained by an increased exciton-electron, exciton-phonon and/or exciton-magnon scattering rate.
Summarizing, after photo-excitation 4*f*-5*d* excitons are formed which are dissociated within a picosecond by scattering with electrons, phonons or magnons. Within few picoseconds some of the free carriers are trapped while others remain free, once trapped the carriers no longer contribute to the transient conductivity. In the next subsection we focus on the dynamics of the free carriers for τ>5 ps.

6.4.2 τ>5 ps: trapping/magnetic exciton/polaron formation and recombination processes

Different relaxation mechanisms unfolding in the 5-1000 ps timescale, were identified in semiconducting materials. Some typical relaxation mechanisms, which includes trapping, recombination (radiative and non-radiative) and exciton formation, are summarized in Fig. 6.35.

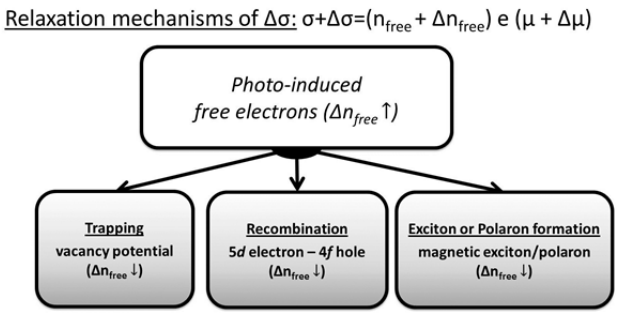

Figure 6.35 | Different possible relaxation mechanisms in a magnetic semiconductor having τ> 5ps.

Before identifying different mechanisms in EuO, let us summarize once more the situation. For $T<<T_c$ and *τ>5 ps*, we observed (mainly) one component with a decay time of τ≈1 ns while for $T>T_c$ we also observed (mainly) one component with a decay time of τ≈20 ps. For intermediate temperatures (T=56 K), there are two components: the first component has τ≈30 ps while the second component has τ≈300 ps, see Fig. 6.24. This two component behavior, essentially, can be explained in two different ways:

A) There are two populations each with its own relaxation dynamics: $\Delta\sigma = \Delta\sigma_1 + \Delta\sigma_2 = \mu_1 e\Delta n_1 e^{-t/\tau_{N1}} + \mu_2 e\Delta n_2 e^{-t/\tau_{N2}}$. At $T<<T_c$, after 5 ps, there is mainly the contribution from population 1, $\Delta\sigma_1$, while at $T>T_c$, there is mainly the contribution from population 2, $\Delta\sigma_2$. At intermediate temperatures there are two populations. Each population has its own decay time. In this example we assume that the mobility for both populations is not changing in time.

B) One of the relaxation times is related to a drop in the mobility while the other relaxation time is related to a drop in the conduction band population. When the mobility decays with τ_μ and the carrier density with τ_N, we can write for the change in the conductivity: $\Delta\sigma = n\,e\left(\Delta\mu_0 e^{-t/\tau_\mu}\right) + \mu e\left(\Delta n_0 e^{-t/\tau_N}\right) + e\left(\Delta n_0 \Delta\mu_0 e^{-t\left[1/\tau_\mu + 1/\tau_N\right]}\right)$. The fact that we also see this two component behavior in stoichiometric EuO (, no oxygen vacancies, n <<Δn_0 , no MIT, n +$\Delta n_0 \cong \Delta n_0$) means that in this scenario, the first term on the right hand side is not essential and we write: $\Delta\sigma \approx \Delta n_0 e\left(\mu\, e^{-t/\tau_N} + \Delta\mu_0 e^{-t\left[1/\tau_\mu + 1/\tau_N\right]}\right)$. In this case two relaxation rates can be observed: $(1/\tau_N)$ and $(1/\tau_\mu + 1/\tau_N)$.

Since we measured $\Delta\sigma$, and we cannot directly measure changes in n or μ, we need to look careful into both cases in order to distinguish between them. In the two population scenario, we have to decide what is the origin of the different populations. We can make several suggestions based on the general knowledge about the dynamics in semiconductors and about EuO. First we look into Case A and we consider three different scenarios (A1/A2/A3), see also Fig. 6.36.

A1) From band structure calculations in EuO, it is known that there are two conduction band minima with similar energy. The 6*s* band has minimum at the Γ-point while the minimum of the 5*d* band is at the X-point. Each population can have its own relaxation dynamics. The magnetization induced changes in the band structure may lead to energy shifts between the minima at the Γ-point and X-point

(see Fig. 6.36) which in turn can affect the populations Δn_1 and Δn_2 (with different mobility) and therefore the conductivity dynamics. We can see this more clearly as follows. When we consider the total amount of free electrons $\Delta n_T = \Delta n_1 + \Delta n_2$, and $R_1 = \Delta n_1/\Delta n_T, R_2 = \Delta n_2/\Delta n_T$, we can write $\Delta\sigma$ as: $\Delta\sigma = e\Delta n_T\left(\mu_1 R_1 e^{-t/\tau_{N1}} + \mu_2(1-R_1)e^{-t/\tau_{N2}}\right)$. From this we can see that energy shifts between the minima may lead to a change in R_1, which in turn will lead to change in $\Delta\sigma$. In this scenario it is important that both populations have different relaxation times τ_{N1} and τ_{N2} and that the n_1 and n_2 are not in equilibrium at the relaxation timescales (τ_{N1} and τ_{N2}, both are more than 15 ps). This is, however, very unlikely because intervalley (electron-phonon) scattering is usually happening at timescales which are <15 ps in semiconductors. Intervalley scattering can make n_1 and n_2 in thermal equilibrium and therefore Δn_T will decay with as single exponential time in this model. Therefore we reject this scenario and consider another case.

A2) It is also possible that part of the carriers are free, and that part of carriers are in some weakly bound but conductive state, such as magnetic polarons. The binding energy can be magnetization - and therefore also temperature-dependent. Now we will consider the rate equations describing irreversible transitions. Let us name the free carriers in the conduction band n_C. The conduction electrons can recombine with the holes in the valence band (V) with decay time τ_{CV} but they can also be bound in the intermediate state (I) with decay time τ_{CI}. The different models are explained in Fig. 6.36.

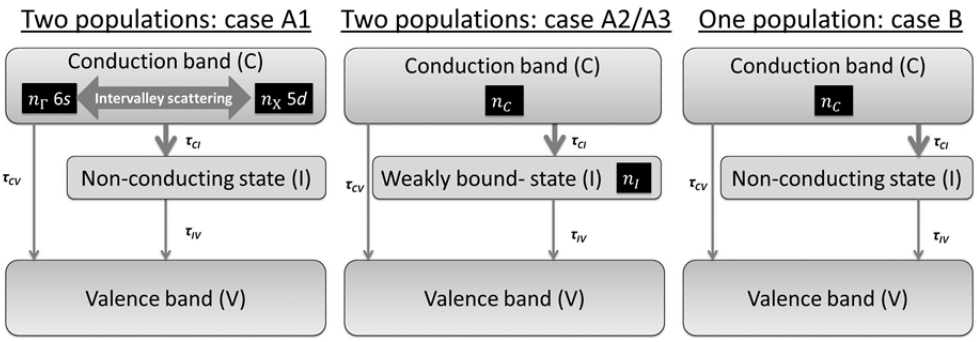

Figure 6.36 | Different possible relaxation mechanisms models which has been discussed in the text. The arrows represent relaxation rates; the larger the arrow, the faster the rate. Herein we consider typical timescales which has been observed in semiconductors like GaAs. The black boxes represents the different contributions to Δσ(t).

We can write for n_C: $n_C(t) = n_{C,0}e^{-t[1/\tau_{CV}+1/\tau_{CI}]}$ which reduces to $n_C(t) = n_{C,0}e^{-t/\tau_{CI}}$ when τ_{CI}<<τ_{CV}. $n_{C,0}$ is the carrier density at t=0; we consider the case when $n_{I,0} = n_{V,0} = 0$. The electrons in the intermediate state can recombine with the holes at decay rate $1/\tau_{IV}$. When τ_{CI}<<τ_{CV}, we can write for n_I: $n_I(t) = n_{C,0}\frac{1/\tau_{CI}}{1/\tau_{IV}-1/\tau_{CI}}\left(e^{-t/\tau_{CI}} - e^{-t/\tau_{IV}}\right)$. Usually the recombination is slower than the trapping τ_{CI}<<τ_{IV}. Then the conductivity becomes $\Delta\sigma = en_{C,0}\left[(\mu_C - \mu_I)e^{-t/\tau_{CI}} + \mu_I e^{-t/\tau_{IV}}\right]$, from which we can see that the decay is double exponential. When we define $R \equiv \mu_C/\mu_I$, the normalized $\Delta\sigma$ becomes: $\Delta\sigma^N \propto (R-1)e^{-t/\tau_{CI}} + e^{-t/\tau_{IV}}$. This equation models the temperature dependence of $\Delta\sigma^N(t)$ by considering a temperature dependent *R(T).* The temperature dependence of $\Delta\sigma^N$ using $\tau_{CI} = 20\ ps$ and $\tau_{IV} = 1000\ ps$ is plotted in Fig. 6.37.

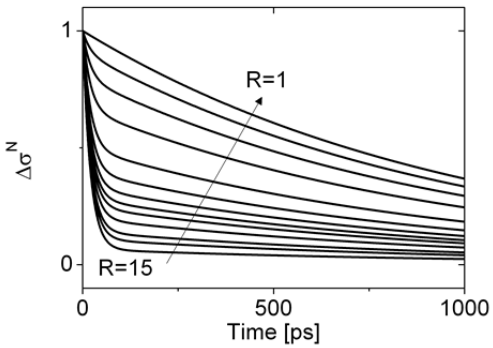

Figure 6.37 | Normalized $\Delta\sigma$ using equation $\Delta\sigma^N \propto (R-1)e^{-t/\tau_{CI}} + e^{-t/\tau_{IV}}$ and $\tau_{CI} = 20\ ps, \tau_{IV} = 1000\ ps$. For details, see text.

For R=1 (T<<T_c), the decay is single exponential and slow while for R=15 (T>T_c), the decay is double exponential: there is large fast component and a smaller slow component. The situation where *R* is temperature dependent is not unphysical and will be discussed later on.

A3) In the model we have discussed in this section (part A2) we assumed that the number of available weakly bound states is infinite, which is not the case for instance when the carriers are bound by traps. When $n_{C,0}$ is larger than the available intermediate states, a two exponential behavior can be observed due to the fact that some electrons going to intermediate state (τ_{CI}, fast) while when these states are filled, the rest of the electrons can recombine with the holes (τ_{CV}). The important parameter in this is the amount of available n_I states with an energy lower the conduction band energy minimum; if the energy of n_I is larger than the

conduction band energy minimum, the electrons will stay in the conduction band. We use the expression for n_I from the previous section $n_I(t) = n_{C,0}\frac{1/\tau_{CI}}{1/\tau_{IV}-1/\tau_{CI}}\left(e^{-t/\tau_{CI}} - e^{-t/\tau_{IV}}\right)$, and we write for n_C: $n_C(t) = n_{C,0}\left[a\, e^{-t/\tau_{CI}} + (1-a)e^{-t/\tau_{CV}}\right]$ in which a is the branching ratio and is in between 0 and 1. In the expression for $n_C(t)$ we assume that there is a sub-population which will relax to n_I (first term) and there is a sub-population which will relax to n_V. In the approximation that τ_{CI}<<τ_{CV}, τ_{CI}<<τ_{IV}, $n_{I,0} = n_{V,0} = 0$ and when we assume that the recombination time from the conduction band and intermediate state are the same ($\tau_{IV} = \tau_{CV} = \tau_V$), we can write for $\Delta\sigma^N$:

$$\Delta\sigma^N \propto \left[a\,(R-1)e^{-t/\tau_{CI}} + \{(1-a)R + a\}\, e^{-t/\tau_V}\right] \quad (6.55)$$

The ratio of the amplitude of the fast component (τ_{CI}) divided by the slow component (τ_V) is plotted in Fig. 6.38; the ratio is plotted against *a* for different $R \equiv \mu_C/\mu_I$.

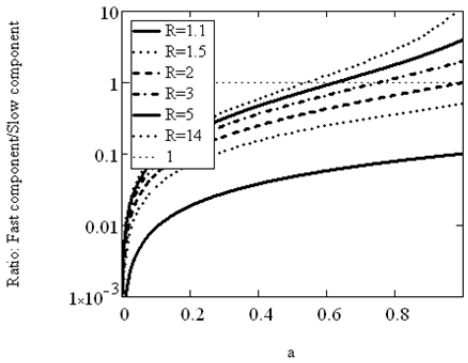

Figure 6.38 | The ratio of the amplitude of the fast component (τ_{CI}) divided by the slow component (τ_V) in Eq. (6.67).

From this graph we can see that for large *R* (*R*>2), this ratio crosses the y=0 line which means that a change in *a* can result in a change in the dynamics, going from a slow (*a*=0) to a fast (*a*=1) single exponential behavior. From this we can conclude that both a change in *a(T)* and *R(T)* can be the origin behind the observed temperature dependence. The physics related to the temperature dependence of *a* and *R,* is discussed later on in this chapter.

B) Until now we considered the case that the two exponential behavior is coming from two different populations with a different mobility. In this case

mobility was considered to be temperature dependent but constant in time (for τ> 5 ps): $\partial\mu(t)/\partial t = 0$. Now we will consider the case where the mobility is time dependent and where there is one population n_C, see the right picture in Fig. 6.38. We can write for n_C: $n_C(t) = n_{C,0}e^{-t[1/\tau_{CV}+1/\tau_{CI}]}$. We define $1/\tau_{CV} + 1/\tau_{CI} = 1/\tau_C$. When we consider the case that $n_C \ll \Delta n_C$, and that the changes in the mobility can be described by an in-growing exponential, we can write for $\Delta\sigma$:

(6.56) $$\Delta\sigma \approx \mu_c e\, \Delta n_{C,0}\, e^{-\frac{t}{\tau_C}}\left(1 + \frac{\Delta\mu_{c,0}}{\mu_c}\left[1 - e^{-\frac{t}{\tau_\mu}}\right]\right) \propto \left(1 + \frac{\Delta\mu_{c,0}}{\mu_c}\right)e^{-\frac{t}{\tau_C}} - \frac{\Delta\mu_{c,0}}{\mu_c}e^{-\frac{t}{\tau_C}[1+F]}$$

resulting in a double exponential decay of $\Delta\sigma$. F is defined as τ_C/τ_μ and is always >0. For F<<1, the behavior is single exponential, τ_C. For larger *F*, the behavior is double exponential and the decay is faster. The normalized $\Delta\sigma$ for different F (fixed $\Delta\mu_{c,0}/\mu_c, \tau_C$), $\Delta\mu_{c,0}/\mu_c$ (fixed F, τ_C) and τ_C (fixed $F, \Delta\mu_{c,0}/\mu_c$) are shown in Fig. 6.39 using Eq. (6.56). From this graph it can be seen that the observed temperature dependence can be modeled by considering a temperature dependent *F* (increasing with increasing temperature), a temperature dependent $\Delta\mu_{c,0}/\mu_c$ (increasing with increasing temperature), or a temperature dependent τ_C (decreasing with increasing temperature). In next section we make a choice which model is the best in explaining our temperature and fluence dependence.

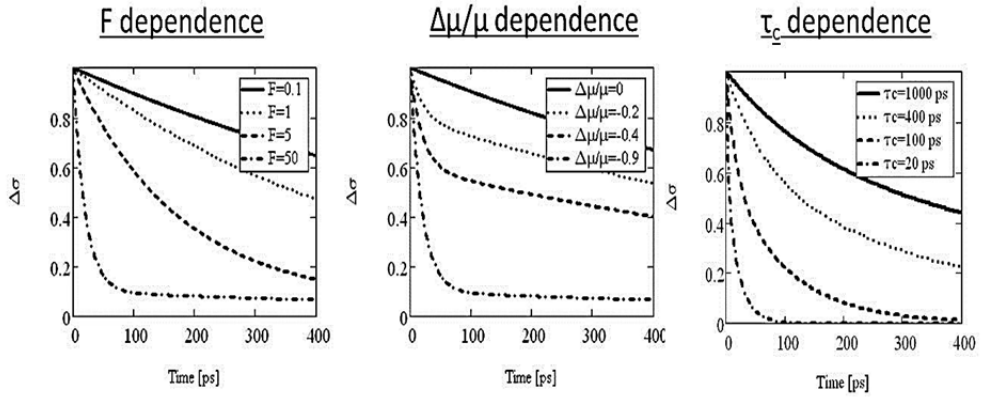

Figure 6.39 | The normalized $\Delta\sigma$ for different $F \equiv \tau_C/\tau_\mu$ (left, $\Delta\mu_{c,0}/\mu_c = -0.9, \tau_C = 1000\,ps$), $\Delta\mu_{c,0}/\mu_c$(middle, *F*=50, $\tau_C = 1000\,ps$) and τ_C (right, $\Delta\mu_{c,0}/\mu_c = -0.4, F = 5$) using Eq. (6.68).

6.4.3 Which is the appropriate model for the dynamics at τ>5 ps?

The discussion of the temperature dependence of $\Delta\sigma$ is summarized in Table 6.2. We found five different parameters (in two different models) which could be responsible for the observed temperature dependence.

Table 6.2 | Different options for explaining the temperature dependence of $\Delta\sigma$. The are two different models and five different possible temperature dependent parameters.

Case	Model	Temp. depend.	Description
A2/A3	n_C(t) + n_I(t)	$R(T) \equiv \mu_C/\mu_I$	ratio mobility of n_C and n_I
A3	n_C(t) + n_I(t)	*a(T)*	factor #e$^-$ in intermediate state
B	n_C(t) + $\Delta\mu_C$(t)	$-\Delta\mu_{c,0}/\mu_c$ *(T)*	pump-induced mobility change
B	n_C(t) + $\Delta\mu_C$(t)	$F(T) \equiv \tau_C/\tau_\mu$	ratio decay times mobility and n_C
B	n_C(t) + $\Delta\mu_C$(t)	$\tau_C(T), \tau_\mu(T)$	conduction e$^-$ relaxation time

We first discuss the one population (mobility change) model B1. When we compare Eq. (6.56) in our model with our fitting equation (X,Y,Z components), we can determine $\Delta\mu_{c,0}/\mu_c, \tau_C, \tau_\mu$ from *Y*/(*Y*+*Z*), *Z*/(*Y*+*Z*) and τ_Y, τ_Z. The slowest component is $\tau_Z = \tau_C$. The faster component is $\tau_Y = \tau_C/(1+F)$: F>0. $\Delta\mu_{c,0}/\mu_c, \tau_C, \tau_\mu$ in this model, for different temperatures, is shown in Fig. 6.40.

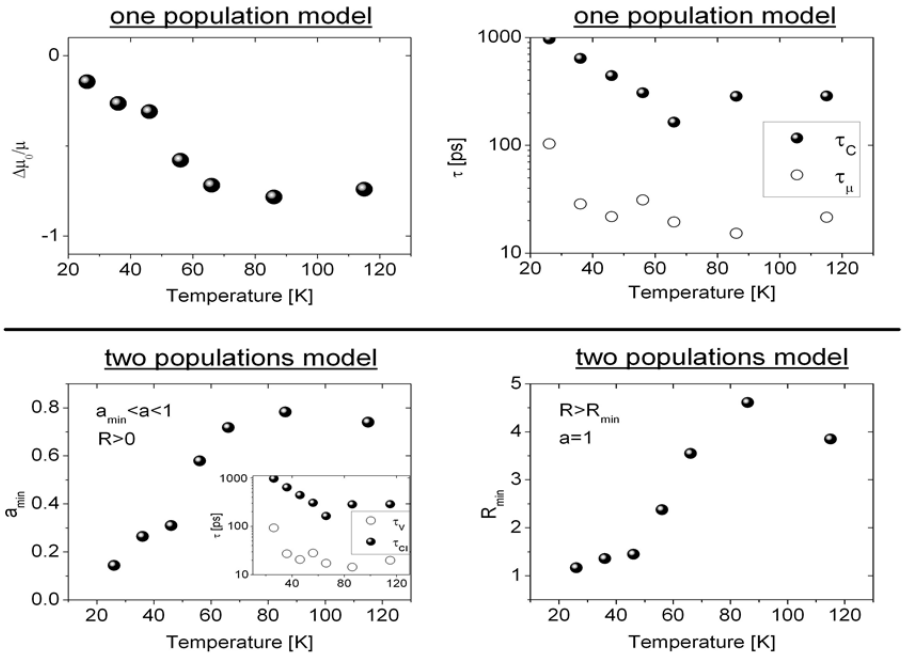

Figure 6.40 | Different parameters versus temperature in the one population and two populations model. See the text for more details. A_{min} is determined by considering the fact that R>0. R_{min} is calculated by considered the fact that a should be in between 0 and 1.

We can see that the change in the mobility is small at low temperature (-0.14 at 26K) and larger at higher temperatures (0.78 at 86 K). The decay times for the n_c

and for the mobility are shown in the upper right graph. We see that τ_μ is more or less constant in the 36-115K range while τ_C is decreasing dramatically with increasing temperature. Let us now have a closer look to the temperature dependence of $-\Delta\mu_{c,0}/\mu_c$.The mobility can be described, by Eq. (6.57), as we did before:

$$\Delta\mu\left(t, T_s, T_p\right) = \frac{\partial\mu\left(T_p,T_s\right)}{\partial T_p}\Delta T_p(t) + C(T)\Delta T_s(t); \quad C \equiv b\,\mu_0 e^{b\,M(T_s)}\frac{\partial M(T_s)}{\partial T_s} \tag{6.57}$$

We discussed before that from Fig. 6.35, we can see that (for T<65K) |C| is larger at low temperatures, which means that we expect $|-\Delta\mu_{c,0}/\mu_c|$ to be large at low temperature, and lower at higher temperatures. Apart from that, we discussed that ΔT_s is expected to be smaller at higher temperature due to the fact that the heat capacity is larger at higher temperatures. Therefore in the model we expect an opposite trend from what is needed to explain the temperature dependence of $\Delta\sigma$. Apart from that, the timescale (≈20 ps) and the amplitude of ΔT_s is much faster and higher, respectively, than we have observed in demagnetization dynamics experiments in EuO, see the previous chapter. Therefore we reject this scenario and we will go back to the two population scenario, see Eq. (6.55).

In this scenario, the long timescale component (Z) corresponds to τ_V, whereas the short term component (Y) corresponds to τ_{CI}, see the inset of the lower left graph in Fig. 6.40. As discussed before, in this model there are two variables which determine the amplitude: $R=\mu_C/\mu_I$ and a. Assuming a=1, R versus temperature can be calculated from $Y/(Y+Z)$, see the lower right graph in Fig. 6.42. This a minimum value for R since a can only be in between 0 and 1, see also Fig. 6.40 where R is plotted for different values of a, is increasing with temperature and is around 4 at $T>T_c$. We can also find a limit for a, by considering the fact that R should be larger than zero: $R>0$. The minimum value for a is plotted in the lower left graph in Fig. 6.40. From this we can see that a_{min} is increasing with temperature and that a_{min} is close to 1 for $T>T_c$. This means that the temperature dependence of $\Delta\sigma$ can be explained in terms of an increase of R or an increase of a (with increasing temperature). In the next section we discuss the nature of the intermediate state and the origin behind the changes in R and a.

6.4.4 The nature of the intermediate state

Until now, we did not specify the nature of the intermediate state since we wanted to keep the discussion general. We know from the previous sections that either the

mobility ratio *R* or the branching ratio *a* is increasing with increasing temperature and based on this we can say something about the intermediate state.

In semiconductors, one candidate for the intermediate state are traps while in magnetic semiconductors, it is also possible to that magnetic polarons (MP) are formed [3,29,37--43]. We do not consider here magnetic excitons because of the fact that this neutral quasi particle is not conductive. Let us consider the mobility of magnetic polarons. For Eu-rich EuO films it was shown that for the measured conductivity holds: $\sigma(M_r) \propto e^{b\,M_r}$ [3]. In [4] was observed that the MIT in films is related to a change in the mobility. Therefore we assume that the mobility is dependent on the magnetization and we can write for the reduced mobility ($\mu_r = \mu(T)/\mu(0K)$):

(6.58) $\mu_{I,r}(T) = \frac{e^{b\,M_r(T)}}{e^{b}}$, $M_r(T) = \frac{\sqrt{69-T}}{\sqrt{69}}$ for T<69K, $M_r(T) = 0$ for T>69K

When we want to explain the static MIT in our Eu-rich EuO measurements (about 15%) in terms of a mobility change, we have to take for *b*=1.92. Now we calculate *R* as follows:

(6.59) $R(T) = \frac{\mu_c}{\mu_I(T)} = \frac{1}{\mu_{I,r}(T)}$

Here we assume for simplicity that the conduction band mobility μ_c, is constant in between 26-115 K and that only μ_I is changing with temperature. That μ_c is not considerable changing with temperature, we discussed before in the results section. After we know *R*, we can determine *a* from Eq. (6.60) as follows:

(6.60) $a(T) = \frac{\frac{Y}{Y+Z}}{1-\frac{1}{R(T)}}$

In which *Y* (medium timescale component) and *Z* (long timescale component) are defined by Eq. (6.60). *R* and *a* are plotted in Fig. 6.41.

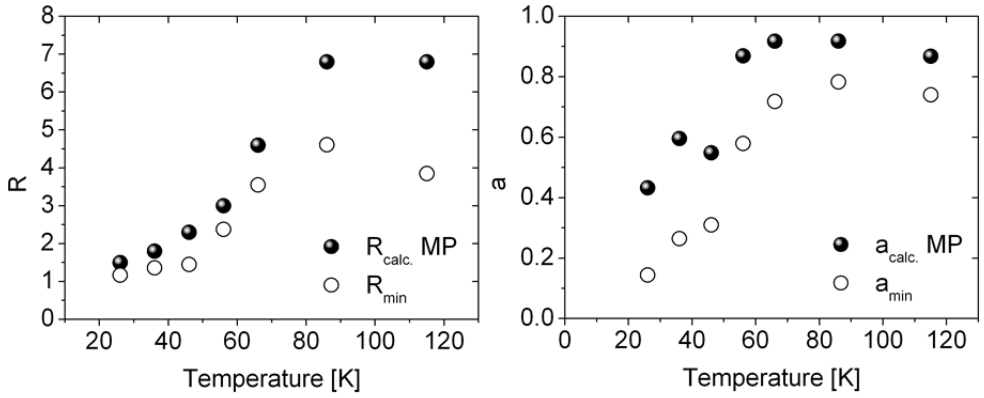

Figure 6.41 | The calculated *R* and *a* in the magnetic polaron model (see Eq. (6.58-6.60)) are compared to the values which are obtained from measurements: the lower limit for *R* and *a*, R_{min} and a_{min}.

From this analysis, we can see that *R* is around 1 for $T<<T_c$, and that *R* is around 7 for $T>T_c$. *a* is increasing from 0.4 at 26 K to about 0.9 at $T>T_c$. Note that *R* and *a* follow the same trend as we observed for R_{min} and a_{min}, see the previous section. The fact that *a* is increasing shows that more MP's are formed with increasing temperature, which is physical since the magnetization is decreasing with increasing temperature. The mobility of the free MP is decreasing, which can be understood within the double exchange model framework, which has been used to describe the conductivity in CMR manganites [16].

In the above analysis, we did not consider traps (vacancies) as an option for the intermediate state. This comes from an analysis of the fluence dependence of the branching ratio *a*, see appendix E. a_{min} is not only increasing with increasing temperature but also with increasing fluence. If the intermediate states would have been traps, we actually would have expected a dramatic drop in *a* with increasing fluences, due to the fact that there is a limited amount of traps, see also the Results section. For high fluences we estimated that the number of free electrons is larger than the number of vacancies, indicating that trapping is not the dominant relaxation mechanism.

In our model, the MP formation time τ_{CI} is weakly temperature dependent in the 36-115 K range and is about 20 ps. The electron-hole recombination time from the conduction band and MP is in 150-1000 ps range. It is large for $T<<T_C$ (large magnetization) and small for $T>T_C$ (small or zero magnetization). This is in line with

the experimentally observed increase of the decay time (with increasing magnetization) of the photo-luminesce in EuTe [43].

6.5 Conclusion

Using a pump wavelength of 800 nm, which corresponds to an electronic 4*f* to 5*d* transition, the electron ends up in a non-conducting state. This is consistent with the magnetic exciton picture in which the electron is bound by both the hole Coulomb potential, and by the exchange interaction with the hole nearest neighbors. Free electrons, in the 5*d* or 6*s* band, are formed after dissociation of the exciton by exciton-magnon, exciton-phonon, and exciton-electron scattering processes at the sub-picosecond time scale.

At longer timescales we observed two relaxation times. One is in the order of 20 ps while the other in in the 150-1000 ps range. The amplitudes of the different components are strongly temperature dependent. The results can be understood in the following framework, see also Fig. 6.42. The free electrons can recombine with holes (time constant τ_V=150-1000 ps) or free (mobile) magnetic polarons can be formed (time constant τ_{CI}≈20 ps). While the recombination time is in the 150-1000 ps range, depending on the temperature, the magnetic polaron formation time is around 20 ps on 36-115K range. The amount of magnetic polarons which are formed is determined by the branching ratio *a*. The branching ratio is increasing with increasing temperature due to the fact that magnetization is decreasing with increasing temperature. The ratio of the mobility of conduction electrons and the magnetic polarons (*R*) is also increasing with the increasing temperature. This can be understood by noting that the MP mobility is magnetization dependent and is decreasing with decreasing magnetization.

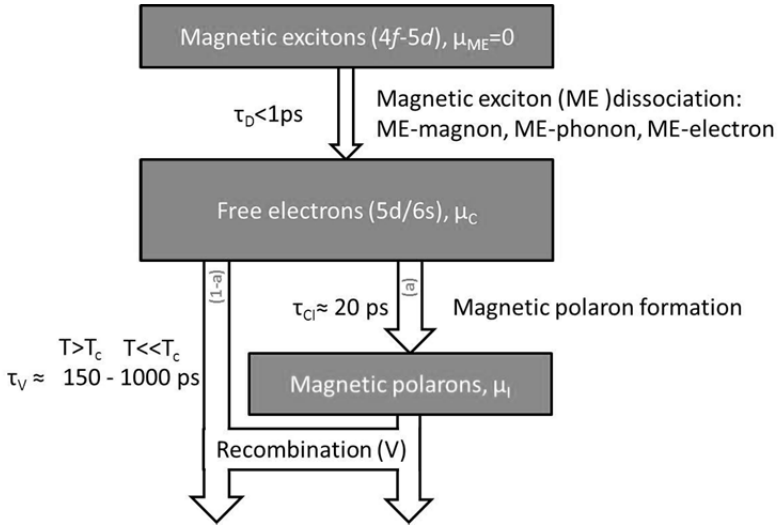

Figure 6.42 | Model of what is happening after a photo-excitation using a pump wavelength of 800 nm, in the low fluence regime (0.2 mJ/cm^2). For details, see the text.

Appendix: pump induced changes in the THz transmission

The pump induced changes in the time domain are:

(A1) $\Delta t(\tau) = t(\tau, pump\ on) - t(\tau, pump\ off)$ - τ is THz sampling pulse delay.

(A2) $t(\tau) = t(\tau, pump\ off)$.

After Fourier transformation (FT) we go to the frequency domain:

(A3) FT[$\Delta t(\tau)$]= $\Delta t(\omega)$= $|\Delta t(\omega)|\ e^{i\,\varphi_{\Delta t}(\omega)}$ - $\varphi_{\Delta t}(\omega)$is the phase

(A4) FT[$t(\tau)$]= $t(\omega)$= $|t(\omega)|\ e^{i\,\varphi_t(\omega)}$ - $|t(\omega)|$ is the amplitude

The ratio of $\frac{\Delta t(\omega)}{t(\omega)}$ is:

(A5) $\frac{FT[\Delta t(\tau)]}{FT[t(\tau)]} = \frac{\Delta t(\omega)}{t(\omega)} = \frac{|\Delta t(\omega)|}{|t(\omega)|}\frac{e^{i\,\varphi_{\Delta t}(\omega)}}{e^{i\,\varphi_t(\omega)}} = \frac{|\Delta t(\omega)|}{|t(\omega)|}e^{i\,(\varphi_{\Delta t}(\omega)-\varphi_t(\omega))}$,

in which $\varphi_{\Delta t}(\omega)-\varphi_t(\omega)$ is the unwrapped phase difference; 2π phase jumps are removed. Now we are interested in $\frac{FT[t(\tau,pump\ on)]}{FT[t(\tau)]}$:

(B6) $\frac{FT[t(\tau,pump\ on)]}{FT[t(\tau))]} = \frac{FT[t(\tau,pump\ on)-t(\tau)+t(\tau)]}{FT[t(\tau)]} = 1 + \frac{FT[\Delta t(\tau)]}{FT[t(\tau)]}$.

We can determine $\frac{|t(\omega,pump\ on)|}{|t(\omega,pump\ off)|}$ as follows:

(A6) $\frac{|t(\omega,pump\ on)|}{|t(\omega,pump\ off)|} = \left|\frac{\Delta t(\omega)}{t(\omega)} + 1\right| = \sqrt{\left(\frac{|\Delta t(\omega)|}{|t(\omega)|}\right)^2 + 1 + 2\frac{|\Delta t(\omega)|}{|t(\omega)|}\cos(\varphi_{\Delta t}(\omega)-\varphi_t(\omega))}$,

(A7) $arg\left(\frac{\Delta t(\omega)}{t(\omega)} + 1\right) = \text{atan}\left(\frac{\frac{|\Delta t(\omega)|}{|t(\omega)|}sin(\varphi_{\Delta t}(\omega)-\varphi_t(\omega))}{\frac{|\Delta t(\omega)|}{|t(\omega)|}cos(\varphi_{\Delta t}(\omega)-\varphi_t(\omega))+1}\right)$.

In in which $arg\left(\frac{\Delta t(\omega)}{t(\omega)} + 1\right)$ is the accumulated (unwrapped) phase. When the phase shift is 0; arg $\left(\frac{\Delta t(\omega)}{t(\omega)}\right) = 0, arg\left(\frac{\Delta t(\omega)}{t(\omega)} + 1\right) = 0$:

(A8) $\left|\frac{\Delta t}{t} + 1\right| = \left|\frac{|\Delta t(\omega)|}{|t(\omega)|}\right| + 1$.

References

[1] A. Mauger and C. Godart, Physics Reports-Review Section of Physics Letters **141**, 51 (1986).
[2] Y. Shapira, S. Foner, and T. B. Reed, Physical Review B **8**, 2299 (1973).
[3] P. Steeneken, *PhD thesis: New light on EuO thin films* (Rijksuniversiteit Groningen, 2002).
[4] T. Yamasaki, K. Ueno, A. Tsukazaki, T. Fukumura, and M. Kawasaki, Appl. Phys. Lett. **98**, 082116 (2011).
[5] T. Mairoser, A. Schmehl, A. Melville*, et al*, Phys. Rev. Lett. **105**, 257206 (2010).
[6] P. Sinjukow and W. Nolting, Physical Review B **69**, 214432 (2004).
[7] M. Fox, *Optical Properties of Solids* (Oxford University Press, 2004).
[8] F. Gao, G. L. Carr, C. D. Porter, D. B. Tanner, G. P. Williams, C. J. Hirschmugl, B. Dutta, X. D. Wu, and S. Etemad, Physical Review B **54**, 700 (1996).
[9] M. C. Nuss, K. W. Goossen, P. M. Mankiewich, and M. L. Omalley, Appl. Phys. Lett. **58**, 2561 (1991).
[10] M. C. Nuss, P. M. Mankiewich, M. L. Omalley, E. H. Westerwick, and P. B. Littlewood, Phys. Rev. Lett. **66**, 3305 (1991).
[11] V. K. Thorsmolle, R. D. Averitt, X. Chi, D. J. Hilton, D. L. Smith, A. P. Ramirez, and A. J. Taylor, Appl. Phys. Lett. **84**, 891 (2004).
[12] R. Ulbricht, E. Hendry, J. Shan, T. F. Heinz, and M. Bonn, Reviews of Modern Physics **83**, 543 (2011).
[13] K. P. H. Lui and F. A. Hegmann, Appl. Phys. Lett. **78**, 3478 (2001).
[14] H. Nemec, P. Kuzel, and V. Sundstrom, Journal of Photochemistry and Photobiology A-Chemistry **215**, 123 (2010).
[15] N. Smith, Physical Review B **64**, 155106 (2001).
[16] R. D. Averitt, A. I. Lobad, C. Kwon, S. A. Trugman, V. K. Thorsmolle, and A. J. Taylor, Phys. Rev. Lett. **87**, 017401 (2001).
[17] S. Sirbu, *PhD thesis: Induced excitations in some metal oxides* (University of Groningen, 2008).
[18] D. Fishman, *PhD thesis: Excitons in Cuprous Oxide* (University of Groningen, 2008).
[19] P. Planken, H. Nienhuys, H. Bakker, and T. Wenckebach, Journal of the Optical Society of America B-Optical Physics **18**, 313 (2001).
[20] R. Sutarto, S. G. Altendorf, B. Coloru*, et al*, Physical Review B **79**, 205318 (2009).
[21] R. Sutarto, S. G. Altendorf, B. Coloru*, et al*, Physical Review B **80**, 085308 (2009).
[22] P. U. Jepsen, W. Schairer, I. H. Libon, U. Lemmer, N. E. Hecker, M. Birkholz, K. Lips, and M. Schall, Appl. Phys. Lett. **79**, 1291 (2001).
[23] M. Beard, G. Turner, and C. Schmuttenmaer, Physical Review B **62**, 15764 (2000).
[24] J. Bigot, M. Portella, R. Schoenlein, J. Cunningham, and C. Shank, Phys. Rev. Lett. **65**, 3429 (1990).

[25] J. Shah, B. Deveaud, T. C. Damen, W. T. Tsang, A. C. Gossard, and P. Lugli, Phys. Rev. Lett. **59**, 2222 (1987).
[26] J. Han, B. K. Woo, W. Chen, M. Sang, X. Lu, and W. Zhang, Journal of Physical Chemistry C **112**, 17512 (2008).
[27] G. Guntherodt, Physics of Condensed Matter **18**, 37 (1974).
[28] G. Guntherodt, P. Wachter, and D. M. Imboden, Physik Der Kondensiterten Materie **12**, 292 (1971).
[29] A. B. Henriques, M. A. Manfrini, P. H. O. Rappl, and E. Abramof, Physical Review B **77**, 035204 (2008).
[30] T. Kasuya, J Magn Magn Mater **195**, 141 (1999).
[31] D. I. Khomskii, *Basic Aspects of the Quantum Theory of Solids: Order and Elementary Excitations* (cambridge university press, 2010).
[32] M. F. Hundley, M. Hawley, R. H. Heffner, Q. X. Jia, J. J. Neumeier, J. Tesmer, J. D. Thompson, and X. D. Wu, Appl. Phys. Lett. **67**, 860 (1995).
[33] T. Kasuya, J Magn Magn Mater **195**, 141 (1999).
[34] M. Takahashi, K. Mitsui, and M. Umehara, Physical Review B **48**, 17053 (1993).
[35] T. Penney and T. Kasuya, J. Appl. Phys. **42**, 1403 (1971).
[36] C. Llinares, C. Duchemin, and G. Bordure, Solid State Commun. **13**, 785 (1973).
[37] C. S. Snow, S. L. Cooper, D. P. Young, Z. Fisk, A. Comment, and J. P. Ansermet, Physical Review B **64**, 174412 (2001).
[38] P. M. S. Monteiro, P. J. Baker, A. Ionescu, C. H. W. Barnes, Z. Salman, A. Suter, T. Prokscha, and S. Langridge, Phys. Rev. Lett. **110**, 217208 (2013).
[39] S. Kimura, T. Ito, H. Miyazaki, T. Mizuno, T. Iizuka, and T. Takahashi, Physical Review B **78**, 052409 (2008).
[40] S. J. Blundell, T. Lancaster, F. L. Pratt, P. J. Baker, W. Hayes, J. -. Ansermet, and A. Comment, Physical Review B **81**, 092407 (2010).
[41] J. B. Torrance, M. W. Shafer, and T. R. Mcguire, Phys. Rev. Lett. **29**, 1168 (1972).
[42] J. P. Lascaray, J. P. Desfours, and M. Averous, Solid State Commun. **19**, 677 (1976).
[43] W. Heiss, R. Kirchschlager, G. Springholz, Z. Chen, M. Debnath, and Y. Oka, Phys. Rev. B **70**, 035209 (2004).

Chapter 7

Laser-induced magnetization dynamics in EuTe and other multi-sublattice systems.

In this chapter we discuss the ultrafast magnetization dynamics due to laser-induced hot conduction electrons in antiferromagnetic EuTe. Like in the case of EuO, we measure pump-induced changes in the magnetization using the Faraday effect. We present and discuss our magnetization dynamics data on EuTe and we will compare this with our results on ferromagnetic EuO. Apart from that we will also discuss the resonant X-ray magnetic scattering data on EuTe (from literature) in which the antiferromagnetic order parameter was probed. These results can also help us in the understanding of the laser-induced demagnetization data on EuO. The focus is on mechanisms which are responsible for inter-sublattice angular momentum transfer.

7.1 Introduction

This introduction focuses on the similarities and differences in the (lased-induced) spin-lattice relaxation and cross relaxation processes between ferro- and antiferromagnets, see also Fig. 7.1. Later on, we will try to understand the laser-induced magnetization dynamics of EuTe in terms of the framework which is presented in this section. In our language, which is similar as is used in the magnetic resonance community, the spin-lattice relaxation refers to angular momentum transfer between spins and the lattice. In this case the total electronic angular momentum is not conserved ($\Delta S \neq 0$). The cross relaxation [1] refers to angular momentum transfer between different magnetic sublattices, in which case

the total electronic angular momentum is conserved (ΔS=0). We also use the term "cross relaxation" for the angular momentum transfer between magnetic moment at different sites, see Fig 7.1 right.

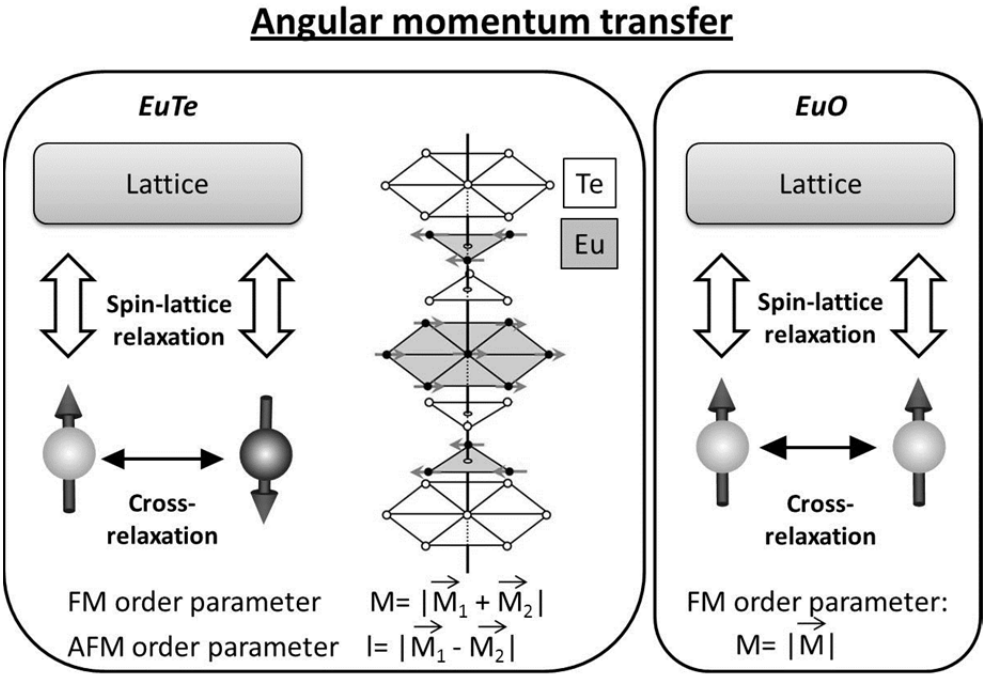

Fig. 7.1. | Angular momentum transfer in EuO (one sub-lattice) and EuTe (two sub-lattices). The interlayer separation in the structure of EuTe has been exaggerated.

In this section we will look into the problem from two different points of view: i) by considering localized excitations (spin-flips, vibrations), and ii) by considering collective excitations (phonons, magnons). For details about framework ii) see the appendix A-F, where we discuss the interaction of magnons with other quasi-particles. Below we focus on the influence of the following interactions on the spin-lattice relaxation and cross relaxation times:

- Exchange coupling between the spins or magnons.
- Magnetic-dipole coupling between the spins or magnons.
- Electron-spin (localized picture) or electron-magnon coupling (collective picture).
- Spin-crystal field (localized picture) or magnon-phonon coupling (collective picture).

We start with the localized picture, followed by the collective picture.

7.1.1 The localized picture.

There are a variety of mechanisms which can contribute to the spin-lattice and cross relaxation in magnetic materials. One of the most important contributions to the cross relaxation arises from the Heisenberg interaction between the localized spins. The Heisenberg (exchange) Hamiltonian, for a single sublattice system consisting of localized magnetic moments, is given by:

(7.1) $H_{ex} = \sum J_{ij}\ \vec{S_i}\vec{S_j} = \sum J_{ij}\left[S_i^z S_j^z + \frac{1}{2}(S_i^+ S_j^- + S_i^- S_j^+)\right]$,

where *i* and *j* are the site indexes (nearest neighbors) and $S^+$and S^- are the usual spin raising and lowering operators. After a Holstein-Primakoff transformation [2], this can be written as:

(7.2) $H_{ex} = H_{ex}^{(0)} + H_{ex}^{(2)} + H_{ex}^{(4)}$,

(7.3) $H_{ex,0} = -\sum J_{ij} S^2$,

(7.4) $H_{ex,2} = -\sum J_{ij} S(a_i^\dagger a_j + a_j a_i^\dagger - a_i a_i - a_j a_j)$,

(7.5) $H_{ex,4} = -\Sigma J_{ij}(a_i^\dagger a_i a_j^\dagger a_j - \frac{1}{4}[a_i^\dagger a_i^\dagger a_i a_j + a_i^\dagger a_j^\dagger a_j a_j + a_j^\dagger a_i^\dagger a_i a_i + a_j^\dagger a_j^\dagger a_j a_i])$.

The number in the subscript refers to the amount of creation or annihilation operators $a, a^\dagger$. The first term in Eq. (7.2) is proportional to S^2. The second term in Eq. (7.2), which is proportional to *S*, contains terms in which angular momentum is transferred from site *i* to site *j*. The first two terms in Eq. (7.4) are the terms we are actually interested in, since they are the dominant terms contributing to the angular momentum transfer between different lattice sites: the cross relaxation. We will neglect the third term in Eq. (7.2) $(H_{ex,4})$ most of the times, since it is weaker than the other terms.

The exchange Hamiltonian we discussed commutes with the total electronic angular momentum S^z which means that S^z is conserved. This does not hold for the magnetic dipole Hamiltonian, which is another type of interaction between spins: S^z does not commute with H_{dp} (why this is we discuss later on). The (pseudo) magnetic dipole Hamiltonian can be written in terms of lowering and raising operators [1]. Not all terms do conserve S^z[1]:

(7.6) $H_{dp} = A + B + C + D + E + F$,

(7.7) $H_{dp}^A \sim S_i^z S_j^z$, (ΔS=0)

(7.8) $H_{dp}^B \sim S_i^+ S_j^- + S_i^- S_j^+$, (ΔS=0)

(7.9) $H_{dp}^C \sim S_i^+ S_j^z + S_i^z S_j^+$, (ΔS= +1)

(7.10) $H_{dp}^D \sim S_i^- S_j^z + S_i^z S_j^-$, (ΔS= -1)

(7.11) $H_{dp}^{E} \sim S_i^+ S_j^+$, (ΔS=+2)

(7.12) $H_{dp}^{F} \sim S_i^- S_j^-$. (ΔS=-2)

Term A connects states with the same energy and S^z. Term B corresponds to a pure cross relaxation process (pure=total electronic angular momentum conserving) in which there is angular transfer between spins at different lattice sites. Term B is similar to the term $H_{ex,2}$ in the exchange Hamiltonian. In terms C-F, the total electronic angular momentum is not conserved (ΔS≠0); there is angular momentum transfer to the lattice [1,3]. Therefore terms C-F contribute to the angular momentum transfer between the spin system and the lattice: the spin-lattice relaxation. Since the total electronic angular momentum is not conserved, these processes are expected to be slow (>>8 ps, see Chapter 3-5). The following processes are expected to be the most relevant ones for cross relaxation:

(7.13) $cross\text{-}relaxation \rightarrow H_{ex,2} + H_{ex,4} + H_{dp}^{B}$+… (ΔS=0).

Usually in ferromagnetic systems, we expect the exchange term to be much stronger than the dipolar term.

As discussed, apart from cross relaxation, the localized spins can also interact with the lattice. A spin flip can for instance occur due to anisotropic crystal field fluctuations. The Hamiltonian relevant for this process contains terms proportional to single spin operators:

(7.14) $H_{spin-crystal\ field} \sim S_i^+ + \sim S_i^- + \sim S_j^+ + \sim S_j^-$. (ΔS=±1).

Since the total angular momentum is not conserved, these processes are expected to be slower than the cross relaxation mechanisms. The following processes are expected to be important in the spin-lattice relaxation:

(7.15) $spin\text{-}lattice \rightarrow H_{dp}^{C} + H_{dp}^{D} + H_{dp}^{E} + H_{dp}^{F} + H_{spin-crystal\ field}$+… (ΔS≠0).

There are actually more terms contributing to the cross and spin-lattice relaxation, like for instance the hyperfine coupling. However they are not important on the timescales we are interested in (< ns).

Summarizing, in this subsection we described the cross- and spin-lattice interaction in a localized picture. In this framework, there is not much difference in the description between ferromagnets with one sub-lattice and systems with more sub-lattices like multi-sublattice ferromagnets, ferrimagnets and antiferromagnets. In the second case ii) we will consider collective excitations, which are the normal modes of the magnetic subsystem. The normal modes in the different systems

(single-sublattice ferromagnets, multi-sublattice ferromagnets, ferrimagnets and antiferromagnets) are completely different in nature, as we will see.

7.1.2. The collective (delocalized) picture: single sub-lattice ferromagnets.

In this scenario we consider collective spin excitations; magnons. We assume that the magnons are completely delocalized, and that no magnon wave packets are formed which localize the magnon in space. We discuss three types of relaxation mechanisms and interactions:

- Spin-lattice relaxation: angular momentum transfer between spins and the lattice.
- Cross-relaxation: angular momentum transfer between spins on different sites. In the scenario that we consider (ferromagnet, delocalized and no wave-packet), there is no cross relaxation. However, we will see that cross-relaxation is important in antiferromagnets.
- Magnon-magnon interaction: interaction between different magnon modes. In this case there is no angular momentum transfer between spins and the lattice.

As mentioned, since we assumed that the magnons are completely delocalized, and that no magnon wave packets are formed which localize the magnon in space, there is no cross relaxation in this picture. In the remainder of this section we discuss the magnon-magnon coupling and the spin-lattice coupling in single sublattice ferromagnets. The collective excitations, in a single-sublattice ferromagnet, can be obtained after doing a Fourier transform of (7.2) [4]:

(7.16) $H_{ex} = constant + \sum_q \omega_q \, a_q^\dagger a_q + \sum_{qq'q''} \sum_{\Delta R} C(q, q', q'', \Delta R) \, a_q^\dagger a_{q'}^\dagger a_{q''} a_{q+q'-q''}$

In which a_q is the usual magnon annihilation operator of a magnon with momentum q. The third term in the exchange Hamilton describes the (four) magnon interactions. Magnons can also interact with other magnons by the magnetic-dipole Hamiltonian. This Hamiltonian contains (3-magnon) terms like [3,5]:

(7.17) $H_{dp,3} \propto a_q^\dagger a_{q'} a_{q''} + \propto a_q^\dagger a_{q'}^\dagger a_{q''}$ (ΔS=±1)

In our language, this is a spin-lattice relaxation process since ΔS≠0. Since in these processes, the total angular momentum is not conserved [1,3], these processes are expected to be slow (>>8 ps). Like is described extensively in the appendix, in doped magnetic semiconductors, magnons can also interact with conduction

electrons [5--8]. The electron-magnon Hamiltonian contains scattering terms like [8]:

(7.18) $H_{e-m} \propto {c^{\dagger}}_{k-q\uparrow}\, c_{k\downarrow}\, {a_q}^{\dagger}$ (localized moments: ΔS=-1)

In which c_k is the conduction electron annihilation operator. In this process a magnon is created (ΔS=+1) while the total electronic angular momentum is conserved (through a simultaneous spin flip of the conduction electron spin). Two consecutive (separated by ;) of this type of process, give effectively a magnon-magnon coupling:

(7.19) $e\text{-}m^{(2)} \rightarrow a_q,\, {c^{\dagger}}_{k-q+q,\downarrow}\, c_{k-q\uparrow}$; ${c^{\dagger}}_{k-q\uparrow}\, c_{k\downarrow}\, {a_q}^{\dagger}$ (ΔS=0)

In which the superscript (2) refers to the fact that this process gives a magnon-magnon interaction in a 2nd order perturbation theory in H_{e-m}. This is, effectively, a 2-magnon scattering process in which a magnon with momentum q is annihilated and a magnon with momentum q' is created. Some important (effective) magnon-magnon scattering processes are:

(7.20) $magnon\text{-}magnon \rightarrow e\text{-}m^{(2)} + H_{ex,4} + \ldots$ (ΔS=0)

Remember, Eq. (7.20) describes the (*total electronic angular momentum conserving*) magnon-magnon interaction. While the 4-magnon exchange process are usually slow (>> 1 ns), an (electron-magnon) 2-magnon process can be (ultra)fast, depending on the conduction electron concentration, conduction electron temperature, and electron-magnon interaction strength.

Apart from electron-magnon interaction, there is also magnon-phonon interaction. The following processes are important: the direct process (one phonon) and the Raman process (two-phonon) [9--12]. For simplicity we neglect the Orbach process (spin excitation via another(third) state [9]). Examples of scattering terms are [5]:

(7.21) $H_{m-p}{}^{direct} \sim a_q^{\dagger} b_q$ (ΔS=-1),

and

(7.22) $H_{m-p}{}^{Raman} \sim a_q^{\dagger} b_{k-q}^{\dagger} b_k$ (ΔS=-1),

where b_q is the phonon annihilation operator. Both processes do not conserve the total magnon angular momentum, and therefore contribute to spin-lattice relaxation processes, in which angular momentum is transferred from the spin system to the lattice, or the other way around. The process described in Eq. (7.18) ($H_{e-m}^{(1)}$), followed by electron-phonon spin flip scattering (for instance $b_{-q}\, {c^{\dagger}}_{k\downarrow} c_{k-q\uparrow}$), can also give rise to spin-lattice relaxation. This effect was

shown to be important in ferromagnetic rare-earth metals (Gd, Tb) and diluted magnetic semiconductors (Mn-doped GaAs) [13,14]. An example of this two-step scattering process is given by:

(7.23) $p\text{-}e\text{-}m \rightarrow \; b_{-q}\, {c^{\dagger}}_{k\downarrow} c_{k-q\uparrow} \; ; \; {c^{\dagger}}_{k-q\uparrow} c_{k\downarrow}\, {a_q}^{\dagger}$ (localized moments: ΔS=-1).

To summarize, including this last two-step process, the following processes are expected to be important in the spin-lattice relaxation in ferromagnetic semiconductors:

(7.24) $spin\text{-}lattice \rightarrow {H_{m-p}}^{direct} + {H_{m-p}}^{Raman} + p\text{-}e\text{-}m + H_{dp,3} + \ldots$ (ΔS≠0)

In the next section we will consider an antiferromagnet with two sublattices.

7.1.3 The collective (delocalized) picture: antiferromagnets. Let us now consider a simple antiferromagnet in which there are two-sublattices. We discuss three types of relaxation mechanisms and interactions:

- Spin-lattice relaxation: angular momentum transfer between spins and the lattice.
- Cross-relaxation: inter-sublattice angular momentum transfer between different antiferromagnetic magnon modes (α,β).
- Magnon-magnon interaction: interaction between different magnon modes. In this case there is no inter-sublattice angular momentum transfer, and there is no angular momentum transfer between spins and the lattice.

In a simple antiferromagnet with two-sublattices, the final diagonalized exchange Hamiltonian becomes [4,15]:

(7.25) $H_{ex} = H_{ex,0} + H_{ex,2} = constant + \sum_q \omega_q \left(\alpha_q^{\dagger}\alpha_q + \beta_q^{\dagger}\beta_q + 1\right)$

In which α (ΔS=+1) and β (ΔS=+1) are the two degenerate (in zero field) antiferromagnetic magnon modes. See for more information appendix B. We will name the total localized moment-angular momentum *M*. *M* is the sum of the *z*-component of the angular momentum of the two sublattices and is defined as: $M=S_{z,1}+S_{z,2}$. In antiferromagnets we can also defined *L*, which is the antiferromagnetic order parameter: $L=S_{z,1}-S_{z,2}$. In contrast to *M*, *L* is not a conserved quantity.

Now we consider magnon-magnon scattering in which the total electronic angular momentum is conserved and in which there is no inter-sublattice angular momentum transfer (Δ*L*=Δ*M*=0). The following processes can give an (effective) magnon-magnon interaction.

(7.26) $magnon\text{-}magnon \rightarrow e\text{-}m^{(2)} + H_{ex,4} + \ldots$ (ΔM=0, ΔL=0)

4-magnon scattering is not expected to be important on the time-scales we are interested in (<1 ns). The (electron-magnon) 2-magnon process can be (ultra)fast, depending on the conduction electron concentration and electron-magnon interaction strength. While some scattering processes in $e\text{-}m^{(2)}$ and $H_{ex,4}$ conserve *L*, there are also processes in which there is inter-sublattice angular momentum transfer (Δ*L*≠0), see the appendix B-D. Therefore the exchange and electron-magnon interaction processes are also important for the cross relaxation:

(7.27) $cross\text{-}relaxation \rightarrow e\text{-}m^{(2)} + H_{ex,4} + \ldots$ (ΔM=0, ΔL≠0)

In this case, the total electronic angular momentum is conserved (ΔM=0) while $\Delta L \neq 0$. Later on we will neglect the slow 4-magnon processes ($H_{ex,4}$). We can make the following statements about the electron-magnon scattering processes which contribute to the cross relaxation in EuTe (for the lengthy discussion of why this is the case, we refer to appendix A-D):

- Inter-sublattice angular momentum transfer (Δ*L*≠0) is only efficient when high q-vectors AFM magnons are involved, see appendix B-D. Moreover, there can be no inter-sublattice angular momentum transfer when only zone center magnons with *q*=0 are involved in the electron-magnon scattering processes.
- Inter-sublattice angular momentum transfer can be ultrafast when there is a strong (conduction) electron-(AFM) magnon interaction.
- In the thermalization of (AFM) magnons (which high q) ΔL is not conserved, while ΔM is conserved.

Before continuing the discussing, we first focus on the spin-lattice relaxation. We expect the dominant spin-lattice relaxation processes to be the same as in the single sub-lattice (ferromagnetic) case:

(7.28) $spin\text{-}lattice \rightarrow {H_{m-p}}^{direct} + {H_{m-p}}^{Raman} + p\text{-}e\text{-}m + H_{dp,3}$ (ΔM≠0, $\Delta L = 0$ or $\Delta L \neq 0$)

Which contains terms in which $\Delta L = 0$ (*q*=0) but also terms in which $\Delta L \neq 0$ (*q*≠0), while one always has $\Delta M \neq 0$. As mentioned before, since the total electronic angular momentum is not conserved, we expect these processes to be relatively slow (>8 ps).

We do not expect the spin-lattice relaxation in single sub-lattice ferromagnets to be much different than in multi-sublattice magnets (ferromagnets, ferrimagnets, antiferromagnets).

Some differences might arise thought from the fact that multi-sublattice magnets have more magnon branches. Two-sublattice ferromagnets and ferrimagnets have apart from an acoustic magnon branch also an optical magnon branch, and two-sublattice antiferromagnets have two (degenerate, in zero field) antiferromagnetic magnon modes with a dispersion which differs qualitatively from the single sub-lattice ferromagnetic case. These differences in dispersion may affect the magnon-phonon coupling due to differences in the way the energy and momentum conservation laws can be fulfilled in the two cases.

7.1.4 Comparison between localized and collective pictures in AFM's with localized moments

In Table 7.1, we consider the ultrafast magnetization dynamics $\Delta \mathrm{L}(\mathrm{t})$ in antiferromagnetic semiconductors, in different limiting cases. The big difference with the ferromagnetic case is that the antiferromagnetic order (*L*) can be affected by both cross and spin-lattice relaxation, while ferromagnetic order (*M*) can be only affected by spin-lattice relaxation processes. The middle (collective picture) and right column (localized picture) in the figure depicts the most important contributions governing the $\Delta \mathrm{L}(\mathrm{t})$ dynamics, based on the general knowledge about magnetization dynamics and typical coupling strengths. In Table 7.2, the same is done for $\Delta M_z(\mathrm{t})$ for an antiferromagnetic sample in an applied magnetic field above the spin-flop field (spin-flop transition).

Let us first consider the collective picture. For *weak* conduction electron-magnon coupling, the $\Delta \mathrm{L}(\mathrm{t})$ dynamics is determined by the magnon-phonon coupling and ΔT_{l-s} (difference in the lattice and localized moment spin temperature). For (very) *strong* conduction electron-magnon coupling, the $\Delta \mathrm{L}(\mathrm{t})$ dynamics is determined by the electron-magnon coupling and ΔT_{e-s} (temperature difference in the conduction electron and localized moment spin temperature).

Table 7.1 | Magnetization dynamics $\Delta L(t)$ in an antiferromagnetic semiconductor for different limiting cases. The middle (collective picture) and right column (localized picture) depicts the most important contributions governing the $\Delta L(t)$ dynamics. The notations: cpl. =coupling. sp=localized spin, la=lattice, m=magnon, p=phonon, ex=exchange, e= electron=conduction electron, cf=crystal field, subl.=sublattice, 1=sublattice 1, 2=sublattice 2, T=temperature, $\Delta T_{l-s} =$ difference in the lattice and localized moment spin temperature, $\Delta T_{e-s} =$ temperature difference in the conduction electron and localized moment spin temperature, A) is the leading term when $\Delta T_{subl} \neq 0$ (ΔT_{subl} is large) while B) is the next most important term when $\Delta T_{subl} = 0$. For $sp - la$ (spin-lattice) holds that ΔM≠0 while for $cr - rx$ (cross-relaxation) holds that ΔM=0 and ΔL≠0.

Conditions	Collective picture	Localized picture
weak conduction electron-magnon/spin cpl.	$\Delta L(t) \rightarrow sp\text{-}la \rightarrow H_{m-p}$ ΔT_{l-s}	A) $\Delta L(t) \rightarrow cr\text{-}rx \rightarrow H_{ex,2}$ $\Delta T_{subl} = T_1 - T_2$ B) $\Delta L(t) \rightarrow sp\text{-}la \rightarrow H_{s-cf}$ ΔT_{l-s}
strong conduction electron-magnon/spin cpl.	$\Delta L(t) \rightarrow cr\text{-}rx \rightarrow e\text{-}m^{(2)}$ ΔT_{e-s}	A) $\Delta L(t) \rightarrow cr\text{-}rx \rightarrow H_{ex,2}$ $\Delta T_{subl} = T_1 - T_2$ B) $\Delta L(t) \rightarrow cr\text{-}rx \rightarrow e\text{-}s^{(2)}$ ΔT_{e-s}
very strong conduction electron-magnon/spin cpl.	$\Delta L(t) \rightarrow cr\text{-}rx \rightarrow e\text{-}m^{(2)}$ ΔT_{e-s}	$\Delta L(t) \rightarrow cr\text{-}rx \rightarrow e\text{-}s^{(2)}$ ΔT_{e-s}

For the localized case, the situation is different. For *weak* conduction electron-magnon coupling, when the temperature between the two sub-lattice is different ($\Delta T_{subl} = T_1 - T_2 \neq 0$), the most important term in determining the $\Delta L(t)$ dynamics is the exchange term ($H_{ex,2}$). However in AFM's like EuTe, T_1=T_2, and the most important term in determining the ultrafast $\Delta L(t)$ dynamics is the spin-crystal field term (H_{s-cf}). In that case L will only change when there is a temperature difference between the lattice and the localized spins, ΔT_{l-s} .

For *strong* conduction electron-magnon coupling, when the temperature between the two sub-lattice is different ($\Delta T_{subl} \neq 0$), the most important term in determining the $\Delta L(t)$ dynamics is also the exchange term ($H_{ex,2}$). However when T_1=T_2, the most important term in determining the ultrafast $\Delta L(t)$ dynamics is the electron-spin term, $e\text{-}s^{(2)}$. In that case L will only change when there is a temperature difference between the conduction electrons and the localized spins, ΔT_{e-s} . For *very strong* conduction electron-magnon coupling, the most important term in determining the ultrafast $\Delta L(t)$ dynamics is also the electron-spin term $e\text{-}s^{(2)}$.

For the pure (as opposed to ferrimagnetic case) AFM case T_1=T_2 always holds, and we can see that the collective and localized picture are the same. However, this does not hold for ferrimagnets where the (spin) temperature T_1 of sublattice-1 is not always equal to that of sublattice-2 (T_2). In this case, there can be efficient angular transfer by the exchange term $(H_{ex,2})$ in the localized picture (weak or strong conduction electron-magnon coupling), while this is not possible in the collective picture. This means when the magnon is very localized in space, one gets closer to a localized picture, and the inter-sublattice angular momentum can be faster. Localization can for instance happen because of magnetic domain formation, or structural domain formation.

The exchange term $(H_{ex,2})$ in the localized picture is also important if one wants to describe the transfer of angular momentum between different magnetic domains. Therefore the inter-sublattice angular momentum in bulk AFM is expected to be faster in polycrystalline materials (large amount of small magnetic domains) than in single crystals (small amount of large magnetic domains). In ferrimagnetic GdFeCo it was shown that ultrafast non-local angular momentum transfer between nano-regions is indeed taking place [16].

The situation for the magnetization dynamics in the spin-flop phase is less complicated, and the collective and localized pictures gives similar results, see Table 7.2. The dynamics is, of course, always determined by terms in $sp\text{-}la$.

Table 7.2 | Magnetization dynamics $\Delta M_z(\mathrm{t})$ in an antiferromagnetic semiconductor a in the spin-flop phase, in different limiting cases. In the middle (collective picture) and right column (localized picture), is depicted what is the most important part in the Hamiltonian which governs the $\Delta\mathrm{M}(\mathrm{t})$ dynamics. See also Table 7.1 for more information. cpl=coupling.

Conditions	Collective picture	Localized picture
weak conduction electron-magnon/spin cpl.	$\Delta\mathrm{M}(\mathrm{t}) \rightarrow sp\text{-}la \rightarrow H_{m-p}$ ΔT_{l-s}	$\Delta\mathrm{M}(\mathrm{t}) \rightarrow sp\text{-}la \rightarrow H_{s-cf}$ ΔT_{l-s}
strong conduction electron-magnon/spin cpl. + <u>weak</u> conduction electron spin-phonon/CF cpl.	$\Delta\mathrm{M}(\mathrm{t}) \rightarrow sp\text{-}la \rightarrow H_{m-p}$ ΔT_{l-s}	$\Delta\mathrm{M}(\mathrm{t}) \rightarrow sp\text{-}la \rightarrow H_{s-cf}$ ΔT_{l-s}
strong conduction electron-magnon/spin cpl. + <u>strong</u> conduction electron spin-phonon/CF cpl.	$\Delta\mathrm{M}(\mathrm{t}) \rightarrow sp\text{-}la \rightarrow p\text{-}e\text{-}m$ $\Delta T_{l-s} + \Delta T_{e-s}$	$\Delta\mathrm{M}(\mathrm{t}) \rightarrow sp\text{-}la \rightarrow cf\text{-}e\text{-}m$ $\Delta T_{l-s} + \Delta T_{e-s}$

When there is a weak conduction electron-magnon coupling and/or a weak conduction electron spin-phonon coupling, the $\Delta M_z(\mathrm{t})$ dynamics is determined by the magnon-phonon (spin-crystal field) coupling and by ΔT_{l-s}. When there is both a strong conduction electron-magnon coupling *and* a strong conduction electron spin-phonon coupling, the $\Delta M_z(\mathrm{t})$ dynamics is determined by the phonon-electron-magnon (crystal field-electron-spin) term. In this case the $\Delta M_z(\mathrm{t})$ dynamics depends on both ΔT_{l-s} and ΔT_{e-s}.

7.1.5 Comparison between ΔL and ΔM dynamics in AFM's with localized moments and conduction electrons

In Table 7.3 we make a comparison between the ΔM_z (spin-flop phase) and ΔL (B=0 mT) dynamics in different cases. We consider the AFM case where both sublattice spin temperatures are the same, T_1=T_2.

Table 7.3 | Comparison of the ΔM_z and ΔL dynamics in different cases. We consider the AFM case when T_1=T_2. See also Table 7.1 and Table 7.2. cpl=coupling.

Conditions	Collective picture	Localized picture
weak conduction electron-magnon/spin cpl.	$\Delta\mathrm{L}(\mathrm{t}) \rightarrow \Delta T_{l-s}$ $\Delta\mathrm{M}(\mathrm{t}) \rightarrow \Delta T_{l-s}$	$\Delta\mathrm{L}(\mathrm{t}) \rightarrow \Delta T_{l-s}$ $\Delta\mathrm{M}(\mathrm{t}) \rightarrow \Delta T_{l-s}$
strong conduction electron-magnon/spin cpl. + <u>weak</u> conduction electron spin-phonon/CF cpl.	$\Delta\mathrm{L}(\mathrm{t}) \rightarrow \Delta T_{e-s}$ $\Delta\mathrm{M}(\mathrm{t}) \rightarrow \Delta T_{l-s}$	$\Delta\mathrm{L}(\mathrm{t}) \rightarrow \Delta T_{e-s}$ $\Delta\mathrm{M}(\mathrm{t}) \rightarrow \Delta T_{l-s}$
strong conduction electron-magnon/spin cpl. + <u>strong</u> conduction electron spin-phonon/CF cpl.	$\Delta\mathrm{L}(\mathrm{t}) \rightarrow \Delta T_{e-s}$ $\Delta\mathrm{M}(\mathrm{t}) \rightarrow \Delta T_{l-s} + \Delta T_{e-s}$	$\Delta\mathrm{L}(\mathrm{t}) \rightarrow \Delta T_{e-s}$ $\Delta\mathrm{M}(\mathrm{t}) \rightarrow \Delta T_{l-s} + \Delta T_{e-s}$

When there is a weak conduction electron-magnon coupling, we expect the ΔM_z and ΔL dynamics to have similar timescales. In this case there is energy transfer from the lattice to the spin system which is determined by ΔT_{l-s}. The ΔM_z and ΔL dynamics is expected to be slow: in the 10 ps-10 ns range typically. The situation is different when there is a strong conduction electron-magnon coupling and a weak conduction electron spin-phonon coupling. In this case the ΔL dynamics is determined by ΔT_{e-s} while the ΔM_z dynamics is determined by $\Delta T_{lattice}$. In this case the ΔM_z dynamics is expected to be slow (in the 10 ps-10 ns range typically) while the ΔL dynamics is expected to be much faster (can be <<1 ps).
Finally we consider the situation where there is both a strong conduction electron-magnon coupling *and* a strong conduction electron spin-phonon coupling. In this

case the ΔL dynamics is set by ΔT_{e-s} (100 fs-ns timescale) while the ΔM_z dynamics is set by both ΔT_{l-s} and ΔT_{e-s} (100 fs-ns timescale).

7.1.6 Outline

The preceding section was meant to create a framework in which we can understand the magnetization dynamics in EuTe (and EuO). The implications of all this for the EuTe case will be discussed throughout the remainder of this chapter, where we will see what is the effect of the difference in spin-spin interaction and magnetic exciton or magnetic polaron formation between EuO and EuTe. The rest of the chapter is organized as followings.

- First we discuss the magnetic and transport properties of EuTe.
- In the subsection after that, we discuss an interesting experiment which has been described in the literature [17]: time-resolved resonant magnetic X-ray scattering (RMXS) on EuTe. This experiment probes the anti-ferromagnetic order parameter *L* directly.
- After that we discuss the four temperature model (in which there are two magnetic sub-lattices) and do some suggestions concerning the interpretation of the RXMS data.
- In the next section, photo-luminescence experiments (from literature) are discussed from which we can learn more about the carrier dynamics in EuTe.
- In section 7.2 we will turn to our own experimental results: A) temperature and magnetic field dependence of the optical absorption edge, and B) time-resolved magnetization dynamics in EuTe in the spin-flop phase.
- The chapter ends with a discussion and conclusion section.

To aid the reader we include several appendices discussing the magnon-phonon/electron/magnon interaction in ferromagnetic and antiferromagnetic semiconductors.

7.1.7 Magnetic properties of EuTe

EuTe orders antiferromagnetic below T_N= 9.8 K with a ferromagnetic spin alignment within the (111) planes and an antiferromagnetic alignment between these planes, see Fig 7.1. This corresponds to type II antiferromagnetic order (in FCC systems) [18--22]. The nearest neighbor (NN) exchange (J_1) is ferromagnetic while the next

NN (NNN) exchange (J_2) in antiferromagnetic. The NN exchange can be explained in terms of a Eu4*f*-Eu5*d*-Eu4*f* mechanism, as described in the chapter 1. The NNN exchange originates from super exchange interactions: by Eu4f-Eu5d-O2p-Eu5d-Eu4f mechanisms. The ratio of the NNN and NN exchange constants is $J_2 / J_1 \approx -2$, making the antiferromagnetic interaction the dominant one [23,24]. The (J_1,J_2) magnetic phase diagram for FCC magnets is shown in Fig. 7.2. In the diagram there are 3 different AFM phases and there is one FM phase. The question now is what will happen when EuTe is *n*-doped. In this case J_1 will most likely gain importance due to the enhanced 4*f*-5*d*-4*f* interaction, as in n-doped EuO [18,19]. The RKKY (like) interaction can also decrease J_2 and even might make J_2 negative (ferromagnetic). This means that EuTe can become FM when it is n-doped, see the arrow in Fig. 7.2. Note that since we expect the NN exchange to be always FM (J_1<0), one can either end up in the FM phase or the Type II AFM phase.

When EuTe is *n*-doped with Gd, indeed, it was shown that the importance of the ferromagnetic interactions can increase. For a doping concentration of 10%, the paramagnetic Curie temperature is positive and about 25 K [25]. Ferromagnetic order sets in at about 10 K, which is almost the same as the antiferromagnetic Néel temperature in un-doped EuTe.

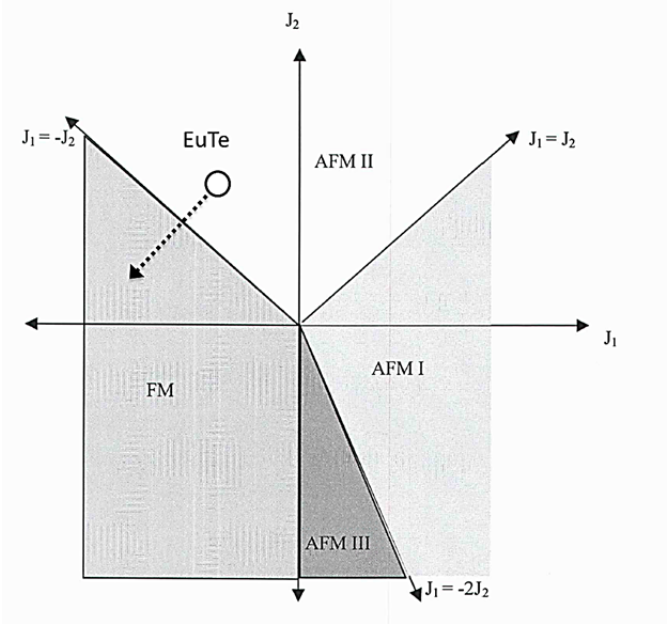

Fig. 7.2 | The (J_1,J_2) magnetic phase diagram for FCC magnets. In this case J<0 corresponds to FM exchange while J>0 corresponds to AFM exchange. For EuTe: $J_2 / J_1 \approx -2$. Taken from [23] with permission.

As mentioned, in EuTe there is ferromagnetic order within the (111) planes. Since there are 4 different possible (111) planes, there are 4 different so-called twin domains (T-domains) [20,20--22,26,26,26,27]. Within one such T domain, the spins are aligned along the <11-2> directions due to the magnetic anisotropy. There are 3 equivalent <11-2> azimuths, the so-called spin-domains (S-domains). Since the magnetization can be orientated in two ways, there are in total 2x3x4=24 magnetic domains.

When a magnetic field in applied perpendicular to the easy axis in a domain, the sub-lattice magnetizations will rotate and there will be a net magnetization. One needs a field of about *B*=7.2 T at 4.2 K to completely ferromagnetically align all the magnetic moments in EuTe. The situation is different when the magnetic field is applied perpendicular to the easy axis of a domain. In this case the magnetization component aligned along the applied field is zero, until a critical field, the spin-flop field is applied [28]. The spin-flop field in EuTe is small: 80mT [29]. Before the spin-flop, the sub-lattices are antiferromagnetically ordered. After the spin-flop, the angle between the sub-lattice magnetization and the applied magnetic field is the same for both sub-lattices. The magnetization saturates at *B*=7.2T [30].

7.1.8 The transport properties of EuTe

The conductivity of EuTe is much less studied than the transport properties of EuO. However, magnetic field dependent conductivity data is available in the literature for Eu-rich EuTe samples [31]. For T>40K (B=0 Tesla), the slope of the conductivity is negative ($\partial\sigma/\partial T < 0$), which is indicative for band like metallic conduction where the scattering of electrons with photons increases with increasing temperature. It also shows that the studied samples were most likely Eu-rich EuTe samples (n-doped) since for semiconducting stoichiometric samples, an activated behavior was expected. For T<40K (B=0 Tesla) the situation is different and one finds $\partial\sigma/\partial T > 0$. The change in the slope was interpreted in terms of a change in the exchange interaction between the conduction electrons and the localized moments upon antiferromagnetic ordering. At T_N there is a small kink in the $\sigma(T)$ graph, which is another indication that the conductivity is sensitive to the magnetic order.

Like EuO, also Eu-rich EuTe exhibits the colossal magneto-resistance phenomenon [31]. The magneto-resistance at 4.2 K can be divided in three field ranges: 1) 0-80mT: the resistivity drops rapidly by about 90% (compared to B=0mT) when a

magnetic field is applied. For the sample described in [] the magnetization is also increasing rapidly in this range. 2) 80mT-7.2 T: the resistivity drops to a value of about -99.8% (compared to B=0mT). 3) >7.2T: the resistivity changes saturate. Simultaneously, also the magnetization saturates.
For B=8.4T, $\partial\sigma/\partial T < 0$ in the hole temperature range, indicating that the ferromagnetic alignment strongly affects the conduction . Hall measurements revealed that the room temperature mobility is about 50 $cm^2/V\,s$ and that the low-temperature magneto-resistance is almost entirely due to an increase of the mobility, and not due to an increase in the carrier concentration. This strongly suggests that double-exchange like mechanisms are also active in EuTe.

7.1.9 $\Delta L(t)$ *dynamics in EuTe: time-resolved resonant X-ray magnetic scattering experiments*

In this section we will describe the time-resolved resonant X-ray magnetic scattering experiments on EuTe which has been published in literature by [[32--34]]. We will do this in quite some detail since it can help us in the interpretation of both the EuO and EuTe magnetization dynamics data. First we discuss what is exactly measured by resonant X-ray magnetic scattering (RXMS) measurements, in which the laser-induced transient changes (4f to 5d excitation) of the antiferromagnetic order parameter are probed. In X-ray diffraction experiments, we have to consider the atomic form factor *f*. The elements of the atomic scattering tensor can be written as [35]

(7.29) $f_{ij} = \delta_{ij} f^0 + f'_{ij} + i f''_{ij},$

in which f^0 is the electron term (which is the Fourier transform of the charge density ρ), *f'* is the dispersion correction, and *f''* related to the absorption. The last two terms are important when one is resonant to an optically allowed transition. The atomic scattering tensor *f*, considering only linear magneto-optical effects, can be written as :

(7.30) $$f = \begin{pmatrix} f^0 + F^{(0)} & iF^{(1)}m_k & -iF^{(1)}m_j \\ -iF^{(1)}m_k & f^0 + F^{(0)} & iF^{(1)}m_i \\ iF^{(1)}m_j & -iF^{(1)}m_i & f^0 + F^{(0)} \end{pmatrix},$$

in which $F^{(0)}$ and $F^{(1)}$are the non-magnetic and magnetic dispersion corrections respectively. *f* is very similar to the magneto-optical susceptibility tensor, and they are related by [35]:

(7.31) $\chi_{ij}(\omega) = \frac{-4r_0\pi\rho}{k^2} f_{ij}(\omega)$,

in which r_0 is the Thompson scattering length, and *k* is the wavevector. The presence of the $F^{(1)}$ terms in 7.30 lead to a (resonant) enhancement of the x-ray scattering from atoms possessing magnetic-circular dichroism or magnetic-circular birefringence, *i.e.* lead to a sensitivity of X-ray diffraction to magnetic order. The scattering amplitude can be calculated as [35]:

(7.32) $f_{ampl} = \hat{e}'^{*} \cdot (f\hat{e})$,

in which $\hat{e}$ and $\hat{e}'^{*}$ are the unit polarization vectors of the incoming and out coming light respectively. Below we will omit the ^ and the * signs. Now we can write for the magnetic (M) and non-magnetic (NM) amplitudes [35]:

(7.33) $f_{ampl}^{NM} = (f^0 + F^{(0)})(e_i'e_i + e_j'e_j + e_k'e_k)$,

(7.34) $f_{ampl}^{M} = F^{(1)}\left[m_i\left(e_j'e_k - e_k'e_j\right) + m_j(e_k'e_i - e_i'e_k) + m_k\left(e_i'e_j - e_j'e_i\right)\right]$.

From this we can see the NM amplitude is only non-zero when the in and out coming photons have equal polarizations, while the M amplitude is only non-zero when the in and out coming photons have different polarizations. In the EuTe experiment, the incoming light is *i*-polarized and is propagating in the *j*-direction. As we will see later, the resonantly scattered light is propagating in the *k*-direction (or very close to), and can therefore be either *i* or *j* polarized. In this case (7.34) an (7.35) reduces to:

(7.35) $f_{ampl}^{NM} = f_{non-resonant}^{NM} + f_{resonant}^{NM} = (f^0 + F^{(0)})(e_i'e_i)$,

(7.36) $f_{ampl}^{M} = F^{(1)}\left[m_k\left(e_j'e_i\right)\right]$

from which we can see there is a NM contribution proportional to $f^0 + F^{(0)}$, and a magnetic contribution proportional to $F^{(1)}m_k$. This means that in this configuration, one is only sensitive to the *k* component of the magnetization. The NM contributions is generally much larger than the M contribution.

Of course the question is how the light can anyway 'see' the magnetic unit cell. This question we actually already answered and is because of the magnetic dichroism or birefringence of the magnetic ions. Depending on the magnetization orientation, the absorption and/or refractive index can be higher or lower which means that the magnetic scattering of spin-up moments will be different than the magnetic

scattering from spin-down magnetic moments. In this way the scattering is spin orientation dependent, and the magnetic periodicity can be observed.

The scattering intensity can be enhanced by going to a resonance. The EuTe experiments have been performed with X-ray photons resonant to the Eu M_5 edge (3*d* to 4*f*, see also chapter 4). The resonant scattering process is depicted In Fig. 7.3 [35].

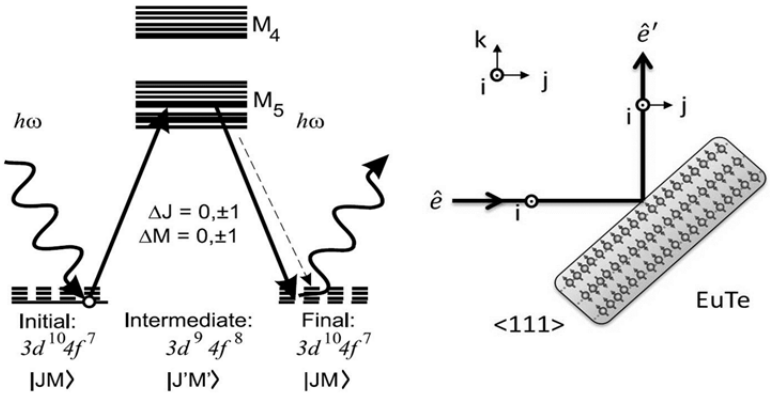

Fig. 7.3. | RXMS at the M_5 edge of Eu^{2+} in EuTe. Left side: The relevant transition for resonant magnetic diffraction is from the $3d^{10}4f^7$ initial state to a $3d^9 4f^8$ intermediate state, and back to the $3d^{10}4f^7$ final state (indicated by black straight arrows). See of more information also chapter 4, where the XMCD at the M_5 edge of Eu is discussed. (picture adapted from ref. [35]). Right side: the experimental configuration, and the definition of the i/j/k axis.

Let us now go back to EuTe. As discussed above, the magnetic ordering of EuTe is ferromagnetic in the <111> planes, and antiferromagnetic between these planes. This means that the periodicity, 2d, of the magnetic structure in the [111] direction is twice that of the crystallographic structure, *d*. From the Bragg condition we know that there is only a non-zero diffraction component when the scattering angle is [35]:

(7.37) Crystallographic (NM): $\sin(\theta) = \frac{m\,\lambda}{2d}$ => first order => $\sin(\theta) = \frac{\lambda}{2d}$

(7.38) Magnetic (M): $\sin(\theta) = \frac{m\,\lambda}{4d}$ => first order => $\sin(\theta) = \frac{\lambda}{4d}$

From this it is clear that means that at the angle for first order magnetic diffraction, there is no crystallographic diffraction and that the magnetic scattering might be visible. RXMS experiment on EuTe have been performed by xxx *et al.* []. It is not clear from that paper whether a single domain sample was probed, but by choosing

θ, only one out of the four possible magnetic T-domains will be observed. This means that in principle one is sensitive to 3x2=6 different domains (3 spin-domains, and two different sub-lattice magnetization directions) since in all these domains the sub-lattices have a non-zero component along the k-direction, see Eq. (7.33-7.36). In particular, one is sensitive to the *k*-component of the antiferromagnetic order parameter l_k: $\vec{l} = \vec{M}_1 - \vec{M}_2$, in which $\vec{M}_1$and $\vec{M}_2$ are the different sub-lattice magnetizations. The total magnetization *M* is: $\vec{M} = \vec{M}_1 + \vec{M}_2$.

In [17], the laser-induced transient changes of the antiferromagnetic-order parameter $|l_k+\Delta l_k|/|l_k|$ have been probed at different time scales. The long time-scale dynamics was probed with 50 ps pulses, like we did in chapter 4. The short timescale dynamics was probed using 100 fs pulses which were obtained using a slicing procedure. The photon energy of the probe was 1128 eV (bandwidth 0.3%) and the photon energy of the pump was 3.1 eV. The pump fluence was 3.7 mJ/cm^2, corresponding to excitation of about 6.7 % of the Eu atoms. The data of the different experiments are (glued and) plotted in Fig. 7.4. The data has been taken from [17]].

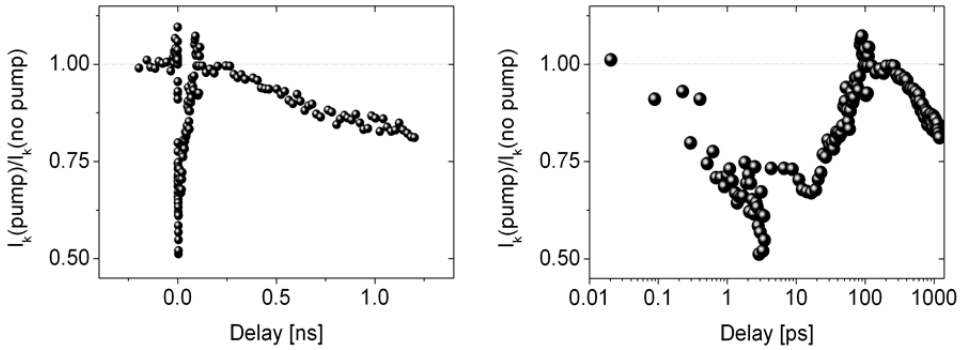

Fig. 7.4. | RXMS intensity versus pump probe delay for EuTe. Right) linear scale. Left) logarithmic scale. The data has been taken from [17].

From Fig. 7.4 one can see that there is a sub-ps decrease of l_k which is almost 50%. Then there is a recovery towards 0 with a ~50 ps timescale, followed by a slow, again decreasing, nanosecond component. l_k reaches a minimum after 75 ns. By a θ/2θ-scan it was verified that after +35 ps (temporal resolution 50ps), the peak and width position was not affected, indicating that the separation between the <111> planes and the AFM coherence were not affected. In a more recent paper, additional experiments in the very high fluence regime were done. At a fluence of

20 mJ/cm^2 (photon energy of 3 eV), about 36% of Eu atoms are excited. A double exponential decay was observed with time constants of about 700 fs and 5 ps. After 10 ps, $|I_k+\Delta I_k|/|I_k|$ is about -60%.
Apart from this also experiments were described in which EuTe was sandwiched in between PbTe layers; see [34]. PbTe is a narrow bandgap material (E_g=0.32 ev) and the absorption coefficient at the pump photon energies (1.5 eV) is large: 5 x10^7 m^{-1}. At 1.5 eV EuTe is not absorbing, which means that the pump photon energy is absorbed in PbTe after which there is thermal diffusion and energy transport to the EuTe layer. High fluence data (15 mJ/cm^2) on these samples reveal an intensity and position change as well as a broadening of the (1/2,1/2,1/2) reflection. There is a broadening by about 40% and a drop in intensity by about 50% in the first 10 ps, after which the intensity and width remain fairly constant up to at least a nanosecond. The peak position, changes less than 5%. More data and information is required, but it is clear that the magnetic correlation length (inversely proportional to the width) decreases at the ps timescales. However it is unclear why in this experiment not the decrease (700 fs)/complete recovery (50 ps)/ decrease (75 ns) behavior of I_k can be observed which has been seen in other experiments (see Fig.7.4). For this one needs to study the energy transfer between the PbTe and EuTe layers in detail.
Because of the difficulties in the interpretation of the PbTe-EuTe experiments, we focus on the data which is presented in the first paper we discussed in this section [17]. Before doing this we discuss the phenomenological so-called four temperature model (4TM).

7.1.10 Four temperature model and three temperature model in simple antiferromagnets

In literature many experiments has been performed on multi-sublattice ferri- or antiferromagnetic materials. In metallic systems, the laser-induced magnetization dynamics was sometimes described in terms of a four temperature model (4TM) in which there are four subsystems with each their own temperature: the electrons, the lattice and two magnetic subsystems [36,37]. A schematic of the 4TM is shown in Fig 7.4.

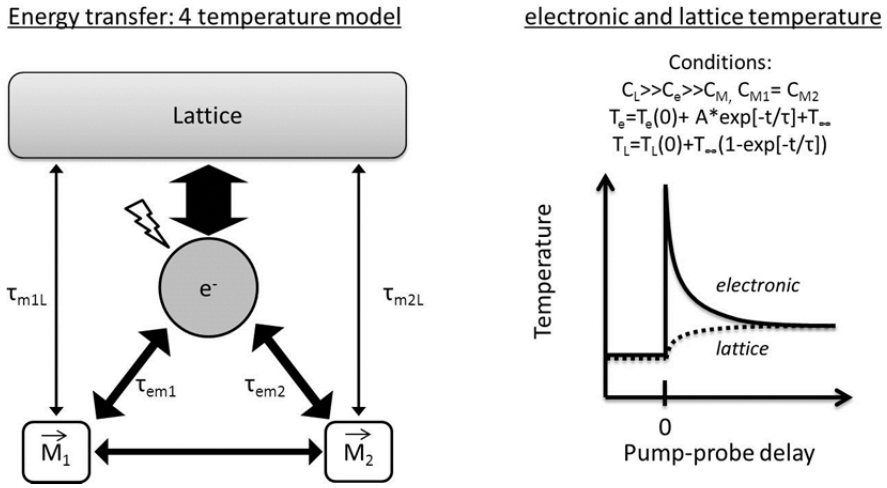

Fig. 7.4. | 4TM model (left) and electronic and lattice temperatures (right),. For simplicity we assume that the heat capacities are not temperature dependent. *m* refers to a magnetic sublattice (magnetic subsystem) and *e* refers to the electronic subsystem. In antiferromagnets holds $\tau_{m1L}= \tau_{m2L}$, $\tau_{em1}= \tau_{em2}$.

Also a microscopic version of the four 4TM temperature model (M4TM) has been developed [36]. Like in the M3TM, one neglects the direct coupling between the magnetic moments and the lattice due to anisotropic crystal field fluctuations (AFCF) and one only considers phonon-mediated Elliot-Yafet spin-flip scattering. In addition to the M3TM, in the M4TM there is exchange scattering between the two different sub-lattices (see introduction and appendix), which leads to angular momentum transfer between the two magnetics sub-systems.

From an energy transfer point of view, it is interesting to note that usually one is in the regime that $C_l>>C_e>>C_{M1,2}$. In simple AFM's, $C_{M1}=C_{M2}$. Both sublattices in a simple antiferromaget have the same dynamics (same equilibration times, see Fig 7.4), at least when *B*=0T. This means that energy transfer in a simple two-sublattice antiferromaget, effectively, can be modeled by the three temperature model (when the behavior is thermal, and when we neglect the effects of holes and the formation of composite particles like polarons or excitons). This has important consequences for the interpretation of the EuTe data, as we will see later, since the dynamics in the 3TM is less rich than the dynamics in the 4TM. In the next section we discuss the carrier dynamics in EuTe.

7.1.11 Carrier dynamics in EuTe: time-resolved photo-luminescence experiments

The time-resolved photoluminescence experiments on EuTe which has been reported in the literature are summarized in Table 7.4. The near-band-gap luminescence has been measured and different peaks were observed which were named: MX_1, MX_2 and HE [30,38]. The narrow MX_1 peak (1.91 eV) was attributed to the magnetic-polaron induced luminescence and the MX_2 peak (1.87 eV) to its magnon replica . In the description in [39], the conduction electron in the magnetic polaron is not bound to the 4*f* hole; there is no magnetic exciton. The optical bandgap of EuTe is 2.27 eV. The Stokes shift, of the MX_1 peak is large relative to the magnetic field dependent optical absorption edge shift (see chapter 2) and shows a strong magnetic field dependence: 350 meV (B=0T,1.7K), 500 meV (6.2T,1.7K) [39]. The large Stokes shift was explained in terms of electron energy relaxation within the 5d/6s conduction band, while the large magnetic field dependence originates from the magnetic field dependent changes in the band structure of EuTe. The high energy peak (HE) only appears at higher fluences (>2kW/cm^2 at 488 nm), and the origin is unknown, although it was suggested that it is also magnetic-polaron related [38]. The rise and decay times of the different peaks are summarized in Table 2 (based on [38,39]).

Table 7.4 | Time-resolved photoluminescence on EuTe. MX_1 is a peak which was attributed to the magnetic-polaron induced luminescence (with MX_2 its magnon replica) The high energy peak (HE) only appears at higher fluences (>2kW/cm^2 at 488 nm). Data taken from [39] and [38].

Excitation	B [mT]	T[K]	Luminesce	Rise time	τ_1 [ps]	τ_2 [ps]
λ=410 nm	0	7	1.89-1.94 eV, MX_1	150 ps	1500	-
λ=410 nm	0	7	1.96-1.98 eV, HE	60 ps	90	-
λ=390nm	0	4.2	1.77-2.07 eV, MX_1 + MX_2	150 ps	650	2 ns
λ=390nm	300	4.2	1.77-2.07 eV, MX_1 + MX_2	150 ps	500	6.5 ns
λ=390nm	500	4.2	1.77-2.07 eV, MX_1 + MX_2	150 ps	1000	17 ns

The rise time of the MX peaks is 150 ps and is related to the magnetic polaron formation time [39]. The rise-time of the HE peaks is shorter, about 60 ps [38]. The decay of the HE peak is fast, 90 ps whereas the decay of the MX peaks is much slower (500 ps-17 ns) and applied magnetic field dependent. Especially the longer time scale component (τ_2) in the double exponential decay increases from 2 ns at B=0 mT towards 17 ns at 500 mT. This change was interpreted in terms of changes in the magnetic polaron binding energy, which is decreasing with increasing applied

magnetic field. Since the luminescence is magnetic polaron induced, this can lead to changes in the dynamics [40].

One thing we have to mention is that there is another more intense luminescence peak at lower energy (1.43 eV at B=0 mT, [41]) from which the dynamics has not been measured yet. The Stokes shift for this peak (relative to the optical bandgap) is about 800 meV at B=0 mT [41]. The energy difference between this peak and the MX_1 peak is about 400 meV and does not show a strong magnetization dependence for B<6T. In [41], the large Stokes shift for this peak was used as evidence for strong electron-phonon coupling (within the Franck-Condon framework). In this picture the conduction electron is localized around the 4f hole and there is a large lattice deformation. This fits well to the magnetic-exciton model for the optical absorption of EuTe in the visible (VIS) range.

Let us now compare this with what we know from EuO. In the previous chapter we showed that after a few picoseconds there are free carriers which live quite long (nanoseconds) at low excitation fluences. This means that there is a conduction band and there are conduction electrons. This is in contrast with the magnetic-exciton model for (both the absorption and) the luminescence, where the conduction electron is *always* bound to the hole and in which there is a large lattice deformation. Also based on the band structure calculations of EuO, it seems reasonable that free carriers relax to the conduction band which is about 350 meV below the optical absorption edge at 2.27 eV. Only when the carriers are cold (at the bottom of the conduction band), *free* magnetic polarons (MP) can be formed. The MP formation time in EuO is about 20 ps (chapter 6) while in EuTe it is about 150 ps [30].

We mentioned that there is no information about the dynamics of the more intense 1.43 eV luminescence peak. But it is possible that on longer timescales the conduction electrons (at the bottom of the band or in magnetic polarons) end up in magnetic excitons, where the electrons are bound by the 4f hole and where there is a large lattice distortion. Since in this case the conduction electron wavefunction is localized, and the center is in the vicinity of the hole, this can explain the larger intensity of the 1.43 eV peak. The large lattice distortion can then explain the additional Stokes shift of about 400 meV compared to the Stokes shift of MX_1.

From this section we learned that the bottom of the conduction band at the X-point is about 350-500 meV below the optical bandgap of 2.27 eV, depending on the magnetic field. This means that of every absorbed 3.1 eV photon, at least 1.2

eV is transferred to the lattice because of optical phonon emission of hot conduction electrons. The magnetic polaron formation time in EuTe is 150 ps.

7.2 Magneto-optical experiments

In this section we describe two sets of data obtained in the present work:

- Temperature and magnetic field dependent optical transmission spectra in the NIR/VIS/UV range using un-polarized light. These experiments where both used to characterize the sample, as well as to obtain information on localized moment/conduction electron interaction based on the red shift of the absorption edge when a magnetic is applied.
- Time-resolved Faraday rotation and ellipticity measurements on EuTe. The sample was excited using a short, 100 fs pump pulse with a photon energy of 3.1 eV (4f to 5d transition). The magnetization dynamics was probed with a short, 100fs, probe pulse with a photon energy of 3.1 eV as well.

7.2.1 Characterization 1 Optical transmission in the NIR/VIS/UV range

In order to characterize the sample, we measured the temperature and magnetic field dependence of the optical transmission spectra of EuTe films. The angle of incidence is 0 degrees and the applied magnetic field is parallel to the wavevector of the incoming light beam. The magnetic field was in the 0-7 T range, and we varied the temperature from 4.2 K to 40 K. We first focus on the magnetic field dependence of the absorption coefficient at 4.5 K, see Fig. 7.5.

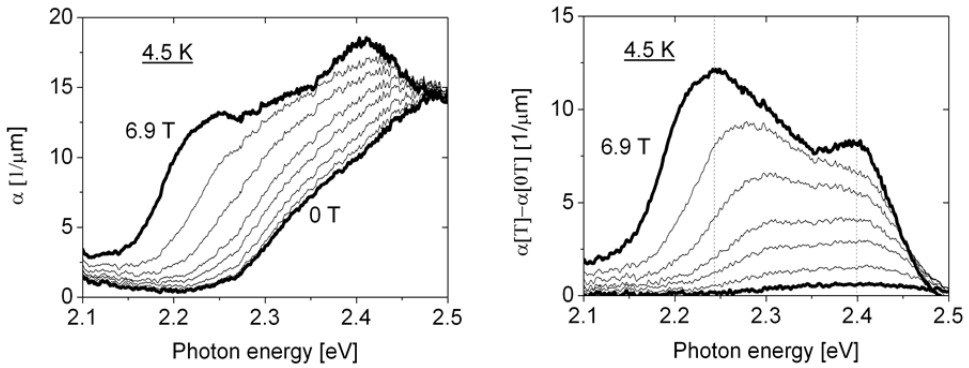

Fig. 7.5. | Absorption spectra in the Faraday configuration at 4.5K for different magnetic fields. The absolute spectra are shown in the left graph whereas the difference spectra (difference with the spectrum at B = 0T) are shown in the right graph. The different lines correspond to: Left) B = 0, 1, 2, 2.8, 3.5, 4.5, 5.5 and 6.9T. Right) B = 1, 2, 2.8, 3.5, 4.5, 5.5 and 6.9 T.

The absorption coefficient was determined from transmission measurements of a 100 nm thick (*d*=100 nm) EuTe film on a BaF_2 substrate. The BaF_2 substrate is not absorbing in the energy range we are interested in (2.1-2.5 eV). The EuTe film was protected from oxidation using a BaF_2 capping layer. The absorption was calculated using

$$\alpha(\omega) = -\ln\left(\frac{I_{EuTe\ sample}(\omega)}{I_{lamp}(\omega)T_{V-B}^2(\omega)T_{B-E}^2(\omega)}\right)/d, \quad (7.39)$$

in which $I_{EuTe\ sample}$ and $I_{lamp}(\omega)$ is the transmitted intensity of the sample and the lamp intensity respectively. T_{V-B} and T_{B-F} are the Fresnel transmittance coefficients for the vacuum(V)/BaF_2(B) interface and the B/EuTe(E) interface, respectively. The frequency dependence of T_{V-B} was modeled by using Sellmeier coefficients, taken from [42] (300 K, B=0T) for the refractive index. We assumed that the refractive index of BaF_2 is not temperature, nor magnetic field dependent. For T_{B-E} we used the refractive index and extinction coefficient of EuTe at room temperature and *B* = 0T. Since $T_{V-B}^2(\omega)T_{B-E}^2(\omega)$ is not too much frequency dependent in the 2.1-2.5 eV range (6% change), we took $T_{V-B}^2(\omega)T_{B-E}^2(\omega)$ as temperature and magnetic field independent. The absolute (left) and relative (right) magnetic field dependence of the absorption coefficient at 4.5 K is shown in Fig. 7.5. We observed a shift in the absorption edge and also the appearance of two absorption peaks at high magnetic fields; one at 2.2 eV and one at 2.4 eV. The absorption edge was defined as follows: From the absorption spectrum we subtracted the average value of α in between 2.12 and 2.14 eV. In between 2.12 and 2.14 eV, one is below the absorption edge at all the magnetic field and temperatures. After that we scaled the graphs to the maximum in the 2.1-2.5 eV range. Now the absorption edge is defined as the energy at half the maximum. The relative absorption edge at different temperatures and applied magnetic fields is shown in Fig. 7.6.

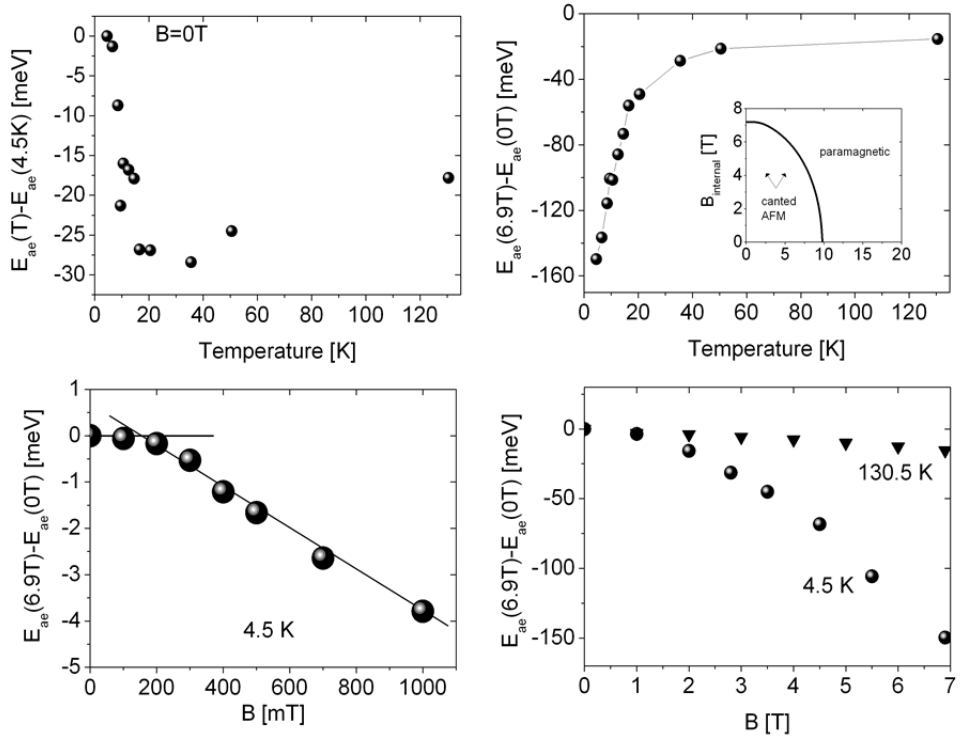

Fig. 7.6. | Absorption edge shift versus temperature (upper graphs) or applied magnetic field (lower graphs). In the upper left graph the (B=0T) absorption edge at a certain temperature is compared with the (B=0T) absorption edge at 4.5 K. In the upper right graph the absorption edge at a certain temperature and B=6.9T is compared to B=0T absorption edge at the same temperature. In the lower graph we show the magnetic field-induced red shift versus applied magnetic field.

In the upper graphs the temperature dependence is shown. From Fig 7.6 (upper, left) we can see that there is a blue shift of about 25 meV in the antiferromagnetic phase in zero applied magnetic field. We can also observe a red shift of about 150 meV when the spins are (partially) ferromagnetically aligned at 4.5 K and B=6.9T. The magnetic field-induced red shift (E_{ae}[B=6.9T]- E_{ae}[B=0T]) is decreasing with increasing temperature. In the lower graph the magnetic field dependence of the absorption edge is shown at 4.5 K (left, low fields), and at 4.5 K and 130 K (high fields). At low fields (4.5K) there is a threshold at about 150 mT. At high field (4.5 K) the behavior is more or less quadratic in the applied magnetic field.

7.2.2 Absorption edge shift: discussion

The magnetization induced red-shift of the optical absorption edge in the paramagnetic phase, has the same origin as described in Chapter 2 for EuO: the strong d-f interaction can affect the conduction band energy and the shift is proportional to the nearest neighbor spin-correlation function. The blue shift in the antiferromagnetic phase, is more difficult to explain. In [43] one tries to explain this. To do this they consider the d-f exchange interaction between the conduction electrons and localized spins in a rigid spin model ($S=S_z$, $S_y=S_x=0$). The energy shift due to the d-f exchange interaction was calculated for different types of magnetic order, using the parameters of EuO (structure, lattice constant/d-f exchange constant, Tc), see Table 7.5.

Table 7.5 | Calculated conduction band shift at k=0 for different types of magnetic ordering; data obtained from [43].

Magnetic order in FCC magnet with EuO parameters (lattice constant/d-f exchange constant etc.)	Numerical estimate of the energy shift of conduction electron at k=0 in rigid spin model ($S=S_z$, $S_y=S_x=0$)
Ferromagnet phase	E_{fm} =330 meV (E_{fm}-E_{pm}= 245 meV)
Type II antiferromagnetic phase	E_{afm} =24 meV (E_{afm}-E_{pm}= -61 meV)
Paramagnetic (pm) phase	E_{pm}=85 meV

The energy shift in the fully ferromagnetically ordered phase is 330 meV, while the red-shift in the paramagnetic phase is much smaller: 85 meV [43]. From this we can see that one (indeed) expects a red shift when the materials order ferromagnetically at low temperatures. The energy shift is the smallest in the type II antiferromagnetic phase: 24 meV [43]. The fact that there is an energy shift in the AFM case (of 24 meV) is surprising. Probably this can be explained by the fact that there is ferromagnetic order within the [111] planes, which means that the nearest in-plane neighbor spin-correlation function is non-zero.

7.2.3 Absorption edge shift: conclusions

One of the reasons for measuring the optical absorption spectra was the characterization of the samples. Based on a comparison with literature spectra [19,30,44--46], we can conclude that we have normal behaving EuTe; the film is of good quality. Another reason was to see whether it is possible to do pump-probe measurements in which the laser-induced changes in the short range magnetic

order can be probed using a white light continuum probe. The theory for doing this was developed in chapter 2. For observing the temperature induced blue shift at 4.5 K and *B*=0 T, one needs a resolution much better than 25 meV. For observing the red shift in applied magnetic field of 6.9 T (4.5 K), one needs to have a resolution much better than 150 meV. In the next section we will characterize the sample further, by measuring the Faraday rotation versus applied magnetic field.

7.2.4 Characterization 2: Faraday rotation/ellipticity versus applied magnetic field

The upper left graph of Fig. 7.7 shows the measured Faraday rotation versus applied magnetic field for two different temperatures. In our experiments, the angle of incidence of the probe beam is about 45 degrees and the applied magnetic field is perpendicular to the wavevector of the incoming light which (the applied magnetic field makes an angle of 45 degrees with the surface normal of the film). The probe pulse is linearly polarized with a polarization close to *p*-polarization.
The sample consist of a 100 nm thick EuTe film, grown on an [111] BaF_2 substrate. The sample is protected against oxidation with a BaF_2 capping layer. Because of the large optical density of the EuTe film at 400 nm, we expect to be mainly sensitive to propagation effects (Faraday effect) while we do not have to consider the Fresnel coefficients (magneto-optical Kerr effect). In that case, in linear magneto-optics, we are sensitive to the magnetization component (anti)parallel to the wavevector of the probe inside the EuTe: $\sim\vec{k}\cdot\vec{M}$. Although the wavevector of the incoming light is perpendicular to the applied magnetic field, due to refraction, the wavevector of the probe inside the EuTe has a component along the applied magnetic field. This means that we are apart from the weak quadratic magneto-optical effects, also sensitive to the stronger linear magneto-optical effects.
From Fig. 7.7 (upper left), we can see that the behavior is linear, and that the slope is steeper in the AFM ordered phase. This indicates that the magnetic susceptibility at 5 K is higher than in the paramagnetic phase at 28 K, as expected. The magnetic phase transition can be more effectively probed by looking to the pump induced Faraday rotation versus applied magnetic field for very long delays (+1 ms), see the next section.

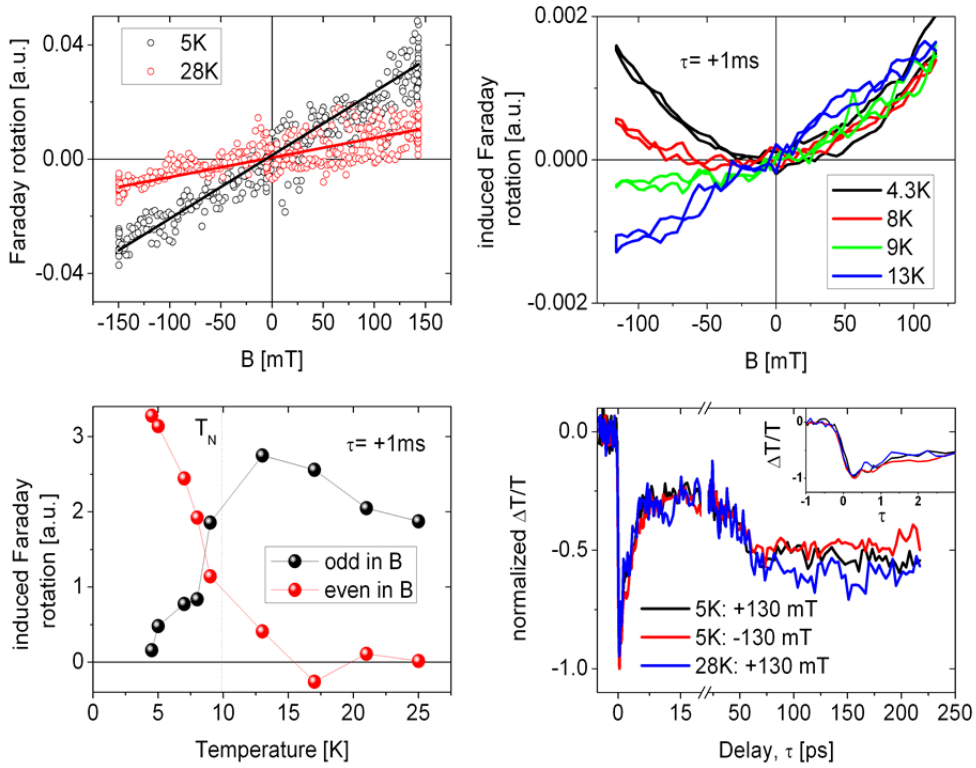

Fig. 7.7. | Sample characterization. Upper left) faraday hysteresis loops. Upper right) pump-induced faraday hysteresis loops. Lower left) pump-induced odd en even components in the faraday rotation at 125 mT. Lower right) pump-induced changes in the transmittance. For details, see text.

7.2.5 Characterization 3: pump-induced Faraday rotation/ellipticity versus applied magnetic field at negative delays.

The pump induced Faraday rotation versus applied magnetic field for different temperatures is shown in the upper right graph of Fig 7.7. The pump fluence is high, about 30 mJ/cm^2. The pump probe delay is about -10 ps, which means that the previous pump pulse is about 1 ms away (the experiments are done in a stroboscopic way at 1 kHz). These measurements provides us with important information about the sample temperature, just before the pump pulse arrives. This is crucial since the average heating due to the strong pump pulse train, can be large, especially at helium temperatures where the heat capacities are low.

Therefore we want to be sure that we are below the Neel temperature, in the AFM phase.

The pump wavelength is the same as the probe wavelength, 400 nm. In order to reduce the pump light in the photo-detectors the pump and probe pulse are approximately orthogonally polarized., *i.e.* the pump polarization s-polarized. We can see that below the magnetic ordering temperature there mainly is a component which is even in the applied field, whereas at in the paramagnetic phase, there mainly is a component which is odd in the applied field. The odd and even component we define as:

(7.40) $\Delta\theta_{odd}(|\vec{B}|) = [\Delta\theta(+\vec{B}) - \Delta\theta(-\vec{B})]/2$

(7.41) $\Delta\theta_{even}(|\vec{B}|) = [\Delta\theta(+\vec{B}) + \Delta\theta(-\vec{B}) - 2\Delta\theta(0)]/2$

The temperature dependence of the odd and even components at 125 mT are shown in Fig. 7.7, lower left graph. From this graph one can see that the even component is sensitive to the AFM order parameter; it is large at low temperature in the AFM phase, and it is small in the paramagnetic phase. The opposite holds for the odd component: it is small at low temperature in the AFM phase, and large in the paramagnetic phase. The even effect, coming from the quadratic magneto-optical tensor, seems to be a good probe for the actual temperature of the sample at negative delays (just before the next pump pulse). The peculiar applied magnetic field dependence hints to an interpretation in terms of a long-lived electronic effect rather than a thermal effect. We conclude this based on the fact the static Faraday rotation does not show a quadratic effect, and that long term heating effects are not expected to be large at kHz repetition rates in a cryostat where the sample (film + substrate) is directly cooled with cold He-gas. The fact that there are long term electronic effects is not surprising; EuO shows a long lived (up to seconds) photocurrent after pulsed illumination has been removed. In the next section we discuss the laser-induced carrier dynamics after valence to conduction band excitation.

7.2.6 Characterization 4: time-resolved Transmittance changes after a valence to conduction band excitation

Time-resolved transmittance changes for different temperatures and magnetic fields (directions) are shown in the lower right graph of Fig. 7.7. The pump fluence is 30 mJ/cm^2. We observed no large temperature or magnetic field (direction)

dependencies. As we will see later, the rise time of the (negative) signal is temporal resolution limited. The signal can be mathematically described by:

(7.42) $\Delta T = G(\sigma, t_0) * \left[H(t_0) \cdot \left(A + Be^{-(t-t_0)/\tau_B} + C\left\{1 - e^{-(t-t_0)/\tau_C}\right\}\right)\right]$

In which G and H represents a Gaussian and a Heaviside step function, respectively. The obtained fit parameters are: $\sigma = 145\ fs, A = -0.13, B = -0.86, \tau_B = 3.3\ ps$, $C = -0.42, \tau_C = 43\ ps$. The fact that the signal is instantaneous and negative, tells us that most likely, the signal is due to free carrier generation, like in EuO. The 3.3 ps decay component can be due to different carrier relaxation processes like trapping. Recombination or magnetic exciton/polaron formation is expected to be much slower, based on luminescence experiments and results presented in Chapter 6.

7.2.7 Results: pump-induced Faraday rotation/ellipticity versus pump-probe delay during the first ns

The laser-induced changes in the rotation of polarization at positive and negative applied magnetic fields are shown in the right graph of Fig. 7.8. The pump fluence is 30 mJ/cm^2 and the temperature is 4.2 K. Also the difference between the two curves is shown (blue). The odd (difference, black) and even (sum, red) components are compared with each other and with the transient transmittance (blue) in the left graph of Fig. 7.8.

As in EuO, the ultrafast component of the even component at pump-probe overlap, is most likely due to the electro-optical Kerr effect and represents the cross-correlation between the pump and probe pulses. The negative peak in the even components a measure of the pulse duration and can be fitted with a Gaussian (*G*). This the even component. After pump-probe overlap, the even component is small and fairly constant in the 1-250 ps range.

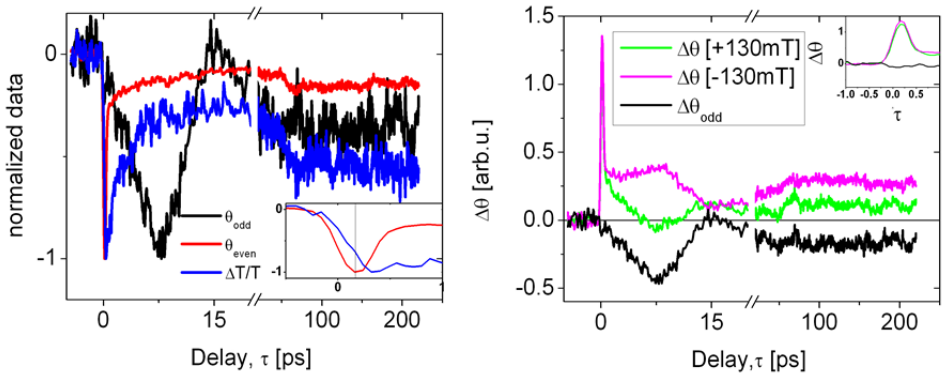

Fig. 7.8. | Right) even (red) and odd (black) components in the laser-induced change in the rotation of polarization. For comparison, the data are normalized, and compared to the transient transmittance. Left) the laser-induced change in the rotation of polarization at positive and negative applied magnetic field. Also the difference is shown. In the inset the same data is shown, but than in between -1 and +1 ps.

The odd component, which is proportional to the magnetization, behaves completely different from the even component or than the transient transmittance. The maximum relative amplitude of the signal (after 7.5 ps) is -5%. It reaches a minimum after about 7.5 ps, and then relaxes back and reaches zero at about 15 ps. After 15 ps, the absolute value of the signal grows again at a timescale of tens of picoseconds, after which it stays more or less constant after 150 ps. In the next section we discuss this result and we will compare the magnetization dynamics (*M*) with the dynamics of the AFM order parameter (*L*).

7.3 Discussion and conclusions: antiferromagnetic (EuTe) and ferromagnetic (EuO) semiconductors

In Fig. 7.9 (upper graphs) we compare the dynamics of the AFM order parameter *L* (from literature [33]) with the magnetization dynamics (*M*) that we measured using the Faraday effect in EuTe. The *L* dynamics experiments were done in zero field, whereas we applied a field of 130 mT in the *M* dynamics experiments. The *L* and *M* dynamics behave differently. Whereas in the *L*-dynamics there is a 700 fs rise time and a 47 ps recovery time, in the *M*-dynamics there is a rise time of a few picosecond and a recovery time of a few picoseconds as well. Also the amplitudes are different. Whereas for a fluence of 30 mJ/cm^2 the *M*-amplitude is $\Delta\theta/\theta$=-0.05, the *L*-amplitude is much larger $\Delta I_{RXMS}/I_{RXMS}$=-0.40.

The fact that the *L* and *M* dynamics are quite different is interesting. As stated in the introduction this can happen because *L* is affected by both spin-lattice and cross relaxation while *M* is only affected by spin-lattice relaxation. The fact that *L* en *M* are different, is thus an indication that cross relaxation (angular momentum transfer between the two sublattices) is important in EuTe. Cross relaxation timescales can be faster than spin-lattice relaxation timescales in doped-semiconductors with strong electron-magnon coupling since it is sensitive to the electronic temperatures instead of the lattice temperature (spin-lattice relaxation). Within our assumptions, therefor electron-magnon coupling plays an important role in the magnetization dynamics in EuTe.

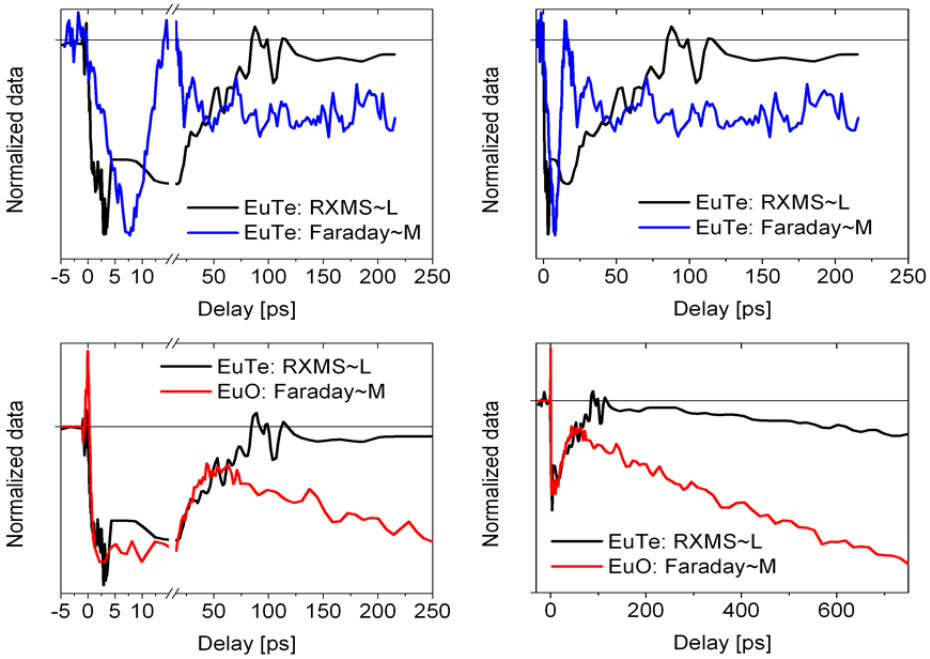

Fig. 7.9. | Comparison between *L*-dynamics and M-dynamics in EuTe (upper graphs), and between the *L*-dynamics in EuTe and the *M*-dynamics in EuO (lower graphs). The EuO measurements has been presented before in Chapter 4 and 5. The L-dynamics of EuTe has been taken from [33].

Now we will continue with the comparison of the more well-studied *L*-dynamics in EuTe and the *M*-dynamics in EuO. This comparison can be really insightful because of the fact that both compounds (EuO and EuTe) are very similar in structure and type of magnetic interactions. In this way we can bypass the problem of not having

a lot of data on the *M*-dynamics in EuTe, and in this way we can still make a fair compassion between the *L* and *M* dynamics in the europium chalcogenides.

In the lower graphs in Fig. 7.9, we compare the dynamics of the AFM order parameter *L* in EuTe with dynamics of the ferromagnetic order parameter *M* in EuO. Again, the *L* dynamics experiments on EuTe were done in zero field, whereas we applied a field of 10 mT in the *M* dynamics experiments on EuO. Remarkably, the rise time (about 700 fs) and (partial) recovery time (tens of ps) of the *L*-dynamics in EuTe and the M-dynamics in EuO are very similar. This similarity, together with the similarity between the materials suggests that the underlying mechanisms might be similar in nature. From Table 7.3 in the introduction section, we can see that we expect similar timescales in AFM's and FM's when 1) the conduction electron-magnon interaction is weak and the demagnetization is due to AFCF spin-lattice relaxation, or 2) there is both a strong conduction electron-magnon coupling and a strong conduction electron spin-phonon coupling. In the first case there is energy transfer from the lattice to the spin system, while in the second case there is energy transfer from the hot electronic system (and the lattice) to the spin system. If mechanism 1) would be dominant, we would have expected a slower demagnetization time. Not in the sub-picosecond regime like we observed, but in the 8-2000 ps range typically. Therefore it looks like we are in the regime where there is both a strong conduction electron-magnon coupling and a strong conduction electron spin-phonon coupling, at least for *hot* conduction electrons on sub-picosecond timescales.

After a few picoseconds, we expect the electrons and phonons to be equilibrated and that the angular momentum transfer between (cold) conduction electrons and the lattice becomes be less efficient. Now we enter into a regime where the magnetization dynamics (recovery) is determined by the AFCF mechanism with a direct angular momentum transfer between the lattice and the localized moments. The fact that the *L* and *M*-dynamics are comparable suggests that the electron-magnon interaction is weak for cold electrons (after electron-phonon equilibration).

Similarly to EuO (see chapter 4 and 5) the recovery observed in EuTe can be understood in terms of magnetic exciton formation, which restores the ferromagnetic order around the 4*f*-hole within the [111] planes of EuTe. This order was partially destroyed on the sub-picosecond timescale by mechanism 2), as we discussed. The magnetic exciton formation time of about 50 ps, is smaller than the free magnetic polaron formation time of about 150 ps. This interpretation could be

verified by doing time-resolved photoluminescence experiments on magnetic exciton peak around 1.43 eV which is attributed to magnetic excitons. After magnetic exciton formation, there are two 4*f* environments in the sample: A) the 4f moments within the magnetic exciton, and B) the 4*f* moments outside the magnetic exciton. At sub-nanosecond or nanosecond timescales, both regions A and B demagnetize because of the interaction with the hot lattice. For more details about this interpretation, see the end of chapter 5.

Appendix: Magnon scattering and $\overrightarrow{M}$ and $\vec{L}$ dynamics in AFM's

In this appendix we discuss magnon scattering processes in which a magnon scatters with:

- Other magnons.
- Phonons.
- Conduction electrons.

The appendix consist of five sections:

- Appendix A considers the magnon scattering in a ferromagnetic insulator or semiconductor.
- Appendix B considers the magnon scattering in an antiferromagnetic insulator or semiconductor.
- Appendix C considers the spin-flip scattering of conduction electrons in a metal or doped semiconductor.
- Appendix D: summary and discussion of Appendix A-C.
- Appendix E: comparing the dynamics of $\Delta L(t)$ and $\Delta M(t)$ in simple antiferromagnets from a phenomenological point of view.
- Appendix F: conclusions.
- Appendix G: different type of AFM ordering in a FCC lattice.

Below we will discuss different scattering terms in second quantization notation. The different operators are defined as followings. For simplicity, we will omit the momentum labels (*k* or *q*) on the operators. We define the following operators:

$c^{\dagger}{}_{\uparrow}/\ c_{\uparrow}$	Creation/annihilation of a conduction electron with spin-up (5*d*)
$a^{\dagger}/\ a$	Creation (ΔS=-1)/annihilation (ΔS=+1) of a ferromagnetic magnon (4*f*)
$b^{\dagger}/\ b$	Creation/annihilation of a phonon
$a1^{\dagger}\ /\ a1^{\dagger}$	Creation (ΔS=-1)/annihilation (ΔS=+1) of magnon in sublattice 1, $S_{z,1}$=+S (4*f*)
$a2^{\dagger}\ /\ a2^{\dagger}$	Creation (ΔS=+1)/annihilation (ΔS=-1) of magnon in sublattice 2, $S_{z,2}$=-S (4*f*)
$\alpha^{\dagger}/\ \alpha$	Creation(ΔS=-1)/annihilation (ΔS=+1) of an antiferromagnetic magnon (4*f*)
$\beta^{\dagger}/\ \beta$	Creation(ΔS=+1)/annihilation(ΔS=-1) of an antiferromagnetic magnon (4*f*)

Appendix A: angular momentum and energy transfer in ferromagnetic insulators or semiconductors

For the ferromagnetic case we define the following quantities:

- ΔS_c: changes in the z-component of the total spin angular momentum of the conduction electrons.
- ΔM: changes in the z-component of the total angular momentum of the localized moments.

- $\Delta M_T=\Delta M+\Delta S_c$: changes in the z-component of the total angular momentum of the electronic system.
- $\Delta J_T= \Delta M_T+\Delta J_{Latt}$; changes in the z-component of the total angular momentum of the electronic system + lattice. ΔJ_{Latt} is the angular momentum of the lattice.

For the ferromagnetic case we consider three different type of scattering processes:

- $\Delta M_T\neq 0$, $\Delta M\neq 0$: the total electronic angular momentum is not conserved. In this case electronic angular momentum (from localized moments) is transferred to the lattice (Table A1).
- $\Delta M_T=0$, $\Delta M\neq 0$: the total electronic angular momentum is conserved but ΔM is not. In this case angular momentum form the localized moments is transferred to the conduction electrons (Table A2).
- $\Delta M_T=0$, $\Delta M=0$: in this case there is no angular momentum transfer; there is only energy transfer (Table A3).

We will consider different scattering processes. In order to describe these processes, different interaction Hamiltonians needs to be considered: magnetic exchange H_{ex}, magnetic dipole H_{md}, magnon-phonon interaction H_{mp} and magnon-electron H_{me}. We should have in mind that the following commutation relations holds:

$[M_T\,, H_{ex}] = 0$	In a magnon-magnon exchange scattering processes, M_T is conserved.
$[M_T\,, H_{md}] \neq 0$	In a magnon-magnon magnetic dipolar scattering processes, M_T is not conserved => transfer to lattice (rotation) [1,3]
$[M_T\,, H_{me}] = 0$	In a magnon-electron scattering processes, M_T is conserved.
$\left[M_T\,, H_{mp}\right] \neq 0$	In a magnon-phonon scattering processes, M_T is not conserved => transfer to lattice
$[J_T\,, H_{total}] = 0$	J_T is always conserved in the scattering processes we discuss $(H_{ex}, H_{md}, H_{mp}, H_{me})$

Examples of phonon-magnon scattering terms for which holds $\Delta M_T\neq 0$, $\Delta M\neq 0$, are shown in Table A1 [5]. In all the cases we will discuss throughout this appendix holds: $\Delta J_T = 0$.

Table A1 | angular momentum transfer to lattice, M_T not conserved: $\Delta M_T=\Delta M+\Delta S_c\neq 0$, $\Delta M\neq 0$

Process	Example of scattering terms	Conditions and systems
phonon-magnon scattering (1-magnon)	$b^\dagger a$ (ΔM=+1) $a^\dagger b$ (ΔM=-1) $b^\dagger b\, a$ (ΔM=+1) $b^\dagger a^\dagger b$ (ΔM=-1)	- Localized magnetic moments + phonon - FM insulator
phonon-magnon scattering (2-magnon)	$b^\dagger a\, a$ (ΔM=+2) $a^\dagger a^\dagger b$ (ΔM=-2)	- Localized magnetic moments + phonon - FM insulator

These processes can be important when there is a hot lattice but a cold spin-system. Spin-lattice relaxation can bring the two systems (lattice and spins) in thermal equilibrium. For the first two scattering terms in Table A1 (direct process) in EuO, there can be only energy and momentum conservation when the k-vector is around k=0. For the third and fourth term (Raman process), all phonon everywhere in the Brillioun zone can participate. In two magnon processes, two magnons are created or annihilated on the same moment. 2-magnon processes are expected to be slow (>8 ps).

In this scheme we did not discuss the 3-magnon scattering processes since they are not important at the timescales we are interested in. In a 3-magnon processes, for instance, two magnons are annihilated and one magnon is created by the magnetic dipolar interactions, see also the first section of this chapter. Since ΔM=+1 in this case, angular is transferred to the lattice.

Since in all the described processes the total electronic angular momentum is not conserved, these processes are expected to be relatively slow (>10 ps). Two magnon processes are expected be only important at very long time scales (>> 1ns). Examples of magnon scattering terms (electron-magnon) for which holds $\Delta M_T=0$, $\Delta M\neq 0$, are shown in Table A2 [8].[6,7]

Table A2 | angular momentum transfer to conduction electrons, M_T conserved, M not conserved: $\Delta M_T=\Delta M+\Delta S_c=0$, $\Delta M\neq 0$

Process	Example of scattering terms	Conditions and systems
electron-magnon scattering (1-magnon)	$c^\dagger_\downarrow c_\uparrow a$ (ΔM=+1) $c^\dagger_\uparrow c_\downarrow a^\dagger$ (ΔM=-1)	- Localized magnetic moments + conduction electrons (*with spin-flip*) - FM semiconductors

The processes in Table A2 describe the case where a conduction electron spin-flip scatters with a magnon. Unlike in the Elliot-Yafet process where a conduction electron spin-flip scatters with a phonon, the total electronic angular momentum is

conserved. Therefore these processes can be ultrafast (<< 1ps). In EuO there is a spin-polarized conduction band. The gap between the majority and minority spins is large (0.6 eV at 10 K) and is much larger than magnon energies. Therefore adiabatic scattering of cold conduction electrons is not possible (like in half metallic systems). Examples of magnon scattering terms (magnon-magnon, magnon phonon, electron-magnon) for which holds $\Delta M_T=0$, $\Delta M=0$, are shown in Table A3 [5,6,8].

Table A3 | energy transfer, *M_T conserved, M conserved*: $\Delta M_T=\Delta M+\Delta S_c=0$, $\Delta M=0$

Process	***Example of scattering terms***	***Conditions and systems***
2-magnon scattering	$a^\dagger a$	- Localized magnetic moments - FM insulator with defects/impurities
4-magnon scattering	$a^\dagger\, a^\dagger a\, a$	- Localized magnetic moments - FM insulator
Electron-magnon scattering	$a^\dagger\, c^\dagger{}_\uparrow\, c_\uparrow\, a$	- Localized magnetic moments + conduction electrons (*without spin-flip*) - FM semiconductors
phonon-magnon scattering	$a^\dagger b a$	- Localized magnetic moments + phonon - FM insulator

The processes in Table A3 describe the case where there is only energy, but not angular momentum, transfer: $\Delta M_T=0$, $\Delta M=0$. 2-magnon scattering can only occur in a sample with defects or impurities (or in ultrathin samples), because otherwise there cannot be momentum conservation. Since we have good quality samples and we will ignore this process later on. 4-magnon scattering *is* possible in a perfect crystal; these scattering terms are present in the exchange Hamiltonian. 4-magnon scattering processes appear in the Heisenberg exchange Hamiltonian after a Holstein-Primakov transformation in which one goes from the spin operators (S_z, S^+, S^-) towards the magnon operators ($a^\dagger, a$). These 4 particle processes are expected to be only important at very long timescales (> 1 ns), and we will ignore them later on. Now we will consider the antiferromagnetic case.

Appendix B: angular momentum and energy transfer in an antiferromagnetic insulator or semiconductor

For the two-sublattice antiferromagnetic case we define the following quantities:

- ΔS_c: changes in the z-component of the total spin angular momentum of the conduction electrons.
- ΔM_1: changes in the z-component of the total angular momentum of the localized moments of sublattice 1.
- ΔM_2: changes in the z-component of the total angular momentum of the localized moments of sublattice 2.
- $\Delta M = \Delta M_1 + \Delta M_2$: changes in the z-component of the total angular momentum of the sum of the two sublattices.
- $\Delta M_T = \Delta M + \Delta S_c = \Delta M_1 + \Delta M_2 + \Delta S_c$: changes in the z-component of the total angular momentum of the electronic system.
- $\Delta L = \Delta M_1 - \Delta M_2$: changes in the z-component of the total angular momentum of the difference of the two sublattices.

Again, we define thee different cases:

- $\Delta M_T \neq 0$: the total electronic angular momentum is not conserved. In this case electronic angular momentum (from localized moments) is transferred to the lattice (Table B1).
- $\Delta M_T = 0$, $\Delta L \neq 0$: the total electronic angular momentum is conserved but ΔL is not. In this case angular momentum from the localized moments is transferred to the conduction electrons (Table B2) or angular momentum is transferred between different sub-lattices. The inter sub-lattice angular momentum transfer is interesting since this component is not present in ferromagnets.
- $\Delta M_T = 0$, $\Delta L = 0$: in this case there is no angular momentum transfer; there is only energy transfer (Table B3).

Unlike in the ferromagnetic case where there is one spin-wave mode, in a two-sublattice antiferromagnet, there are two degenerate (in zero field) magnon modes. Again, using the Holstein-Primakof transformation, the Hamiltonian for a two sublattice AFM can be written as [4,15]:

(B1) $$H = E_0 + 2S\sum_q \{J(0)(a1_q^\dagger a1_q + a2_q^\dagger a2_q) + J(q)(a1_q^\dagger a2_q^\dagger + a1_q a2_q)\}$$

In which $a1$ and $a2$ are the (ferromagnetic) magnon operators for sublattice 1 and 2 respectively. Sublattice one has $S_{z,1}$=+S while sublattice two has $S_{z,2}$=-S. $a1_q^\dagger$ corresponds to an excitation with $\Delta S_{z,1}$=-1 while $a2_q^\dagger$ corresponds to an excitation with $\Delta S_{z,2}$=+1. This non-diagonal Hamiltonian can be diagonalized by a Bogoliobov transformation [2,4,15]. By doing this the AFM magnon operators α and β are written in terms of FM sublattice operators $a1$ and $a2$. For instance:

(B2) $$\alpha_q^\dagger = u_q a1_q^\dagger - v_q a2_{-q} \; ; \; \beta_q^\dagger = u_q a2_{-q}^\dagger - v_q a1_q$$

u_q and v_q can be calculated using:

(B3) $u_q = \cosh(\theta_q)\,;\; v_q = \sinh(\theta_q);\; \theta_q = \frac{1}{2}\, atanh[J(q)/J(0)]$

In this way it is ensured that a single AFM magnon corresponds to an excitation with ΔM=±1. Whereas the α mode corresponds to ΔM=-1 (=> $\alpha_q^\dagger$), the β mode corresponds to ΔM=+1 (=> $\beta_q^\dagger$). Interestingly at an arbitrary q-vector, the antiferromagnetic magnetic moment affects the z-component of both sub-lattices ($\Delta M_1 \neq 0$, $\Delta M_2 \neq 0$). For a certain AFM magnon mode (α or β) and q-vector, using equations (B2) and (B3), the z-component of the total spin of one sublattice can be calculated. For θ_q=0, Eq. (B2) becomes:

(B4) $\alpha_q^\dagger = u_q a1_q^\dagger \quad ; \quad \beta_q^\dagger = u_q a2_{-q}^\dagger$

In this case, the α and β mode makes excitations on sub-lattice 1 and 2, respectively. For very large θ_q (=>$J(q)/J(0)$ close to 1, center Brillioun zone), however, Eq. (B2) becomes:

(B5) $\alpha_q^\dagger \cong \frac{e^{\theta_q}}{2}\left[a1_q^\dagger - a2_{-q}\right]$

(B6) $\beta_q^\dagger \cong \frac{e^{\theta_q}}{2}\left[a2_{-q}^\dagger - a1_q\right]$

In this case the α and β mode makes excitations on both sub-lattices with equal probabilities. Now we will calculate θ_q. We consider the case of a FCC lattice with nearest neighbor exchange. In this case we can write for $J(q)/J(0)$:

(B4) $\frac{J(q)}{J(0)} = \frac{1}{3}\left[\cos\left(\frac{1}{2}q_x a\right)\cos\left(\frac{1}{2}q_y a\right) + \cos\left(\frac{1}{2}q_y a\right)\cos\left(\frac{1}{2}q_z a\right) + \cos\left(\frac{1}{2}q_z a\right)\cos\left(\frac{1}{2}q_x a\right)\right]$

By calculating the probability ($|u_q|^2$, $|v_q|^2$), we can plot ΔM_1 and ΔM_1 for the α mode for different wavevectors, see Fig. B1. We took $q_x = q_y = q_z = q$; this corresponds to the [111] direction.

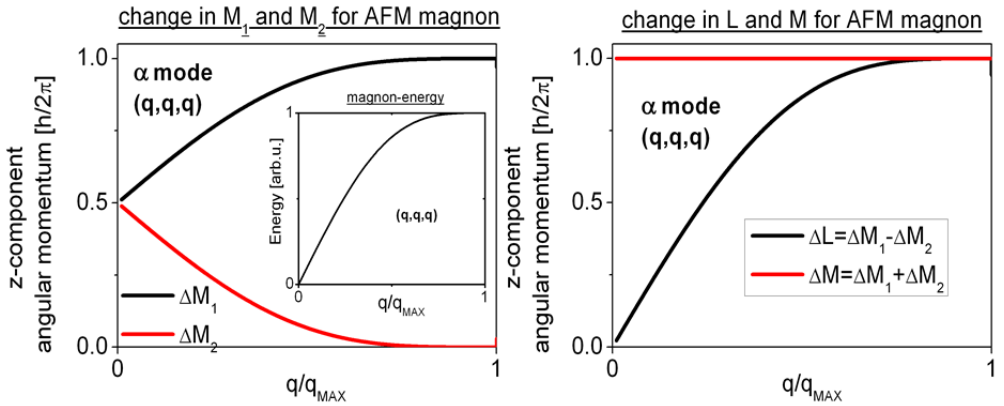

Fig. B1. | ΔM_1 and ΔM_1 for the α mode for different wavevectors (left). The inset shows the magnon energy for a fcc lattice along the [111] direction. ΔL and ΔM for the α mode for different wavevectors (right).

Interestingly, ΔM_1 and ΔM_1 are the same for q=0, while for $q/q_{max}=1$, both component differ by 1. ΔL and ΔM are plotted in the right graph. Whereas ΔM is always one, ΔL can range from 0 (q=0) to about one (q/q_{max}). At q=0, both sub-lattice magnons have the same change in the z-component of the angular momentum $\Delta M_1 = \Delta M_2$.

In the different tables (TableB1-B3), we show ΔM_T and ΔL, but also the value for ΔM_1 and ΔM_2 *at the Brillioun zone boundary* (q_{max}, q_{max}, q_{max}). Examples of magnon scattering terms for which holds $\Delta M_T \neq 0$, are shown in Table B1 [5].

Table B1 | angular momentum transfer to lattice, *M_T not conserved*:
angular momentum transfer to lattice, $\Delta M_T = \Delta M_1 + \Delta M_2 + \Delta S_c \neq 0$

Process	***Example of scattering terms***	***Conditions and systems***
phonon-magnon scattering* (1-magnon)	$b^\dagger\ \alpha$ (ΔM_1=+1, ΔM_2=0, ΔM=+1,ΔL=+1) $b\ \alpha^\dagger$ (ΔM_1=-1, ΔM_2=0, ΔM=-1,ΔL=-1) $b^\dagger b\ \alpha$ (ΔM_1=+1, ΔM_2=0, ΔM=+1,ΔL=+1) $b^\dagger b\ \alpha^\dagger$ (ΔM_1=-1, ΔM_2=0, ΔM=-1,ΔL=-1)	- Localized magnetic moments + phonon - AFM insulator * only 2x this process can lead to inter sub-lattice angular momentum transfer
phonon-magnon scattering (2-magnon)	$\beta^\dagger b\ \alpha$ (ΔM_1=+1, ΔM_2=+1, ΔM=+2,ΔL=0) $\beta\ b\ \alpha^\dagger$ (ΔM_1=-1, ΔM_2=-1, ΔM=-2,ΔL=0)	- Localized magnetic moments + phonon - AFM insulator

Again, these processes can be important when there is a hot lattice but a cold spin-system. Spin-lattice relaxation can bring the two systems (lattice and spins) in

thermal equilibrium. If one looks at the magnon and phonon dispersion curve in EuTe, one can see that can be only energy and momentum conservation for the first two scattering terms in Table B1 when k=0. For the third and fourth term, all phonon everywhere in the Brillioun zone can participate. Like for EuO, since the total electronic angular momentum is not conserved, these processes are expected to be slow (>10 ps). Two magnon processes are expected be only important at even longer time scales (>> 1ns). Also due to the fact that the 2-magnon process requires a large change angular momentum transfer to the lattice (ΔM=±2), we do not expect this mechanism to be relevant on our time scales (< 5ns). Examples of magnon scattering terms for which holds $\Delta M_T=0$, $\Delta L\neq 0$, are shown in Table B2 [5--8,47].

Table B2 | *M_T conserved, L not conserved ($\Delta M_1\neq 0$ or $\Delta M_2\neq 0$)*:
$\Delta M_T=\Delta M_1+\Delta M_2+\Delta S_c=0$, $\Delta L= \Delta M_1-\Delta M_2\neq 0$

Process	***Example of scattering terms***	***Conditions and systems***
4-magnon scattering	$\beta^\dagger\alpha^\dagger\,\alpha^\dagger\alpha$ (ΔM_1=-1, ΔM_2=+1, ΔL=-2) $\beta\,\alpha\,\alpha^\dagger\alpha$ (ΔM_1=+1, ΔM_2=-1, ΔL=+2)	- Localized magnetic moments - AFM insulator
electron-magnon scattering (2-magnon)	$\beta\,c^\dagger{}_\uparrow\,c_\uparrow\,\alpha$ (ΔM_1=+1, ΔM_2=-1, ΔL=+2) $\beta^\dagger\,c^\dagger{}_\uparrow\,c_\uparrow\,\alpha^\dagger$ (ΔM_1=-1,ΔM_2=+1,ΔL=-2)	- Localized magnetic moments + conduction electrons (*without spin-flip*) - AFM semiconductors
electron-magnon scattering* (1-magnon)	$c^\dagger{}_\downarrow\,c_\uparrow\,\alpha$ (ΔM_1=+1, ΔM_2=0 ΔL=+1) $c^\dagger{}_\uparrow\,c_\downarrow\,\alpha^\dagger$ (ΔM_1=-1, ΔM_2=0 ΔL=-1) $c^\dagger{}_\downarrow\,c_\uparrow\,\beta^\dagger$ (ΔM_1=0, ΔM_2=+1 ΔL=+1) $c^\dagger{}_\uparrow\,c_\downarrow\,\beta$ (ΔM_1=0, ΔM_2=-1 ΔL=-1)	- Localized magnetic moments + conduction electrons (*with spin-flip*) - AFM semiconductors * only 2x this process can lead to inter sub-lattice angular momentum transfer
phonon-magnon scattering (2-magnon)	$\beta\,b^\dagger\,\alpha$ (ΔM_1=+1, ΔM_2=-1, ΔL=+2) $\beta^\dagger b\,\alpha^\dagger$ (ΔM_1=-1, ΔM_2=+1, ΔL=-2)	- Localized magnetic moments + phonons - AFM insulator

Like mentioned before, 4 magnon scattering processes are only important at very long timescales (> 1 ns), and we will ignore them later on. What is left are electron-magnon and phonon-magnon scattering processes. The 1-magnon electron-magnon process is similar as in ferromagnets. Two consecutive of these processes can lead to inter-sublattice angular momentum transfer. Inter-sublattice angular

momentum transfer is also possible by a 2-magnon electron-magnon process or by 2-magnon phonon-magnon scattering processes. Since all these processes conserve the total electronic momentum, they are not limited by the slow spin-to-lattice angular momentum transfer, and they can be in principle ultrafast (<<1 ps). As discussed before, 2 magnon processes are expected to be slow (>1 ns). Examples of magnon scattering terms for which holds $\Delta M_T=0$, $\Delta L=0$, are shown in Table B3 [3,5,48,49].

Table B3 | energy transfer, *M_T and L conserved,* ($\Delta M_1=0$ and $\Delta M_2=0$):

$\Delta M_T=\Delta M_1+\Delta M_2+\Delta S_c=0$, $\Delta M=\Delta M_1+\Delta M_2=0$, $\Delta L=M_1-M_2=0$

Process	***Example of scattering terms***	***Conditions and systems***
2-magnon scattering	$\alpha^\dagger\alpha$ *intra-sublattice* $\beta^\dagger\beta$ *intra-sublattice*	- Localized magnetic moments - AFM insulator with defects/impurities
4-magnon scattering	$\alpha^\dagger\,\alpha^\dagger\alpha\,\alpha$ *intra-sublattice* $\beta^\dagger\,\beta^\dagger\beta\,\beta$ *intra-sublattice* $\alpha^\dagger\,\beta^\dagger\alpha\,\beta$ *inter-sublattice*	- Localized magnetic moments - AFM insulator
electron-magnon scattering (2-magnon)	$\alpha^\dagger\,c^\dagger_\uparrow\,c_\uparrow\,\alpha$ *intra-sublattice* $\beta^\dagger\,c^\dagger_\uparrow\,c_\uparrow\,\beta$ *intra-sublattice*	- Localized magnetic moments + conduction electrons (*without spin-flip*) - AFM semiconductors
phonon-magnon scattering (2-magnon)	$\alpha^\dagger b\alpha$ *intra-sublattice* $\beta^\dagger b\beta$ *intra-sublattice*	- Localized magnetic moments + phonon - AFM insulator

The processes in Table B3 describe the case where there is only energy, but not angular momentum transfer. As discussed before, we ignore 2-magnon and 4-magnon scattering processes because they are not important on timescale we are interested in (<5 ns). Now we will consider angular momentum transfer in metals or doped-semiconductors.

Appendix C: angular momentum transfer in metals or doped semiconductors

Until now we discussed the case in which there are magnetically-ordered localized magnetic moments. Now we will consider conduction electrons in metals or in

doped-semiconductors. We will only focus on Stoner excitations in ferromagnetic metals, rather than on magnons which we discussed before. This discussion is also important in systems with both localized and itinerant electrons, because the spin-lattice interaction of itinerant electrons can be much stronger than the spin-lattice interaction of localized magnetic moments. In this case the angular momentum of the localized moments can be transferred to the lattice *via* the itinerant electrons, provided that the coupling between the itinerant electrons and the localized moments is strong. Examples of electron-electron scattering terms (for which holds $\Delta S_c=0$), and electron-phonon scattering terms (for which holds $\Delta S_c=\pm1$) are shown in Table C [50,51].[52]

Table C | angular momentum transfer in metals or doped semiconductors

Process	***Example of scattering terms***	***Description***
Electron-electron scattering: Exchange scattering	$c^{\dagger}{}_{k-q\downarrow}c^{\dagger}{}_{k'+q\uparrow}\,c_{k'\downarrow}c_{k\uparrow}$ ($\Delta S_c=0$)	Angular momentum transfer within the electron system
Electron-phonon scattering: Eliott-Yafet spin-flip scattering	$c^{\dagger}{}_{\uparrow}\,b\,c_{\downarrow}$ ($\Delta S_c=+1$) $c^{\dagger}{}_{\uparrow}\,b^{\dagger}\,c_{\downarrow}$ ($\Delta S_c=-1$)	Angular momentum transfer to/from the lattice

The first case represents the exchange scattering between two conduction electrons and which angular momentum is transferred between an electron which momentum *k* and an electron with momentum *k'*. In this case the electronic angular momentum is conserved. The second case represents the electron phonon scattering between a conduction electron and a phonon in which angular momentum is transferred to/from the lattice. In this case the electronic angular momentum is not conserved. In next section, the results from appendix A-C will be discussed.

Appendix D: summary and discussion

Now we will compare the different mechanism in ferromagnets and antiferromagnets. We consider the following cases:

- Angular momentum transfer to/from lattice: M_T not conserved.
- Energy transfer: M_T conserved, $M/M_1/M_2$ conserved.

- Conduction electron-magnon angular momentum transfer or inter-sublattice angular momentum transfer: $\underline{M_T \text{ conserved}}$, M(FM)/ M_1(AFM)/M_2 (AFM) not conserved. (A)FM= (Anti) Ferromagnet.

Angular momentum transfer to lattice: $\underline{M_T \text{ not conserved}}$

The most important spin-lattice relaxation mechanisms (phonon-magnon scattering, M_T not conserved) in a ferromagnetic insulator and antiferromagnetic insulator are depicted below. In this case energy (and angular momentum) can be transferred from the hot lattice system to the cold magnon system, in ultrafast magnetization dynamics measurements.

phonon-magnon scattering (1-magnon)	FM: $b\ a^\dagger$ (ΔM=-1) FM: $b^\dagger a^\dagger b$ (ΔM=-1) AFM: $b\ \alpha^\dagger$ (ΔM_1=-1, ΔM_2=0, ΔM=-1,ΔL=-1) AFM: $b\ \beta^\dagger$ (ΔM_1=0, ΔM_2=+1, ΔM=+1,ΔL=-1) AFM: $b^\dagger\ \alpha^\dagger\ b$ (ΔM_1=-1, ΔM_2=0, ΔM=-1,ΔL=-1) AFM: $b^\dagger\ \beta^\dagger\ b$ (ΔM_1=0, ΔM_2=+1, ΔM=+1,ΔL=-1)

The terms are very similar in the ferromagnetic and antiferromagnetic case. There is no reason to assume that those spin-lattice relaxation rates will be much different in EuO (FM) than in EuTe. The magnetic excitations are different (energy/nature of excitation) but in both cases the energy scale is small compared to the phonon energies at the Brillioun zone. Note that in the AFM case, that the same amount of degenerate α and β magnons are created; no net magnetization is created. As discussed, because of energy and momentum conservation, only phonons and magnon which wavevectors around q=0 are involved in one-phonon-one-magnon scattering processes in EuO and EuTe. As mentioned in appendix B, at q=0 the magnitude of the spin excitations are equal on both sub-lattices; ΔL=0.

Energy transfer: M_T conserved, $M/M_1/M_2$ conserved

The most important energy transfer mechanisms (from theory) in a ferromagnetic and antiferromagnetic insulator/semiconductor at the sub-nanosecond timescale are depicted below. Both M_T and $M/M_1/M_2$ are conserved (ΔL=0 at Brillioun zone boundary).

electron-magnon scattering (2-magnon)	FM: $a^\dagger\, c^\dagger{}_\uparrow\, c_\uparrow\, a$ (ΔM=0) AFM: $\alpha^\dagger\, c^\dagger{}_\uparrow\, c_\uparrow\, \alpha$ (ΔM_1=0, ΔM_2=0) AFM: $\beta^\dagger\, c^\dagger{}_\uparrow\, c_\uparrow\, \beta$ (ΔM_1=0, ΔM_2=0)
phonon-magnon scattering (2-magnon)	FM: $a^\dagger b a$ (ΔM=0) AFM: $\alpha^\dagger b \alpha$ (ΔM_1=0, ΔM_2=0) AFM: $\beta^\dagger b \beta$ (ΔM_1=0, ΔM_2=0)

Again, the terms are very similar in the ferromagnetic and antiferromagnetic case. Also in this case there is no reason to assume that energy transfer rates will be much different in EuO (FM) than in EuTe. Until now, in the tables we considered the case of magnons with $q = q_{MAX}$. Let us now consider the case (electron-magnon) where an magnon with wavevector q is annihilated and a magnon with wavevector $q + \delta$ is created (δ is small).

L conserved	AFM: ${\alpha_{q+\delta}}^\dagger\, c^\dagger{}_\uparrow\, c_\uparrow\, \alpha_q$ (ΔL=0)
L not conserved	AFM: ${\alpha_0}^\dagger\, c^\dagger{}_\uparrow\, c_\uparrow\, \alpha_{q_{MAX}}$ (ΔL=+1) AFM: ${\beta_0}^\dagger\, c^\dagger{}_\uparrow\, c_\uparrow\, \beta_{q_{MAX}}$ (ΔL=+1) AFM: ${\alpha_{q_{MAX}}}^\dagger\, c^\dagger{}_\uparrow\, c_\uparrow\, \alpha_0$ (ΔL=-1) AFM: ${\beta_{q_{MAX}}}^\dagger\, c^\dagger{}_\uparrow\, \beta_\uparrow\, \alpha_0$ (ΔL=-1)

In this case L is conserved; Δ*L*=0.This does not hold for the case where a magnon with wavevector q_{MAX} is annihilated and a magnon with wavevector $q = 0$ is created. In this case L is not conserved; Δ*L*=+1. We can understand this from the fact the excitation at q_{MAX} is on one sub-lattice while the excitation at $q = 0$ is on both sub-lattices, see appendix B. This means that the thermalization ($q_{MAX} \rightarrow q = 0$) of the magnons leads to an increase in *L* (the $q \rightarrow q_{MAX}$ case corresponds to Δ*L*=-1).

Conduction electron-magnon angular momentum transfer or inter-sublattice angular momentum transfer: <u>M_T conserved, M(FM)/ M_1(AFM)/M_2 (AFM) not conserved</u>

The most important angular momentum transfer mechanisms (from theory) in a ferromagnetic and antiferromagnetic insulator/semiconductor in which M_T is conserved but in which $M/M_1/M_2$ is not conserved, are depicted below.

electron-magnon scattering (1-magnon)	FM: $c^{\dagger}_{\uparrow}\, c_{\downarrow}\, a^{\dagger}$ (ΔM=-1) AFM: $c^{\dagger}_{\uparrow}\, c_{\downarrow}\, \alpha^{\dagger}$ (ΔM_1=-1, ΔM_2=0 ΔL=-1, ΔM=-1) AFM: $c^{\dagger}_{\downarrow}\, c_{\uparrow}\, \beta^{\dagger}$ (ΔM_1=0, ΔM_2=+1 ΔL=+1, ΔM=-1)

These processes can lead to a change in M and L, and we do not expect a large difference in timescales for EuO and EuTe. These processes can be fast when there are a lot of conduction electrons (since M_T is conserved). Two consecutive of these processes (separated by ";") are depicted below.

FM	$a\, c^{\dagger}_{\downarrow}\, c_{\uparrow}$; $c^{\dagger}_{\uparrow}\, c_{\downarrow}\, a^{\dagger}$ (ΔM=0)
AFM	Two operators: ($\alpha^{\dagger}$, α) or ($\beta^{\dagger}$, β) $\alpha_q\, c^{\dagger}_{\downarrow}\, c_{\uparrow}$; $c^{\dagger}_{\uparrow}\, c_{\downarrow}\, \alpha_q{}^{\dagger}$ (ΔM=0, ΔL=0) $\beta_q\, c^{\dagger}_{\uparrow}\, c_{\downarrow}$; $c^{\dagger}_{\downarrow}\, c_{\uparrow}\, \beta_q{}^{\dagger}$ (ΔM=0, ΔL=0) $\alpha_{q_{MAX}}\, c^{\dagger}_{\downarrow}\, c_{\uparrow}$; $c^{\dagger}_{\uparrow}\, c_{\downarrow}\, \alpha_0{}^{\dagger}$ (ΔM=0, ΔL=+1) $\beta_{q_{MAX}}\, c^{\dagger}_{\uparrow}\, c_{\downarrow}$; $c^{\dagger}_{\downarrow}\, c_{\uparrow}\, \beta_q{}^{\dagger}$ (ΔM=0, ΔL=+1) $\alpha_0\, c^{\dagger}_{\downarrow}\, c_{\uparrow}$; $c^{\dagger}_{\uparrow}\, c_{\downarrow}\, \alpha_{q_{MAX}}{}^{\dagger}$ (ΔM=0, ΔL=-1) $\beta_0\, c^{\dagger}_{\uparrow}\, c_{\downarrow}$; $c^{\dagger}_{\downarrow}\, c_{\uparrow}\, \beta_{q_{MAX}}{}^{\dagger}$ (ΔM=0, ΔL=-1)
AFM	Two operators: ($\alpha^{\dagger}$, $\beta^{\dagger}$) creation $\beta_{q_{MAX}}{}^{\dagger}\, c^{\dagger}_{\downarrow}\, c_{\uparrow}$; $c^{\dagger}_{\uparrow}\, c_{\downarrow}\, \alpha_{q_{MAX}}{}^{\dagger}$ (ΔM=0, ΔL=-2) $\beta_0{}^{\dagger}\, c^{\dagger}_{\downarrow}\, c_{\uparrow}$; $c^{\dagger}_{\uparrow}\, c_{\downarrow}\, \alpha_{q_{MAX}}{}^{\dagger}$ (ΔM=0, ΔL=-1) $\beta_{q_{MAX}}{}^{\dagger}\, c^{\dagger}_{\downarrow}\, c_{\uparrow}$; $c^{\dagger}_{\uparrow}\, c_{\downarrow}\, \alpha_0{}^{\dagger}$ (ΔM=0, ΔL=-1) $\beta_0{}^{\dagger}\, c^{\dagger}_{\downarrow}\, c_{\uparrow}$; $c^{\dagger}_{\uparrow}\, c_{\downarrow}\, \alpha_0{}^{\dagger}$ (ΔM=0, ΔL=0)
AFM	Two operators: (α , β) annihilation $\beta_{q_{MAX}}\, c^{\dagger}_{\uparrow}\, c_{\downarrow}$; $c^{\dagger}_{\downarrow}\, c_{\uparrow}\, \alpha_{q_{MAX}}$ (ΔM=0, ΔL=+2) $\beta_0\, c^{\dagger}_{\uparrow}\, c_{\downarrow}$; $c^{\dagger}_{\downarrow}\, c_{\uparrow}\, \alpha_{q_{MAX}}$ (ΔM=0, ΔL=+1) $\beta_{q_{MAX}}\, c^{\dagger}_{\uparrow}\, c_{\downarrow}$; $c^{\dagger}_{\downarrow}\, c_{\uparrow}\, \alpha_0$ (ΔM=0, ΔL=+1) $\beta_0\, c^{\dagger}_{\uparrow}\, c_{\downarrow}$; $c^{\dagger}_{\downarrow}\, c_{\uparrow}\, \alpha_0$ (ΔM=0, ΔL=0)

We can see that depending on the q-vector of the magnon, |ΔL| can be in between 0 and 2 (the gray shaded processes have a nonzero ΔL). From this table we can see that there is only inter sub-lattice angular momentum transfer when one of the following holds:

1) There is a pair of α and β operators (α, β) or ($\alpha^{\dagger}$, $\beta^{\dagger}$) and $q_{\beta}\neq 0$ or $q_{\alpha}\neq 0$.
2) There is a pair of α operators (α, $\alpha^{\dagger}$) with different q.
3) There is a pair of α operators (β, $\beta^{\dagger}$) with different q.

There is maximum inter-sublattice angular momentum transfer for a pair of α and β operators when $q_\beta = q_\alpha = q_{MAX}$. In general we can see that there is only efficient inter-sublattice angular momentum transfer when large q-vector magnons are involved. In the next section we are comparing the dynamics of $\Delta L(t)$ and $\Delta M(t)$ in simple antiferromagnets from a phenomenological point of view. Here we try to see whether there can be a correlation between the $\Delta L(t)$ and $\Delta M(t)$ dynamics. After that there is a conclusion section.

Appendix E: conclusions

Based on appendix A-D we draw the following conclusions about fast (<1 ns) dynamics in AFM insulators or semiconductors:

i. Inter-sublattice angular momentum transfer is only efficient when high q-vectors AFM magnons are involved.

ii. Inter-sublattice angular momentum transfer can be ultrafast when there is a strong (conduction) electron-(AFM) magnon interaction.

iii. Inter-sublattice angular momentum transfer by (AFM) 4-magnon (exchange) scattering processes is expected to be slow (>>1ns).

iv. 1 phonon-1 magnon scattering (direct process) in EuO and EuTe can only happen at the center of the Brillioun zone. In these processes ΔL is conserved while ΔM is not conserved.

v. 2 phonon-1 magnon scattering (Raman process) can happen everywhere in the Brillioun zone in EuO and EuTe. In this case both ΔM and ΔL are not conserved (when q≠0).

vi. In the thermalization of (AFM) magnons, ΔL is not conserved, while ΔM is conserved.

vii. For $B>B_{spin\text{-}flop}$, a simultaneous drop in $|M_1|$and $|M_2|$ (with $\Delta M_1 = -\Delta M_2$) leads to the situation where $\Delta L/L$ and $\Delta M/M$ are fully correlated: $\Delta L_{x,y}(t)/L_{x,y} = \Delta M_z(t)/M_z$.

viii. For $B>B_{spin\text{-}flop}$, a change in $\theta = \angle(M_1, B)$ (with $\angle(M_1, B) = \angle(M_2, B)$) leads to the situation where ΔL and ΔM are anti-correlated: $L_{x,y}/M_z = \tan(\theta)$.

ix. The resonant X-ray magnetic scattering signal (I_{RXMS}) is not always proportional to the AFM order parameter L. This can happen, for instance, when the type of AFM order changes (from type II to type I or III). Of course, a change in the lattice constant can also affect the proportionality.

References

[1] N. Bloembergen, S. Shapiro, P. S. Pershan, and J. O. Artman, Physical Review **114**, 445 (1959).
[2] P. L. Taylor and O. Heinonen, *A Quantum Approach to Condensed Matter Physics* (Cambridge University Press, 2002).
[3] H. Kurebayashi, O. Dzyapko, V. E. Demidov, D. Fang, A. J. Ferguson, and S. O. Demokritov, Nature Materials **10**, 660 (2011).
[4] C. Timm, *Lecture notes: Theory of Magnetism (International Max Planck Research School for Dynamical Processes in Atoms, Molecules and Solids)*, 2011).
[5] A. G. Gurevich and G. A. Melkov, *Magnetization Oscillations and Waves* (CRC Press, 1996).
[6] I. Y. Korenblit and Y. P. Lazarenko, Physica Status Solidi B-Basic Research **71**, K107 (1975).
[7] R. B. Woolsey and R. M. White, Physical Review B **1**, 4474 (1970).
[8] A. A. Samokhvalov, V. V. Osipov, N. I. Solin, A. F. Gunichev, I. A. Korenblit, and A. P. Galdikas, J Magn Magn Mater **46**, 191 (1984).
[9] C. Kittel, *Introduction to Solid State Physics* (Wiley, 1996).
[10] R. Orbach, Proceedings of the Royal Society of London Series A-Mathematical and Physical Sciences **264**, 458 (1961).
[11] R. Orbach, Proceedings of the Royal Society of London Series A-Mathematical and Physical Sciences **264**, 485 (1961).
[12] W. Hubner and K. H. Bennemann, Physical Review B **53**, 3422 (1996).
[13] M. Wietstruk, A. Melnikov, C. Stamm, T. Kachel, N. Pontius, M. Sultan, C. Gahl, M. Weinelt, H. A. Duerr, and U. Bovensiepen, Phys. Rev. Lett. **106**, 127401 (2011).
[14] J. Wang, C. Sun, J. Kono, A. Oiwa, H. Munekata, L. Cywinski, and L. J. Sham, Phys. Rev. Lett. **95**, 167401 (2005).
[15] D. I. Khomskii, *Basic Aspects of the Quantum Theory of Solids: Order and Elementary Excitations* (cambridge university press, 2010).
[16] C. E. Graves, A. H. Reid, T. Wang*, et al*, Nature Materials **12**, 293 (2013).
[17] K. Holldack, N. Pontius, E. Schierle, T. Kachel, V. Soltwisch, R. Mitzner, T. Quast, G. Springholz, and E. Weschke, Appl. Phys. Lett. **97**, 062502 (2010).
[18] A. Mauger and C. Godart, Physics Reports-Review Section of Physics Letters **141**, 51 (1986).
[19] P. Steeneken, *PhD thesis: New light on EuO thin films* (Rijksuniversiteit Groningen, 2002).

[20] H. Kepa, T. Giebultowicz, K. Goldman, V. Nunez, C. Majkrzak, G. Springholz, and G. Bauer, J. Appl. Phys. **81**, 5373 (1997).
[21] T. Giebultowicz, V. Nunez, G. Springholz, G. Bauer, J. Chen, M. Dresselhaus, and J. Furdyna, J. Appl. Phys. **76**, 6291 (1994).
[22] B. Diaz, E. Granado, E. Abramof, P. H. O. Rappl, V. A. Chitta, and A. B. Henriques, Phys. Rev. B **78**, 134423 (2008).
[23] S. M. Scott, *Monte Carlo Simulations of Magnetic Semiconducting Superlattices* (Oregon State University, 2004).
[24] S. M. Scott and T. M. Giebultowicz, J. Appl. Phys. **91**, 8724 (2002).
[25] Holtzber.F, T. R. Mcguire, and Methfess.S, J. Appl. Phys. **37**, 976 (1966).
[26] H. Kepa, G. Springholz, T. Giebultowicz, K. Goldman, C. Majkrzak, P. Kacman, J. Blinowski, S. Holl, H. Krenn, and G. Bauer, Physical Review B **68**, 024419 (2003).
[27] B. Diaz, E. Granado, E. Abramof, P. H. O. Rappl, V. A. Chitta, and A. B. Henriques, Appl. Phys. Lett. **92**, 242511 (2008).
[28] S. J. Blundell, *Magnetism in Condensed Matter* (oxford university press, 2011).
[29] N. F. Oliveira, Y. Shapira, T. B. Reed, and S. Foner, Physical Review B-Solid State **5**, 2634 (1972).
[30] W. Heiss, R. Kirchschlager, G. Springholz, Z. Chen, M. Debnath, and Y. Oka, Physical Review B **70**, 035209 (2004).
[31] Y. Shapira, S. Foner, T. B. Reed, and N. F. Oliveira, Physical Review B-Solid State **5**, 2647 (1972).
[32] T. Kachel, N. Pontius, C. Stamm, M. Wietstruk, E. F. Aziz, H. A. Duerr, W. Eberhardt, and F. M. F. de Groot, Physical Review B **80**, 092404 (2009).
[33] K. Holldack, N. Pontius, E. Schierle, T. Kachel, V. Soltwisch, R. Mitzner, T. Quast, G. Springholz, and E. Weschke, Appl. Phys. Lett. **97**, 062502 (2010).
[34] C. Trabant, N. Pontius, E. Schierle, Weschke E., T. Kachel, Springholz G., K. Holldack, and A. Föhlisch Schüßler-Langeheine C., in *XVIII th International Conference on Ultrafast Phenomena, Lausanne, Switzerland* (EPJ web conferences, 2012).
[35] J. F. Peters, *Resonant soft x-ray scattering studies of the magnetic nanostructure of stripe domains* (Universiteit van Amsterdam, 2003).
[36] A. J. Schellekens and B. Koopmans, Physical Review B **87**, 020407 (2013).
[37] A. Mekonnen, A. R. Khorsand, M. Cormier, A. V. Kimel, A. Kirilyuk, A. Hrabec, L. Ranno, A. Tsukamoto, A. Itoh, and T. Rasing, Physical Review B **87**, 180406 (2013).

[38] E. Heredia, P. Motisuke, P. H. de Oliveira Rappl, M. J. S. P. Brasil, and F. Iikawa, Appl. Phys. Lett. **101**, 092108 (2012).
[39] W. Heiss, R. Kirchschlager, G. Springholz, Z. Chen, M. Debnath, and Y. Oka, Physical Review B **70**, 035209 (2004).
[40] W. Heiss, R. Kirchschlager, G. Springholz, Z. Chen, M. Debnath, and Y. Oka, Phys. Rev. B **70**, 035209 (2004).
[41] R. Akimoto, M. Kobayashi, and T. Suzuki, Journal of the Physical Society of Japan **63**, 4616 (1994).
[42] M. Bass, D. DeCusatis, J. Enoch, V. Lakshminarayanan, G. Li, C. MacDonald, V. Mahajan, and Van Stryland E, *Handbook of Optics, Third Edition Volume IV: Optical Properties of Materials, Nonlinear Optics, Quantum Optics* (McGraw Hill Professional, 2009).
[43] F. Rys, J. S. Helman, and Baltensp.W, Physik Der Kondensiterten Materie **6**, 105 (1967).
[44] G. Guntherodt, Physics of Condensed Matter **18**, 37 (1974).
[45] G. Guntherodt, P. Wachter, and D. M. Imboden, Physik Der Kondensiterten Materie **12**, 292 (1971).
[46] P. Wachter and P. Weber, Solid State Commun. **8**, 1133 (1970).
[47] E. G. Petrov, Soviet Physics Jetp-Ussr **25**, 524 (1967).
[48] J. Goulon, A. Rogalev, F. Wilhelm, G. Goujon, C. Brouder, A. Yaresko, J. Ben Youssef, and M. V. Indenbom, J Magn Magn Mater **322**, 2308 (2010).
[49] J. Igarashi and A. Watabe, Physical Review B **43**, 13456 (1991).
[50] B. Koopmans, G. Malinowski, F. Dalla Longa, D. Steiauf, M. Faehnle, T. Roth, M. Cinchetti, and M. Aeschlimann, Nature Materials **9**, 259 (2010).
[51] G. M. Mueller, J. Walowski, M. Djordjevic*, et al*, Nature Materials **8**, 56 (2009).
[52] M. G. Muenzenberg, Nature Materials **9**, 184 (2010).

Samenvatting

In dit proefschrift worden magnetische materialen bestudeerd. Magnetische materialen kan je onderverdelen in verschillende categorieën. Zo heb je goede elektrische geleiders zoals de bekende magnetische metalen ijzer, nikkel en kobalt. In deze materialen is er een hoge concentratie van elektronen die bijdragen aan de elektrische geleiding (geleidingselektronen). Ook heb je materialen die zeer slecht stroom geleiden, zogenaamde isolatoren, waarin de geleidingselektron concentratie zeer laag is. Verschillende magnetische ceramische materialen vallen hieronder.

Zeer interessant zijn magnetische materialen met geleidingskarakteristieken tussen een metaal en een isolator in, de magnetische halfgeleiders. In een halfgeleider is de geleidingselektron concentratie vrij laag maar kan door middel van het introduceren van onzuiverheden (het doteren) de geleidingselektronconcentratie worden veranderd. Terwijl de niet-gedoteerde halfgeleiders zich meer gedragen als een isolator, kan een sterk gedoteerde halfgeleider zich meer gedragen als een metaal.

In dit proefschrift worden de algemeen bekende magnetische halgeleiders EuO en EuTe bestudeerd. EuO bevat europium atomen met ongepaarde spins hetgeen betekent dat elk europium atoom een klein magneetje is. In EuO hebben verschillende Eu atomen op een zodanige manier interactie met elkaar dat bij lage temperatuur het magnetisch moment van alle Eu atomen dezelfde kant is opgericht. Beneden een bepaalde temperatuur, de magnetische ordeningstemperatuur T_c, is er dan een (netto) magnetische polarisatie. Een materiaal waarin dit gebeurt wordt een ferromagneet genoemd. Niet-gedoteerd EuO is een ferromagnetische halgeleider.

Het interessante aan EuO is dat dotering kan leiden tot een grote verandering in zowel de geleiding als in de magnetische eigenschappen. De geïntroduceerde geleidingselektronen kunnen de interactie tussen verschillende europium atomen (magneetjes) versterken zodat de magnetische ordeningstemperatuur T_c omhoog gaat. Het doteren van EuO kan er echter ook toe leiden dat EuO zich gaat gedragen als een metaal beneden T_c. Nabij de magnetische ordeningstemperatuur is er een zeer sterke correlatie tussen de magnetische polarisatie in het materiaal en de weerstand van het materiaal. Bij deze temperatuur kan het aanbrengen van een klein magnetisch veld leiden tot een dramatische verlaging van de weerstand

(enkele orde-groottes). Om deze effecten te kunnen begrijpen moet men in detail kijken naar de interactie tussen de geleidingselektronen en de gelokaliseerde magnetische momenten, en dit is het onderwerp van dit proefschrift. Het doel is om de interactie tussen de geleidingselektronen en de gelokaliseerde magnetische momenten beter te begrijpen en op deze manier nieuw licht te laten schijnen op de intrigerende magnetische, optische en geleidingseigenschappen van EuO. Een uitgebreide introductie in het onderwerp wordt gegeven in Hoofdstuk 1. Ook wordt hierin kort beschreven welke optische experimentele technieken zijn gebruikt in dit proefschrift om dit probleem aan te pakken.

In Hoofdstukken 4-7 van dit proefschrift worden experimenten beschreven waarin de geleidingselektron concentratie wordt vergroot waarna er vervolgens wordt gekeken hoe de magnetische en geleidingseigenschappen zijn veranderd. In ons geval wordt de geleidingselektronconcentratie niet veranderd op de gebruikelijke manier (door middel van het introduceren van onzuiverheden) maar is deze verandert door het materiaal optisch te exciteren. Door de absorptie van licht met een golflengte van 800 nm (nabij-infrarood licht) worden elektronen geëxciteerd vanuit gelokaliseerde toestanden (4*f*) naar de geleidingsband (5*d*), waarin ze uiteindelijk kunnen bijdragen aan de elektrische geleiding. Doordat de geleidingselektronen een sterke magnetische uitwisselingsinteractie hebben met de elektronen in de gelokaliseerde toestanden (4*f*), is de positie van de geleidingsband ten opzichte van de gelokaliseerde toestanden afhankelijk van de grootte van de magnetische (4*f*) polarisatie van het materiaal. Dit betekent dat beneden en boven de magnetische ordeningstemperatuur, het optische absorptie spectrum in het nabije infrarood sterk van elkaar verschilt. De sterke absorptie piek in het nabij-infrarood verschuift (ongeveer 300 meV) naar lagere energieën beneden T_c.

Om beter te begrijpen wat er precies gebeurt wanneer we het materiaal optisch doteren, is in Hoofdstuk 2 het optische en magneto-optische spectrum gemodelleerd als functie van temperatuur en aangebracht magneetveld. Hiervoor is een methode uit de literatuur, die alleen het spectrum kan uitrekenen bij een temperatuur van 0 K, verder uitgebreid om zo ook de temperatuursinvloeden te kunnen beschouwen. Hoofdstuk 2 dient verder ook als introductie in de elektronische en optische eigenschappen van EuO. Uit de simulaties is naar voren gekomen dat de verschuiving van de sterke absorptie piek (in het nabij infrarood) niet alleen het gevolg is van de verschuiving van de positie van de geleidingsband (5*d*) maar ook het gevolg is van de veranderingen in de omvang van de optische

matrix elementen beneden T_c. Ook kwam naar voren dat de sterke magneto-optische effecten in EuO worden veroorzaakt door de sterke *4f* spin-baan koppeling in de eindtoestand (na foto-excitatie). De magneto-optische effecten worden in Hoofdstuk 5 en 7 gebruikt om de magnetische polarisatie op een optische wijze te meten.

In Hoofdstuk 3 wordt een introductie gegeven in wat er in verschillende categorieën magnetische materialen (metalen, halfgeleiders en half-metalen) gebeurt met de magnetische polarisatie na een optische excitatie. In dit hoofdstuk worden experimenten beschreven waar vrije- en geleiding elektronen in deze materialen worden geëxciteerd of gegenereerd door middel van een zeer sterke ultrakorte (10^{-13} s = 100 fs) laser puls, net als wij hebben gedaan in experimenten op EuO (en EuTe) die worden beschreven in Hoofdstuk 4-7.

In de literatuur zijn er verschillende manieren bekend over hoe zo'n optische excitatie kan leiden tot een verandering in de magnetische polarisatie. De magnetische polarisatie kan alleen veranderen wanneer er een overdracht is van impulsmoment van de elektronische spins naar het kristalrooster. Door de magnetische polarisatie dynamica te meten, meet men uiteindelijk dus de spin-rooster impulsoverdracht. Echter door naar de tijdschalen (en mechanismen) te kijken waarop dit gebeurt, kan informatie worden verkregen over de interactie tussen de geleidingselektronen en de gelokaliseerde magnetische ($4f^7$) momenten. Hieronder bespreken we in het kort de twee meest belangrijke universele spin-rooster relaxatie mechanismen die zijn geobserveerd in verschillende materialen en die uitgebreid zijn beschreven in de literatuur.

Direct na foto-excitatie zijn de geleidingselektronen warm. Verschillende relaxatie paden kunnen ervoor zorgen dat de magnetische polarisatie in een materiaal verandert. Zo kunnen geleidingselektronen worden verstrooid door onzuiverheden of fononen. Door de spin-baan koppeling is er bij elke verstrooiing een kans dat de spin van geleidingselektron flipt, met een verandering van de magnetische polarisatie tot gevolg. In nikkel kunnen deze effecten ervoor zorgen dat er een sterke daling van de magnetische polarisatie optreedt. Doordat de hete geleidingselektronen sterk worden verstrooid, gebeurt deze verlaging op een tijdschaal van rond de 100 fs. Om zulke snelle processen te kunnen waarnemen, wordt de magnetische polarisatie gemeten met een zeer korte (100 fs) optische puls waarvan de timing ten opzichte van de optische excitatie puls kan worden veranderd. Op een stroboscopische manier kan zo via magneto-optische effecten, de magnetisatie worden gevolgd in tijd.

Ook zijn er materialen waarin een ander relaxatie pad kan leiden tot een aanzienlijke verandering in de magnetische polarisatie. Na honderden femtosecondes of enkele picosecondes, zullen in de meeste materialen de geleidingselektronen zijn afgekoeld en hebben ze hun energie overgebracht aan het kristalrooster. Nu kan het warme kristalrooster op zijn beurt weer interactie hebben met de magnetische momenten wat kan leiden tot een verlaging van de magnetische polarisatie. Dit kan worden begrepen doordat anisotrope fluctuaties van het kristalveld koppelen met het orbitaal impulsmoment, welke op zijn beurt weer is gekoppeld aan het spin impulsmoment. Door in EuO te kijken naar hoe de magnetische polarisatie verandert in de tijd na een optische excitatie, kan informatie worden verkregen over hoe de geleidingselektronen invloed hebben op de magnetische eigenschappen van EuO. Verschillende magnetische polarisatie dynamica experimenten worden beschreven in Hoofdstuk 4 en 5.

In Hoofdstuk 4 worden experimenten beschreven waarin EuO is geëxciteerd met een sterke korte (ongeveer 100 fs) nabij-infrarode laserpuls. Vervolgens is de magnetische polarisatie gemeten met een circulair gepolariseerde zachte-Röntgen lichtpuls van 50 picoseconden (ps) op een stroboscopische manier. Voor de experimenten met zachte Röntgen pulsen ($h\nu \approx 1150$ eV) hebben we twee succesvolle onderzoeksvoorstellen geschreven en zijn we naar een synchrotron faciliteit gegaan (BESSY in Berlijn). Het meten van de magnetische polarisatie met zachte Röntgen pulsen garandeert dat de meting zuiver is, terwijl met de meer gangbare magnetische metingen gebruikmakende van nabij-infrarood/ultraviolet dit niet altijd het geval is. Extra controles zijn is dat geval nodig om de zuiverheid te verifiëren. Een nadeel in onze experimenten met zachte-Röntgen pulsen was wel de beperkte tijdsresolutie van 50 ps.

Uit de experimenten gebruikmakende van met de zachte-Röntgen pulsen kwam naar voren dat de daling in de magnetische polarisatie na een optische excitatie een stuk langzamer is als in magnetische metalen als nikkel. In de literatuur in nikkel werd een verlaging van de magnetische polarisatie gezien met een exponentiële tijdsconstante van ongeveer 100 fs, terwijl de verlaging in EuO gebeurt met een tijdsconstante in de orde van 1-3 nanoseconde. Dit laat zien dat de spin-rooster koppeling vrij zwak is in EuO. Dit komt als een verassing omdat na foto-excitatie, de foto geëxciteerde europium ($4f^6$) momenten een sterke spin-baan koppeling hebben, wat meestal ook resulteert in een sterke spin-rooster koppeling. Zoals eerder werd gezegd is deze sterke spin-baan koppeling de reden voor de sterke magneto-optische effecten in EuO. Het feit dat we hebben waargenomen

dat er een zwakke spin-rooster koppeling is suggereert dat er iets interessants gebeurt in EuO, en dat misschien inderdaad de geleidingselektronen hierin een rol spelen.

Meer informatie hierover kan worden verkregen door het experiment te herhalen met een betere tijdsresolutie. Dit is gedaan in Hoofdstuk 5 gebruikmakende van ultraviolet excitatie-pulsen en nabij-infrarode meet-pulsen met een lengte van ongeveer 100 fs. Net als in de Röntgen meet-puls experimenten, werd hier ook een langzame component met een tijdsconstante van een nanoseconde waargenomen. Echter er werd ook een snelle, sub-picoseconde, verlaging van de magnetische polarisatie waargenomen, die werd opgevolgd door een herstel (een groei in de magnetische polarisatie tot het oude niveau) met een tijdsconstante van enkele tientallen picoseconden. Het complexe gedrag van de magnetische polarisatie in de tijd (een verlaging gevolgd door een verhoging en daarna weer een verlaging) is vrij uniek en laat zien dat er twee magnetische subsystemen zijn die elk hun eigen interactie hebben met het rooster, met de geleidingselektronen en met elkaar. Eén magnetische subsysteem bestaat uit de niet geëxciteerde Eu atomen ($4f^7$) terwijl het andere subsysteem bestaat uit geëxciteerde Eu atomen ($4f^6$). Het interessante complexe gedrag van de magnetische polarisatie kan nu als volgt worden verklaard. Op sub-picoseconde tijdschaal is er een daling in de magnetische polarisatie (ook wel demagnetisatie genoemd) omdat de hete geleidingselektronen spin-flip verstrooien aan fononen en geëxciteerde Eu atomen ($4f^6$). Doordat er een sterke magnetische uitwisselingsinteractie is tussen de geleidingselektronen en de gelokaliseerde Eu ($4f$) momenten, leidt de demagnetisatie van de geleidingselektronen ook tot een demagnetisatie van de gelokaliseerde Eu ($4f$) momenten.

De toename van de magnetische polarisatie op een tijdschaal van enkele tientallen picoseconden kan worden verklaard doordat er zogenaamde magnetische excitonen worden gevormd. Een magnetisch exciton is een quasi-deeltje waarin een negatief geladen geleidingselektron is gebonden aan een positief geladen Eu $4f^6$ atoom (wat je kunt zien als een gat), net als in een normaal exciton. Echter een magnetisch exciton wordt ook gestabiliseerd door de magnetische uitwisselingsinteractie tussen het gebonden elektron en de gelokaliseerde momenten van de naaste buren van het gat ($4f^6$). Deze uitwisselingsinteractie heeft tot gevolg dat er een toename is van de magnetische polarisatie rond het positief geladen Eu $4f^6$ atoom op een tijdschaal van enkele picoseconden. Hierbij is er een

impulsmoment overdacht nodig van het kristalrooster terug naar de magnetische excitonen.

De nanoseconde afname van de magnetische polarisatie kan worden verklaard door een impulsmoment overdacht van de niet exciteerde Eu atomen ($4f^7$) en (complete) magnetische excitonen naar het inmiddels warme kristalrooster. Deze resultaten laten zien dat de geleidingselektron-gelokaliseerde magnetische moment interactie kan leiden tot opmerkelijke effecten.

Meer over deze interactie kan worden geleerd door ook de elektrische geleiding te meten als functie van de tijd tussen de excitatie en meet puls. Dat is gedaan in Hoofdstuk 6. Om de elektrische gelding te meten als functie van de tijd, met picoseconde tijdsresolutie, is ook een optische techniek gebruikt. Met ultrakorte, laag frequente terahertz (= 10^{12} Hz, laag vergeleken met typische optische frequenties) optische pulsen kan de optische geleiding worden gemeten door naar de transmissie door het materiaal te kijken. Deze transmissie coëfficiënt kan vervolgens direct worden gerelateerd aan de elektrische geleiding. Via deze optische techniek hebben we ons sample gekarakteriseerd en hebben we laten zien dat er ook in ons sample een metaal-isolator overgang nabij de magnetische ordeningstemperatuur is. Vervolgens hebben we de elektrische geleiding gemeten als functie van de tijd na een korte optische excitatie puls. Hieruit kwamen twee interessante punten naar voren.

Ten eerste hebben we laten zien dat er direct na de excitatie puls niet meteen een toename is in de geleiding, maar dat dit pas na honderden femtoseconden gebeurt bij lage temperatuur. Dat betekent dat er naar een toestand wordt geëxciteerd waarvan de elektrische geleiding slecht is. Dit kan worden verklaard als er wordt aangenomen dat er op tijd t=0 een (magnetisch) exciton wordt gevormd met een lage elektrische geleiding. Vervolgens dissocieert het (magnetische) exciton na enkele honderden femtoseconden waarbij er geleidingselektronen ontstaan. Dit is een belangrijk resultaat dat aangeeft dat de belangrijkste piek in het absorptie spectrum in het nabij-infrarode gebied misschien wel niet voortkomt uit een excitatie naar een geleidingsband, maar een exciton piek is (met toestanden afgeleid van de geleidingsband).

Een afname in de elektrische geleiding op een tijdschaal van ongeveer 20 ps kan worden verklaard als wordt aangenomen dat er magnetische polaronen wordt gevormd met een lagere mobiliteit dan de vrije geleidingselektronen. Een vrije magnetisch polaron is een geleidingselektron met een wolk van magnetische polarisatie om zich heen. Deze quasi-deeltjes kunnen ontstaan doordat de lokale

magnetische polarisatie de energie van het geleidingselektron verlaagd via de sterke magnetische uitwisselingsinteractie. Bij lage temparuur is de mobiliteit van magnetische polaronen hoog doordat het materiaal magnetisch geordend is. Bij hogere temperatuur is de mobiliteit van de magnetische polaronen laag doordat als het geleidingselektron zich beweegt door het kristal, er op elke nieuwe locatie een nieuwe wolk van magnetische polarisatie moet worden gevormd. De temperatuursafhankelijkheid van de 20 ps component van het geleidingssignaal kan worden verklaard ervan uitgaande dat er magnetische polaronen worden gevormd en de mobiliteit van deze magnetische polaronen afhangt van de temperatuur.

Tot slot wordt er in Hoofdstuk 7 gekeken naar de magnetische polarisatie dynamica in EuTe. EuTe heeft een soortgelijke kristalstructuur en heeft soortgelijke elektronische en eigenschappen als EuO. Echter doordat de roosterconstante verschilt ten opzichte van EuO is de magnetische structuur anders. In EuO heb je ferromagnetisch geordende lagen (magnetische momenten parallel) en is er ook een ferromagnetisch interactie tussen de verschillende lagen. In EuTe zijn de lagen ook ferromagnetisch geordend maar is een anti-ferromagnetische interactie (anti-parallel) tussen de verschillende lagen. Dit maakt EuTe een antiferromagneet met twee magnetische sub-roosters (met anti-parallelle oriëntatie). Interessant aan antiferromagneten is de mogelijkheid van overdacht van impulsmoment tussen deze twee verschillende sub-roosters na een optische excitatie. Dit leid tot een verandering in de anti-ferromagnetische ordeningsparameter.

In Hoofdstuk 7 is geprobeerd een kader te creëren waarin experimenten kunnen worden geïnterpreteerd waar de anti-ferromagnetische ordeningsparameter is gemeten na een optische excitatie puls. Zulke experimenten op EuTe zijn beschreven in de literatuur maar zijn daarin niet gemodelleerd. In Hoofdstuk 7 presenteren we ook een beperkte hoeveelheid data waarin de magnetische polarisatie dynamica in EuTe is gemeten als functie van de tijd. Om een magnetische polarisatie te creëren werd een klein magneet veld aangebracht. Vervolgens zijn voor het eerst de ferromagnetische ordeningsparameter (de magnetische polarisatie) en de anti-ferromagnetische ordeningsparameter in een materiaal (EuTe) met elkaar zijn vergeleken. Een combinatie van deze metingen heeft de potentie om een goed beeld te krijgen van de overdacht van impulsmoment tussen twee verschillende magnetische sub-roosters, en van magnetische polaron en exciton formatie in EuTe (en EuO).

In dit proefschrift heb ik laten zien dat moderne optische technieken kunnen bijdragen aan een de fundamentele kennis over de magnetische, optische en geleidingseigenschappen van EuO en EuTe. In het bijzonder hebben we gekeken naar het bestaan van en het gedrag van verschillende quasi-deeltjes zoals magnetische polaronen en magnetische excitonen in EuO en EuTe. De nieuw opgedane kennis kan bijdragen aan technologische ontwikkelingen in de optische controle van de magnetische- en geleidingseigenschappen van magnetische materialen die uiteindelijk kunnen leiden tot diverse applicaties. Ook kan het bijdragen aan de ontwikkeling van nieuwe magnetische halfgeleiders met een hogere magnetische ordeningstemperatuur.

Acknowledgements

In order to obtain a PhD degree one has to show that one is able to carry out independent scientific research. However, the research described in this thesis could not have been accomplished without the support of many people. Those persons I will acknowledge below.

Prof. Paul van Loosdrecht. You designed the EuO project already quite some time ago. I started working on it from the beginning, and even after all those years, I am still enthusiastic about this very nice and challenging project. By now you started a new group in Cologne. I wish you all the best with this important step in your career.

The project would not have been possible without good EuO samples. I want to thank Prof. Hao Tjeng, Dr. Simone Altendorf and Dr. Ronny Sutarto for giving me high quality samples, but also for sharing your expertise on the physics of EuO and XMCD.

The XMCD proposal for the measurements at BESSY was written together with Dr. Niko Pontius and Prof. Hermann Dürr. I want to thank you for your support on the EuO XMCD project.

I also want to acknowledge the members of the reading committee, Prof. Bert Koopmans, Prof. Ria Broer, and Prof. Hao Tjeng for reading my thesis and for giving me very useful feedback.

During a PhD it is important to be surrounded by good and nice group members. I especially want to acknowledge the group members which were directly or indirectly involved in the EuO project:

Matteo, I want to thank you for your input on the XMCD and THz chapter and for joining me to Berlin for the synchrotron measurements. It was nice to be your office mate, and I really enjoyed the dinner parties at your house.
Toni, I really enjoyed working with you, and I will remember our numerous scientific discussions, coffee breaks, dinners and beers. I cannot express in words how important you were for me during my PhD. Thanks you so much for being a perfect colleague and a good friend! Also thanks for being my paranymph.
Dima (Fishman), you are one of my teachers in optics and a good friend. Thank you so much for this. During my master and later on during my PhD, we spend so much time in the lab and I am still impressed by your experimental skills!
Special thanks go to our very helpful technicians Ben, Foppe and Arjen, to our secretary Jeannette, to my student Ryota, and to Dmitry (Mazurenko) for his help during the initial phase of the project.
During a PhD it is important to also have support from people which were not directly involved in the PhD project. I want to thank my Aegir/Gyas/Hunze rowing team members, the Polish community, and the chemistry guys. I especially want to thank my paranymph and dear friend Hans. Thanks so much for making my cover, and I will remember our bike rides & beers.
It feels great to be always supported by my family. I want to thank my parents, my brother, and Ira for showing so much interest in my PhD project and for your great support.
The last words in this acknowledgements are for you, Justyna. The best thing that happened during my PhD was meeting you! You are a wonderful person, and I want to thank you so much for your patience, interest and support last years, which was very important for me. Love you!

Michiel, May 2014